

CHARACTERIZATION OF URANIUM METAL ALLOY FUEL FORMS FOR
ADVANCED NUCLEAR REACTOR APPLICATIONS

A Dissertation

by

BRANDON JAMES BLAMER

Submitted to the Office of Graduate and Professional Studies of
Texas A&M University
in partial fulfillment of the requirements for the degree of

DOCTOR OF PHILOSOPHY

Chair of Committee,	Sean McDeavitt
Committee Members,	Pavel Tsvetkov
	Tahir Cagin
	Delia Perez-Nunez
	Luis Ortega

Head of Department,	Yassin Hassan
---------------------	---------------

May 2017

Major Subject: Nuclear Engineering

Copyright 2017 Brandon James Blamer

ABSTRACT

An engineering investigation of the fabrication process for low smear density uranium alloy nuclear fuel forms was completed and the resulting alloys were characterized. The metal fuel alloys investigated in this project were uranium metal, uranium – 5 wt% zirconium (U-5Zr), and uranium – 10 wt% zirconium (U-10Zr). The physical fuel forms of interest included 1) dense, solid rods that could be used in low smear density nuclear fuel applications, 2) extruded tubes designed to begin fuel service in constant contact with cladding yet having a low smear density, and 3) low density pellets designed to simulate low density fuel structures.

Extrusion was shown to be an industrially viable option for the production of uranium and U-10Zr rods and tubes. Extrusion experiments were performed in the uranium alpha phase in the temperatures range of 550 to 650°C. The reduction ratio was varied between 4 and 15. The extrusion constant, K , was empirically estimated from the data collected and ranged from 45 to 160 ksi over the course of this study. Larger extrusion ratios as well as higher temperatures resulted in lower extrusion constants.

The microstructures of the extruded products were studied using scanning electron microscopy and neutron diffraction. The specimens exhibited elongated grains in the extrusion direction. The U-10Zr also displayed aligned and elongated α zirconium grains. Neutron diffraction of the U-10Zr product revealed α uranium texture in the (100) and (110) direction as well as δ -UZr₂ texture in the (0001) direction. The δ -UZr₂ texture was found to persist through high temperature heat treatment, but the α uranium texture did not.

To examine low density porous alloys, U, U-5Zr, and U-10Zr powders were fabricated with a range of densities from ~45 to ~89 %TD. The resulting alloy microstructures were characterized via scanning electron microscopy. The structures of the pellets were typically homogeneous. The microstructures created were similar to the microstructures of fuel that has undergone irradiation swelling.

The porosity-dependent thermal diffusivity of the alloys was measured in the temperatures range of 20 to 300°C. As sample porosity increased, the diffusivity was observed to decrease linearly over the entire sample set. Diffusivity values for uranium ranged from 10.7 mm²/s at 88.6 %TD and 300°C to 2.54 mm²/s at 46.6 %TD and 30°C. The empirical relationship between the thermal conductivity and porosity corresponded well with the predicted values from the effective medium theory structural model for modelling the thermal conductivity of two phase materials.

ACKNOWLEDGEMENTS

I would like to thank Dr. McDeavitt and my committee as well as my fellow FCML students, for their guidance and support throughout the course of this research.

Thank you to TerraPower for giving me the wonderful opportunity to work on this important research project.

Thanks also go to my friends, colleagues, and the nuclear engineering department faculty and staff for making my time at Texas A&M University a great experience.

Finally, I would like to thank my family for their support and encouragement throughout my education at Texas A&M University and throughout the course of this research project.

CONTRIBUTORS AND FUNDING SOURCES

Contributors

This work was supported by a dissertation committee consisting of Professor Sean M. McDevitt [advisor] and Pavel Tsvetkov and Delia Perez-Nunez and Luis Ortega of the Department of Nuclear Engineering and Professor Tahir Cagin of the Department of Material Science and Engineering.

The U, U-5Zr, and U-10Zr, powders and pellets used in this research project were fabricated with the assistance of Dr. Luis Ortega and Karyn Stern of the Department of Nuclear Engineering. The neutron diffraction analysis was performed with the assistance of Sandeep Irukuvarghula and Sven Vogel at the HIPPO diffractometer at the Lujan Center of the Los Alamos Neutron Science Center.

All other work conducted for the dissertation was completed by the student independently.

Funding Sources

Graduate study and dissertation research was primarily funded by TerraPower. Secondary, partial support was received from the Nuclear Engineering Department of Texas A&M University.

NOMENCLATURE

FCML	Fuel Cycle and Materials Laboratory
U	Depleted Uranium Metal
U-10Zr	Uranium – 10wt% Zirconium Alloy
U-5Zr	Uranium – 5wt% Zirconium Alloy
LVDT	Linear Variable Differential Transformer
SEM	Scanning Electron Microscope
EBSA	Electron Back Scatter Diffraction
BSE	Back Scatter Electron
EDX	Energy Dispersive X-ray Spectroscopy
LC	Load Cell
TC	Thermocouple
LFA	Light Flash Apparatus
HDH	Hydride/de-hydride Process
UHP	Ultra-High Purity, in reference to argon gas of purity 99.999%
FIMA	Fissions per Initial Metal Atom
HV	Vickers Hardness

TABLE OF CONTENTS

	Page
ABSTRACT	ii
ACKNOWLEDGEMENTS	iv
CONTRIBUTORS AND FUNDING SOURCES	v
NOMENCLATURE.....	vi
TABLE OF CONTENTS	vii
LIST OF FIGURES.....	x
LIST OF TABLES	xix
1 INTRODUCTION.....	1
2 BACKGROUND.....	6
2.1 Uranium and Uranium-zirconium Alloy Nuclear Fuel.....	6
2.2 Rod, Tube, and Low Density Pellet Fuel Forms and Swelling	8
2.3 Extrusion Theory	10
2.4 Pressing and Sintering of Metal Powder Pellets.....	13
2.5 Thermal Conductivity in Nuclear Fuel	14
2.6 Heat Transfer in a Porous Medium.....	15
3 EXPERIMENTAL METHODS.....	20
3.1 Extrusion Experiments	20
3.2 Extrusion Experimental Set Up	21
3.3 Extrusion Experiment Procedure.....	26
3.4 Extrusion Tooling	28
3.5 Heat Treatment of Tool Steel	32
3.6 Test Extrusions	35
3.7 Preparation of Uranium Billets for Extrusion.....	45
3.7.1 Melt Casting Procedure	45
3.7.2 U-10Zr Billets.....	47
3.7.3 Uranium Billets.....	48
3.7.4 Reusable Graphite Casting Mold.....	50
3.8 Production of Powder for Use in Pellet Manufacturing	52
3.9 Production of U, U-5Zr, and U-10Zr Pellets	54

3.10	Density Measurements	56
3.11	Light Flash Analysis (LFA) Technique.....	58
3.12	Preparation of Samples for Microstructure Analysis	62
3.13	Electron Microscopy of Samples.....	63
3.14	Neutron Diffraction	64
4	RESULTS	65
4.1	U-10Zr Rod Extrusions	65
4.1.1	Extrusion 1.....	65
4.1.2	Extrusion 2.....	68
4.1.3	Extrusion 3.....	70
4.1.4	Extrusion 4.....	74
4.1.5	Extrusion 5.....	78
4.1.6	Extrusion 6.....	81
4.1.7	Extrusion 11.....	85
4.1.8	Extrusion 13.....	88
4.2	U Tube Extrusions	91
4.2.1	Extrusion 7.....	91
4.2.2	Extrusion 8.....	94
4.2.3	Extrusion 9.....	97
4.2.4	Extrusion 10.....	100
4.3	U Rod Extrusions.....	103
4.3.1	Extrusion 12.....	103
4.4	Microstructure Analysis of Extruded Products	106
4.5	Neutron Diffraction Results.....	117
4.6	Thermal Conductivity of Uranium Pellets.....	123
4.7	Thermal Conductivity of U-5Zr Pellets.....	126
4.8	Thermal Conductivity of U-10Zr Pellets.....	128
4.9	Microstructure Analysis of Low Density Pellets.....	130
5	DISCUSSION	147
5.1	Comments on the Extruded U and U-10Zr Products.....	147
5.2	Observations from Extrusion Tooling Development.....	148
5.3	Temperature Rise during Extrusion.....	150
5.4	Extrusion Constant	151
5.5	Extruded Grain Structure.....	154
5.6	Neutron Diffraction Analysis of Extruded U-10Zr	158
5.7	Thermal Conductivity of Low Density Pellets	159
5.8	Microstructure of LFA Pellets.....	168
6	CONCLUSION	173

REFERENCES.....	177
APPENDIX 1	183
APPENDIX 2	192
APPENDIX 3	193
APPENDIX 4.....	218
APPENDIX 5	219
APPENDIX 6	247
APPENDIX 7	252

LIST OF FIGURES

	Page
Figure 2-1: Assessed U-Zr phase diagram with selected experimental data. Reprinted with permission from Springer. [12]	7
Figure 2-2: Schematic of the direct extrusion of a tube	11
Figure 2-3: Example force vs time curve	12
Figure 2-4. Physical representation of each structural model	16
Figure 2-5: Comparison of 6 fundamental models with $k_1/k_2=100$	19
Figure 3-1: Enerpac 100 ton press and control unit	22
Figure 3-2: Press head before repair	23
Figure 3-3: The load cell used for all extrusion experiments.....	24
Figure 3-4: Load cell set up.....	25
Figure 3-5: Final tooling design (side view)	31
Figure 3-6: Final tooling design (bottom view)	32
Figure 3-7: Extrusion tooling sealed in steel foil	34
Figure 3-8: (Left) Thermolyne furnace (Right) Lindberg furnace	34
Figure 3-9: Copper rod test 1	36
Figure 3-10: Copper tube test 1	37
Figure 3-11: Tooling used in copper tube test 2.....	38
Figure 3-12: Copper tube test 2.....	38
Figure 3-13: Copper tube from test 2	38
Figure 3-14: Extrusion tooling and billet for copper rod test 2.....	40
Figure 3-15: Copper rod from rod test 2	40

Figure 3-16: Data from copper rod test 2	41
Figure 3-17: Temperature profile for copper rod test extrusion 2.....	41
Figure 3-18: Die temperature profile during extrusion	42
Figure 3-19: Extrusion tooling used in copper tube test 3	43
Figure 3-20: Copper tube from tube extrusion test 3	43
Figure 3-21: Data from copper tube test 3	44
Figure 3-22: Temperature profile for copper tube test extrusion 3	44
Figure 3-23: Die temperature profile during extrusion	45
Figure 3-24: Primary Y_2O_3 crucible in a secondary Y_2O_3 crucible	46
Figure 3-25: Materials Research Furnace	46
Figure 3-26: Drilling equipment for uranium billets.....	50
Figure 3-27: Uranium billet with central hole.....	50
Figure 3-28: Graphite casting mold disassembled	51
Figure 3-29: Graphite casting mold assembled.....	52
Figure 3-30: Hydride/de-hydride system located inside of an inert atmosphere glovebox.	53
Figure 3-31: Tooling used for pressing pellets.....	55
Figure 3-32: U HDH pellet representative of all low density pellets created	56
Figure 3-33: Archimedes immersion method measurement setup	58
Figure 3-34: LFA 447 Nanoflash	60
Figure 3-35: Diagram of LFA 447 Nanoflash.....	60
Figure 3-36: Inert atmosphere LFA sample holder	62
Figure 4-1: Force and position vs time for extrusion 1	66

Figure 4-2: Temperature profile of extrusion 1	66
Figure 4-3: multiple views of tooling used in extrusion 1	67
Figure 4-4: U-10Zr rod from extrusion 1	68
Figure 4-5: U-10Zr rod from extrusion 2	69
Figure 4-6: Temperature profile of extrusion 2	69
Figure 4-7: Multiple views of tooling used in extrusion 2	70
Figure 4-8: Force and position vs time for extrusion 3	71
Figure 4-9: Temperature profile of extrusion 3	72
Figure 4-10: Die temperature increase during extrusion 3	72
Figure 4-11: Multiple views of tooling after use in extrusion 3	73
Figure 4-12: U-10Zr rod from extrusion 3	74
Figure 4-13: Extrusion tooling before use in extrusion 4	75
Figure 4-14: Tooling used in extrusion 4	75
Figure 4-15: Top (left) and bottom (right) of holder after extrusion 4	76
Figure 4-16: Force and position vs time for extrusion 4	77
Figure 4-17: Temperature profile of extrusion 4	77
Figure 4-18: Die temperature increase during extrusion 4	78
Figure 4-19: Extrusion tooling before use in extrusion 5	79
Figure 4-20: Top (left) and bottom (right) of holder after extrusion 5	79
Figure 4-21: Force and position vs time for extrusion 5	80
Figure 4-22: Temperature profile of extrusion 5	81
Figure 4-23: Die temperature increase during extrusion 5	81

Figure 4-24: Failed ram of extrusion 6.....	82
Figure 4-25: Partially extruded U-10Zr rod from extrusion 6	83
Figure 4-26: Force and position vs time for extrusion 6	84
Figure 4-27: Temperature profile of extrusion 6.....	84
Figure 4-28: Die temperature increase during extrusion 6.....	85
Figure 4-29: U-10Zr rod from extrusion 11	86
Figure 4-30: Force and position vs time for extrusion 11	87
Figure 4-31: Temperature profile of extrusion 11.....	87
Figure 4-32: Die temperature increase during extrusion 11.....	88
Figure 4-33: U-10Zr billet for extrusion 13	89
Figure 4-34: U-10Zr rod from extrusion 13	89
Figure 4-35: Force and position vs time for extrusion 13	90
Figure 4-36: Temperature profile of extrusion 13.....	90
Figure 4-37: Die temperature increase during extrusion 13.....	91
Figure 4-38: Extrusion 7 tooling before use.....	92
Figure 4-39: Multiple pictures of the U tube from extrusion 7	92
Figure 4-40: Force and position vs time for extrusion 7	93
Figure 4-41: Temperature profile of extrusion 7.....	94
Figure 4-42: Extrusion 8 tooling and partially extruded product.....	95
Figure 4-43: Force and position vs time for extrusion 8	96
Figure 4-44: Temperature profile during extrusion 8.....	96
Figure 4-45: Die temperature increase during extrusion 8	97

Figure 4-46: U billet used in extrusion 9.....	98
Figure 4-47: U tube from extrusion 9.....	98
Figure 4-48: Force and position vs time for extrusion 9.....	99
Figure 4-49: Temperature profile of extrusion 9.....	99
Figure 4-50: Die temperature increase during extrusion 9.....	100
Figure 4-51: U tube from extrusion 10.....	101
Figure 4-52: Force and position vs time for extrusion 10.....	102
Figure 4-53: Temperature profile of extrusion 10.....	102
Figure 4-54: Die temperature increase during extrusion 10.....	103
Figure 4-55: Uranium billet for extrusion 12.....	104
Figure 4-56: U rod from extrusion 12 after a small section was removed.....	104
Figure 4-57: Tooling set used in extrusion 12.....	104
Figure 4-58: Force and position vs time for extrusion 12.....	105
Figure 4-59: Temperature profile of extrusion 12.....	106
Figure 4-60: Die temperature increase during extrusion 12.....	106
Figure 4-61: BSE image of extrusion 1 U-10Zr rod at 424X.....	107
Figure 4-62: Higher magnification BSE image of Figure 4-61.....	108
Figure 4-63: BSE image of extrusion 1 U-10Zr rod at 2061X.....	108
Figure 4-64: Higher magnification BSE image of Figure 4-63.....	109
Figure 4-65: BSE image of extrusion 1 U-10Zr rod – radial slice.....	110
Figure 4-66: BSE image of extrusion 11 U-10Zr rod at 100X.....	111
Figure 4-67: BSE image 1 of extrusion 11 U-10Zr rod at 1500X.....	111

Figure 4-68: BSE image 2 of extrusion 11 U-10Zr rod at 1500X.....	112
Figure 4-69: BSE image of heat treated extrusion 11 U-10Zr rod at 100X	113
Figure 4-70: BSE image of heat treated extrusion 11 U-10Zr rod at 1000X	114
Figure 4-71: BSE image of heat treated extrusion 11 U-10Zr rod at 1500X	114
Figure 4-72: BSE image of extrusion 7 U tube at 200X	115
Figure 4-73: BSE image of extrusion 7 U tube at 750X	116
Figure 4-74: BSE image of extrusion 12 U rod at 250X.....	116
Figure 4-75: Pole figures of α -U: (a) as-cast alloy (b) extruded alloy at room temperature (c) at 600°C during heating (d) at 650°C during heating (e) at 600°C during cooling. Extrusion direction is at the center.	118
Figure 4-76: Pole figures of δ -UZr ₂ (a) in the as-cast alloy (b) extruded alloy at room temperature (c) at 200°C (d) at 600°C during heating (e) at 600°C during cooling. Extrusion direction is at the center.	120
Figure 4-77: Pole figures of extruded sample for (a) β -U at 680°C (b) γ -U at 650°C during heating (c) γ -U at 700°C during heating (d) γ -U at 800°C during heating (e) γ -U at 700°C during cooling. Extrusion direction is at the center. ...	122
Figure 4-78: Thermal diffusivity of U HDH pellets	124
Figure 4-79: Thermal diffusivity of U HDH and U spheres pellets at 30°C	125
Figure 4-80: Thermal conductivity of U HDH and U spheres pellets at 30°C.....	125
Figure 4-81: Thermal conductivity of U HDH pellets at 30 and 300°C.....	126
Figure 4-82: Thermal diffusivity of U-5Zr HDH pellets	127
Figure 4-83: Thermal diffusivity of U-5Zr HDH pellets at 30 and 300°C	127
Figure 4-84: Thermal conductivity of U-5Zr HDH pellets at 30 and 300°C	128
Figure 4-85: Thermal diffusivity of U-10Zr HDH pellets	129
Figure 4-86: Thermal diffusivity of U-10Zr HDH and U-10Zr spheres pellets at 30°C	129

Figure 4-87: Thermal diffusivity of U-10Zr HDH and U-10Zr spheres pellets at 300°C	130
Figure 4-88: Thermal conductivity of U-10Zr HDH pellets at 30 and 300°C.....	130
Figure 4-89: BSE image of 45.5 %TD U HDH pellet (26-182) at 100X.....	133
Figure 4-90: BSE image of 45.5 %TD U HDH pellet (26-182) at 500X.....	133
Figure 4-91: BSE image of 53.7 %TD U HDH pellet (31-32) at 200X.....	134
Figure 4-92: BSE image of 53.7 %TD U HDH pellet (31-32) at 500X.....	134
Figure 4-93: BSE image of 60.1 %TD U HDH pellet (31-31) at 200X.....	135
Figure 4-94: BSE image of 60.1 %TD U HDH pellet (31-31) at 500X.....	135
Figure 4-95: BSE image of 64.8 %TD U HDH pellet (31-29) at 100X.....	136
Figure 4-96: BSE image of 64.8 %TD U HDH pellet (31-29) at 500X.....	137
Figure 4-97: BSE image 1 of 87.0 %TD U HDH pellet (26-184) at 150X.....	137
Figure 4-98: BSE image 2 of 87.0 %TD U HDH pellet (26-184) at 150X.....	138
Figure 4-99: BSE image of 65.6 %TD U spheres pellet (26-156) at 300X	139
Figure 4-100: BSE image of 65.6 %TD U spheres pellet (26-156) at 75X	139
Figure 4-101: BSE image of 65.6 %TD U spheres pellet (26-156) at 250X	140
Figure 4-102: BSE image of 75.1 %TD U spheres pellet (26-121) at 150X	140
Figure 4-103: BSE image of 68.0 %TD U-5Zr HDH pellet (17-14) at 100X.....	141
Figure 4-104: BSE image of 68.0 %TD U-5Zr HDH pellet (17-14) at 500X.....	142
Figure 4-105: BSE image of 80.6 %TD U-5Zr HDH pellet (31-63B) at 100X	142
Figure 4-106: BSE image of 80.6 %TD U-5Zr HDH pellet (31-63B) at 500X	143
Figure 4-107: BSE image of 54.7 %TD U-10Zr HDH pellet (17-5A) at 100X.....	144
Figure 4-108: BSE image of 54.7 %TD U-10Zr HDH pellet (17-5A) at 300X.....	144

Figure 4-109: BSE image of 76.1 %TD U-10Zr HDH pellet (17-9B) at 100X	145
Figure 4-110: BSE image of 76.1 %TD U-10Zr HDH pellet (17-9B) at 500X	145
Figure 4-111: BSE image 1 of 83.5 %TD U-10Zr HDH pellet (17-11A) at 500X.....	146
Figure 4-112: BSE image 2 of 83.5 %TD U-10Zr HDH pellet (17-11A) at 500X.....	146
Figure 5-1: Final tooling design (side view)	149
Figure 5-2: Final tooling design (bottom view)	150
Figure 5-3: U-10Zr Extrusion constants plotted with the reduction ratio	152
Figure 5-4: Uranium extrusion constants plotted with the reduction ratio	153
Figure 5-5: Uranium metal extrusion constants plotted with the reduction ratio [11] ...	154
Figure 5-6: BSE image of extrusion 12 U rod at 250X, extrusion direction is horizontal.....	155
Figure 5-7: BSE image of extrusion 11 U-10Zr rod exhibiting α -U + δ -UZr ₂	157
Figure 5-8: BSE image of extrusion 11 U-10Zr rod post heat treatment	158
Figure 5-9: Pole figures of α -U (100): (left) extruded alloy at room temperature (right) at 600°C during cooling. Extrusion direction is at the center.	159
Figure 5-10: Pole figures of δ -UZr ₂ (0001): (left) extruded alloy at room temperature (right) at 600°C during cooling. Extrusion direction is at the center.	159
Figure 5-11: Linear fits of thermal conductivity of U at 30 and 300°C	161
Figure 5-12: Linear fits of thermal conductivity of U-5Zr at 30 and 300°C.....	161
Figure 5-13: Linear fits of thermal conductivity of U-10Zr at 30 and 300°C.....	162
Figure 5-14: Theoretical thermal conductivity for U, U-5Zr, and U-10Zr [23].....	163
Figure 5-15: Thermal conductivity models for U at 30°C	165
Figure 5-16: Thermal conductivity models for U-10UO ₂ at 30°C	165

Figure 5-17: Thermal conductivity models for U at 300°C	166
Figure 5-18: Thermal conductivity models for U-5Zr at 30°C	166
Figure 5-19: Thermal conductivity models for U-5Zr at 300°C	167
Figure 5-20: Thermal conductivity models for U-10Zr at 30°C	167
Figure 5-21: Thermal conductivity models for U-10Zr at 300°C	168
Figure 5-22: BSE images of U HDH pellets: (left) 45.5 %TD (right) 70.9 %TD	171
Figure 5-23: BSE images of U-10Zr HDH pellets: (left) 61.2%TD (right) 83.5%TD ..	171
Figure 5-24: Fission gas pore morphology in irradiated U-10Zr fuel. Reprinted with permission from Elsevier. [2].....	172

LIST OF TABLES

	Page
Table 2-1: Properties of UO ₂ , U, Zr, and U-10Zr at Room Temperature [13] [14] [15] ...	7
Table 2-2: Thermal Conductivity of U, U-5Zr, and U-10Zr	15
Table 3-1: Extrusion Experiments.....	21
Table 3-2: Properties of H13 and C350	29
Table 3-3: Heat Treatment Plan for H-13 Tool Steel.....	33
Table 3-4: Heat Treatment Plan for C350 Tool Steel	33
Table 3-5: Comparison of the Physical Properties of Uranium and Copper.....	35
Table 3-6: Copper Test Extrusions.....	36
Table 3-7: U-10Zr Billet Masses.....	48
Table 3-8: U Billet List	49
Table 3-9: Specific heat of U, U-5Zr, and U-10Zr in units of J/gK [4] [23] [34].....	59
Table 3-10: General Sequence for Polishing.....	62
Table 4-1: List of LFA Pellets that were Analyzed with SEM	132
Table 5-1: Extrusion Experiments.....	152
Table 5-2: Linear Fit Coefficients	160
Table 5-3: Quadratic Fit Coefficients.....	160
Table 5-4: Comparison of theoretical values and linear fits	164

1 INTRODUCTION

This applied engineering research was performed in the context of a larger nuclear energy system development program being carried out by the sponsor, TerraPower, LLC (Bellevue, WA). The development of novel nuclear fuel designs and their fabrication methods is vital for the development of future nuclear reactor designs. The Traveling Wave Reactor (TWR), under development by TerraPower, has many significant material and fuel related challenges due to its goal of achieving burn up in the range of 20-50% FIMA (fissions per initial metal atom) This is a significant goal due to historic difficulty in reaching such high burnups. This difficulty arises from several challenges including, but not limited to, the nuclear fuel degradation due to fission gas swelling and other issues, the nuclear fuel cladding deteriorating and lacking structural integrity, lack of understanding of high burn up fuel structures, and lack of data for use in reactor simulation. [1] [2] [3]

The objective was to investigate fabrication and behavior characteristics of low-density fast reactor fuel alloys for potential use in the TWR design or other future reactor designs. The metal fuel alloys investigated were uranium metal, uranium – 5 wt% zirconium (U-5Zr), and uranium – 10 wt% zirconium (U-10Zr). The unifying concept across all samples was the creation of low density metal fuel alloys and the quantification of processing and/or behavior characteristics. The physical fuel forms of interest included 1) dense, solid rods up to 10 cm long that could be used in low smear density nuclear fuel applications, 2) extruded tubes up to 10 cm long designed to begin fuel service in constant contact with cladding yet having a very low smear density,

and 3) low density pellets ranging from ~45 to ~89 % TD to simulate low density fuel structures. The porous pellets may be considered representative of the rods and tubes after fuel swelling. The fabrication methods utilized were hot uniaxial extrusion of rods and tubes and the cold pressing and sintering of representative pellets.

Metallic uranium alloys, such as U-5Zr and U-10Zr, offer many advantages in a fast reactor system including higher thermal conductivity, known recycling processes, and favorable fuel performance related to neutron populations [4] [2]. However, they are not without their drawbacks, such as fuel swelling. The fuel forms investigated offer a way to potentially resolve this swelling issue.

Hot extrusion was selected to prepare the rod and tube samples noted above, but several other methods are possible and were considered before this selection. Uranium alloy metal rods and tubes can be produced through pour casting, injection casting, and machining. All have their strengths and limitations. Pour casting and injection casting tend to be more expensive processes since they require the use of large high temperature furnaces as well as melt-containment through either single-use or expensive multi-use crucibles. Injection casting was used to produce rods for the Experimental Breeder Reactor II (EBR II) and material losses exceeding 20% were reported. The quartz casting molds used for injection casting EBR-II pins were one time use only. [5] [6] Machining uranium causes shaving losses of material and it is challenging due to the tendency of uranium metal to rapidly oxidize. [7] [8]

Hot extrusion is a common industrial fabrication process that is used to manufacture cost-effective simple shapes from many various materials such as

aluminum, copper, and steel. [9] Extrusion of uranium is not a common practice; however, it has been previously investigated. For example, extruded fuel pins were tested in EBR-I. [10] The process parameters for the extrusion of uranium and uranium-zirconium alloys are not well characterized with precision instrumentation or reliable process documentation. For this reason, a study of the extrusion fabrication process was undertaken to characterize the extrusion processing parameters for U and U-10Zr.

Several extrusions of rods and tubes were completed; different process parameters were varied in order to characterize the extrusion process. The extrusion temperature was varied between 550 and 650°C. The extrusion ratio, which is defined as the ratio of final cross sectional area of the extruded sample to the initial cross sectional area of the billet container, was varied between ~5 to 1 and ~15 to 1. In order to acquire the necessary data, the applied force from the extrusion press was recorded using a load cell; the temperature was recorded before, during, and after the extrusion with thermocouples; detailed measurements of the billets, rods, tubes, dies, and containers were recorded with calipers; and the rate of extrusion was recorded using a linear variable differential transformer (LVDT). Once the extrusions were completed, the microstructures of the samples were studied via SEM, optical microscopy, and neutron diffraction, in order to understand the characteristics of the extruded product. There is currently very little data regarding the microstructure of these products..

The second aspect of this project was the evaluation of the thermal conductivity of the subject alloys with various porosity levels. A detailed knowledge of the thermal conductivity of nuclear fuel is vital to any reactor design. This data is used in nuclear

reactor simulations to determine the optimum power plant design taking into account both the efficiency of the reactor system as well as the overall safety. A higher thermal conductivity can allow for an increase of power production since more of the heat generated can be transferred to the coolant. A higher coolant temperature generally improves turbine efficiency which improves power production. A higher thermal conductivity also results in less thermal peaking across the fuel pellets. [4]

The high target burnup and fuel smear density requires knowledge of the variation of thermal conductivity with porosity. The thermal conductivity of uranium, U-5Zr, and U-10Zr as a function of density was not well characterized at the onset of this work. Low density U-alloy pellets were created with porosities ranging from ~45 to ~80 % TD in order to simulate nuclear fuel that had already undergone fuel swelling.

The low density pellets were fabricated via pressing and sintering of metal powders. The pressing pressure, sintering time, and sintering temperature, were varied in order to create pellets with a range of densities. The pressing force ranged from 70 to 140 MPa (10 to 20 ksi), the sintering time ranged from 1 minute to 48 hours, and the sintering temperature ranged from 800°C to 1100°C. The densities of the pellets ranged from ~45 to 89 %TD. The thermal diffusivity of each pellet was measured via the light flash technique with a LFA 447 Nanoflash manufactured by Netzsch Instruments. The thermal diffusivity, along with the density and the specific heat, was used to calculate the thermal conductivity. An empirical model to explain the relationship between the thermal conductivity and the porosity was evaluated and compared to six structural models that have been previously used to predict the thermal conductivity in other two

phase systems. The microstructures of the pellets were studied with scanning electron microscopy.

The remaining sections of this document present information regarding the background, experimental designs, data, results, and interpretation. Section 2 describes the background and scientific theory related to this project. Section 3 details the experimental procedures and equipment utilized throughout the study. Section 4 presents the gathered data. Section 5 is a discussion of the results. Section 6 is a summary and conclusion of the research project.

2 BACKGROUND

2.1 Uranium and Uranium-zirconium Alloy Nuclear Fuel

Commercial nuclear energy systems for electricity generation in the United States are exclusively light water reactors (LWRs), which use UO_2 pellets stacked in Zircaloy tube cladding as their fuel. However, there are many other possible fuel materials that can be used in a multitude of different nuclear reactor designs. Some fuel materials that have been investigated include pure uranium metal and uranium-zirconium alloys. These fuel materials will be investigated in this dissertation.

Uranium exists in three phases: α , β , and γ . The α phase is stable at temperatures below 667°C and has a complex orthorhombic structure. The β phase is stable between 667°C and 772°C and has a complex tetragonal structure. The γ phase is stable from 772°C to the melting point at 1132°C and has a body centered cubic structure. [11]

Zirconium exists in two phases: α and β . The α phase is a hexagonal structure and is stable up to 862°C and the β phase is a body center cubic structure and is stable from 826°C to the melting point 1852°C . The U-Zr binary phase diagram can be seen in Figure 2-1. In the U-Zr binary alloy system, an intermetallic phase, δ , is stable below 617°C . The δ phase consists of UZr_2 and has a ω -type structure. The U-Zr alloy also contains a γ phase which exhibits full mutual solubility of U and Zr because γ -U and β -Zr share the same structure, BCC. However, the uranium β phase can only dissolve a maximum of 0.4 Wt% of Zr (at 693°C) and the uranium α phase can only dissolve a maximum of 0.2 Wt% of Zr (at 662°C). Also, with the addition of zirconium to the system the α -U to β -U phase transition line is lowered to 662°C .

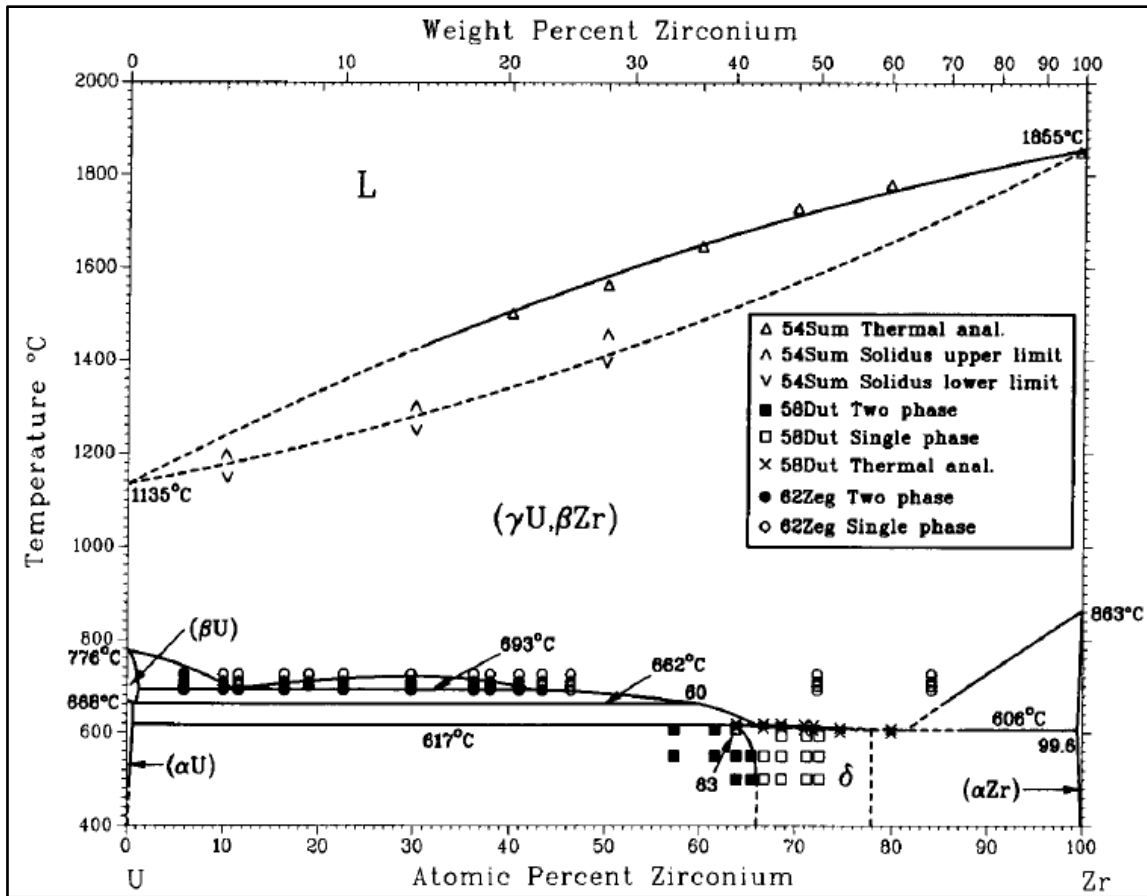


Figure 2-1: Assessed U-Zr phase diagram with selected experimental data. Reprinted with permission from Springer.¹ [12]

Table 2-1: Properties of UO_2 , U, Zr, and U-10Zr at Room Temperature [13] [14] [15]

	UO_2	U	U-10Zr	Zr
T_{melt} [°C]	2865	1132	1250	1850
Yield Strength [MPa]		450	760	180
Vickers Hardness	470-650	200-250	340-360	100-140
K [W/mK]	7.5	27	16.85	16.7
Density [g/cm^3]	10.97	19.1	16.02	6.53

A summary of some of the physical properties of UO_2 , U, Zr, and U-10Zr, can be seen in Table 2-1. Uranium metal has a much higher thermal conductivity than UO_2 with

¹ Reprinted from Bulletin of alloy phase diagrams, The U-Zr (Uranium Zirconium) system, 10, 1989, R. I. Sheldon, (1989) with permission of Springer

a value of ~ 27 W/m K rather than ~ 7 W/m K at room temperature. However, the melting point of uranium is much lower at 1130°C whereas UO_2 is 2865°C . [16] The addition of zirconium to uranium as an alloying agent slightly increases the melting temperature. The melting temperature of U-10Zr is $\sim 1250^{\circ}\text{C}$. [12] But the addition of zirconium lowers the thermal conductivity of uranium from 27 to 16.7 W/m K. The yield strength and Vickers hardness of U-10Zr are higher than pure uranium and pure zirconium.

In addition to affecting mechanical properties, the addition of zirconium has some other effects. Uranium has very poor corrosion resistance. Uranium readily oxidizes in air and in water and does not form a significant passivation layer. The addition of zirconium slightly improves this corrosion behavior. [14] Zirconium also increased the compatibility between uranium and steel cladding materials. The diffusion of iron and nickel into the fuel was halted by the addition of zirconium. The mixing of iron and nickel with uranium decreases the melting point of uranium. An unexpected peak in the fuel temperature would then be more likely to cause a cladding failure and the release of radioactive material into the primary coolant loop. [3] [6]

2.2 Rod, Tube, and Low Density Pellet Fuel Forms and Swelling

One of the historical challenges associated with the application of uranium and uranium-zirconium alloys as nuclear fuel is the fission gas bubble swelling. [17] Swelling can lead to serious problems for reactors including increased fuel cladding chemical interactions (FCCI), deformed fuel assemblies, and even ruptured fuel cladding. A ruptured fuel cladding is a completely unacceptable scenario for reactor

operation because it would result in a release of radioactive material into the primary cooling loop.

Research conducted at EBR-II showed that a low smear density allowed the fuel to swell into the open volume and remain intact after swelling. Once the fuel swelled to a certain extent the fission gas bubbles became interconnected and the fission gas escaped to the plenum. There has been renewed interest in an annular fuel form and other low density fuel forms since a lower smear density has been shown to allow the fuel to achieve a higher burnup. [2] [3] With an annular fuel form, the ideal scenario would be that the fuel swells inward, closing the open area. A solid rod fuel form would swell outward to fill the open area between the fuel and the cladding. With the low density pellets, there is already somewhat continuous porosity throughout the pellet. This porosity could allow room for swelling and allow the easier release of fission gasses.

Smear density is defined as the percentage of a cross sectional area that is filled with 100% TD material. For example, if a 100% TD fuel rod that is 9 mm in diameter is located inside of a cladding tube with inner diameter of 10 mm, the smear density of the fuel rod in the cladding tube would be 81%. If the rod itself was only 75% TD, then the smear density would only be 61%.

As burnup increases the smear density increases because one heavy atom fissions and produces two lighter atoms with a lower density. According to tests performed at EBR-II a 75% smear would become a 90% smear at 20 at% burn up. [4] [3] EBR-II performed many different irradiation tests with a few different fuel materials. The final tests contained U-10Zr fuel rods that achieved 19.9 at% burnup at the time the program

was shut down. At the time of the shutdown the fuel pins could have undergone further irradiation to a higher burnup. These high burnup fuel pins were designed with smear densities of 75%. For comparison, current LWRs in the USA that use UO₂ pellets have a smear density of about 98% at the start of irradiation. [2] [6] [3]

2.3 Extrusion Theory

The general process of extrusion involves taking a material of one cross sectional shape and pushing it through a die to form the material into a different cross sectional shape or size. This process is used on an industrial scale to easily manufacture goods and supplies with many different materials. [9] [18] For metals, extrusion is typically performed at elevated temperatures to enable satisfactory results.

There are a three notable extrusion methods that are employed in industry: direct extrusion, indirect extrusion, and equal channel angular extrusion. Direct extrusion is used for most applications including but not limited to the extrusion of rods, thick walled tubes, bars, and complex shapes. [9] [18] Indirect extrusion is primarily used for creating thin walled tubes. Equal channel angular extrusion is used to create a product with a large amount of internal strain similar to cold working. [19] The direct extrusion method was selected for this project because the forms of interest are rods and thick walled tubes. There are several key process parameters that are varied to control direct extrusion; these include force the ram applies to the billet, the ram travel speed, the reduction ratio, and the billet temperature. Additionally, there are process details that can

be altered including choice of lubrication, tooling design, tooling material, and billet heating method.

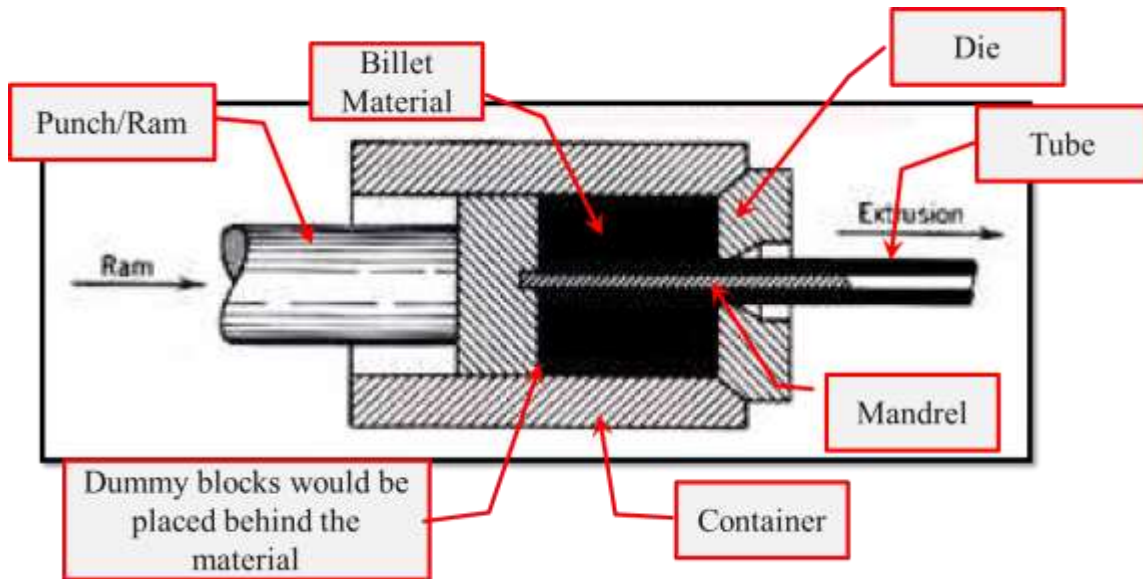


Figure 2-2: Schematic of the direct extrusion of a tube

Extrusion engineering utilizes the general equation,

$$P = K * \ln \left(\frac{A_i}{A_f} \right) \quad 2-1$$

In this equation P is the extrusion pressure on the billet, A_i is the area of the holder that the billet is placed in, A_f is the cross sectional area of the extruded product, and K is the extrusion constant. The extrusion constant is a function of many parameters including die design, lubrication, and temperature. [9] The pressure, P, is the max pressure needed to extrude a billet and can be taken from a force vs time or displacement curve that would be generated during an extrusion. A nominally ideal representation of an example curve is presented in Figure 2-3.

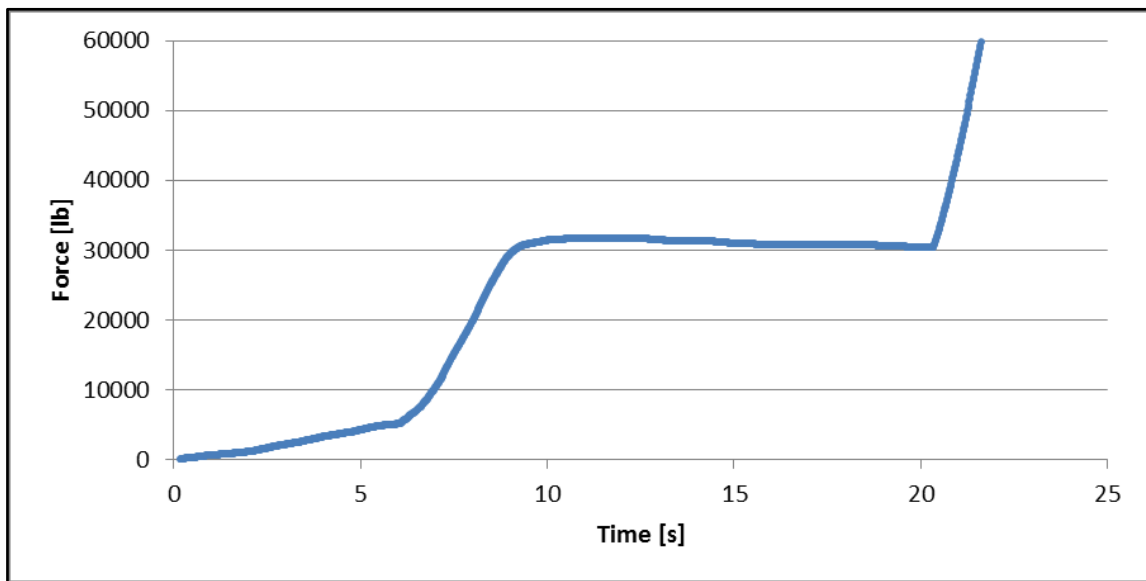


Figure 2-3: Example force vs time curve

On this diagram the maximum force can be easily recognized. Force vs displacement or force vs time plots are generated by recording the force and displacement during an extrusion and keeping the ram speed constant. As an extrusion progresses, the force first dramatically increases as the ram presses against the billet and begins to deform it to fill the open volume before the die. This initial process is termed the “billet upsetting” and the maximum force occurs during this step. Immediately after billet upsetting, the billet material begins to flow out of the die opening and will take the shape of the die opening. As the extrusion progresses the force required will decrease as more the material has already been completely deformed and has left the die. As soon as the billet material has all been extruded the force applied will suddenly increase since the ram will essentially be pressing against the die itself which is designed to be stationary. It is at this point that the extrusion is stopped.

2.4 Pressing and Sintering of Metal Powder Pellets

Powder metallurgical methods of pressing and sintering were selected for the creation of low density fuel pellets. This process begins with the pressing together of fine metal powders into a compact which is also known as a green pellet. Powder is loaded into an appropriate die and then pressed for a short time with a constant force. The pressing force must be great enough that the green pellet does not fall apart when removed from the die. If the pressing force is too great a relaxation effect can occur that causes delamination of the green pellet when removed from the die. After pressing, the green pellet is placed into a high temperature environment where it undergoes the physical process known as sintering. [20]

Sintering is the process of compacted particles transforming into a denser structure at elevated temperatures through diffusion controlled mechanisms. The driving force of this process is the reduction of surface area to minimize surface energy within the body. A volume filled with fine particles has a much larger surface area than the resulting solid volume. Initially, the green pellet has only minimal point contact between each particle. These points of contact will initially have a local radius of curvature near zero, which creates a large driving force for diffusion into that point to form a neck or bridge between the particles. [21] [20]

As sintering continues the particles come together and the necks connecting the particles become larger. The internal void space between particles begins to close and internal porosity is formed. Initially, pores are large irregular shapes but over time they become spherical shapes in order to minimize surface energy. With time at temperature,

the volume fraction of the porosity is reduced as the diffusive driving force continues to drive the body toward higher density. [22]

Much of the previous research into the sintering process has been done with the goal of creating pellets near 100% theoretical density (TD). However, the present investigation is concerned with creating pellets with a range of low densities. Therefore, sintering temperatures will be much lower and sintering times will be much shorter than most other sintering experiments related to uranium metal powder compacts.

2.5 Thermal Conductivity in Nuclear Fuel

The thermal conductivity of uranium metal has been thoroughly investigated and based on a least squares fit to the compiled data from Touloukian et al. and Takhashi et al. Equation 2-2 was developed and is valid from 255.4 to 1173.2 K. [23]

$$k_U(T) = 21.73 + 1.591 * 10^{-2} * T + 5.907 * 10^{-6} * T^2 \quad 2-2$$

The thermal conductivity of pure zirconium is also well characterized and based on the data compiled by Touloukian et al. and Fink et al. Equation 2-3 was developed and is valid from 298 to 2000K. [23]

$$k_{Zr}(T) = 8.853 + 7.082 * 10^{-3} * T + 2.533 * 10^{-6} * T^2 + 2.992 * 10^3 * T^{-1} \quad 2-3$$

Using the previously mentioned data, a correlation for the thermal conductivity of U-Zr alloys was developed. This correlation is as follows:

$$k_{U-Zr} = (1 - \sqrt{1 - x_{Zr}})k_{Zr} + \sqrt{1 - x_{Zr}}\{x_{Zr}k_{c,U} + (1 - x_{Zr})k_U\} \quad 2-4$$

$$k_{c,U} = -102.0 + 200.1 * x_{Zr} - 109.2 * x_{Zr}^2 + .009435 * T + 3.459 \quad 2-5$$

$$* 10^{-5} * T^2 - .02093 * x_{Zr}T$$

Where x_{Zr} is the Zr weight fraction, k_{Zr} is the thermal conductivity of Zr, k_U is the thermal conductivity of uranium, and $k_{c,U}$ is a thermal conductivity correlation due to the alloying effect. This correlation is valid from 298 to 1173 K. The standard error of estimate for this data fitting is 1.29 W/mK. [23] Using the above listed equations values for the thermal conductivity at 30 and 300°C were calculated for U, U-5Zr, and U-10Zr, for use in this research project and these values can be seen in Table 2-2.

Table 2-2: Thermal Conductivity of U, U-5Zr, and U-10Zr

T [°C]	U	U-5Zr	U-10Zr
30	27.10	21.41	16.85
300	32.80	27.14	22.57

2.6 Heat Transfer in a Porous Medium

Heat transfer in a porous medium has been studied for use in many different fields of science and engineering. A porous medium can also be called a low theoretical density material or a material with a high pore density. In this project the porous materials considered are U, U-5Zr, and U-10Zr pellets. Many different pellets were created with varying densities for this project. As the density decreased; the pore volume increased.

There are six fundamental structural models that are used to describe the effective thermal conductivity of two phase materials. For this project, the first phase is

the metallic phase and the second phase is porosity; the pores are assumed to be filled with argon gas. The thermal conductivity of argon at atmospheric pressure at 30°C is 0.0188 W/mK and at 300°C it is 0.0292 W/mK. [24] The equations that represent the six models can be seen below. Each model mentioned is a representation of a real physical geometry. Physical representation of each structural model can be seen in Figure 2-4. From left to right the models displayed are the parallel model, the Maxwell-Eucken 1 model, the Effective Medium Theory model, Maxwell-Eucken 2 model, and the series model. [25]



Figure 2-4. Physical representation of each structural model

In each equation, K , is the effective thermal conductivity, K_p is the effective thermal conductivity using the parallel model, K_s is the effective thermal conductivity using the series model, v_i is the volume fraction of phase “i”, and k_i is the thermal conductivity of phase “i”. The subscript 1 refers to the solid material and the subscript 2 refers to the argon filled porosity. [25]

The first model listed is the parallel model and it can be seen in Equation 2-6. In this model the geometry of the two phase material is assumed to be divided into layers and the heat flow is parallel to the layers. This would allow the heat to travel through the most conductive phase without interference from the other phase. This model is

generally an overestimation of the effective thermal conductivity unless the geometry is exactly as the model assumes. [25] [26]

$$K_p = \sum_{i=1}^N v_i k_i \quad 2-6$$

The second model is the Maxwell-Eucken 1 model (ME 1) and it can be seen in Equation 2-7. This model assumes a dispersion of phase 2 in a matrix of phase 1. It also assumes the dispersed phase is mostly spherical and that the spherical phase 2 inclusions are far enough apart such that they do not interfere with one another. [25] [26]

$$K = \frac{v_1 k_1 + v_2 k_2 \frac{3k_1}{2k_1 + k_2}}{v_1 + v_2 \frac{3k_1}{2k_1 + k_2}} \quad 2-7$$

The third model is the Effective Medium Theory (EMT) and it is shown in 2-8. This model assumes a completely random distribution of each of the two components. [25] [26]

$$v_1 \frac{k_1 - K}{k_1 + 2K} + v_2 \frac{k_2 - K}{k_2 + 2K} = 0 \quad 2-8$$

The fourth model is the Maxwell-Eucken 2 model (ME 2) and it can be seen in 2-9. This model assumes a dispersion of phase 1 in a matrix of phase 2. This model is much like the Maxwell-Eucken 1 except that the phase locations are reversed. [25] [26]

$$K = \frac{v_2 k_2 + v_1 k_1 \frac{3k_2}{2k_2 + k_1}}{v_2 + v_1 \frac{3k_2}{2k_2 + k_1}} \quad 2-9$$

The fifth model is the series model. This model can be seen in Equation 2-10. In this model, the two phase material is assumed to be arranged in layers like the parallel

model. However, in this model the heat flow is in the direction perpendicular to the layers. This would require the heat to be conducted through each layer individually in a series. This model generally underestimates the effective thermal conductivity unless the geometry is exactly as described. [25] [26]

$$K_s = \frac{1}{\sum_{i=1}^N \frac{v_i}{k_i}} \quad 2-10$$

The sixth and final model is the Co-Continuous model (CC) and it can be seen in Equation 2-11. This model is a combination of the parallel and series models. But it is its own distinctive fundamental model. The physical representation of this model is two phases that are both completely continuous but also well dispersed. [25] [26]

$$K = \frac{K_s}{2} \left(\sqrt{1 + 8 \frac{K_p}{K_s}} - 1 \right) \quad 2-11$$

A comparison of each model can be seen plotted in Figure 2-5. For this comparison the ratio of k_1/k_2 was set to 100. K_e was plotted as K_e/k_1 to illustrate the highest thermal conductivity of a mix of two phases can only be the greater thermal conductivity of one of the phases when the lower conductivity phase is not present. As mentioned previously, the parallel model is the highest approximation and the series model is the lowest. These two models are sometimes referred to as the Weiner bounds. It has been shown that when the thermal conductivity of a given material falls into an area in between plotted lines of a thermal conductivity model, that material will have a microstructure that is a combination of the microstructure of the bounds of that area. [25] [26] [27] [28]

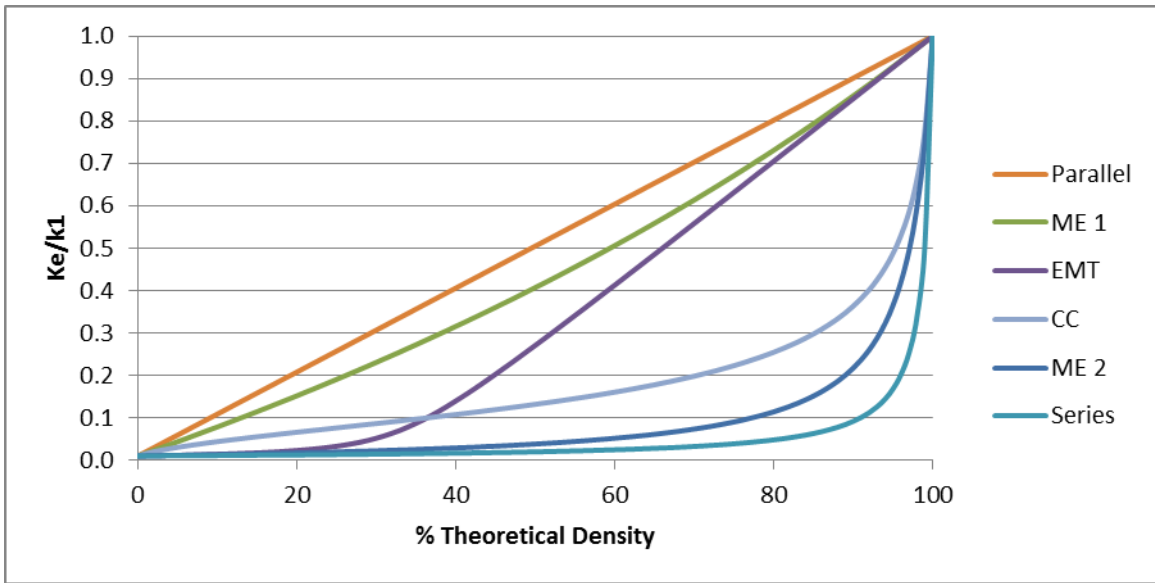


Figure 2-5: Comparison of 6 fundamental models with $k_1/k_2=100$

3 EXPERIMENTAL METHODS

3.1 Extrusion Experiments

In order to characterize the extrusion process, several extrusions were attempted with different process parameters. The extrusion temperature was varied between 550°C and 650°C. The reduction ratio was varied between ~5 and ~15. This range of extrusion ratios was selected for several reasons. Larger reduction ratios would require larger billets which in turn would require larger tooling and use more uranium, which is a limited resource for the lab. Additionally, a larger reduction ratio would increase the force required for extrusion, but the maximum force was limited by the capacity of the press that was available. A list of the extrusion experiments can be seen in Table 3-1. The table lists the ID# associated with the extrusion, the type of extruded product, the billet material, the temperature of the extrusion, the reduction ratio, and the extrusion constant.

Table 3-1: Extrusion Experiments

ID#	Type	Material	T	RR	K
1	Rod	U-10Zr	600	11.1	64.64
2	Rod	U-10Zr	650	10.7	
3	Rod	U-10Zr	650	10.9	75.82
4	Rod	U-10Zr	550	11.3	101.13
5	Rod	U-10Zr	620	5.2	159.48
6	Rod	U-10Zr	620	15.4	83.35
7	Tube	U	600	10.1	65.85
8	Tube	U	600	10.1	104.99
9	Tube	U	600	13.3	55.01
10	Tube	U	600	5.0	108.90
11	Rod	U-10Zr	650	15.5	55.06
12	Rod	U	630	15.2	46.22
13	Rod	U-10Zr	650	15.3	60.98

3.2 Extrusion Experimental Set Up

An Enerpac 100 ton press was used for all extrusions in this project. The maximum capacity of the press is quoted as being 100 tons, but the highest force attempted and achieved during these experiments was 85 tons. The press was designed to have automatic pressure control, but this control unit was not functioning. Due to the nature of the experiments it was not necessary that it be repaired for this project. Instead, manual control was used for all extrusions. The manual control option moves the press head up or down at a mostly constant rate of 2 mm/s and increased force as needed to continue moving up or down.

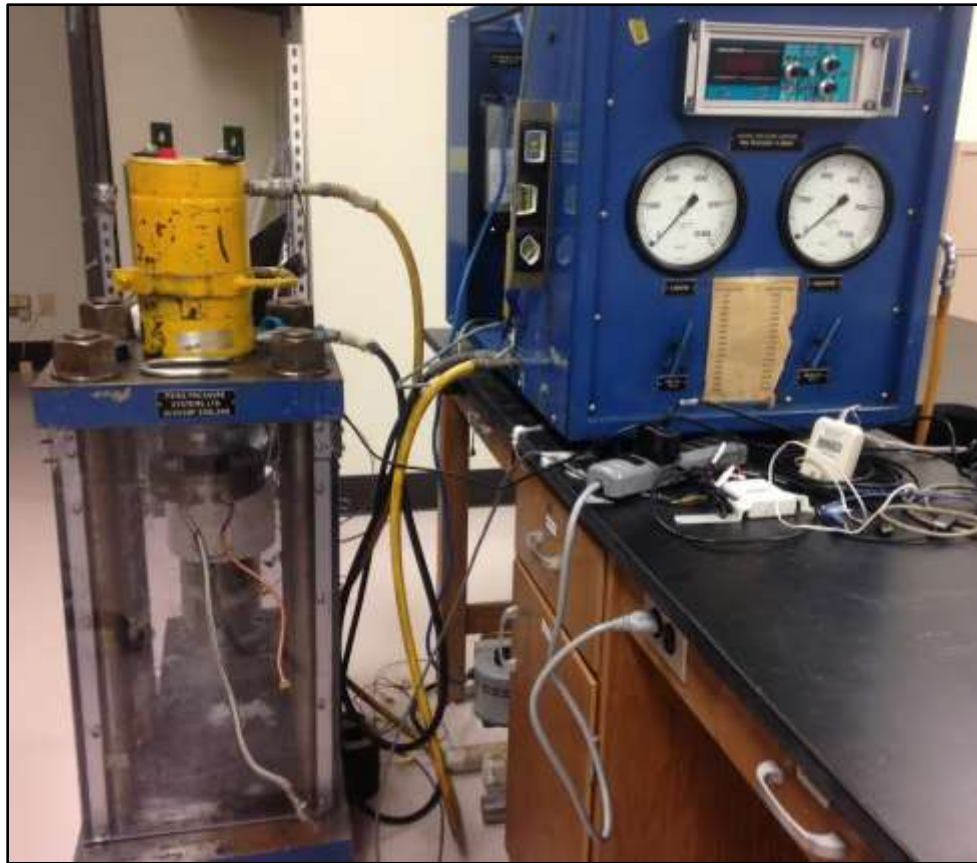


Figure 3-1: Enerpac 100 ton press and control unit

At the start of the project, the head of the press was found to be deformed at the very end due to previous activities not germane to this research(Figure 3-2). This did not affect press operation. However, since the face of the press that came into contact with the load cell was not perpendicular to the extrusion direction it was necessary to repair it to enable the load cell and other equipment to function reliably since the force of the press would not have been applied uniformly. The press unit was removed and taken to the Brazos Valley Drivelines machine shop where they removed ~0.2 inches of material from the head of the press in order for it to be flat and perpendicular to the direction of press head movement. The press unit was then reinstalled. The surface of the extrusion

tooling support structure was also found to be uneven. The support was taken to the nuclear engineering machine shop and ~0.2 inches of material was removed.



Figure 3-2: Press head before repair

Several other repairs were also implemented to prepare the press for use. The wire which attached the manual up/down controller was cut and needed to be repaired. The wires that were attached to the potentiometer that was used to control the pump speed also required repair. The safety enclosure that surrounded the pressing area was found to be inadequate and it was replaced with 0.5 inch polycarbonate. This safety enclosure was built to be removable when necessary.

A load cell (model: Load Cell Central SCS3-200K) was attached to the head of the press in order to record the force during extrusions. When the project was started this load cell was determined to be damaged by a previous user so it was sent to the manufacturer, Load Cell Central, for repair and calibration before it was used in any extrusion experiments. Upon return, the load cell was certified to be safely used up to 200,000 lbs and be accurate within 50 lbs of the total load applied. The repaired load cell

can be seen in Figure 3-3. The load cell was used only for this project. To prevent the load cell from overheating or providing inaccurate readings due to elevated temperatures a large cylindrical piece of steel was placed below the load cell as a separator between the extrusion tooling and the load cell. This piece of steel was fitted with a water coolant jacket to keep it at roughly room temperature. The load cell was connected to a signal conditioner provided by load cell central. The conditioner was a Weight Sense OM-232-10 Digital Signal Conditioner and it was connected to a laptop for data acquisition. The program provided by the manufacturer to actively monitor and record the load during the extrusion was called Scale Watch. The force was set to record 60 times every second during the extrusion.



Figure 3-3: The load cell used for all extrusion experiments

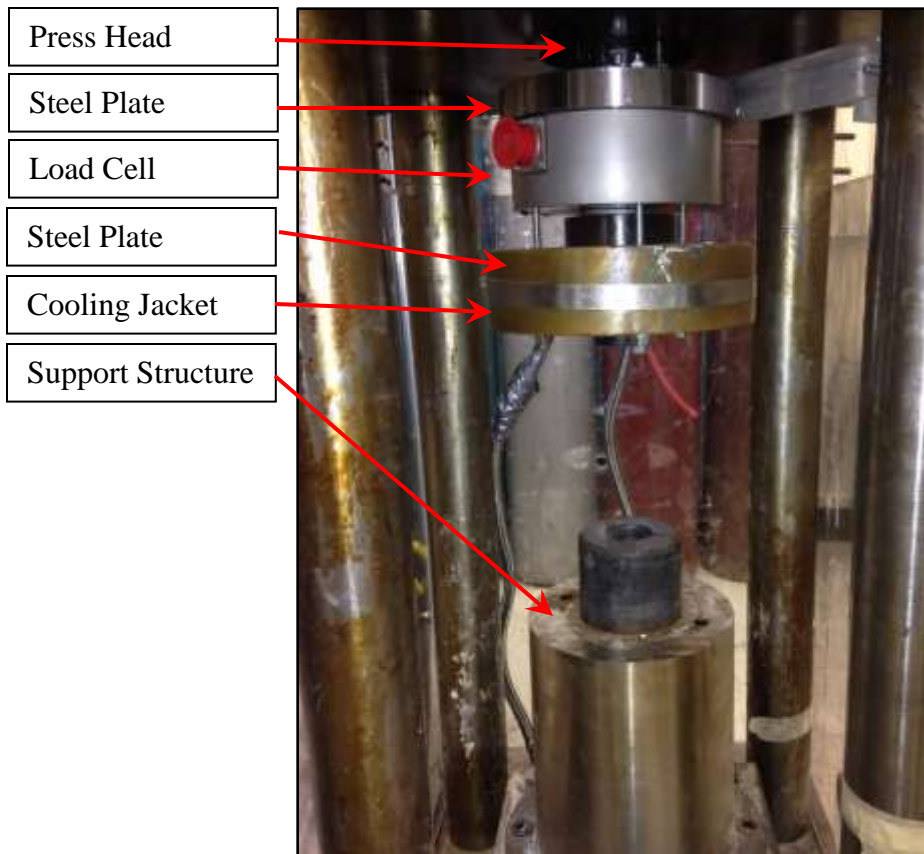


Figure 3-4: Load cell set up

In order to measure the distance traveled during the extrusion, a linear variable differential transformer (LVDT) was connected to the press system. The LVDT (model: Macro Sensors LPER 750 7500) was mounted on the enclosure of the press and the rod and core were attached to the head of the press. The LVDT wires were connected to a DAQ card which was connected to a laptop. The signal from the LVDT was monitored using a Labview program. The distance signal was verified using certified gage blocks of a specific length.

A Watlow tube furnace with an inner diameter of 4 inches was used to uniformly heat the tooling set and the billet. It was placed over the entire tooling set but still open

at the top so that press head could press down on the ram without interfering with the furnace. Two certified type K thermocouples (model: Omega KMQSS-O4OU-24) were purchased for the purpose of measuring the billet temperature prior to extrusion and for measuring the temperature of the die during extrusion. One thermocouple was placed to enter through the bottom of the press support structure and reach up through the die opening and be in direct contact with the billet. This thermocouple was then removed at the time of extrusion. The second thermocouple was placed as close as possible to the die opening. These thermocouples were only used for the purpose of extrusion experiments. A certified data logger (model OMEGA HH306A Data Logger Thermometer) was also purchased for this project in order to properly record the temperature over time. The data logger was also connected to the previously mentioned laptop. A program provided by the manufacturer titled SE305 was used to monitor and record the temperature. Prior to the extrusion, the temperature was recorded every 1 minute, but during the extrusion the rate was changed to every 1 second.

3.3 Extrusion Experiment Procedure

A general procedure was crafted and followed for the extrusion experiments. Improvements to the procedure were added after each experiment when necessary. After deciding the process parameters for a given experiment, a billet and tooling set were fabricated. The first step before an extrusion experiment was to measure the dimensions of the tooling set and the billet. The billet and the inside of the die and holder were all coated with boron nitride lubricant. They were then placed inside of the press enclosure

on top of the tooling support structure and centered under the press head. All pieces were checked to be clean and flat and level. For early experiments, the ram was set in place during the heating phase. For later experiments the ram was not set in place until after the billet reached a stable temperature. The ram was inserted this way because the steel was much stronger at a lower temperature. The dummy block was still placed in the correct position on top of the billet during heating and this served to protect the top of the billet from oxidation during heating.

The thermocouples were placed in position and the Watlow furnace was placed around the tooling set and plugged into a Variac variable voltage transformer. Insulation was placed around the heater and secured in place. The heater was not turned on until all of the set up steps were completed. A tube was inserted at an opening in the bottom of the press support structure that supplied argon from an argon gas bottle at a low flow rate. This was done so that the extruded product would enter a low-oxygen environment while it was still at elevated temperatures. Uranium oxidizes rapidly in air and even more so when it is at an elevated temperature. The cooling jacket was then attached to the water chiller and turned on.

All of the data collection equipment was turned on and attached to the laptop. The thermocouples were attached to the thermocouple reader and the reader was attached to the laptop. The LVDT was attached to the DAQ card and the DAQ card was attached to the laptop computer. Finally, the load cell was attached to the weight sense and the weight sense was attached to the laptop. Each program was turned on and checked to be in proper working order and test data files were saved for each one.

After the completion of all of the set up steps, the furnace was turned on by setting the Variac to 80%. The correct temperature was reached and stabilized by manually adjusting the power input. Once the temperature was stable, the press was turned on by first switching on the power supply and then slowly increasing the pump speed to maximum. When it was time for the extrusion to commence the down button on the manual control was pressed. This button continued to be pressed while watching the LVDT and load cell data on the laptop. When the force decreased and then began to increase and the LVDT signal showed no further movement, the extrusion was stopped. The up button was then pressed to return the press to its normal position and all of the data was saved. The press and the furnace were then turned off and the extruded product was allowed to cool to room temperature under flowing argon.

3.4 Extrusion Tooling

The first step in extrusion tooling design was to select the appropriate material. H-13 tool steel was chosen as the tooling material for most of the extrusion experiments because of its favorable strength properties at elevated temperature. In the later extrusion experiments the ram and dummy block were replaced with C350 because H13 could not adequately withstand the stress at high temperatures. The room temperature properties of heat treated H13 and C350 provided by the manufacturer can be seen in Table 3-2.

Table 3-2: Properties of H13 and C350

Material	Hardness [Rc]	Yield Strength [ksi]	Fracture Toughness	Elongation
H-13	54	233	21	13%
C350	56	330	25	2.8%

Industrial scale extrusion tooling can be quite complex. For this project, much smaller and simpler designs were created and used. The tooling design was changed in between most extrusions to improve performance. Due to the number of different custom tooling designs in this project, the details of each design are located in Appendix 3 organized by extrusion number. However, the final design can be seen below in Figure 3-5 and Figure 3-6. Additionally, a picture of each individual tooling set can be seen in the section describing each extrusion experiment. This design had several parts which include the ram, dummy block, holder, and die. Also, the holder and die are bolted together with 4 bolts and 4 nuts and aligned with 2 set pins.

The purpose of the holder is only to contain the billet. Large forces can be exerted on the interior wall of the central hole of the holder during the extrusion because the billet is being deformed. The holder must maintain its original shape intact so that the reduction cone of the die aligns with the central hole. Additionally, there is friction on the wall of the central hole so it should be as smooth as possible. Set pins were added to make the center of the die and center of holder aligned. The holder and the die were bolted together because during the extrusion the holder can be pushed up away from the die by any billet material that was forced between the holder and the die as well as any billet material that was forced up around the ram or dummy block.

The dummy block is placed between the ram and the billet material. The dummy block is machined to fit tightly in the central hole of the holder and thin enough that it does not cause excessive friction between the holder and the dummy block. The dummy block is designed to be replaced if it undergoes any deformation during the extrusion as a sacrificial piece. The ram is of a smaller diameter than the dummy block. When the extrusion is underway and the force is high enough the ram and dummy block undergo lateral deformation in accordance with the Poisson effect. The effect was likely the cause of the failure of several extrusions where the ram became stuck in the holder. The addition of the dummy block solved this issue.

The reduction die has a central hole. This hole begins with the same diameter of the holder at the surface and then decreases down to the desired product diameter. The reduction angle is set at 45 degrees. There are 6 holes around the perimeter of the die. Two of these holes are for the set pins. The other 4 holes are for the bolts. The bolts go in from the bottom of the die and the nuts are on the top of the holder. The head of the bolts as well as the nuts are recessed in the tooling to prevent interference. The bottom of the die has a slight raised area around the center. This raised area loosely matches with the tooling support structure to ensure that the die opening is aligned with the hole in the support structure.

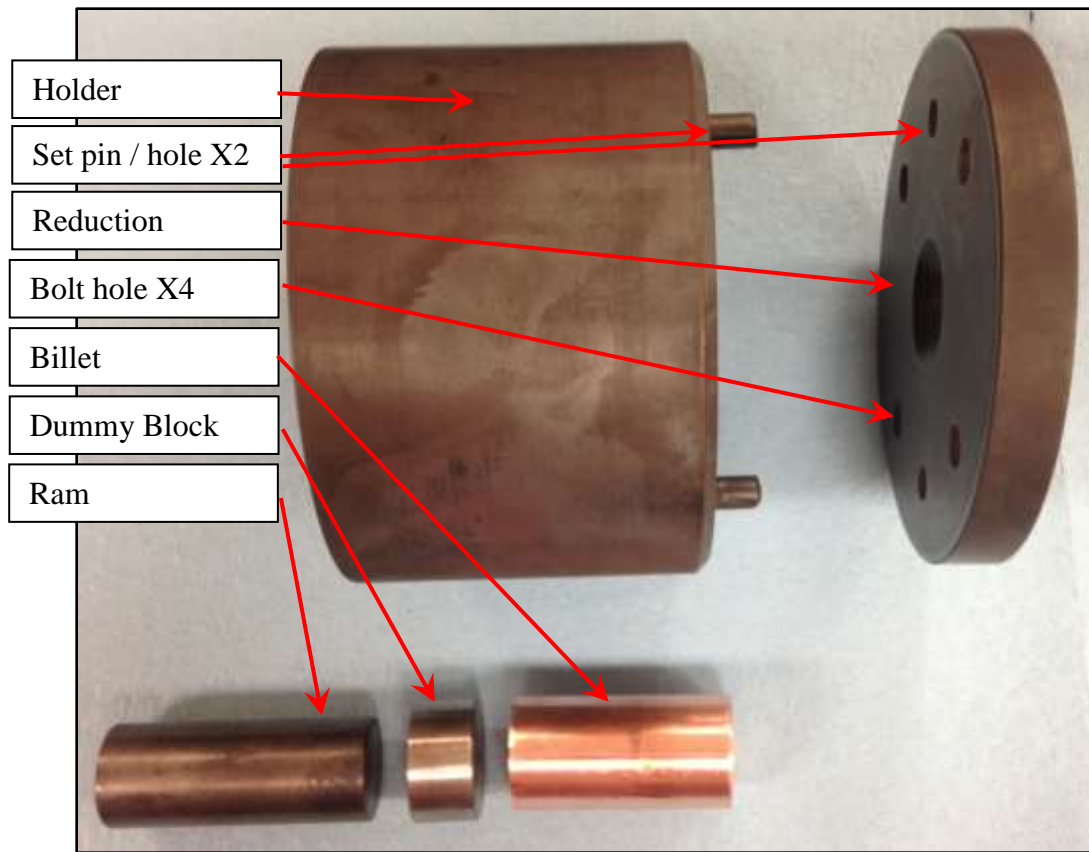


Figure 3-5: Final tooling design (side view)

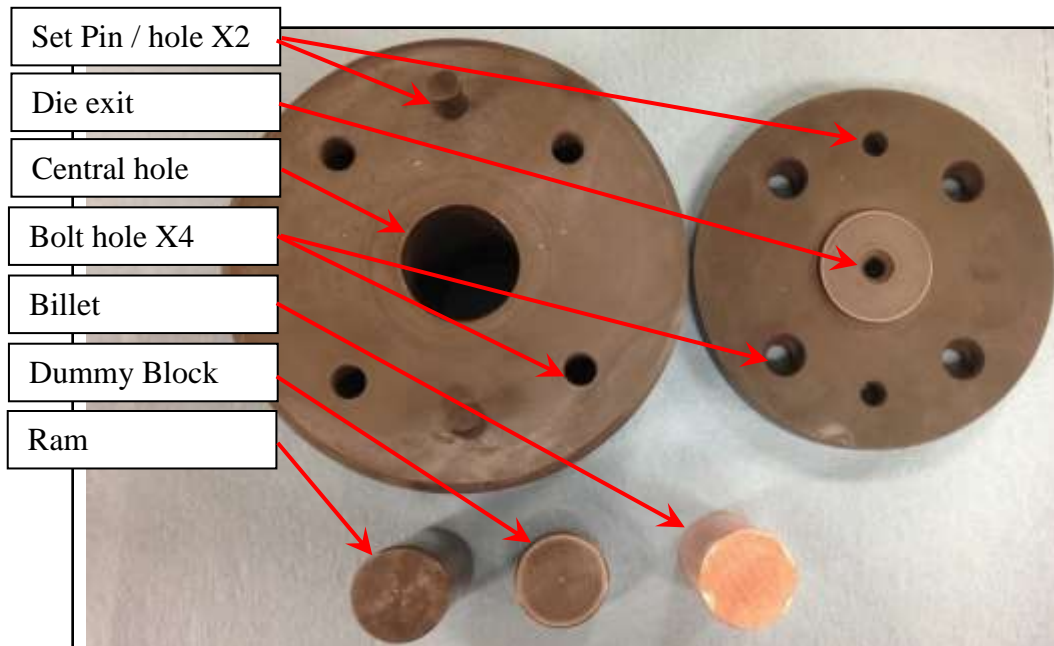


Figure 3-6: Final tooling design (bottom view)

3.5 Heat Treatment of Tool Steel

The proper heat treatment of steel alloys is crucial since the material properties are determined by this process. The H13 for this project was purchased from Diehl Steel. The heat treatment plan was received from the engineers at Diehl Steel. All H13 heat treatments followed the plan laid out in Table 3-3. The C350 that was used for this project was purchased from Dynamic Metals International. The heat treatment plan for this steel was received from the engineers at that company and can be seen in Table 3-4.

Table 3-3: Heat Treatment Plan for H-13 Tool Steel

Phase	Temperature	Duration	Notes
Pre-heat	800°C	1 hr	No O ₂ present
Harden	1110-1120°C	1.5 hr	No O ₂ present
Cool	Room temperature	Until cool	Under forced convection in air
Temper 1	565°C	2.5 hr	In air
Cool	Room temperature	Until cool	Still cooling in air
Temper 2	565°C	2.5 hr	In air
Cool	Room temperature	Until cool	Still cooling in air

Table 3-4: Heat Treatment Plan for C350 Tool Steel

Phase	Temperature	Duration	Notes
Harden	520°C	6 hr	In air
Cool	Room temperature	Until cool	Stil cooling in air

In order to maintain a low oxygen environment during the first two phases of the heat treatment, the H13 pieces were sealed inside of steel foil with paper. The paper burned up the oxygen that was then trapped inside of the foil and reduced the level of oxygen. Since the foil is sealed, oxygen is not added to the system as annealing continued. A picture of a sealed foil bag ready for heat treatment can be seen in Figure 3-7.



Figure 3-7: Extrusion tooling sealed in steel foil

The heat treatments were done in two different furnaces due to use of the furnaces by other graduate students. The following furnaces were used: Barnstead/Thermolyne F62730-33 and Lindberg Blue Model 51442. In order to be sure of the temperature of the part, a thermocouple was placed in contact with the part during the heat treatment.



Figure 3-8: (Left) Thermolyne furnace (Right) Lindberg furnace

3.6 Test Extrusions

Copper was used for initial extrusion tests because it is simpler to extrude than uranium. It is also easier to machine so the production of copper annular billets was much easier than the production of the uranium annular billets. A comparison of some of the basic physical properties of uranium and copper can be seen in Table 3-5. Additionally, copper is much less costly than uranium. Most importantly, copper is significantly less hazardous than uranium because it is not radioactive and does not oxidize rapidly in air under normal conditions.

Table 3-5: Comparison of the Physical Properties of Uranium and Copper

	T _{melt} [°C]	Yield Strength [MPa]	Vickers Hardness
Copper	1084	33	50
Uranium	1132	200	190

Copper rods and copper tubes were extruded. Most of the copper extrusions were conducted at approximately 600°C since this was in the range of the planned temperatures for the uranium extrusions. Table 3-6 lists all of the copper test extrusions completed. Three of the tests were conducted before the load cell repairs were completed and are listed as “Pre LC”. For the copper tests that did utilize the load cell an extrusion constant was calculated. These extrusion constants corresponded well with literature values.

Table 3-6: Copper Test Extrusions

ID#	Type	Material	T	RR	K
RT 1	Rod	Cu	600	6.0	Pre LC
RT 2	Rod	Cu	650	15.4	27.18
TT 1	Tube	Cu	600	8.0	Pre LC
TT 2	Tube	Cu	600	8.0	Pre LC
TT 3	Tube	Cu	600	8.2	31.74

The first test was the extrusion of a copper rod. Copper rod test 1 was conducted at a temperature of 600°C and a reduction ratio of 6.0. The extruded copper rod can be seen in Figure 3-9. This picture was taken shortly after the extrusion and the rod had not yet been removed from the die. The curvature of this rod is likely due to the low precision of the tooling. The surface of the copper rod was only slightly oxidized. The surface of the copper tube was smooth and the diameter did not vary over the length of the product.



Figure 3-9: Copper rod test 1

Copper tube test 1 was conducted at a temperature of 600°C and a reduction ratio of 8.0. The first copper tube test failed due to the hollow area of the supporting structure not being in proper alignment with the opening of the die. When the extrusion was underway, the copper tube pressed into the side of the supporting structure and the tube

and die were deformed. The designs of all future dies were changed so that this would not happen. The parts were machined in such a way that they were no longer free to move laterally. A short lip was machined so that the die would fit into the supporting structure and be loosely centered.



Figure 3-10: Copper tube test 1

The second copper tube extrusion attempt was successful. Copper tube test 2 was conducted at a temperature of 600°C and a reduction ratio of 8.0. The tooling used in this extrusion can be seen in Figure 3-11. The copper tube that was formed can be seen in Figure 3-12, this picture was taken shortly after the extrusion. The tube was then removed from the die and can be seen in Figure 3-13.



Figure 3-11: Tooling used in copper tube test 2



Figure 3-12: Copper tube test 2



Figure 3-13: Copper tube from test 2

After the completion of the load cell repairs, additional tests were performed to collect the necessary data to calculate extrusion constants for comparison to literature data as proof of the system accuracy. Copper rod test 2 was conducted at a temperature of 647°C and a reduction ratio of 15.4. The tooling and billet can be seen in Figure 3-14. The resulting extruded rod can be seen in Figure 3-15. The tooling used in this extrusion

test was the final design used in the uranium extrusion tests. The extruded copper rod is severely bent because it exceeded the maximum length allowed for an extruded rod in the extrusion experiment setup. The maximum length allowed is set by the distance between the die opening and the bottom of the press structure and this was about 14 inches. The billet for this test extrusion was too large and should have been machined shorter.

However, despite this error, no equipment was damaged during the extrusion and the test was considered successful. Data gathered in this extrusion can be seen in Figure 3-16. As was discussed in the background section, the force reaches a peak during the extrusion and then begins to decline as the extrusion progresses. The maximum force can be extracted from this plot at 50,269 lbs. The point at which the extruded rod ran out of open volume to extrude into and it began to curl can be seen at about 45 seconds. At the end of the extrusion the force suddenly and rapidly increases since there is no more copper billet to be extruded. The plateau that follows the sudden increase is created by the release of the manual down button but before the manual up button has been pressed.

The LVDT portion of the plot shows that the press head was moving fairly uniformly over the course of the extrusion. At the end of the extrusion the position value is held constant before decreasing. This corresponds to when the press head stopped moving and the extrusion was halted. As the up button is pressed and the force drops to 0 the LVDT shows the press head beginning to retract. The portion of the force vs time plot that corresponds to the end of the extrusion is omitted from most other data plots to focus on the relevant data. Lastly, the temperature profile of the increase in temperature

to 647°C and the die temperature profile during the extrusion can be seen in Figure 3-17 and Figure 3-18 respectively. The die temperature profile shows an increase in temperature of 7°C.

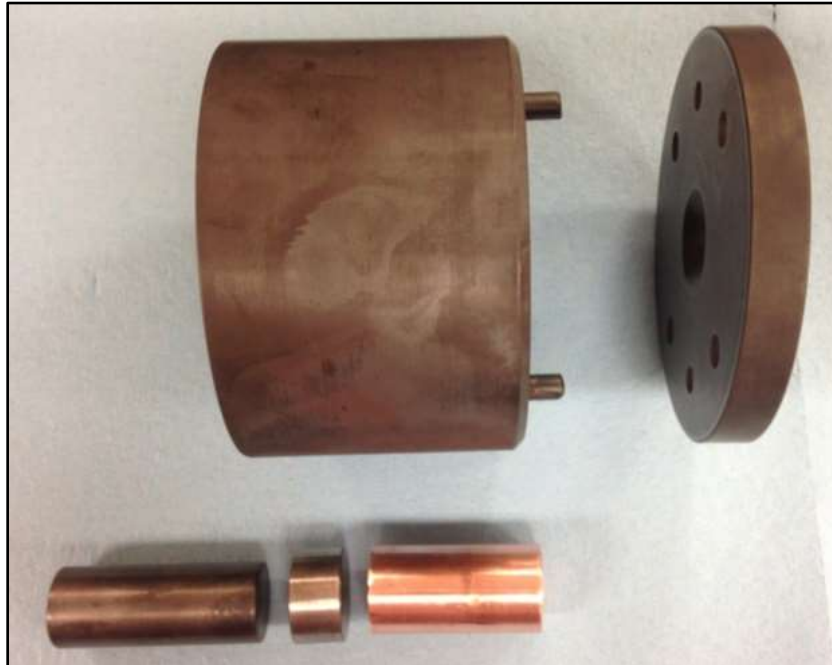


Figure 3-14: Extrusion tooling and billet for copper rod test 2

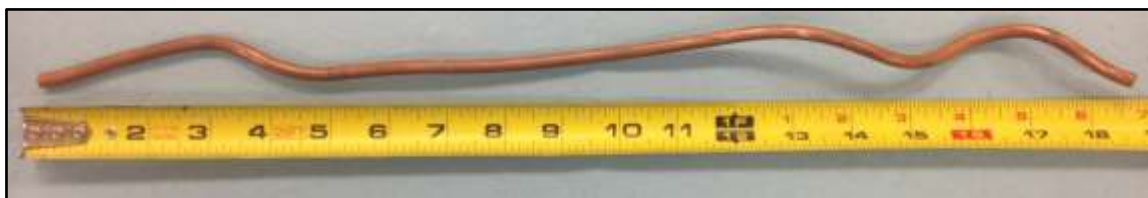


Figure 3-15: Copper rod from rod test 2

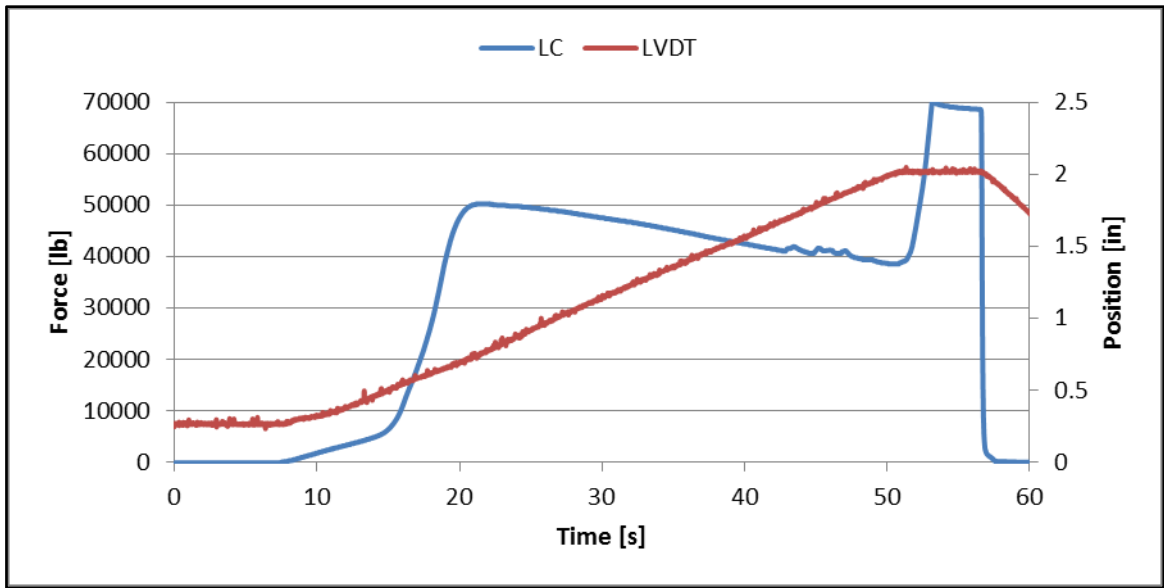


Figure 3-16: Data from copper rod test 2

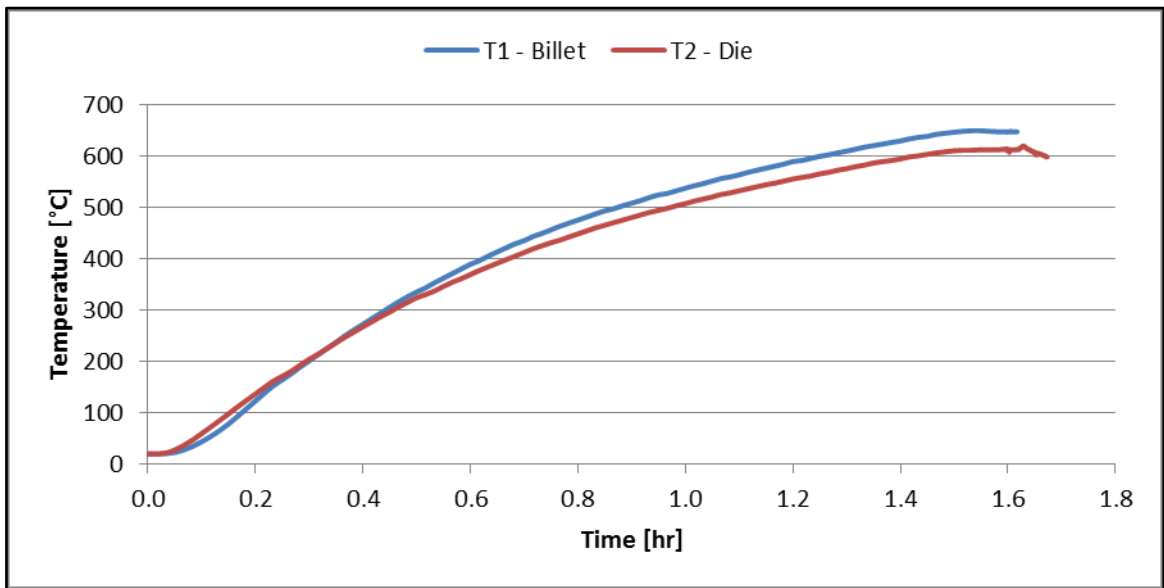


Figure 3-17: Temperature profile for copper rod test extrusion 2

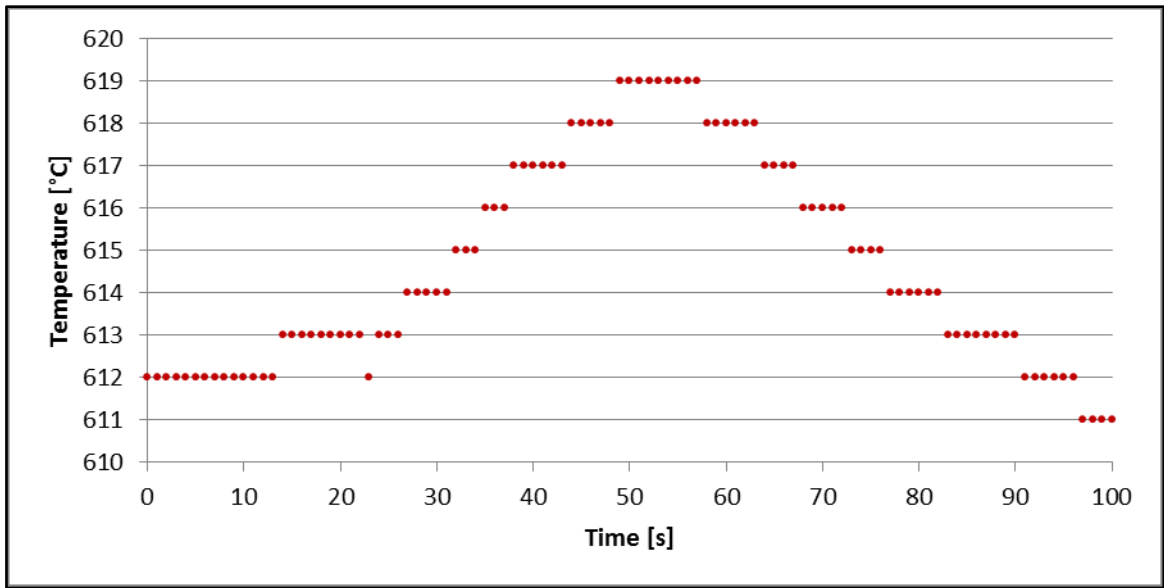


Figure 3-18: Die temperature profile during extrusion

Copper tube test 3 was conducted at 600°C and with a reduction ratio of 8.2. The tooling used for this extrusion can be seen in Figure 3-19 and the extruded tube can be seen in Figure 3-20. The LVDT malfunctioned during this test resulting in a loss of data. Notes taken at the time of the extrusion indicate that the ram movement and speed were smooth and similar to other extrusions. The force vs time plot can be seen in Figure 3-21. The temperature profile of the increase in temperature to 600°C and the die temperature profile during the extrusion can be seen in Figure 3-22 and Figure 3-23 respectively. The die temperature profile does not show a consistent increase in die temperature. This was due to the thermocouple being placed in a different location on the tooling which resulted in inaccurate readings. This location was not used in any future experiments.



Figure 3-19: Extrusion tooling used in copper tube test 3



Figure 3-20: Copper tube from tube extrusion test 3

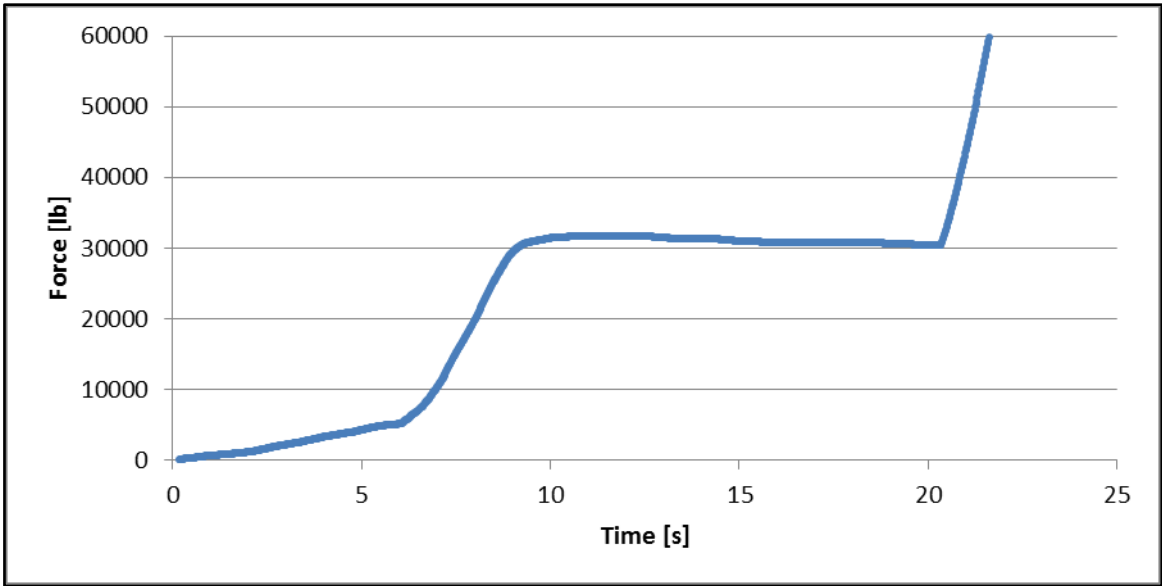


Figure 3-21: Data from copper tube test 3

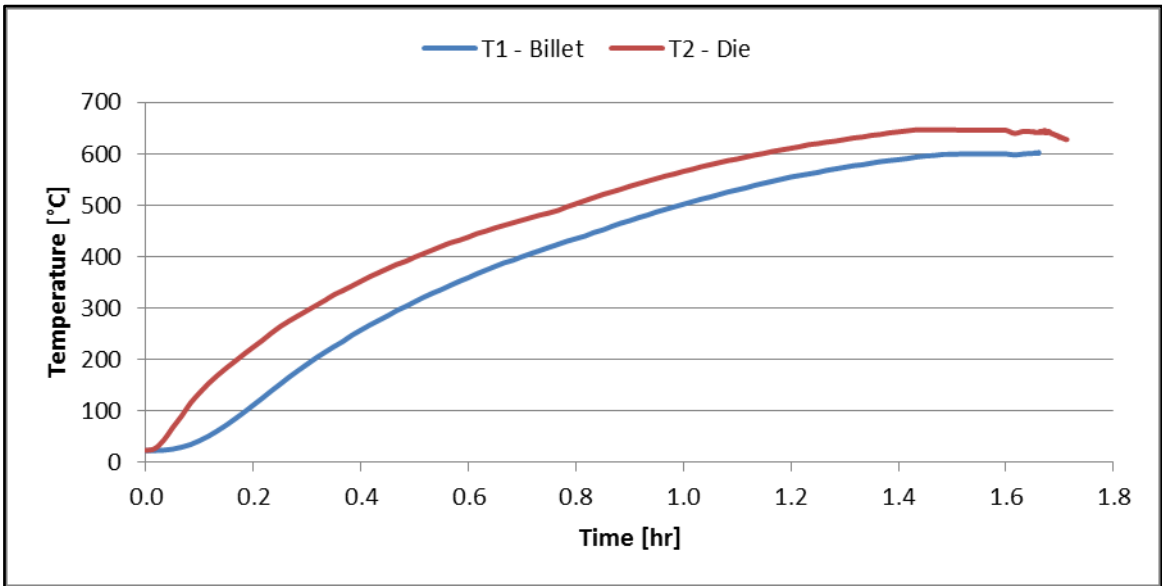


Figure 3-22: Temperature profile for copper tube test extrusion 3

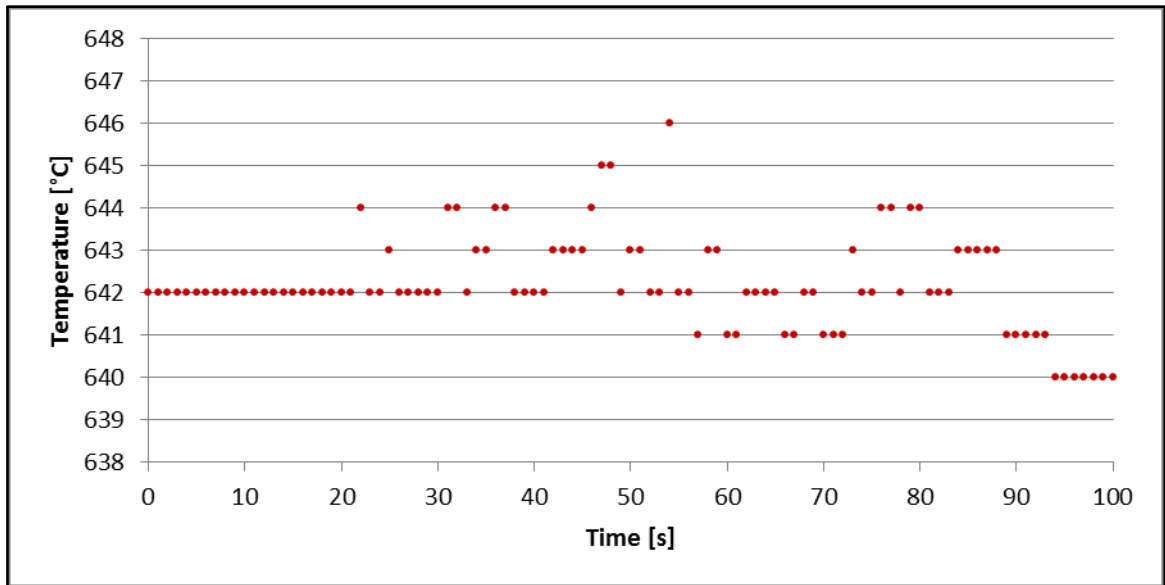


Figure 3-23: Die temperature profile during extrusion

3.7 Preparation of Uranium Billets for Extrusion

3.7.1 Melt Casting Procedure

Melt casting was done in order to create alloys of metals or to melt a metal into a specific shape. Metals are placed in a crucible and placed into a furnace at high temperatures. Yttrium oxide (Y_2O_3) crucibles were purchased from Hadron Technologies to provide melt containment and establish the shape of the billet. Each melt utilized the Materials Research Furnace (MRF), model number: B-5x12-W-1800-UHV, which can be seen in Figure 3-25. This furnace has a maximum temperature of $\sim 2000^\circ C$. All melts were completed under a flowing, ultra-high purity argon atmosphere.



Figure 3-24: Primary Y₂O₃ crucible in a secondary Y₂O₃ crucible



Figure 3-25: Materials Research Furnace

Pieces of the constituent metals were cut to appropriate sizes using a diamond saw. Since the uranium metal source material is not stored in argon, a thin layered of oxidation is always present on the surface. The surface oxidation was removed to enable

melting. The uranium slugs were first sanded to remove sharp edges and the majority of the oxidation. Once sanding was completed, the uranium metal pieces were pickled in 20% nitric acid to more thoroughly remove the oxide layer until the pieces were shiny and silver colored. The zirconium metal pieces were only sanded. After the oxide layer removal, each piece of metal was carefully weighed on a scale in order to ensure the desired weight percent of uranium and zirconium. Before each weighing session the scale was cleaned and calibrated as well as verified with a class 1 ASTM 200 g standard.

3.7.2 U-10Zr Billets

The U-10Zr rod extrusions required solid, cylindrical billets of U-10Zr. The billets were created through melt casting. Ideally, a billet would be perfectly homogenous, but after melting this was not always observed to be the case after a single melt since there are large chunks of metal at the start of the process. In order to increase homogeneity each alloy billet was melted twice. In the first melt, solid pieces of uranium metal and zirconium metal are placed in a Y_2O_3 crucible. In the second melt, the billet that resulted from the first melt is flipped upside down and then melted again in another Y_2O_3 crucible that is slightly larger. The U-10Zr billets that were used in extrusions can be seen in Table 3-7. Each of the U-10Zr billets were created using the following temperature profile: increase to 1800°C over 1.5 hr, hold for 2 hr, decrease to 25°C over 1.5 hr.

Table 3-7: U-10Zr Billet Masses

Ext #	U [g]	Zr [g]	Wt% Zr	H [in]	D [in]	Billet Mass [g]
1	73.06	8.19	10.08%	0.63	0.76	72.76
2	76.28	8.46	9.98%	0.61	0.78	81.03
3	86.58	9.64	10.02%	0.63	0.77	82.41
4	68.85	7.12	9.37%	1.25	0.52	70.00
5	93.39	10.55	10.15%	0.97	0.76	103.14
6	93.30	10.28	9.92%	0.67	0.90	102.77
11	134.69	15.00	10.02%	0.92	0.91	146.08
13	114.89	12.72	9.97%	0.86	0.90	127.25

3.7.3 Uranium Billets

For the uranium rod extrusions, a solid cylindrical billet was required, but for the tube extrusions an annular billet was required. In order to achieve the annular shape, solid cylindrical billets were first cast in Y_2O_3 crucibles. Each of the U billets were melted with the following temperature profile: increase to 1400°C over 1 hr, hold for 1 hr, decrease to 25°C over 1 hr. A hole was then drilled through the center of the solid billet. The central hole was drilled to be slightly larger than the mandrel required for the extrusion of a tube.

Machining of uranium is not a simple task due to its density, strength, and pyrophoricity, but it has been demonstrated in the past. Based on results from previous studies, a low drilling speed of 20-25 ft/min was required to drill holes in U metal. [7] [8] [29] A small multi speed drill press was purchased for this project. The drill press was mounted to a heavy duty table. A vice was mounted inside of a square bucket on the drill press platform. The bucket was filled with a mixture of 90% water and 10% oil. The oil used was Mobil: Mobilcut 102 Multi-purpose Water Soluble Cutting Oil. The oil

level was just enough to cover the uranium billet. This was done to minimize contamination as well ensure that any uranium chips or turnings would not rapidly oxidize in the air. The U billets were first indented on the top surface in the center to mark the location for the drill bit. The drilling was done in 2 steps, first using a 1/8" bit at 690 RPM and second using a 1/4" bit at 470 RPM. The final parameters for the U billets that were used in tube extrusions can be seen in Table 3-8. The drilling set up can be seen in Figure 3-26 and one of the annular billets can be seen in Figure 3-27.

Table 3-8: U Billet List

Ext #	U [g]	H [in]	OD [in]	ID [in]	Billet Mass [g]
7	96.15	0.77	0.72	0.25	83.93
8	100.13	0.78	0.74	0.25	87.84
9	104.33	0.56	0.91	0.25	95.78
10	67.00	1.06	0.51	0.25	50.84
12	144.30	0.77	0.91	0.00	144.10



Figure 3-26: Drilling equipment for uranium billets



Figure 3-27: Uranium billet with central hole

3.7.4 Reusable Graphite Casting Mold

Early in the project an attempt was made to create a reusable graphite casting mold to cast both U billets and U-10Zr billets. The graphite was coated with a layer of Y_2O_3 . The Y_2O_3 was applied to the surface of the graphite in two different methods. The first method that was attempted was with an aerosol spray can. The second method was a

liquid solution that was brushed on with a small paintbrush. Both solutions were purchased from ZYP Coatings.

Once the graphite mold was coated with Y_2O_3 , the uranium was placed into the mold and a melt was attempted. Each time a melt was attempted the uranium did not fully melt and the coating did not survive the melt. Melts were tried at several different temperatures. However, since the melting temperature of uranium is $1130^\circ C$ the furnace would need to be at least $1300^\circ C$ to ensure thorough melting and mixing. This method of melt casting has been used in other programs, but melts were not able to be completed with the graphite casting mold during this project.



Figure 3-28: Graphite casting mold disassembled



Figure 3-29: Graphite casting mold assembled

3.8 Production of Powder for Use in Pellet Manufacturing

In order to characterize the relationship between density and thermal conductivity, it was necessary to create porous pellets with a range of densities. The first step in pellet production was to create high quality metal powder. This was accomplished using two previously-established methods: 1) a hydride/de-hydride process (HDH) method that produces fine uranium powder (nominal 1 to 10 μm flakes) and 2) a rotating electrode process that produces coarse microspheres (nominal 40 to 500 μm diameter)

For the HDH method, small pieces of uranium metal were first cleaned by sanding and pickling in a 20% nitric acid solution to remove the surface oxidation similar to the process described in the previous section regarding melt casting. The clean piece of uranium was then placed in an Al_2O_3 dish which was placed in an Al_2O_3 tube

that had only one open end. The tube was placed in the center of a Watlow furnace and wrapped with insulation. A cap was placed on the end of the tube that had three feed through holes. The feed through holes were for gas in, gas out, and a thermocouple. The system setup can be seen in Figure 3-30. Due to the sensitivity of uranium metal to oxygen, all work with uranium metal powder was done in an inert argon atmosphere glove box.



Figure 3-30: Hydride/de-hydride system located inside of an inert atmosphere glovebox.

After placing the uranium metal piece in the tube and closing up the hydride/de-hydride system, 5% H_2 -95%UHP argon gas flow was started. The temperature was then increased to 225°C. The gas flow was continuous for 18 hours. The gas was then shut off and the system was evacuated. While under vacuum, the temperature was increased to 325°C. The temperature remained at 325°C until the vacuum reached the millitorr range signaling that all of the hydrogen had been driven off. Further details of this process can

be seen in “The Powder Metallurgy of Uranium” [30] as well as the previous work by D. Garnetti. [31]

For the second method, microspheres were used to create pellets. The microspheres were produced via a rotating electrode system (RES). In this process a rod of uranium or U-10Zr was rotated at high speeds, and a welder tip was slowly brought closer to the rotating face of the rod. When the rod was close enough to the welding tip an arc of electricity would then melt the surface of the rod. Since the rod was rotating at high speeds, centripetal force would cause small droplets of the liquid metal to fly off of the edge of the rod. The droplets would cool in air before landing in the surrounding catch pan and form mostly spherical powder. Further details of this manufacturing process can be seen in thesis of previous FCML student Chad Thompson. [32]

3.9 Production of U, U-5Zr, and U-10Zr Pellets

Once the powder was collected from the hydride/de-hydride process or the RES process it was sieved to remove large pieces. To make a U-5Zr pellet or a U-10Zr pellet from the U HDH powder, zirconium powder was mixed into the uranium powder to create the desired mixture. The mixing process was completed via tumbling in an argon atmosphere in a sealed jar for 1 hour. The U, U-5Zr, or U-10Zr powder was then pressed uniaxially using a 13 mm split die set (Figure 3-31). This size was selected so the pellets would fit the inert atmosphere LFA holders. When sintering for longer periods of time, it was necessary to use a slightly larger die set due to the pellets shrinking in diameter. The green pellets were sintered under flowing UHP argon. The pressing force, sintering

temperature, and sintering time were all varied in order to create pellets with a range of densities. The sinter temperature ranged from 800 to 1100°C and the sinter time ranged from 1 minute to 48 hours. The sintering data for each pellet can be found in Appendix 6. In general, the pellets were 11-13 mm in diameter and 2-3 mm thick after sintering.



Figure 3-31: Tooling used for pressing pellets



Figure 3-32: U HDH pellet representative of all low density pellets created

3.10 Density Measurements

The density of each pellet was measured geometrically using calipers as well as by using an immersion measurement method based on Archimedes buoyancy principles. When using calipers, the diameter and thickness were measured at least three times in different locations around the pellet. The measurements were then averaged and used to calculate the volume. Equation 3-1 was used to calculate the density from measured values. The equation is the general formula for calculating density, ρ , of a right cylinder with m as the mass, H as the thickness or height of the pellet, and D as the diameter.

$$\rho \left[\frac{g}{cm^3} \right] = \frac{mass}{Volume} = \frac{m}{\frac{\pi HD^2}{4}} \quad 3-1$$

The immersion method was set up to calculate a more precise and accurate density by weighing the mass of the ethanol that was displaced by the pellet. This was done by first measuring the mass of the sample when it was dry and next when the sample was immersed in ethanol and finally when the sample was soaked in ethanol. The dry mass was easily measured on a balance. The balance used in this process was an

AB204S and it was checked and calibrated each time with a class 1 ASTM 200 gram standard. The immersed mass was measured by setting up a hanging basket which was supported on the balance with the basket completely immersed in ethanol. The soaked mass was measured by first soaking the samples in ethanol until bubbles were no longer leaving the sample, wiping the wet sample on paper towels pre-soaked with ethanol, quickly placing the sample in an airtight container, and finally the mass of the pellet and ethanol minus the weight of the dry container gave the desired measurement. At the time of each measurement the mass of 25 ml of ethanol was checked for comparison to the theoretical density of ethanol and the value found for that test was used for the calculations related to that specific sample. The Archimedes system can be seen in Figure 3-33. The equations used for the Archimedes density calculations are as follows:

$$\rho_{sample} = \frac{m_d}{m_s - m_i} \rho_{eth} \quad 3-2$$

$$Porosity = \frac{m_s - m_d}{m_s - m_i} \quad 3-3$$

where ρ_{sample} is the density of the sample being measured, ρ_{eth} is the density of ethanol, m_d is the mass of the dry sample, m_s is the mass of the sample soaked in ethanol, and m_i is the mass weighed when the sample is immersed in ethanol. [33]

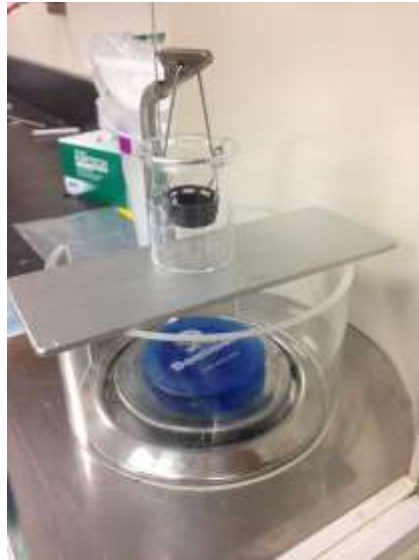


Figure 3-33: Archimedes immersion method measurement setup

3.11 Light Flash Analysis (LFA) Technique

The light flash technique is a widely used method for determining thermal conductivity. In this project a NETSCH LFA 447 Nanoflash (Figure 3-34) was used to conduct light flash technique experiments. The basic concept is that a high-intensity xenon lamp briefly flashes light onto one side of the sample and then an infrared detector is used to measure the temperature increase over time on the other side of a sample. A schematic showing the location of the sample, the detector, and the flash lamp can be seen in Figure 3-35. This temperature increase over time, along with the thickness of the sample, is then used to calculate the thermal diffusivity. The thermal diffusivity can then be used to calculate the thermal conductivity using Equation 3-4 where k_e is the effective thermal conductivity, α is the thermal diffusivity, ρ is the density of the sample, and c_p is the specific heat.

$$k_e = \alpha * \rho * c_p \quad 3-4$$

The specific heat used for calculation of the thermal conductivity for uranium was calculated from Equation 3-5 which is valid in the temperature range of 298 to 942 K. [23]

$$C_p = 24.959 + .002132 * T + .0000237 * T^2 \quad 3-5$$

The specific heat used for calculation of the thermal conductivity for U-10Zr was calculated from Equation 3-6. [4]

$$C_p = 1.359 + .05812 * T + 1086000 * T^{-2} \quad 3-6$$

The specific heat used for calculation of the thermal conductivity for U-5Zr was calculated by using linear interpolation between the value for U and U-10Zr. [4] A table that contains the values of the specific heat for U, U-5Zr, and U-10Zr at 30 and 300°C based on the above equations can be seen in Table 3-9. The specific heat is expressed units of J/gK. The specific heat is the heat capacity per unit mass of a material, so it is independent of the density of a given material.

Table 3-9: Specific heat of U, U-5Zr, and U-10Zr in units of J/gK [4] [23] [34]

T [C]	U	U-5Zr	U-10Zr
30	0.117	0.110	0.138
300	0.143	0.131	0.170



Figure 3-34: LFA 447 Nanoflash

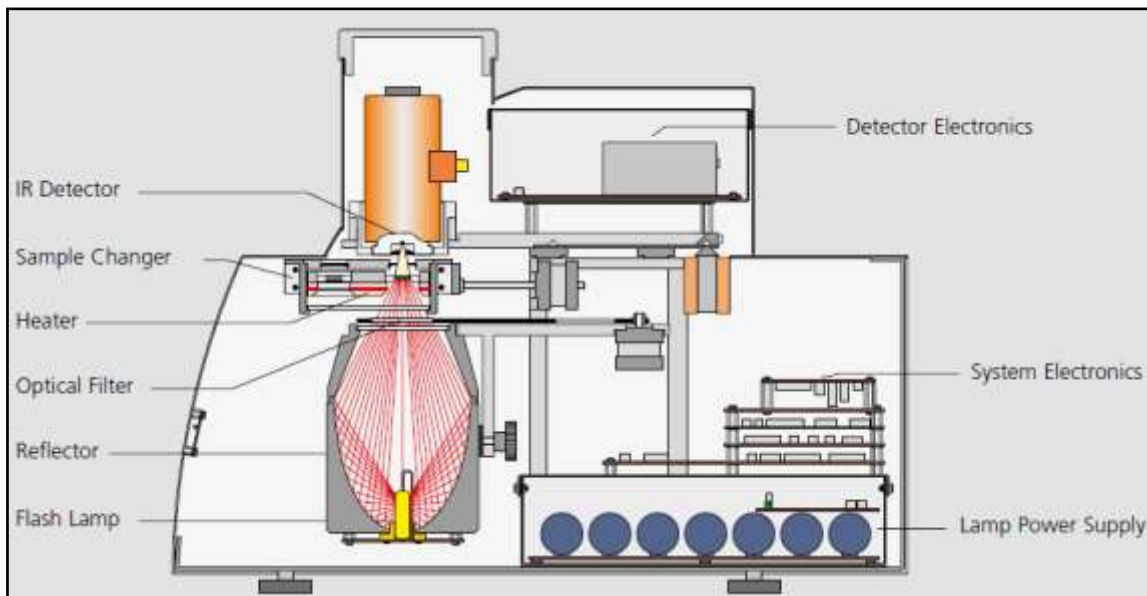


Figure 3-35: Diagram of LFA 447 Nanoflash

There are multiple models in the LFA software that can be chosen to calculate the thermal diffusivity from the plot of signal vs time. The Cape-Lehman model was selected for this project because it fit the generated plots better than the other models. Additionally, it is the most widely used model for thermal conductivity measurements via LFA. [35]

Prior to loading sample into the LFA, each sample was coated with Sprayon Dry Film Graphite Lubricant, LU 204. The graphite enabled the samples surfaces to act as a "black body," absorbing the entire thermal pulse. The temperature of each sample was varied from 20°C to 300°C and 5 measurements were taken every 10°C and 10 measurements were taken at 300°C. Normally, this instrument is operated in air, but due to the sensitivity of uranium metal to oxygen, the samples were tested inside of the inert atmosphere holders. Picture of the assembled and disabled inert atmosphere holder can be seen in Figure 3-36. The holders seal the sample inside an argon atmosphere so that the sample does not oxidize. The sample was loaded into the holder while inside of an inert atmosphere glovebox. A high temperature O-ring was used to make a seal and 4 screws are tightened to hold the 2 halves together. A window on each half allows the light to pass in and out so that the test may still be completed. The holders are made of stainless steel 409 and the windows are made of sapphire. The holders were tested with standards multiple times to ensure that the resulting data would still be accurate. The standard tests can be seen in Appendix 4.

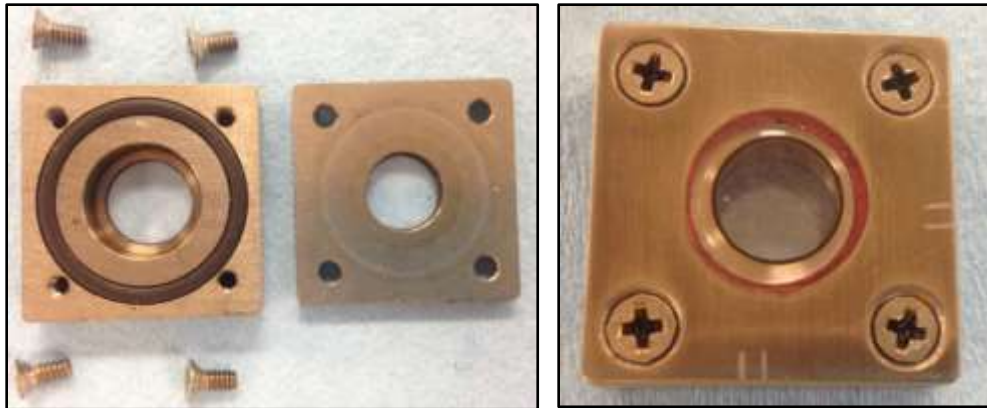


Figure 3-36: Inert atmosphere LFA sample holder

3.12 Preparation of Samples for Microstructure Analysis

In order to view the microstructure of samples with electron microscopy it was necessary to secure them in a mount of some sort and polish the surface to as close to perfectly flat as possible. After an extrusion, the rod or tube was removed from the die. The rod or tube was then cut using a diamond abrasive saw. The samples were first cut radially and then cut in half axially. Samples were mounted in epoxy after sectioning and polished for imaging. The samples were polished either by hand or using the Buehler Minimet 1000 Grinder/Polisher. A rough sequence for the polishing regimen can be seen in Table 3-10.

Table 3-10: General Sequence for Polishing

Grit Size	Force [N]	Speed Setting	Time [min]	Number of Times
400	30	30	5	1-3
600	30	30	5	2-6
800	30	30	5	2-3
1200	20	30	5	1-2
3 um	10	30	15	1-2
1 um	5	30	15	1-2
0.25 um	5	30	15	1-2

In some cases, samples were also electro-polished and electro-etched. The etching was necessary to see the grain structure of the uranium samples. The electro-polish consisted of a supply of 3 V in a solution of 5% phosphoric acid. The electro-etch consisted of a supply of 4 V and a 10% solution of oxalic acid. The voltage was supplied by a TDK-Lambda power supply. The positive voltage supply was connected to a tantalum wire and was placed in contact with the sample surface. The negative voltage supply was attached to a small sheet of stainless steel which was placed a few millimeters from the surface of the sample. The procedure was based on results from working with S. Irukuvarghula as well as other polishing procedures in literature. [36]

The LFA samples were similarly cut, mounted, and polished, with the exception that they were first mounted in epoxy and then cut. This was done to ensure that the pellet did not fall apart when being cut on the diamond saw. Most pellets were cut axially.

3.13 Electron Microscopy of Samples

After polishing was completed, samples were carbon coated in a Cressington Carbon Coater 108 carbon/A. The carbon coating not only helped create a conductive surface for better imaging but also helped to decrease the oxidation rate of the sample surface. Most SEM images were acquired using the JEOL 6400 at the FCML but additional images were also acquired using the FEI Quanta 600 FE-SEM at the TAMU Microscopy department. Several imaging techniques were used including back scatter

electron (BSE) imaging, energy-dispersive x-ray spectroscopy (EDX) imaging, and electron back scatter diffraction (EBSD) scans.

The BSE images were used to see the general structure of the samples and investigate any interesting parts of the sample. The EDX images were used to show the distribution of the uranium and zirconium. The EBSD scans were used to investigate whether or not there was a crystal structure texture in the large zirconium grains of the U-10Zr alloy.

3.14 Neutron Diffraction

Neutron diffraction texture measurements were performed at the Los Alamos National Laboratory Neutron Science Center (LANSCE) on the time of flight diffractometer, HIPPO. [37] A sample of the extruded rod from U-10Zr extrusion 1 was used. Measurements were taken at 600°C, 650°C, 680°C, 700°C, and 800°C, during heating and cooling. These temperatures were chosen based off of the phase changes in the U-10Zr system.

For texture analysis, the diffraction spectra from all detector banks and sample rotations were simultaneously refined by Rietveld method using MAUD software which utilizes the E-WIMV approach to calculate the ODF's. [38] Individual pole figures were recalculated using MTEX software after exporting the data from MAUD. [39]

4 RESULTS

4.1 U-10Zr Rod Extrusions

4.1.1 Extrusion 1

Extrusion 1 was the first experimental extrusion with U-10Zr. The billet temperature was 600°C and the reduction ratio was 11.1. The plot of the extrusion force and position vs time can be seen in Figure 4-1. This plot has many peaks and valleys due to the way the press was operated during the extrusion. The increase in force was due to the down button being pressed and then the peak and following valley results from releasing the down button. There was a short in the control cord that caused the loss of signal in the down button. This was repaired before future extrusions. Based on the LVDT movement and the load cell data the maximum force was taken to be 68947 lb and an extrusion constant of 64.64 was calculated.

The temperature profile of the extrusion can be seen in Figure 4-2. The time axis begins at approximately the time the heater was turned on. The time axis for the temperature profile is plotted this way for all of the extrusions. The die temperature profile is not shown separately at the time of the extrusion because the thermocouple was not placed close enough to the die opening to register a temperature increase.

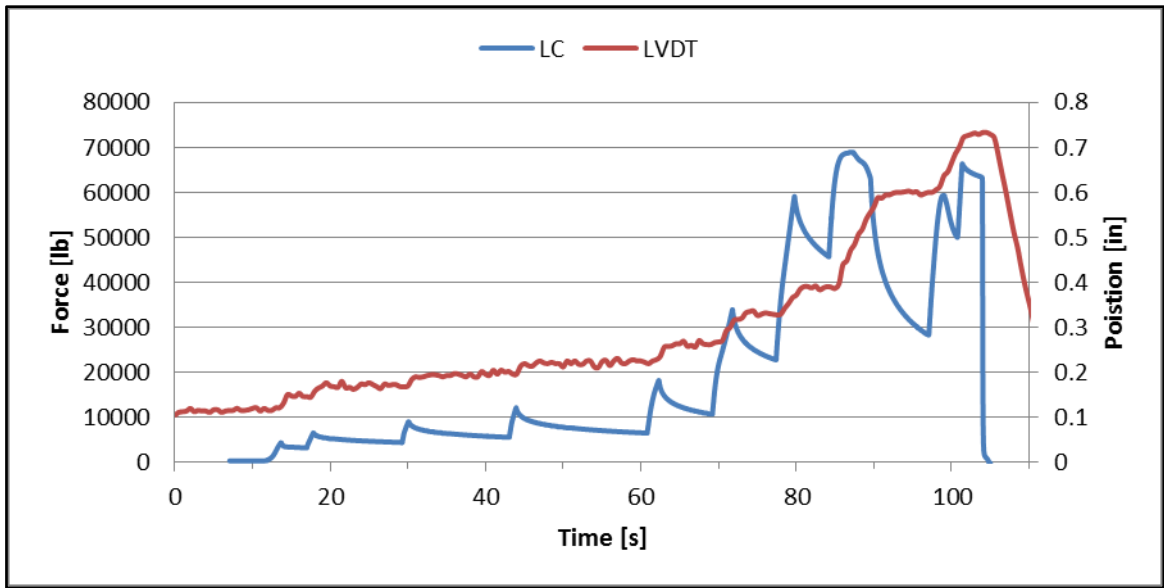


Figure 4-1: Force and position vs time for extrusion 1

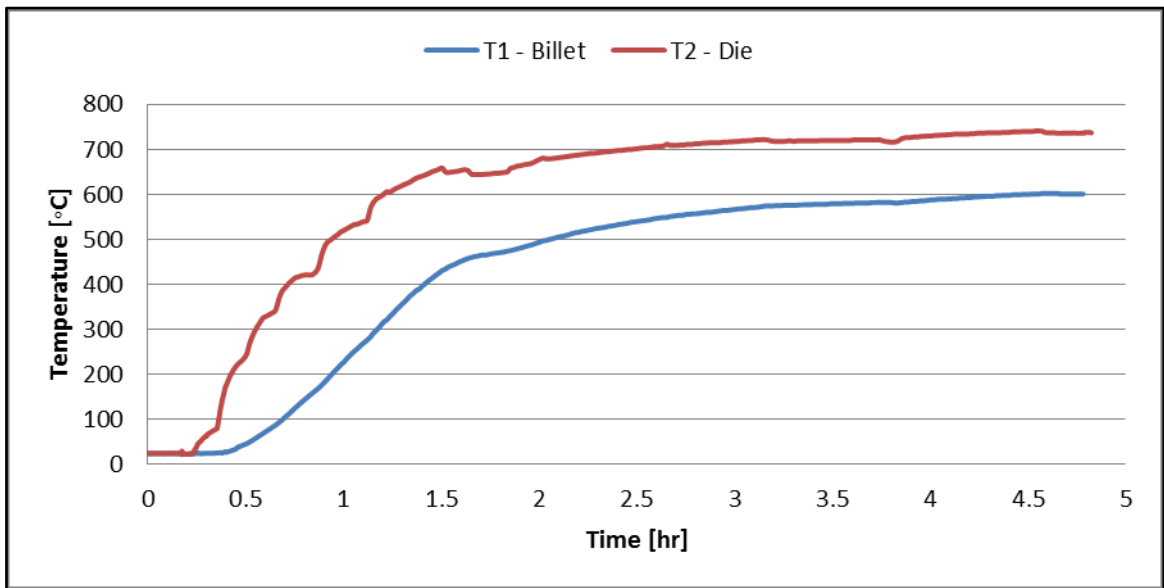


Figure 4-2: Temperature profile of extrusion 1

A picture of the tooling used in this extrusion can be seen in Figure 4-3. The extrusion tooling was all made of H-13 tool steel. The cross section of the ram was a “T” so that it would not be pressed down into the die too far. This design was later

abandoned. The ram was heated in place with the rest of the tooling in this extrusion experiment.

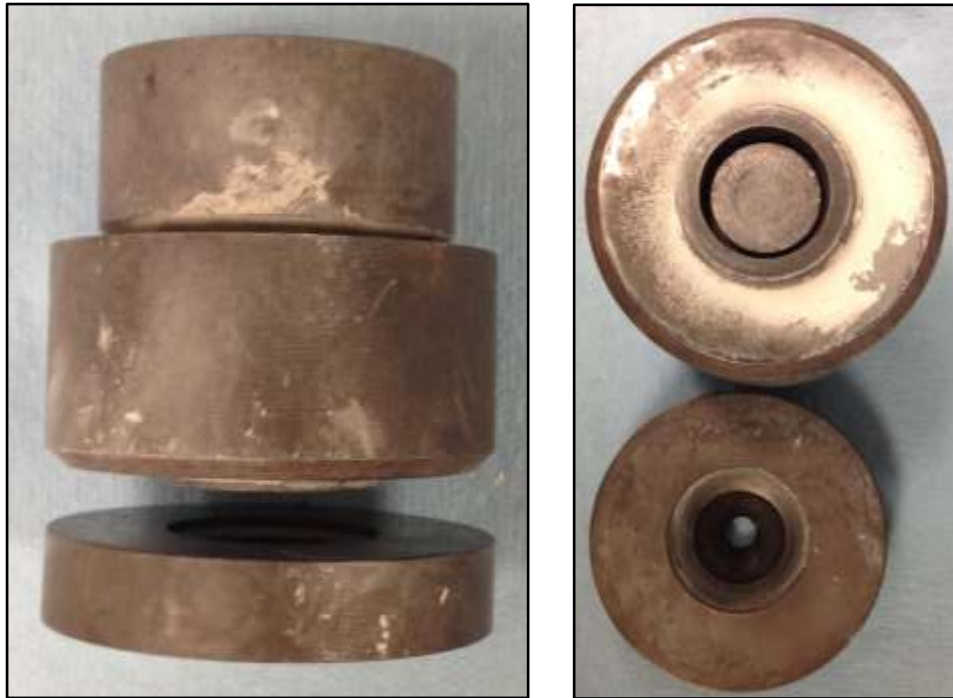


Figure 4-3: multiple views of tooling used in extrusion 1

The extruded rod was about 1.5 in long and a picture of the extruded rod can be seen in Figure 4-4. The unextruded portion of the billet can still be seen with the rod. Every extrusion had some unextruded portion remaining due to the reduction cone area. The odd shape of this unextruded portion is due to the billet being forced up around the ram inside of the holder and also in between the holder and the die. From this result it was decided that the holder and the die should be bolted together and the ram must have a tighter fit in the holder. The tighter fitting ram ultimately caused problems in other extrusion experiments and a dummy block was added instead.



Figure 4-4: U-10Zr rod from extrusion 1

4.1.2 Extrusion 2

Extrusion 2 was a U-10Zr rod extrusion and was performed at 650°C and with a reduction ratio of 10.7. During this extrusion there was a malfunction and the load cell data was not recorded. Since the load cell data was not recorded the extrusion constant could not be calculated. The extruded rod was about 2 inches long and can be seen Figure 4-5.

The temperature profile of the extrusion can be seen in Figure 4-6. The die temperature profile is not shown separately because without the load cell data the exact time of the extrusion relative to the temperature is not known.



Figure 4-5: U-10Zr rod from extrusion 2

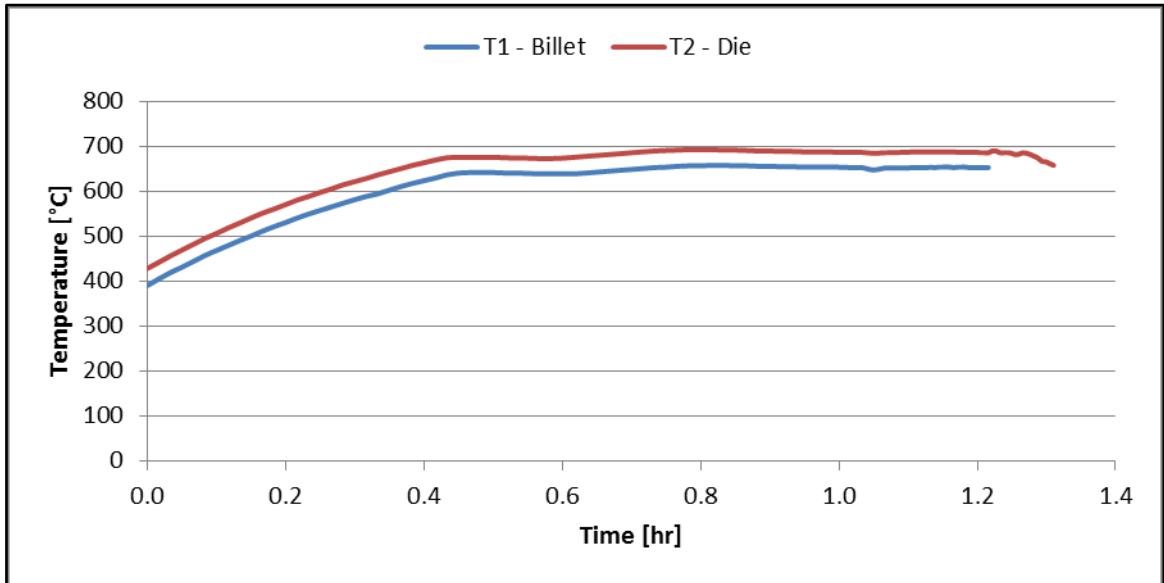


Figure 4-6: Temperature profile of extrusion 2

The tooling used in extrusion 2 can be seen in Figure 4-7. All tooling in this set was made of H-13 tool steel. The ram was heated in place with the rest of the tooling set prior to extrusion. The ram of this tooling set had a 45 degree reduction cone at the bottom end which reduced the head of the ram to a smaller flat area. This was done to increase the amount of the material that was extruded. This was not done in any other extrusions because it did not succeed. Additionally, the ram was pressed too far into the holder during the extrusion process and was unable to be removed due to the deformation of the ram and holder. The bolts that held the die and holder together were

cut in order to separate the die from the holder. The bolts did serve their purpose and keep the holder and the die together. Some of the unextruded billet did push up between the ram and holder.



Figure 4-7: Multiple views of tooling used in extrusion 2

4.1.3 Extrusion 3

Extrusion 3 was a U-10Zr rod extrusion and was conducted at a temperature of 650°C and a reduction ratio of 10.9. The force and position vs time plot, Figure 4-8, shows a mostly constant rate of extrusion until closer to the end of the extrusion when the billet material was almost fully extruded. The extrusion is stopped as the force required increases abruptly. The maximum force was taken to be 88857 lb and the extrusion constant was calculated as 75.82.

Figure 4-10 is a plot of the temperature of the die during the extrusion. This plot shows that the temperature increase during this extrusion was about 15°C. Unfortunately, the temperature was only recorded every 30 seconds rather than every second. The time axis of this plot corresponds with the same time axis in the force and position vs time plot show in Figure 4-8. The time axis is plotted this way for the die temperature profile for all of the extrusions.

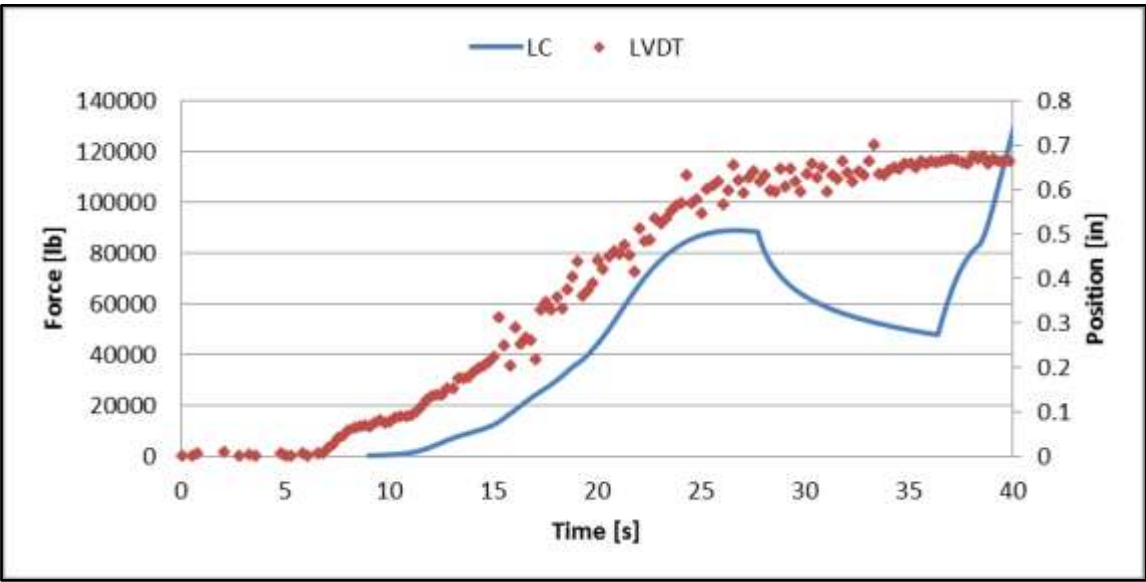


Figure 4-8: Force and position vs time for extrusion 3

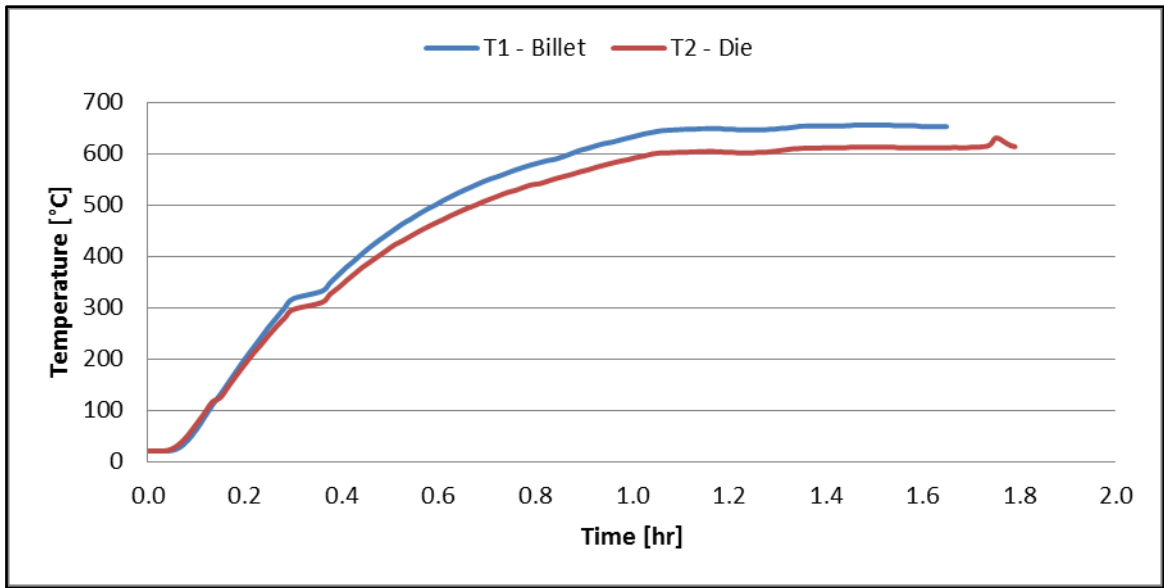


Figure 4-9: Temperature profile of extrusion 3

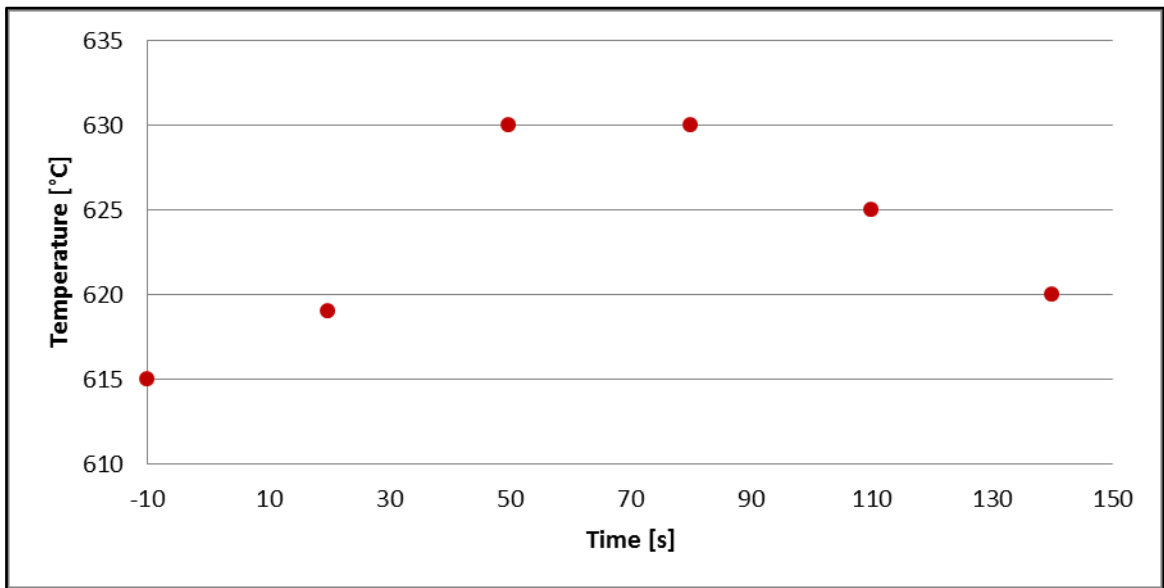


Figure 4-10: Die temperature increase during extrusion 3

The die used in extrusion 2 was reused in extrusion 3. The tooling used in extrusion 3 was made of H-13 and can be seen in Figure 4-11. This was the first extrusion to use a ram that was only a cylinder rather than the previous style that had a top portion

that was a larger diameter, forming a cross section that is a “T”. The ram was machined to be the same length as the holder so that it could not be forced into the reducing die. A cylinder that was 2 inches in diameter and 1 inch thick was placed on top of the ram and was in contact with the steel plate during the extrusion. The cylinder was pressed against the top of the holder when the extrusion ended. The tooling set was slightly deformed during this extrusion. The ram was slightly shortened and ballooned out at one end. The holder was widened at the bottom slightly corresponding with the ram. The die was slightly indented where it came into contact with the holder. The extruded rod was about 2 inches long and can be seen in Figure 4-12.

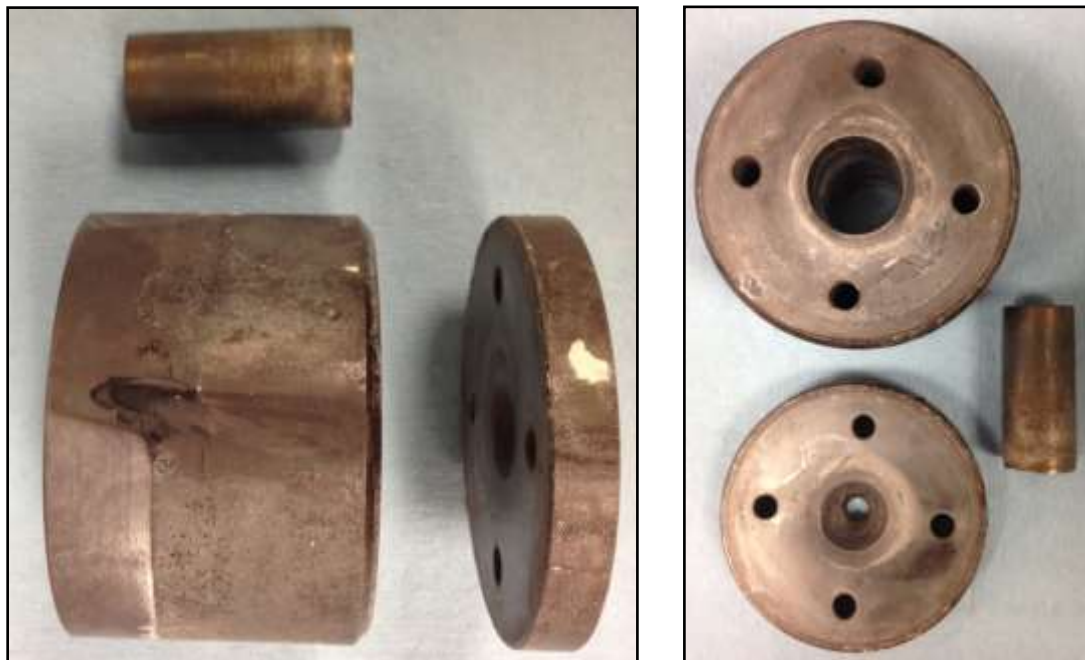


Figure 4-11: Multiple views of tooling after use in extrusion 3



Figure 4-12: U-10Zr rod from extrusion 3

4.1.4 Extrusion 4

The temperature of extrusion 4 was 550°C and the reduction ratio was 11.3. The tooling used in extrusion 4 was all made of H-13 and can be seen in Figure 4-13 as it was prior to the extrusion. The ram failed during the extrusion process at the point of maximum force and the extrusion was halted. Pictures of the tooling after the extrusion can be seen in Figure 4-15 and Figure 4-14. In Figure 4-15 the U billet can be seen in the shape of the reduction cone because it had begun to extrude and had just reached the point of filling the reduction cone before it would begin to exit the die opening. It is at this point that the ram began to fail. The ram most likely first ballooned out and came into contact with the holder wall and became stuck. Next, the portion of the ram that was outside the holder ballooned out in all directions as it was pressed down. This ram failed for two reasons, the first being that the extrusion temperature was only 550°C and this was too low a temperature to deform the uranium instead of deforming the steel. The second reason, which was addressed in Section 3.4, was that the tolerance between the ram and the die was too tight.



Figure 4-13: Extrusion tooling before use in extrusion 4



Figure 4-14: Tooling used in extrusion 4



Figure 4-15: Top (left) and bottom (right) of holder after extrusion 4

Taking the maximum force to be 120752 lb, the extrusion constant was calculated to be 101.13. The maximum force was taken at this point because of the change in slope of the force plot at this point which represents that something else was undergoing deformation rather than the uranium billet. The extrusion was halted because the force display was at 160000 lb and that was higher than expected.

The temperature profile of the extrusion and the die temperature profile can be seen in Figure 4-17 and Figure 4-18 respectively. The time axis of the overall temperature profile corresponds to the heater being turned on while the time axis of the die temperature profile corresponds to the force and position vs time plot. The measured increase in die temperature was only 3°C. This was due to the extrusion being stopped before completion.

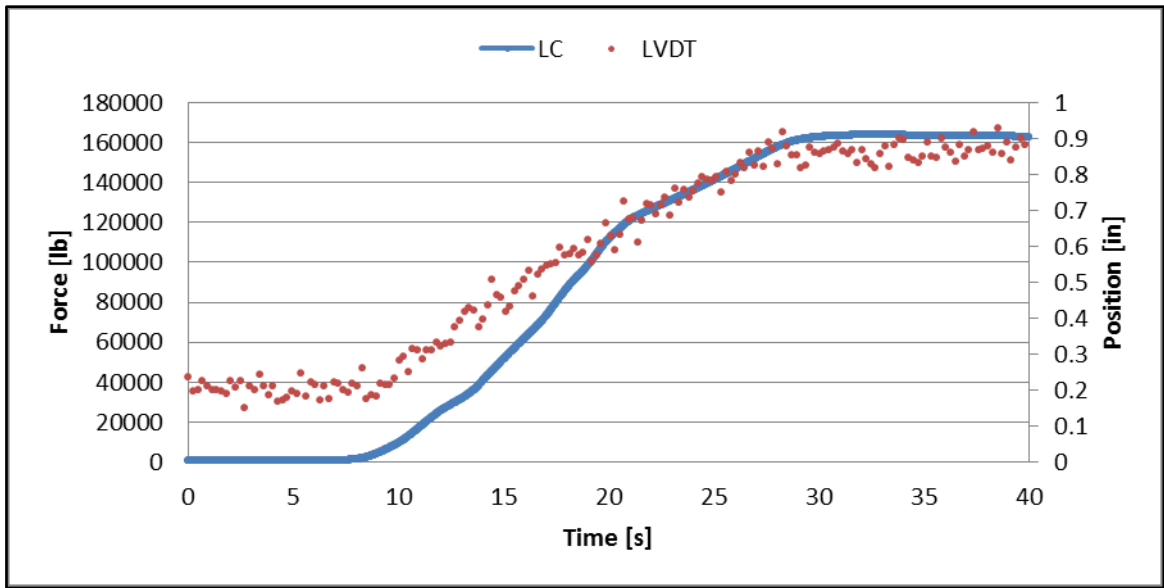


Figure 4-16: Force and position vs time for extrusion 4

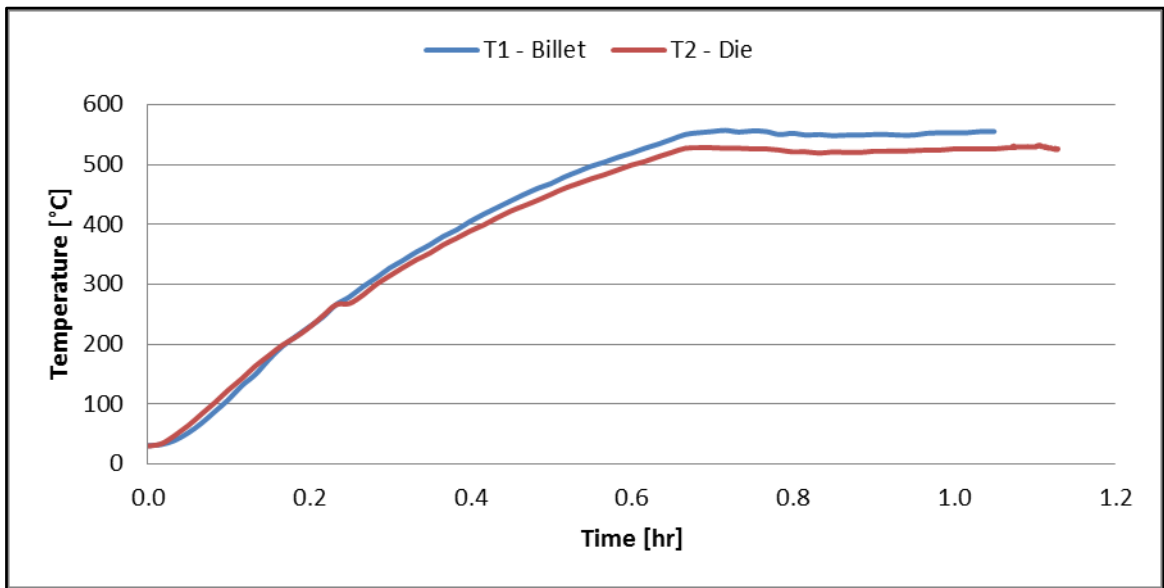


Figure 4-17: Temperature profile of extrusion 4

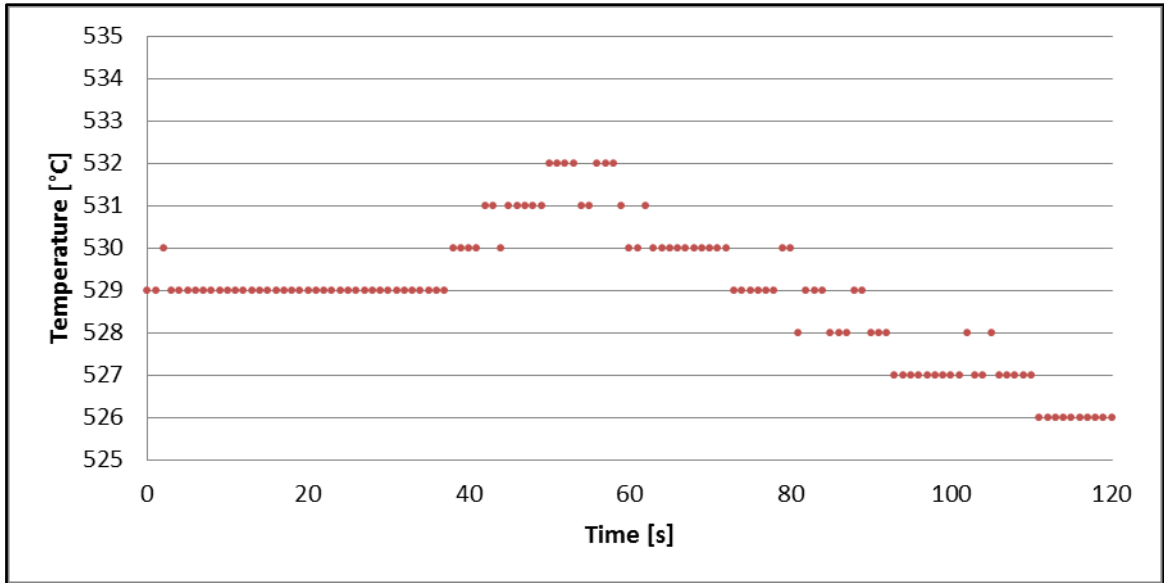


Figure 4-18: Die temperature increase during extrusion 4

4.1.5 Extrusion 5

Extrusion 5 was a U-10Zr rod extrusion conducted at 620°C with a reduction ratio of 5.2. The tooling used in extrusion 5 can be seen in Figure 4-19 and Figure 4-20. This extrusion had a similar outcome as the previous extrusion. The ram began to deform, became stuck in the holder, and then deformed severely. The reason for this failure is the same as extrusion 5; the tolerance between the ram and the die was too tight. This extrusion did progress slightly farther than the previous one and a very short section of rod was produced.

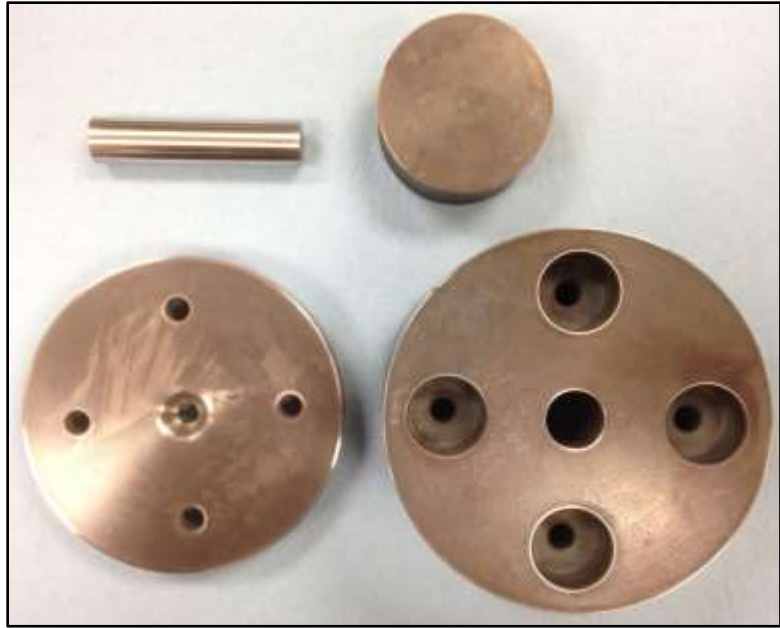


Figure 4-19: Extrusion tooling before use in extrusion 5

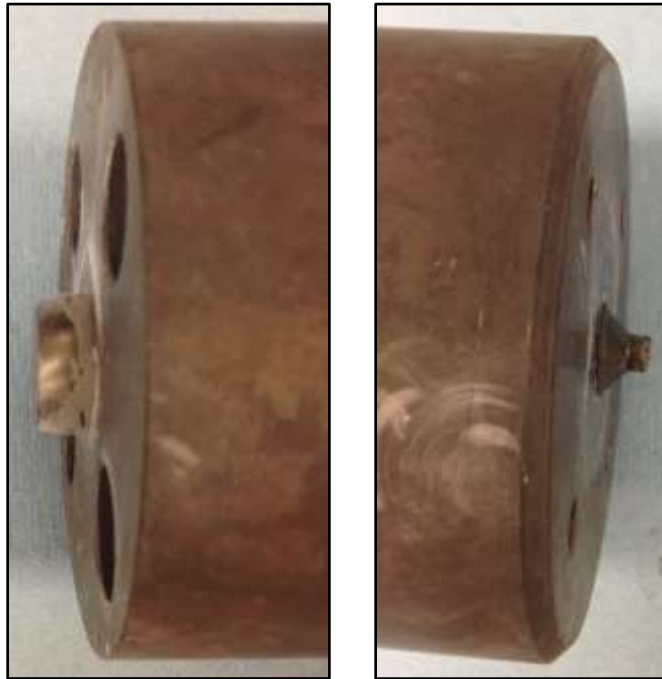


Figure 4-20: Top (left) and bottom (right) of holder after extrusion 5

The maximum force was taken to be 52939 lb and the extrusion constant was calculated to be 159.48. The maximum force was taken at this point because of the change in slope of the force plot at this point which represents that something else was undergoing deformation rather than the uranium billet. The force and position vs time plot can be seen in Figure 4-21.

The time axis of the die temperature profile corresponds to the time scale of the load cell and LVDT plot. The temperature increase of the die was measured to be 9°C.

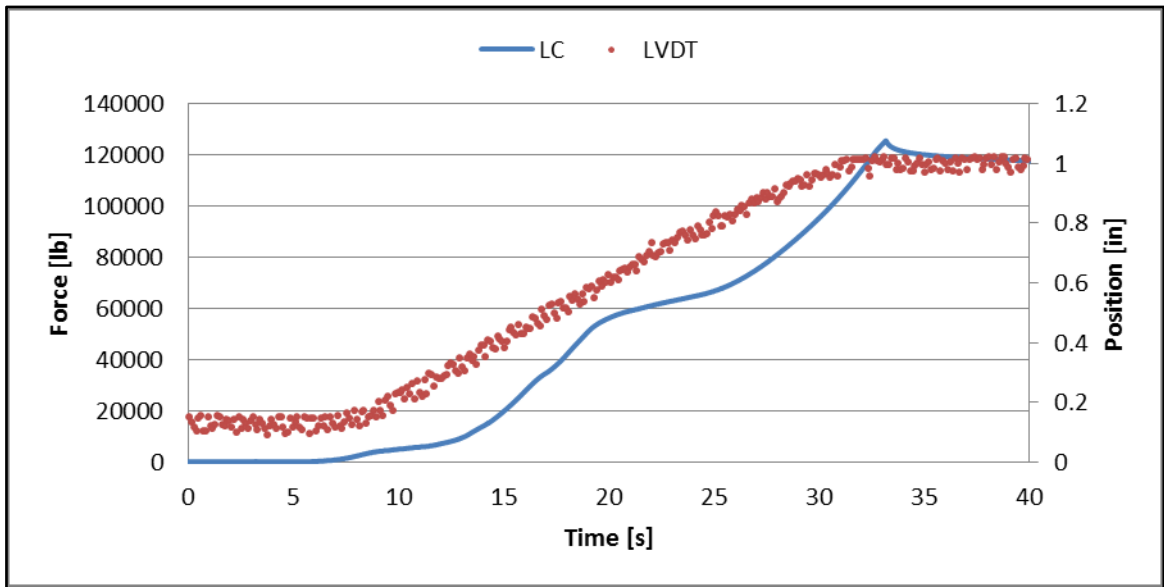


Figure 4-21: Force and position vs time for extrusion 5

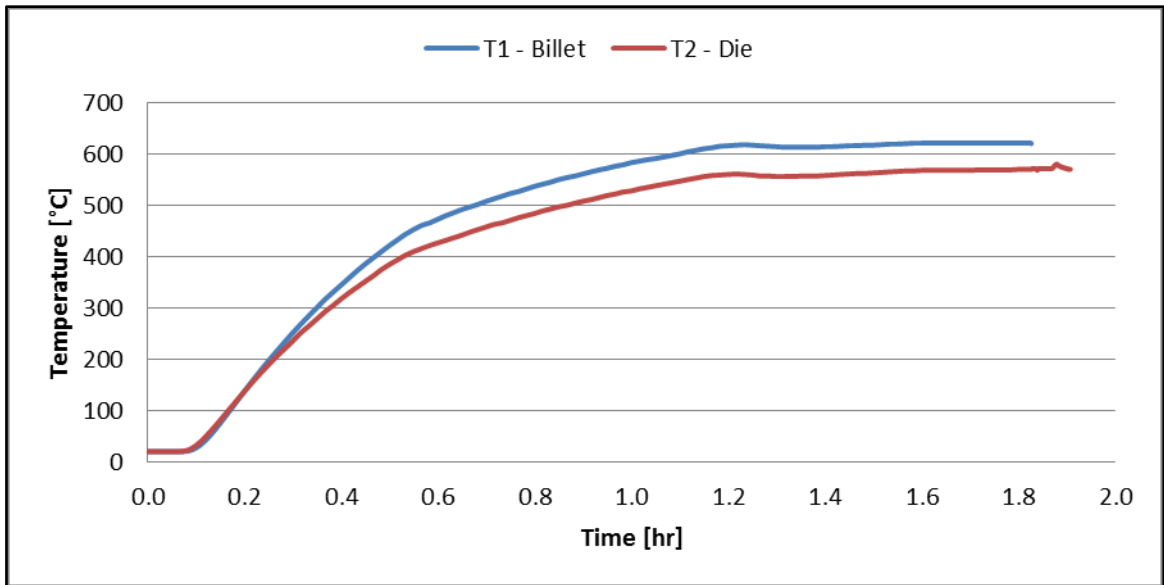


Figure 4-22: Temperature profile of extrusion 5

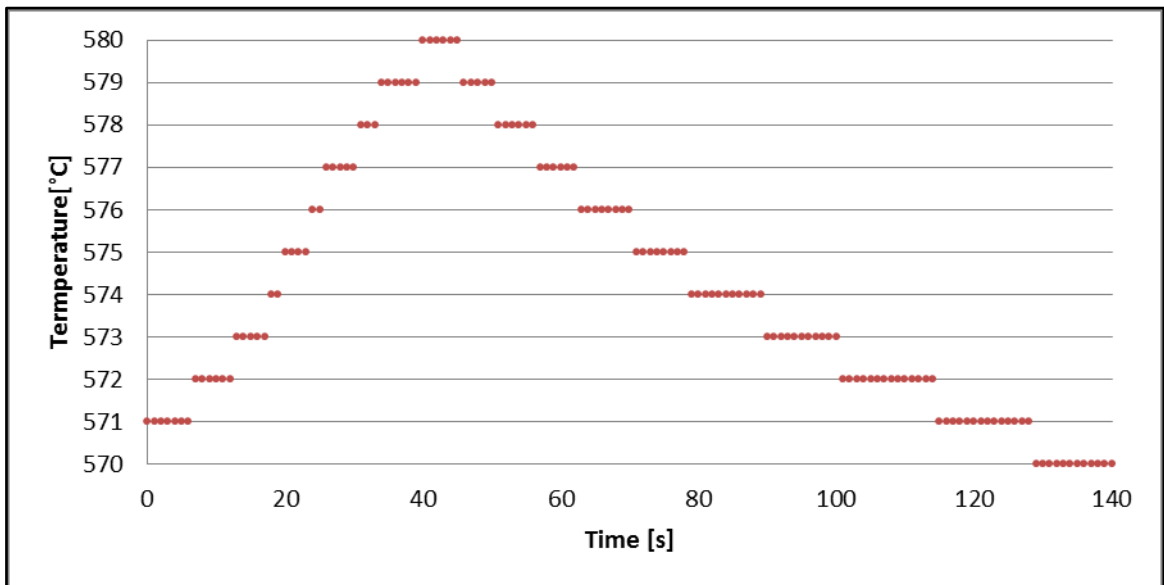


Figure 4-23: Die temperature increase during extrusion 5

4.1.6 Extrusion 6

Extrusion 6 was a U-10Zr rod extrusion conducted at 620°C with a reduction ratio of 15.4. Extrusion 6 was only a partial extrusion due to the ram becoming stuck in

the holder during the extrusion. The top of the ram can be seen in Figure 4-24. The ram is only slightly deformed. The extruded rod was 1.5 in long. It was accidentally bent during the attempted removal from the die. The billet is only partially extruded and can still be seen in Figure 4-25.



Figure 4-24: Failed ram of extrusion 6

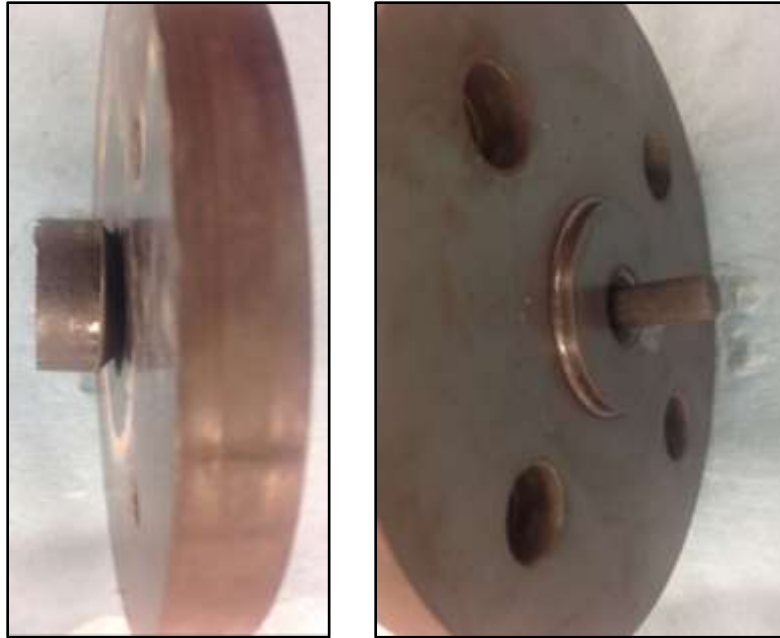


Figure 4-25: Partially extruded U-10Zr rod from extrusion 6

The extrusion was halted when the force reached 150000 lb because this was higher than expected. The force and position vs time plot for this extrusion can be seen in Figure 4-26. The extrusion was stopped at about 15 s. As previous extrusions, the maximum force used for the calculation of the extrusion constant was found at the point of the change in slope which represents when the ram began to deform. The maximum force was taken to be 135000 lb and the extrusion constant was calculated at 74.03. The temperature rise in the die can be seen in Figure 4-28, and it was measured to be 7°C.

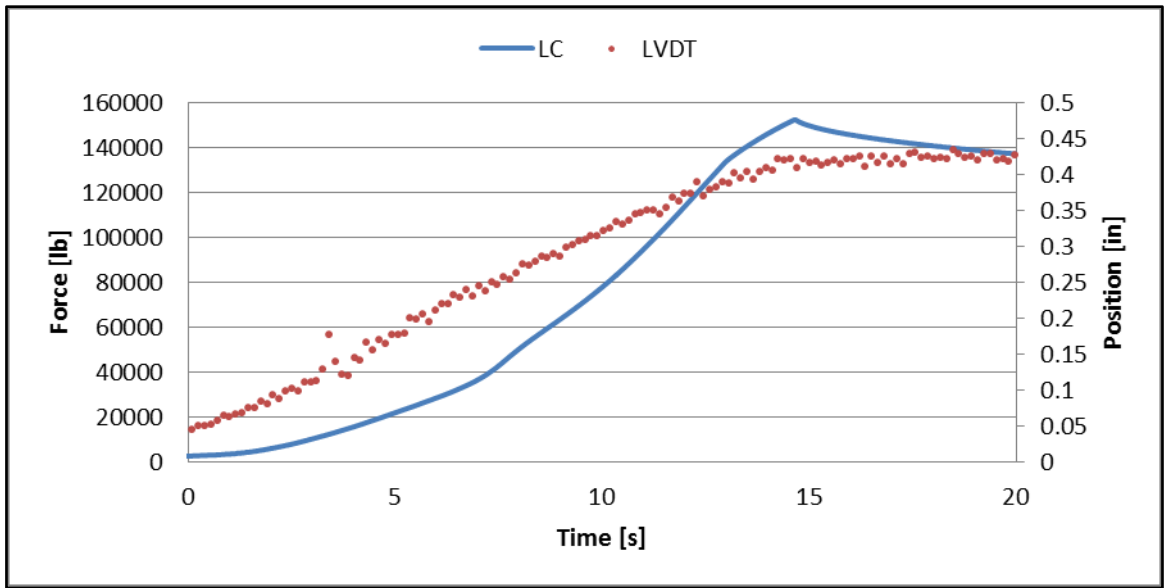


Figure 4-26: Force and position vs time for extrusion 6

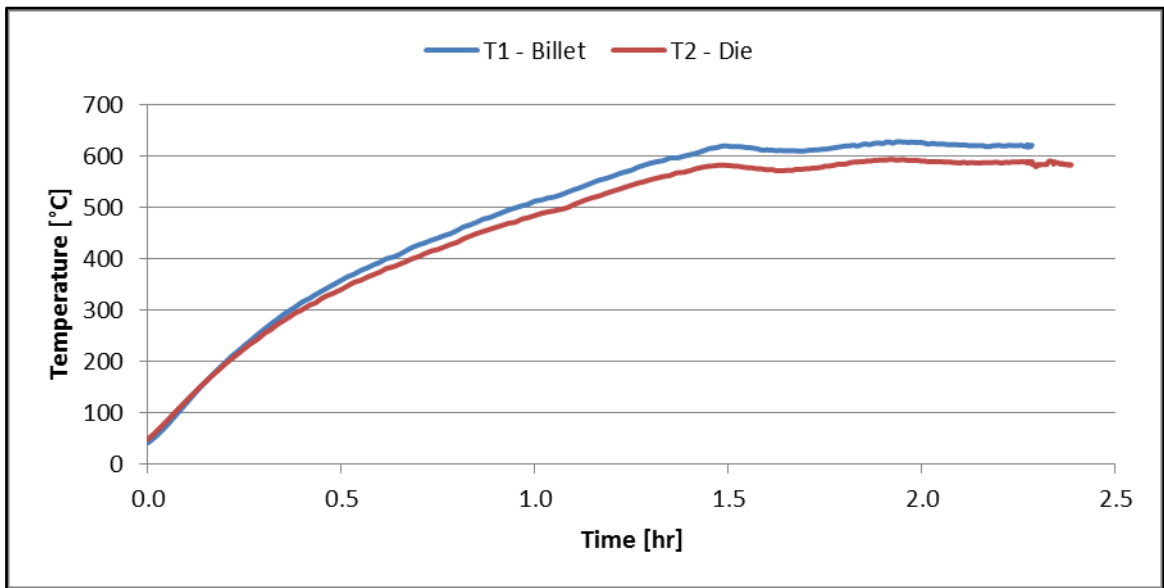


Figure 4-27: Temperature profile of extrusion 6

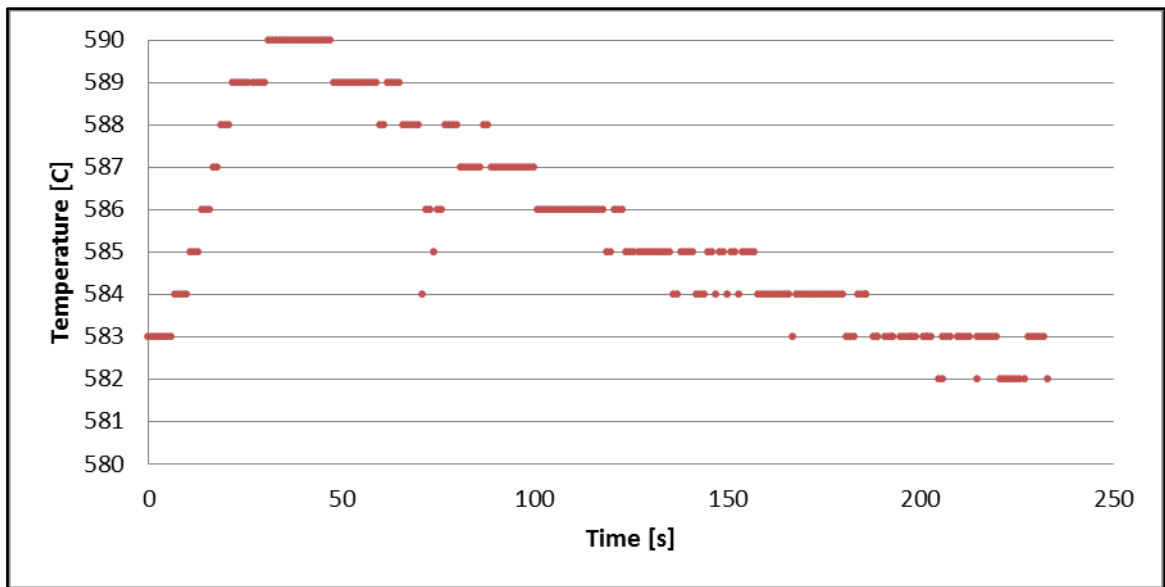


Figure 4-28: Die temperature increase during extrusion 6

4.1.7 Extrusion 11

Extrusion 11 was a U-10Zr rod extrusion conducted at 650°C with a reduction ratio of 15.5. The ram and dummy block used in this extrusion were made of C350. The ram was inserted cold after the rest of the tooling and billet achieved a stable temperature. The tooling set also featured 2 set pins to align the center of the holder and the die. This tooling set was the same tooling set used in the copper rod test 2 extrusion. The holder of the tooling set was slightly deformed after that extrusion, leaving the opening very slightly larger (+.008 in) than it was originally.

The extruded rod was 4.0 inches long and can be seen in Figure 4-29. The rod starts out with a slight curve before it straightens out for the rest of the extrusion. Some of the uranium billet did press up around the dummy block and out in between the holder and the die. The uranium was able to press up around the dummy block due to the previously mentioned deformation of the holder which resulted in the dummy block not

fitting tight enough in the holder. This product appears similar to the extruded product from U-10Zr extrusion 1 because that extrusion had the same issue. This loss of material resulted in a slightly shorter rod than anticipated.

The load cell and LVDT plot can be seen in Figure 4-30. The maximum force was taken to be 101802 lb and the extrusion constant was calculated as 55.06. The temperature rise during the extrusion was about 9°C and can be seen in the die temperature profile plot, Figure 4-32.



Figure 4-29: U-10Zr rod from extrusion 11

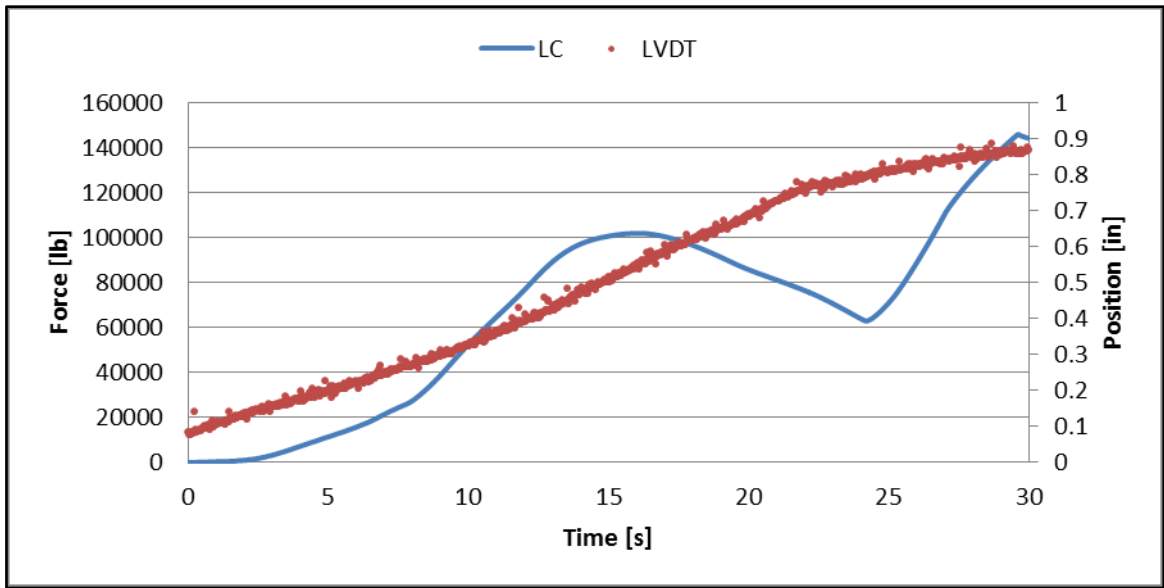


Figure 4-30: Force and position vs time for extrusion 11

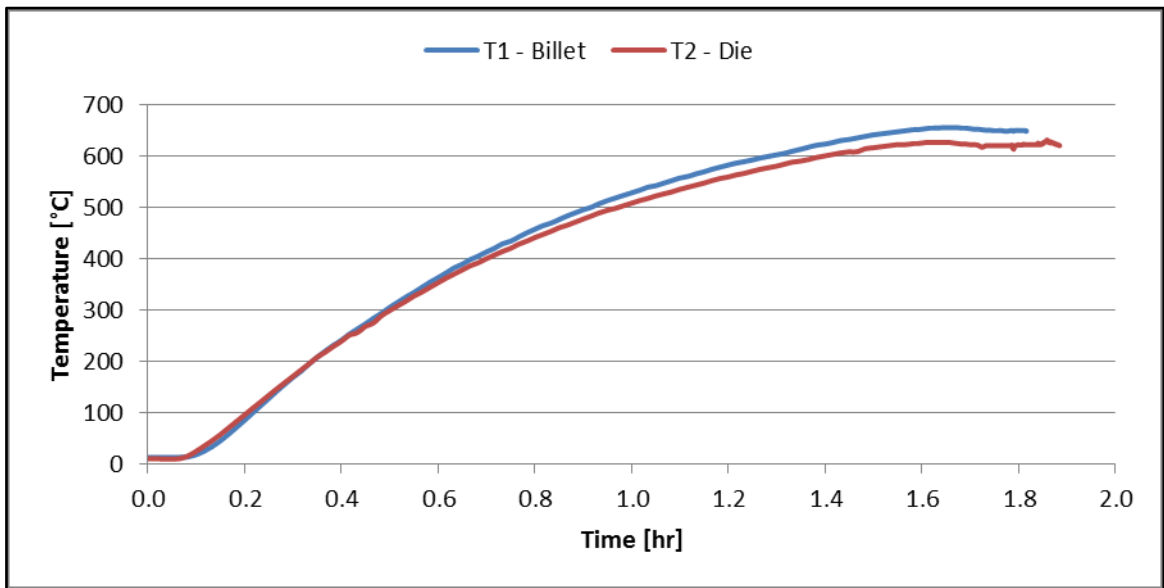


Figure 4-31: Temperature profile of extrusion 11

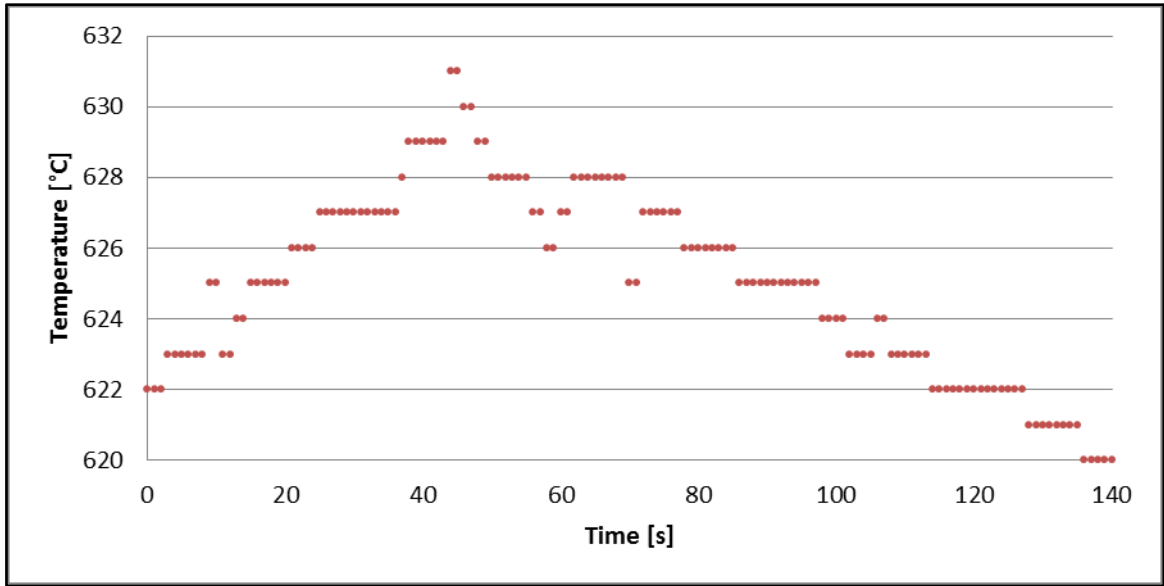


Figure 4-32: Die temperature increase during extrusion 11

4.1.8 Extrusion 13

Extrusion 13 was a U-10Zr rod extrusion conducted at 650°C with a reduction ratio of 15.3. The extruded product was the longest U-10Zr extrusion at 7.5 inches. This rod was longer than all of the others due to the billet being larger, the billet being fully extruded, and the tooling design. The billet used for this extrusion can be seen in Figure 4-33. The rod, Figure 4-34, starts out slightly curved and then straightens out as the extrusion progresses. This tooling set was the same design as the tooling used in copper rod test 2. The ram and dummy block used in this extrusion were made of C350. The ram was inserted cold after the rest of the tooling and billet achieved a stable temperature.



Figure 4-33: U-10Zr billet for extrusion 13



Figure 4-34: U-10Zr rod from extrusion 13

The maximum force was taken to be 112513 lb and the extrusion constant was calculated as 60.98. The force and position vs time plot can be seen in Figure 4-35. This extrusion plot is the closest to the theoretical plots mentioned in the background section of this dissertation. There is first the initial increase and then the plateau as the extrusion progresses followed by a sudden increase and the end of the extrusion. There is a slight change in slope of the position plot at the peak of maximum force. The rate of extrusion increased slightly after the upsetting section. The temperature rise in the die during the extrusion was measured to be 15°C and can be seen in Figure 4-37.

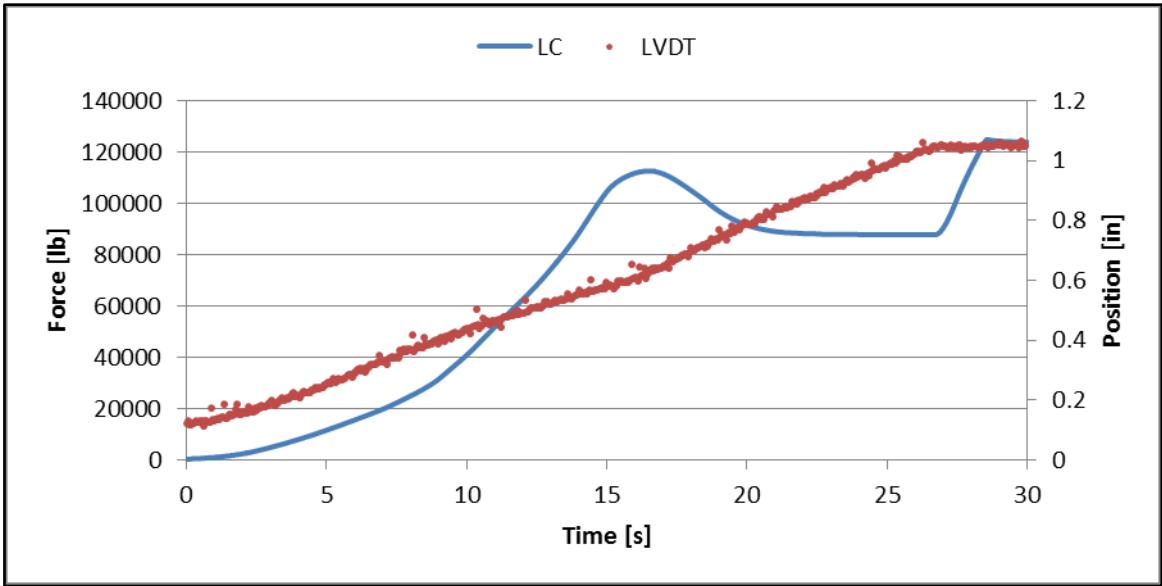


Figure 4-35: Force and position vs time for extrusion 13

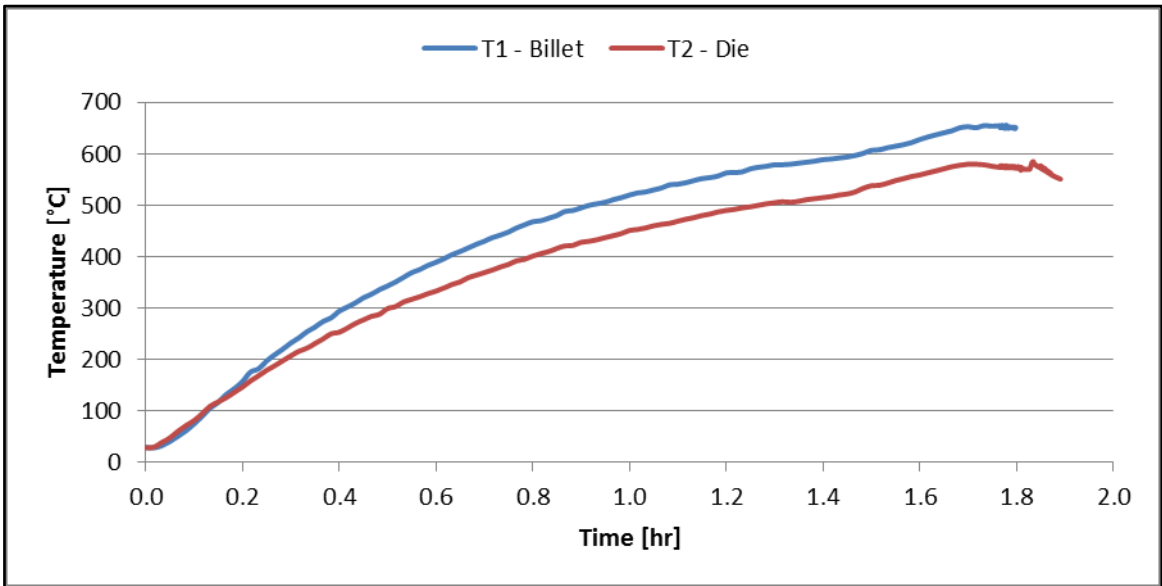


Figure 4-36: Temperature profile of extrusion 13

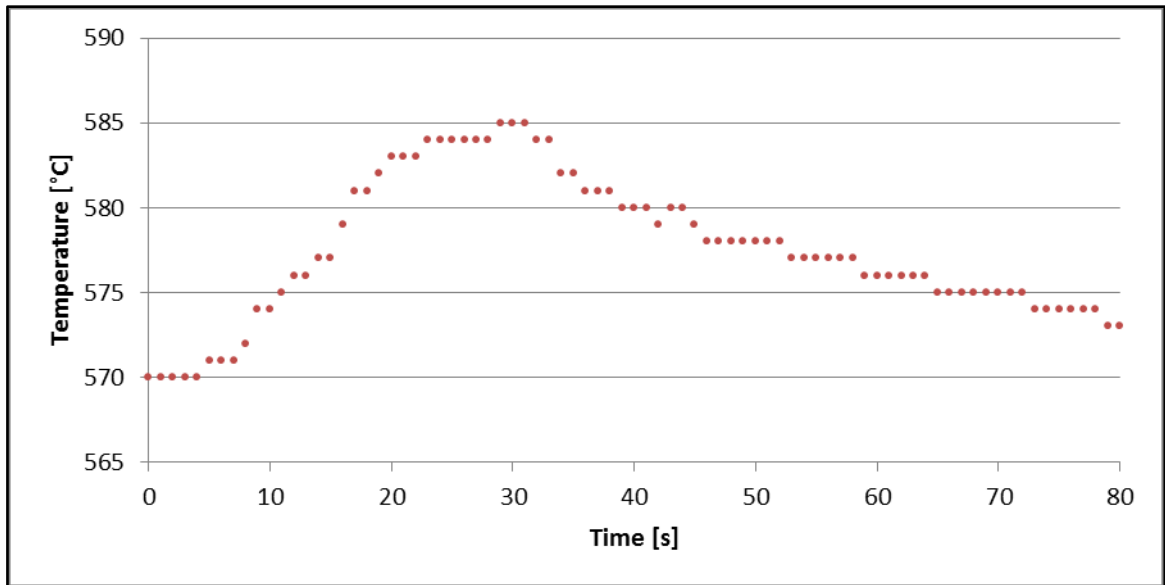


Figure 4-37: Die temperature increase during extrusion 13

4.2 U Tube Extrusions

4.2.1 Extrusion 7

Extrusion 7 was a U tube extrusion conducted at a temperature of 600°C with a reduction ratio of 10.1. During the extrusion, the mandrel broken off of the ram and the uranium carried the mandrel out of the die opening. This resulted in an extruded product that is partially tube and partially rod. The extruded product can be seen in Figure 4-39. In the upper image the product is still connected to the ram. The broken mandrel piece is located to the right of the cut inside of the tube cross section. Therefore, to the right of the cut is a tube, and to the left is mostly a solid rod. The right half was further sectioned; this can be seen in the other 2 images in Figure 4-39.



Figure 4-38: Extrusion 7 tooling before use



Figure 4-39: Multiple pictures of the U tube from extrusion 7

Since the first portion of this extrusion is a tube, the force plot can still be used to generate a reliable value for the extrusion constant. The maximum force was taken to be 75136 lb and the extrusion constant was calculated to be 65.85. Following the maximum force, the force required for the extrusion dramatically decreases. This is due to the cross section of the extrusion changing from a tube to a rod and thus decreasing the extrusion

ratio. This resulted in an easier extrusion so less force was required. The extrusion was then ended after the force abruptly increased to 90000 lb. The temperature of the die was recorded only every minute so the die temperature profile was not collected with enough data points to be analyzed.

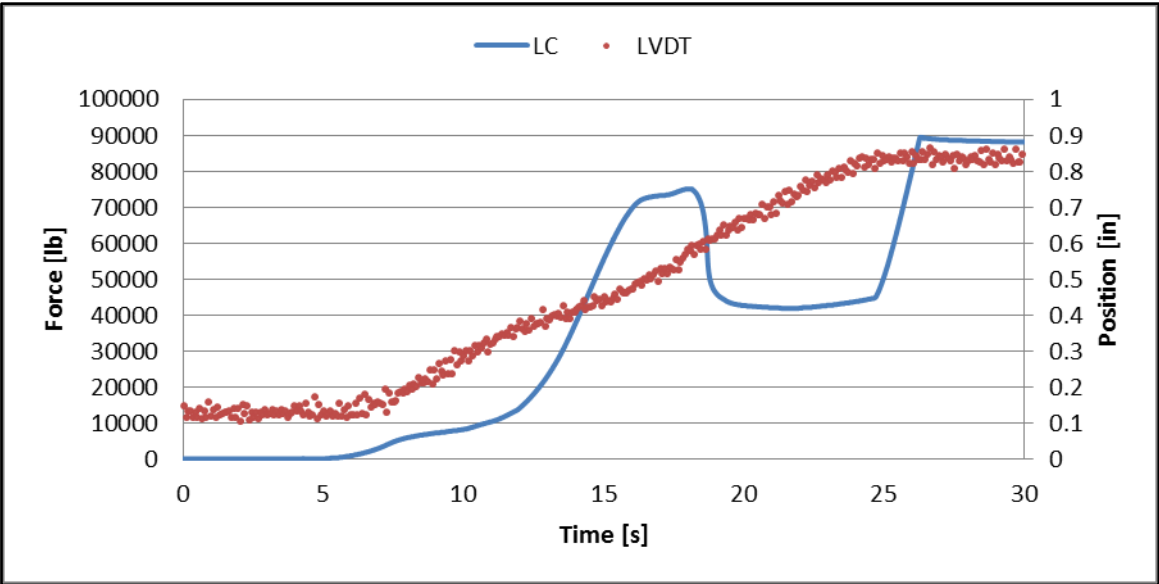


Figure 4-40: Force and position vs time for extrusion 7

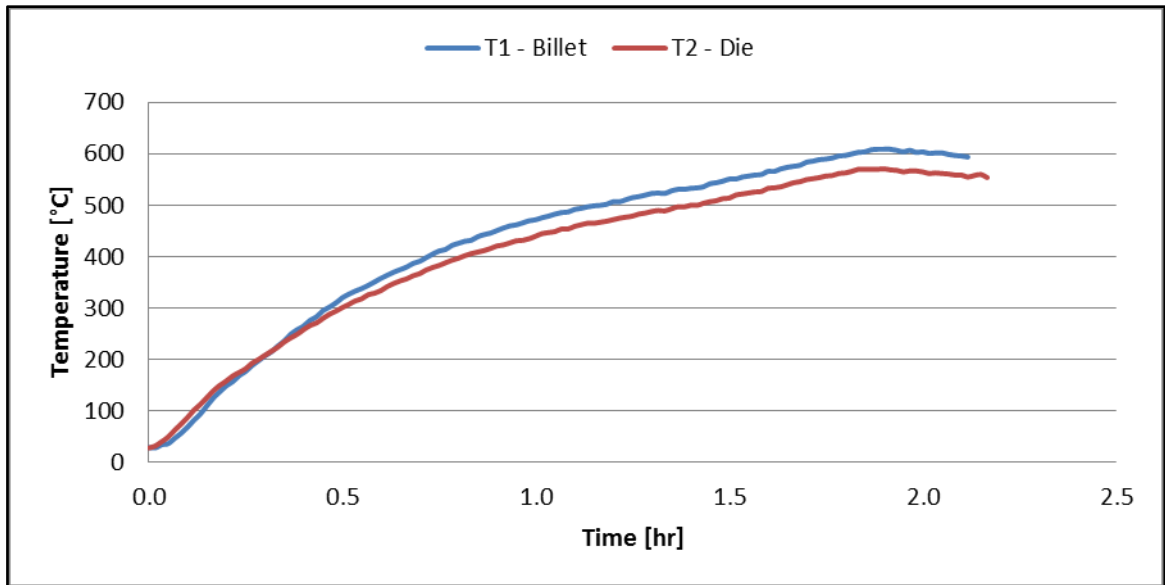


Figure 4-41: Temperature profile of extrusion 7

4.2.2 Extrusion 8

Extrusion 8 was a U tube extrusion conducted at a temperature of 600°C with a reduction ratio of 10.1. The ram in extrusion 8 failed before the extrusion could progress fully. The ram appears to have gotten stuck and then begin to deform above the holder. The central hole of this billet was not very straight relative to the sides of the billet. The crooked central hole caused the ram to be forced into the side of the holder and gall the inside. This in turn caused the ram to become stuck in the holder. The extrusion tooling and partial extrusion can be seen in Figure 4-42.

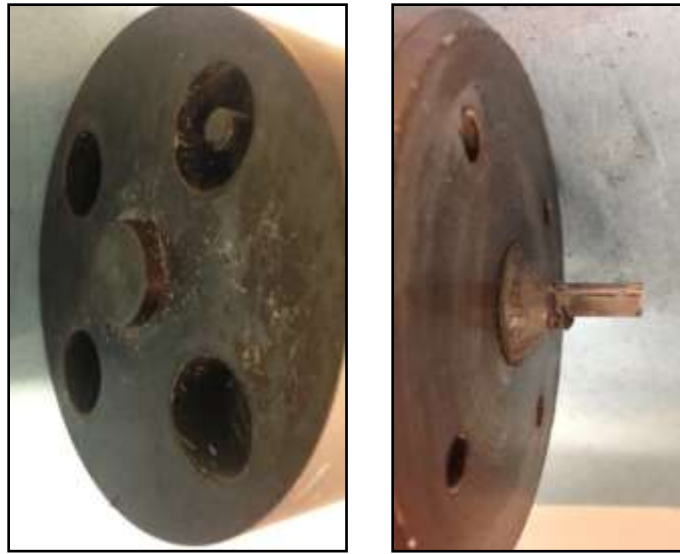


Figure 4-42: Extrusion 8 tooling and partially extruded product

Since the peak force is at the start of the extrusion and since this extrusion appears to have started it can be assumed that the failure occurred near the maximum force and the force plot can be used to get a value for the extrusion constant. The maximum force was taken to be 120979 lb and the extrusion constant was calculated as 104.99.

The temperature profile has a large decrease at about 1.4 hr. This temperature dip corresponds to the point when the cold ram was inserted for extrusion. However, the ram insertion took too long and the temperature of the billet significantly dropped so the decision was made to wait until the billet returned to the desired temperature. The die temperature profile shows a significant increase in temperature during the extrusion of 40°C. This could be related to the billet temperature being non uniform or the ram still being colder than the billet and as the ram pressed into the billet it cooled it down more.

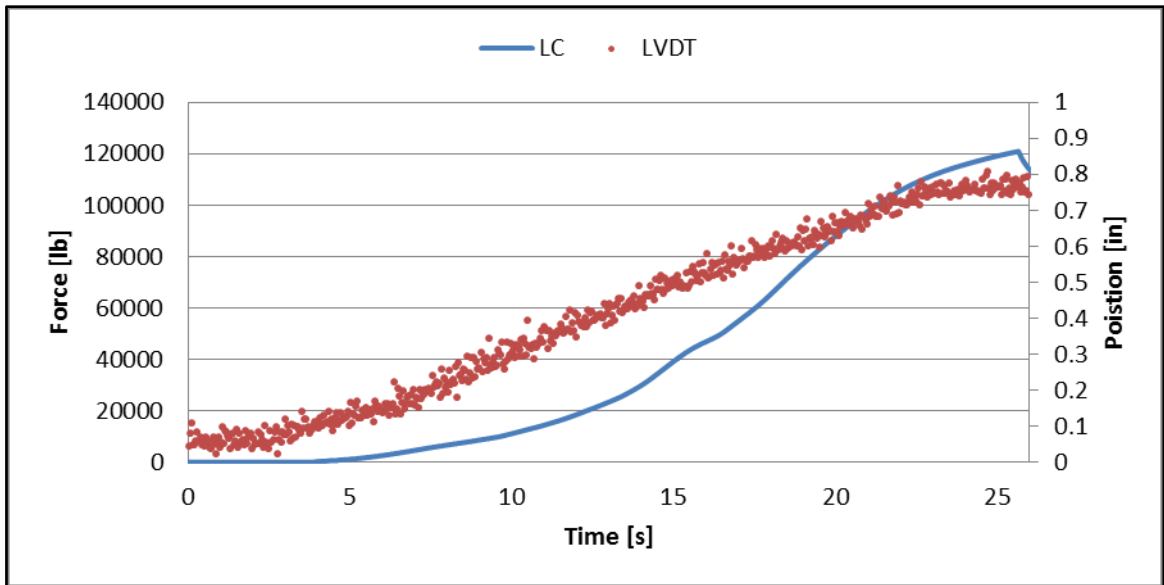


Figure 4-43: Force and position vs time for extrusion 8

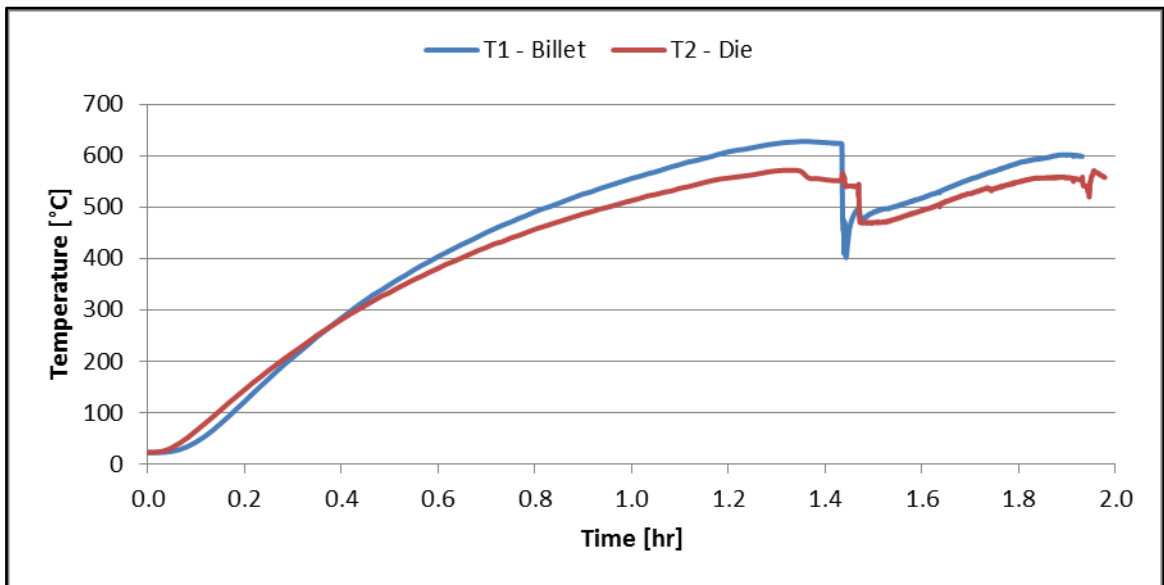


Figure 4-44: Temperature profile during extrusion 8

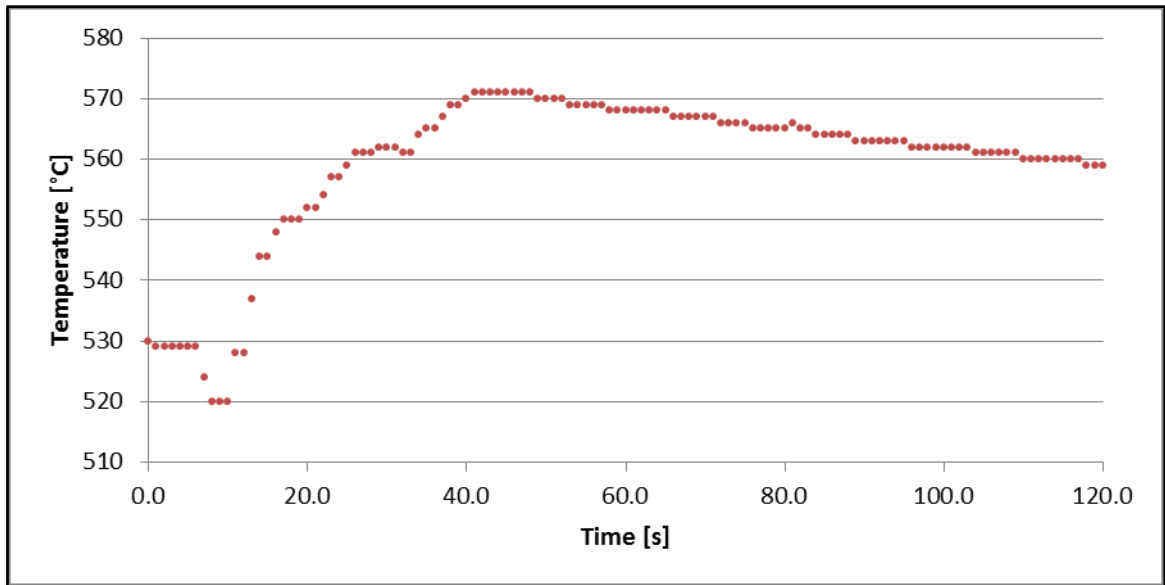


Figure 4-45: Die temperature increase during extrusion 8

4.2.3 Extrusion 9

Extrusion 9 was a U tube extrusion conducted at a temperature of 600°C with a reduction ratio of 13.3. The holder used in this extrusion was also used in extrusion 6. The mandrel failed during the course of the extrusion which resulted in a partial rod and partial tube product similar to extrusion 7. The mandrel most likely failed due to the central hole of the billet not being in the center of the billet. This forced the mandrel to the side and it broke due to lateral forces. The billet used in this extrusion can be seen in Figure 4-46. The extrusion was carried out despite of this not ideal billet because supplies of billets were limited.



Figure 4-46: U billet used in extrusion 9



Figure 4-47: U tube from extrusion 9

The maximum force was taken to be 95601 lb and the extrusion constant was calculated as 55.01. The extrusion was stopped at about 15 s because it was apparent that the mandrel had broken based on the significant decrease in the force plot. The increase in the temperature of the die was measured to be 31°C and can be seen in Figure 4-50.

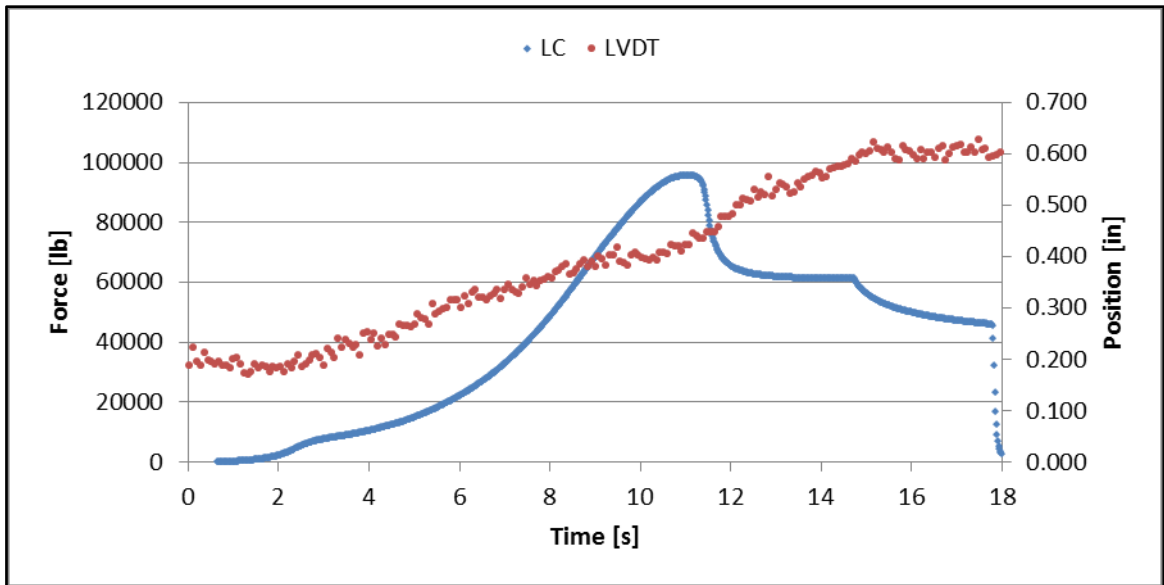


Figure 4-48: Force and position vs time for extrusion 9

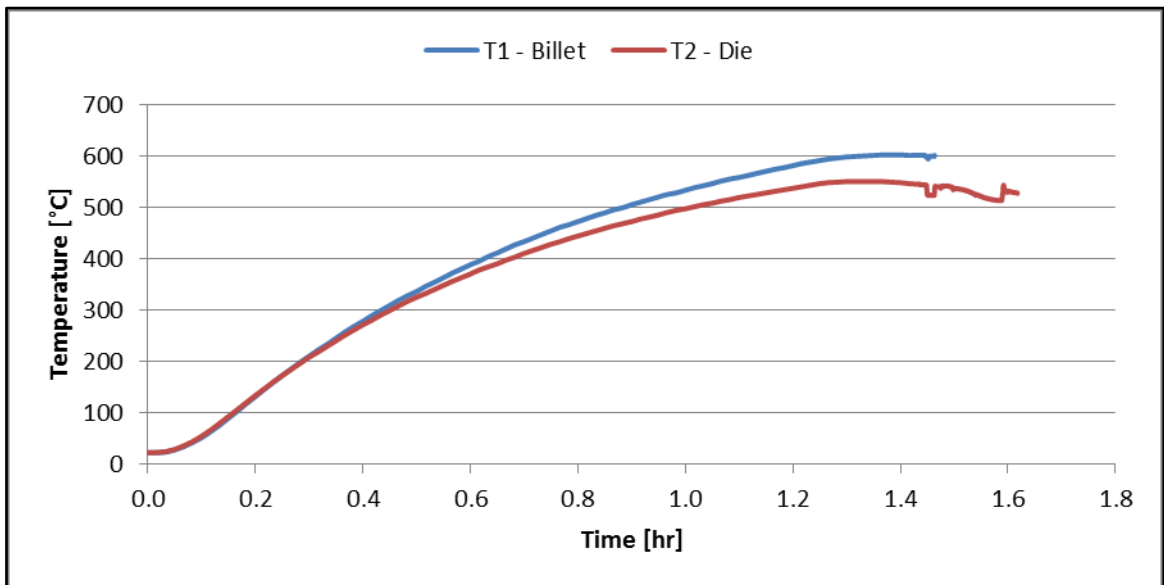


Figure 4-49: Temperature profile of extrusion 9

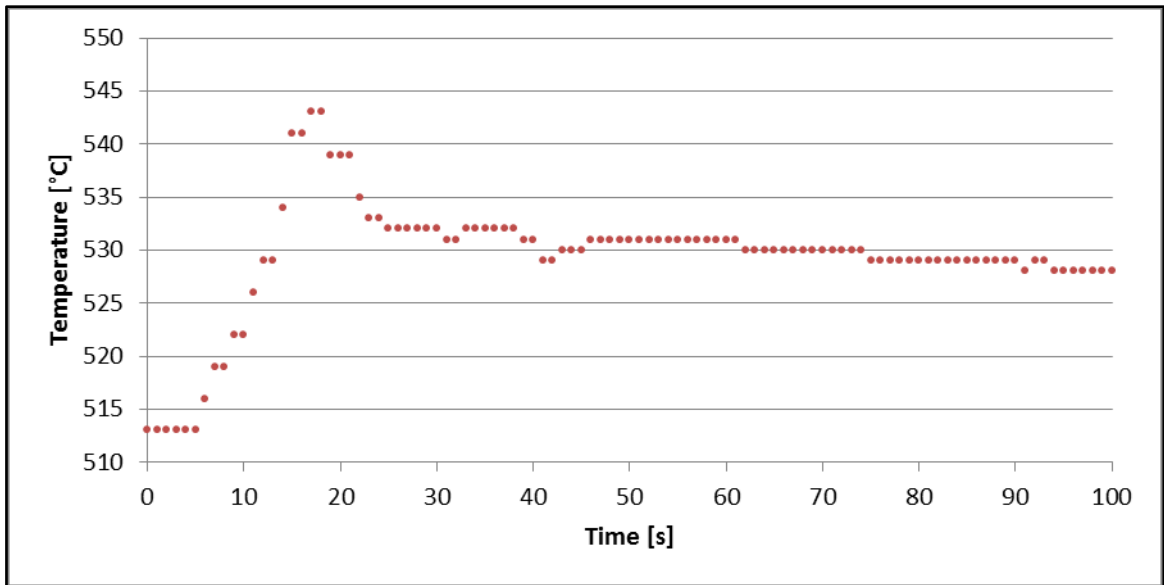


Figure 4-50: Die temperature increase during extrusion 9

4.2.4 Extrusion 10

Extrusion 10 was a U tube extrusion conducted at a temperature of 600 °C with a reduction ratio of 5.0. During this extrusion the mandrel broke off from the ram and was carried through with the uranium. The final extruded product was partially tube and partially rod. The maximum force recorded from the extrusion occurred when the extrusion was still a tube cross section so the tube cross section was used for the calculations. The tube section of the product is fairly straight and uniform, but at the point where the mandrel breaks the rod is curved. After this curve the rod section of the extruded product is fairly straight. The extruded product and the tooling can be seen together in Figure 4-51.



Figure 4-51: U tube from extrusion 10

The maximum force was taken to be 42074 lb and the extrusion constant was calculated as 108.9. The force and position vs time plot has a deep valley after the maximum force, similar to extrusions 7 and extrusion 9. The cause was also the same as extrusion 7 and extrusion 9; the final cross section became larger and the extrusion became easier and thus a lower force was required for the extrusion. Throughout the extrusion, the rate of the press head movement was constant. At the end of the extrusion it can be clearly seen when the press head was unable to move down any further and the force increasing suddenly. The increase in the temperature of the die was measured to 9°C and can be seen in Figure 4-54.

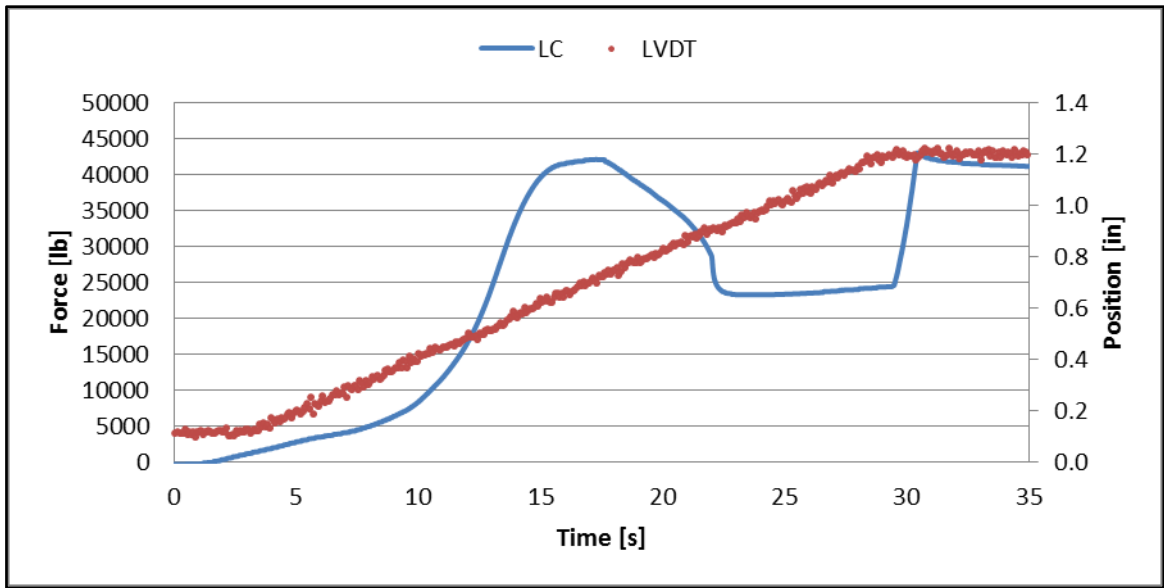


Figure 4-52: Force and position vs time for extrusion 10

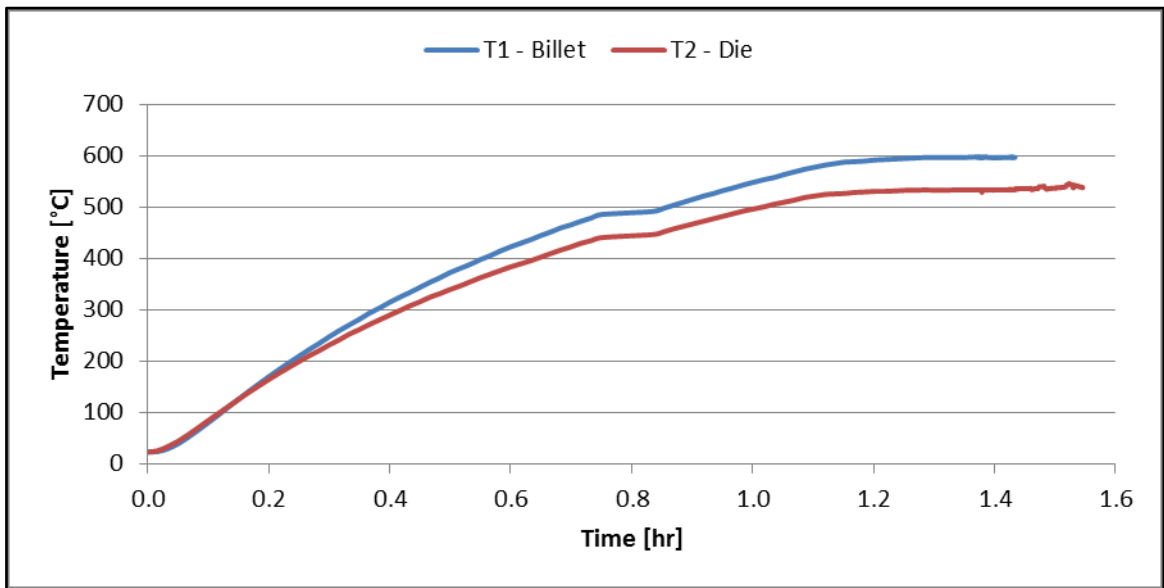


Figure 4-53: Temperature profile of extrusion 10

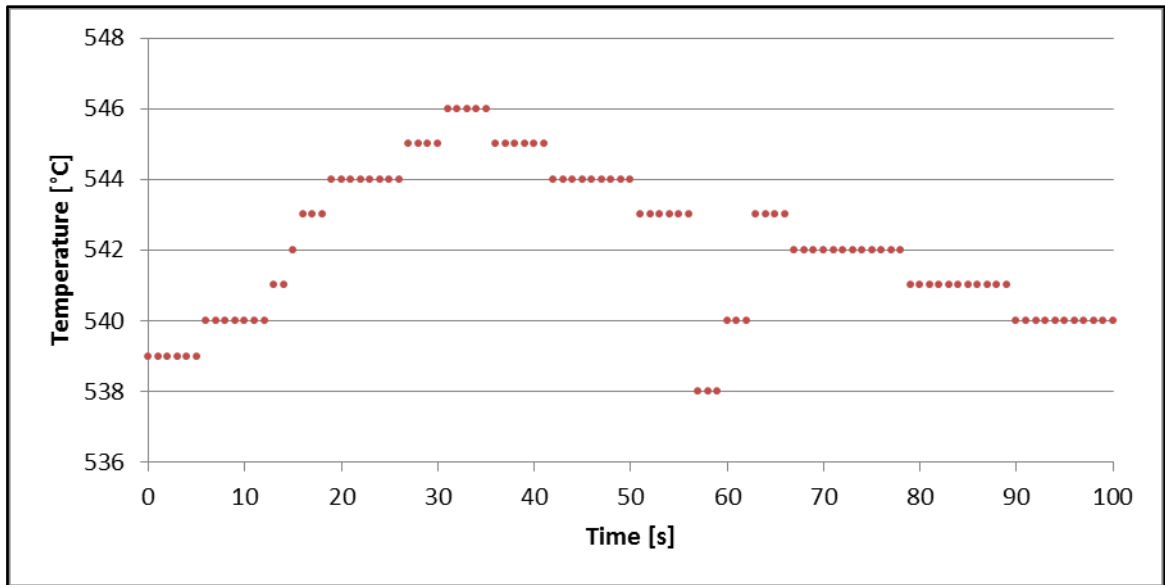


Figure 4-54: Die temperature increase during extrusion 10

4.3 U Rod Extrusions

4.3.1 Extrusion 12

Extrusion 12 was a U rod extrusion conducted at a temperature of 630°C with a reduction ratio of 15.2. The extruded rod was 7.5 inches long. The length of this extrusion was due to the billet being fully extruded, the size of the billet, and the precision and design of the extrusion tooling. The billet used for this extrusion can be seen in Figure 4-55. The extruded rod was very straight after the initial curve in the extrusion. The rod can be seen in Figure 4-56. This was the only uranium rod to be extruded due to the fuel form of interest for pure uranium being tubes rather than rods. This rod was extruded for comparison purposes, but also because uranium rod extrusion did not require the use of a mandrel. The tooling used in this extrusion can be seen in Figure 4-57. This set includes a dummy block and ram made of C350 and also includes 2

set pins to align the central hole. The ram was inserted cold after the rest of the tooling and billet achieved a stable temperature.



Figure 4-55: Uranium billet for extrusion 12



Figure 4-56: U rod from extrusion 12 after a small section was removed

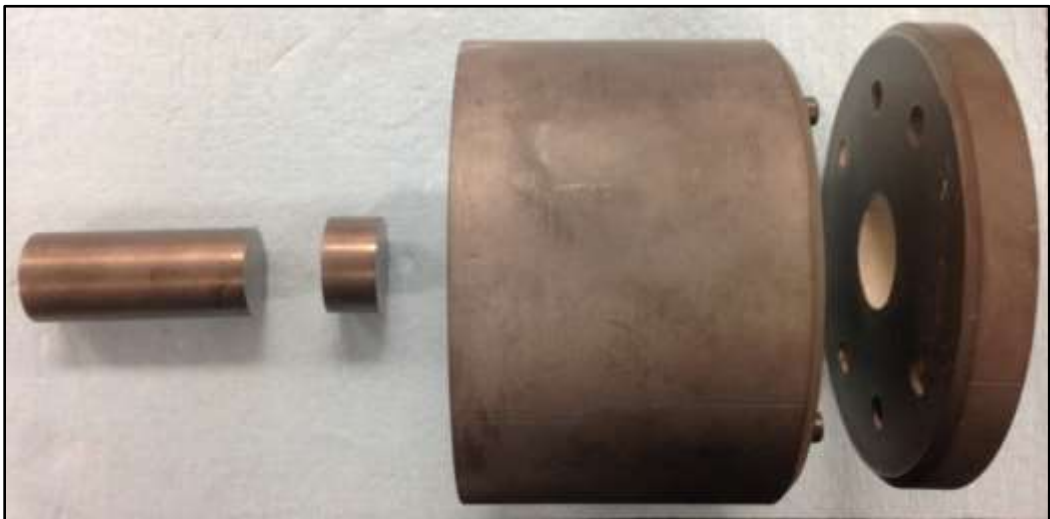


Figure 4-57: Tooling set used in extrusion 12

The force and position vs time plot can be seen in Figure 4-58. The maximum force was taken to be 85147 lb and the extrusion constant was calculated as 46.22. This force plot is also very similar to the theoretical force plots presented in the background section of this dissertation. The speed of the ram is mostly constant, but with a slight change in slope at the point of maximum force. The speed increased slightly after the initial upsetting length. Also, the point at which the extrusion has finished can be clearly seen when the position becomes constant and the force increases abruptly.

The temperature increase in the die during the extrusion was measured to be 9°C. The plot showing the die temperature during the extrusion can be seen in Figure 4-60. It is not clear why the temperature of the die first decreases then increases during the extrusion.

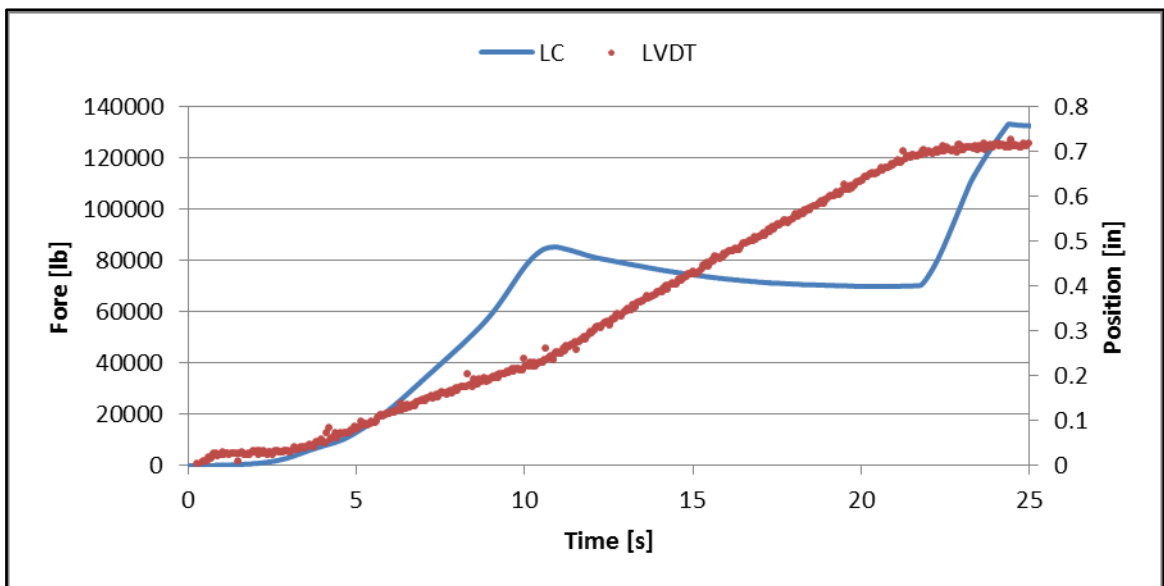


Figure 4-58: Force and position vs time for extrusion 12

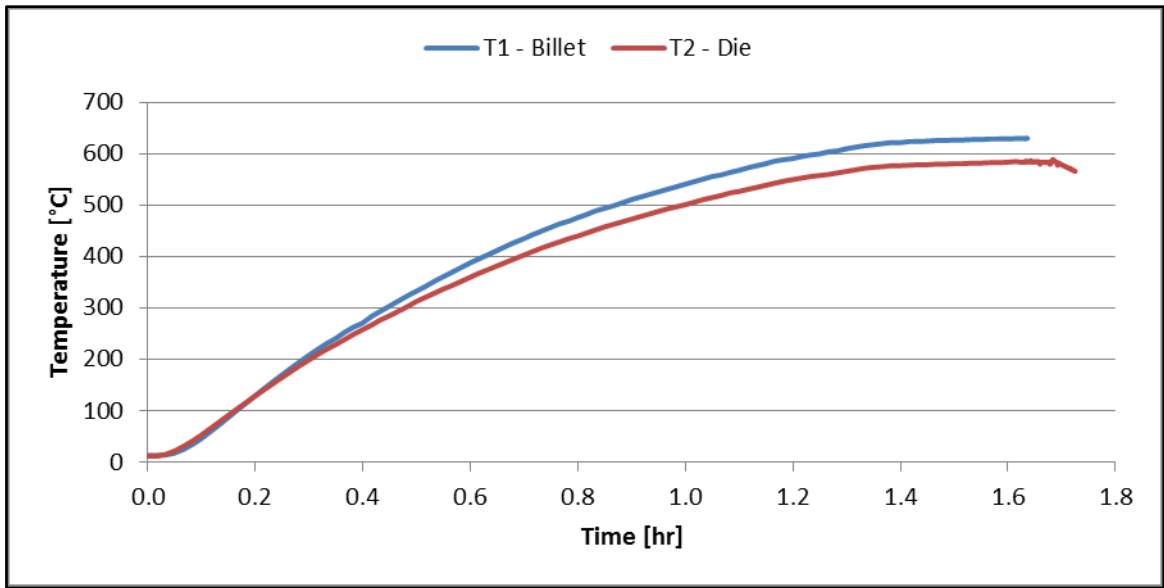


Figure 4-59: Temperature profile of extrusion 12

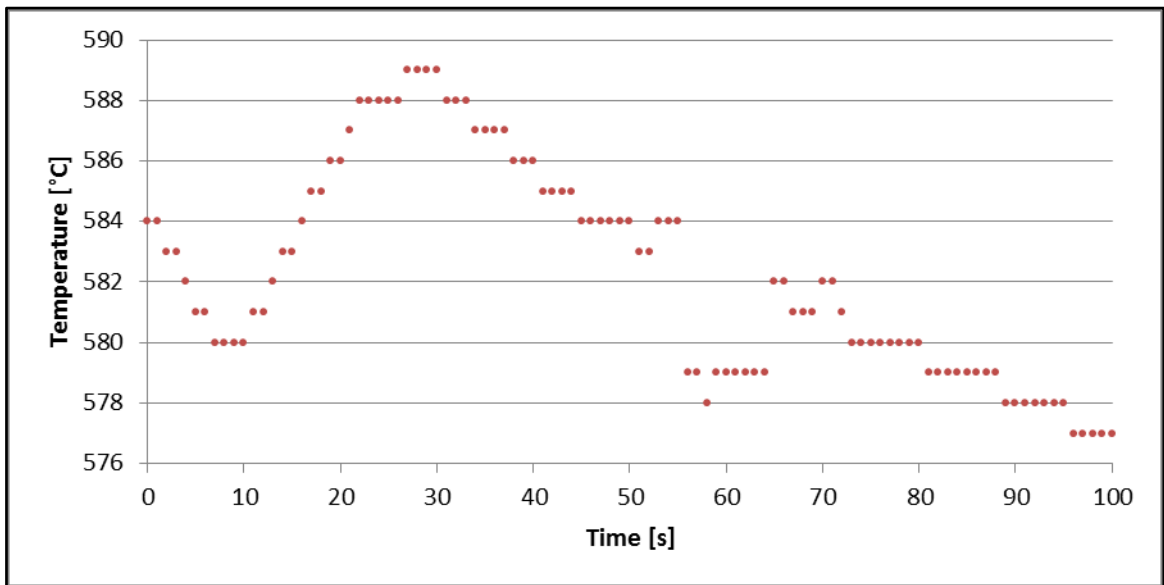


Figure 4-60: Die temperature increase during extrusion 12

4.4 Microstructure Analysis of Extruded Products

Extruded rods and tubes were sectioned, mounted, and polished for examination.

The primary mode of examination was electron microscopy. The study of the U-10Zr

products revealed zirconium rich grains. These grains were found throughout all U-10Zr samples.

The zirconium rich grains were distributed uniformly in the radial slices, but they were aligned in the axial slices. The images in Figure 4-61 through Figure 4-64 are all axial slices of U-10Zr extrusion 1. The extrusion orientation for these images is up and down. In each of these images there are large dark grains. These grains are the aforementioned zirconium rich grains, and they can be seen to be elongated and aligned in the extrusion direction. In addition to the zirconium rich grains, the α -U + δ -UZr₂ phase grains are elongated in the extrusion direction. This structure is more apparent in the higher magnification images.

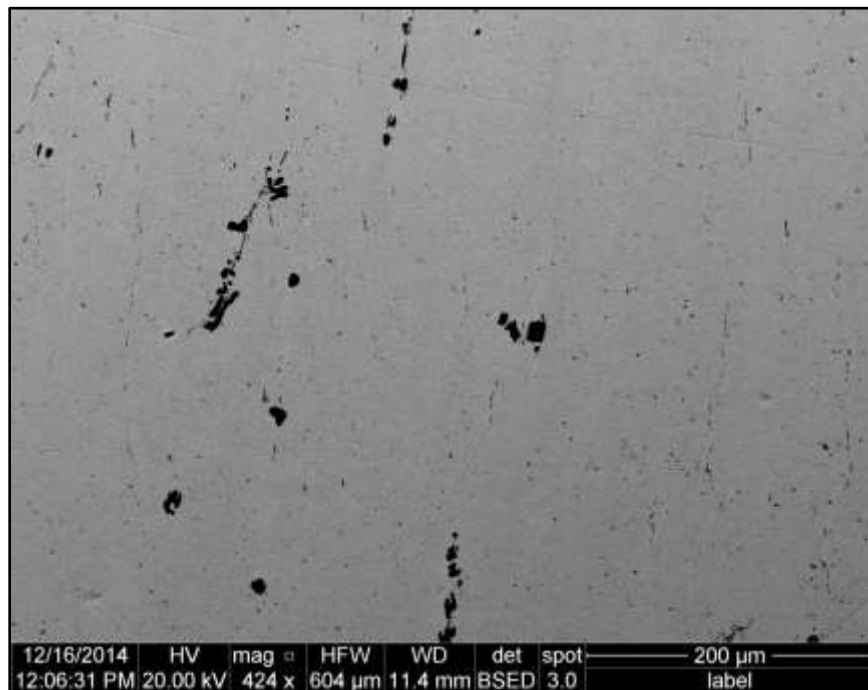


Figure 4-61: BSE image of extrusion 1 U-10Zr rod at 424X

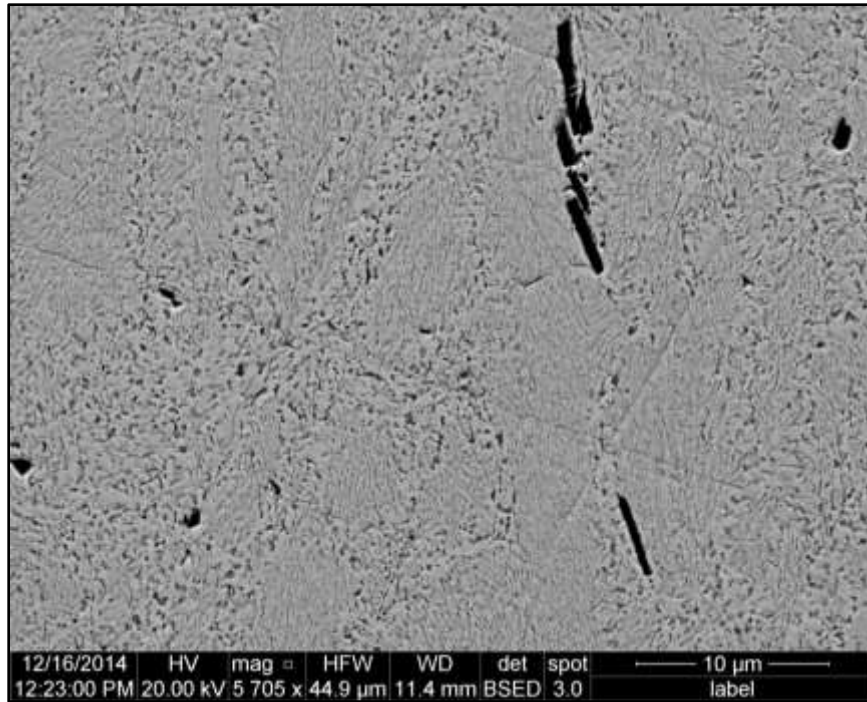


Figure 4-62: Higher magnification BSE image of Figure 4-61

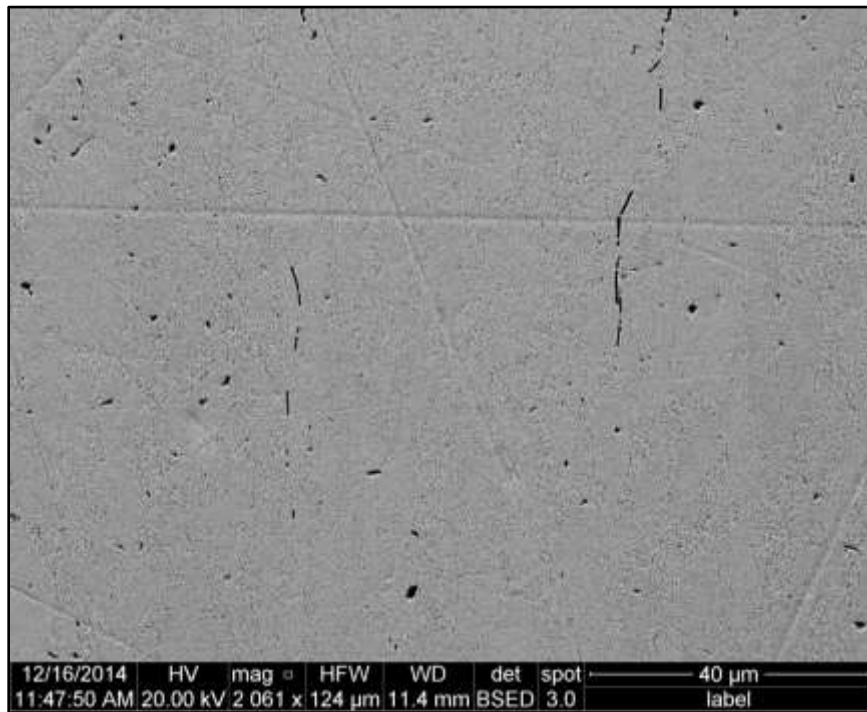


Figure 4-63: BSE image of extrusion 1 U-10Zr rod at 2061X

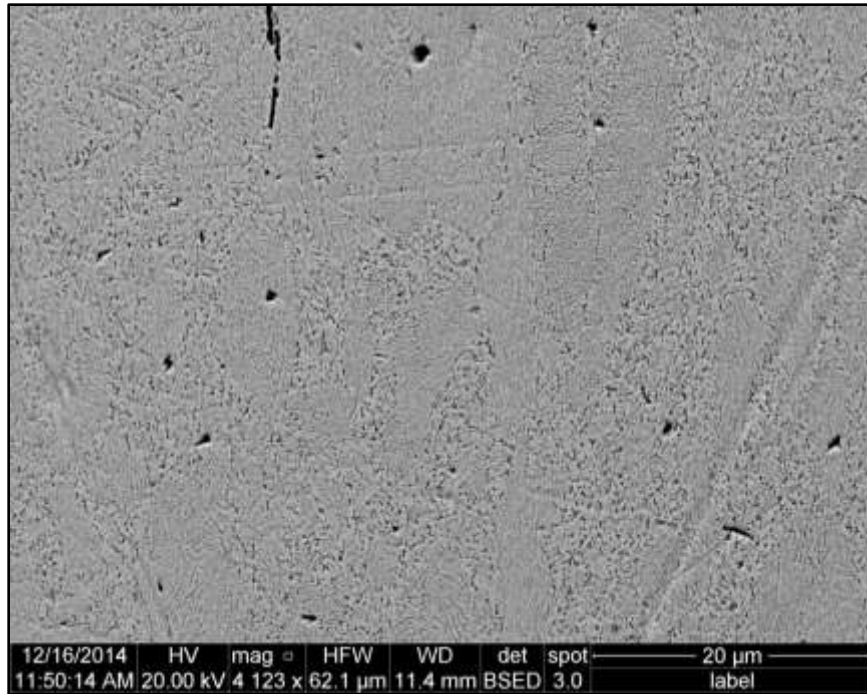


Figure 4-64: Higher magnification BSE image of Figure 4-63

The following image is a radial slice of U-10Zr extrusion 1. This image illustrates that the zirconium rich grains are distributed uniformly. Additionally, there are no elongated grains. The large dark areas are the zirconium rich grains. The small dark spots are pores created from over etching the sample.

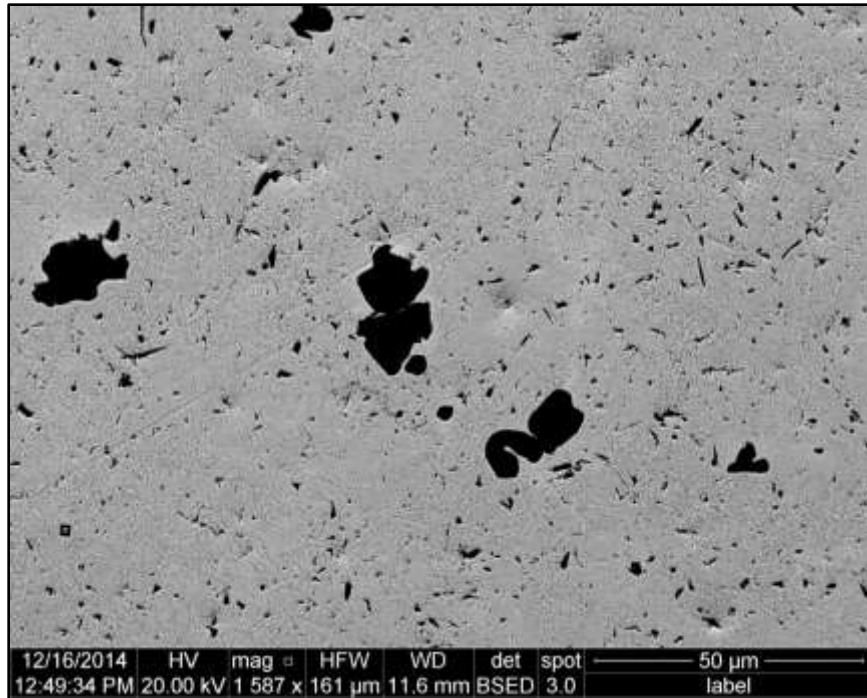


Figure 4-65: BSE image of extrusion 1 U-10Zr rod – radial slice

The following images, Figure 4-66 through Figure 4-68, are BSE images of extrusion 11, a U-10Zr rod. In these images the extrusion direction is left to right. These images exhibit the same structure found in the previous sample. The zirconium rich grains as well as the bulk the α -U + δ -UZr₂ phase grains are all elongated in the extrusion direction.

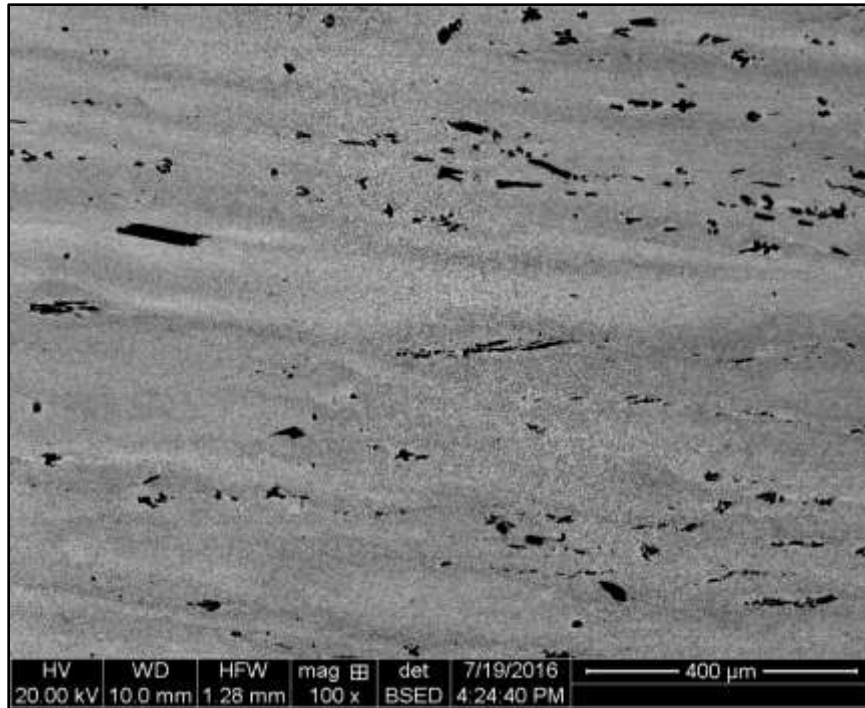


Figure 4-66: BSE image of extrusion 11 U-10Zr rod at 100X

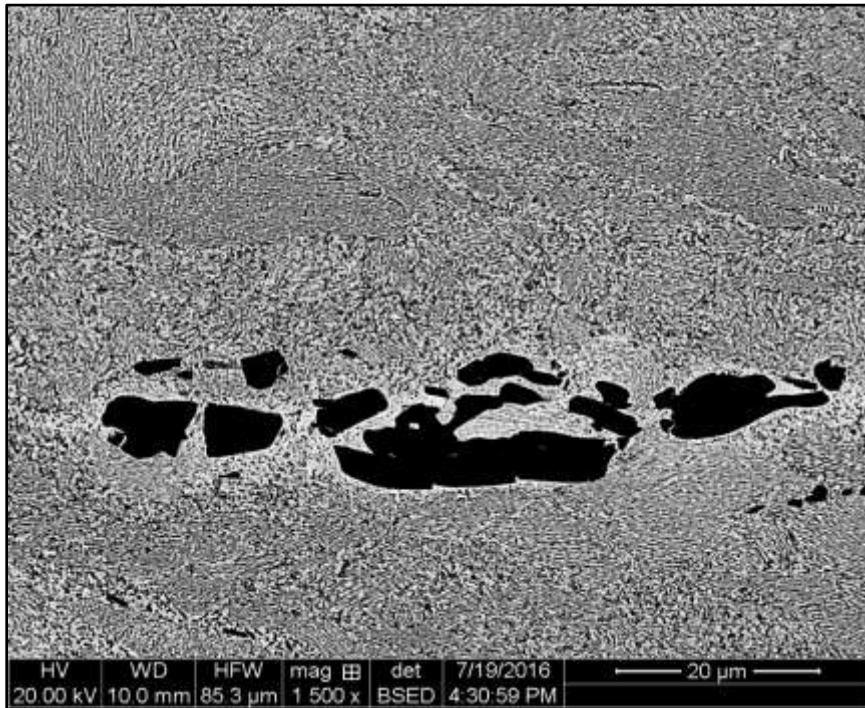


Figure 4-67: BSE image 1 of extrusion 11 U-10Zr rod at 1500X

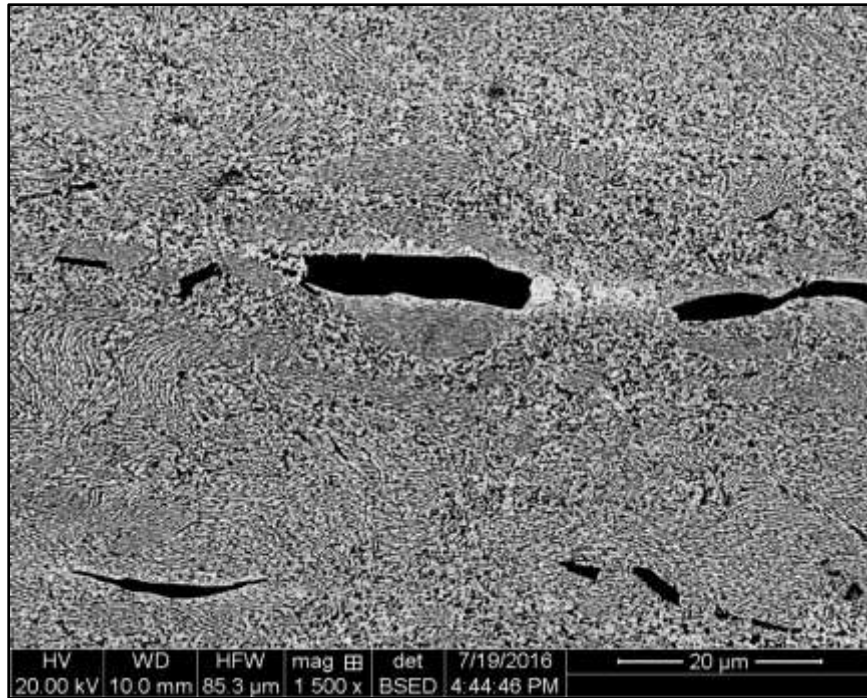


Figure 4-68: BSE image 2 of extrusion 11 U-10Zr rod at 1500X

The other half of the axial cut of the extrusion 11 sample that was used for the previous set of images was heat treated at 800°C for 48 hr. This temperature was chosen because it was in the gamma phase. This temperature was also chosen because it correlates with the chosen temperature for the neutron diffraction experiments which will be discussed in the next section. The heat treatment was done inside of the Ionex inert atmosphere glovebox. The sample was placed on an Al₂O₃ crucible and placed in a Al₂O₃ tube which was located inside of a furnace. Flowing UHP argon was used during the course of the heat treatment.

The following images, Figure 4-69 through Figure 4-71, are BSE images of the heat treated extrusion 11 sample. In these images the extrusion direction is left to right. The sample still exhibits the large zirconium rich grains and they are still oriented in the

extrusion direction. However, the α -U + δ -UZr₂ phase bulk region has undergone some changes. Some of the zirconium has migrated from the bulk into the large grains as well as congregated into smaller zirconium rich grains.

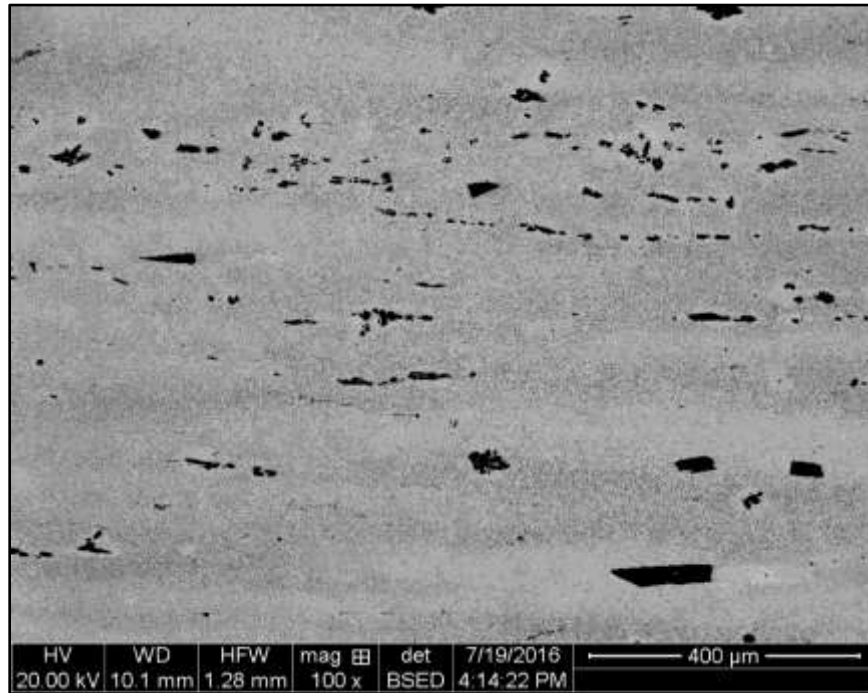


Figure 4-69: BSE image of heat treated extrusion 11 U-10Zr rod at 100X

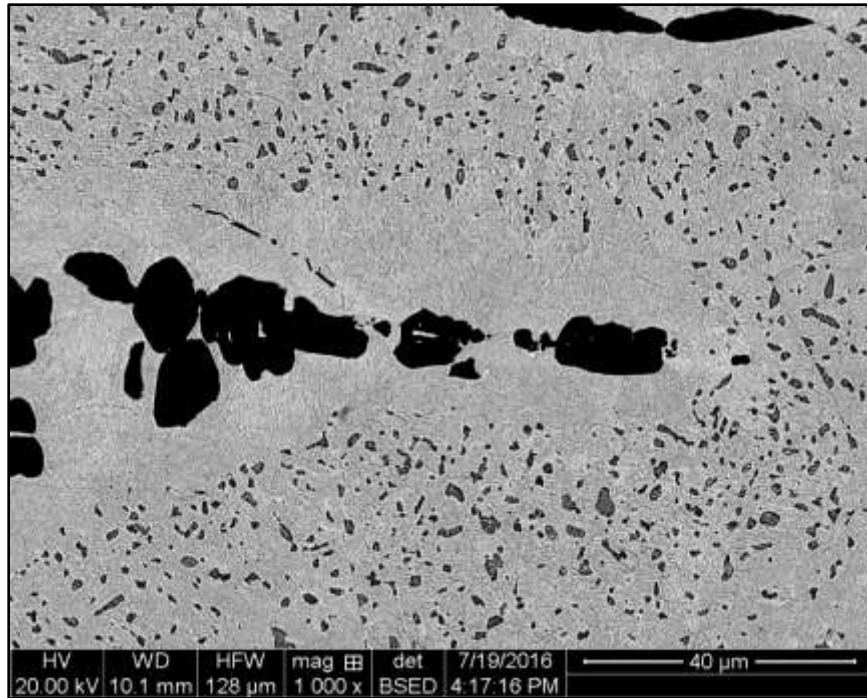


Figure 4-70: BSE image of heat treated extrusion 11 U-10Zr rod at 1000X

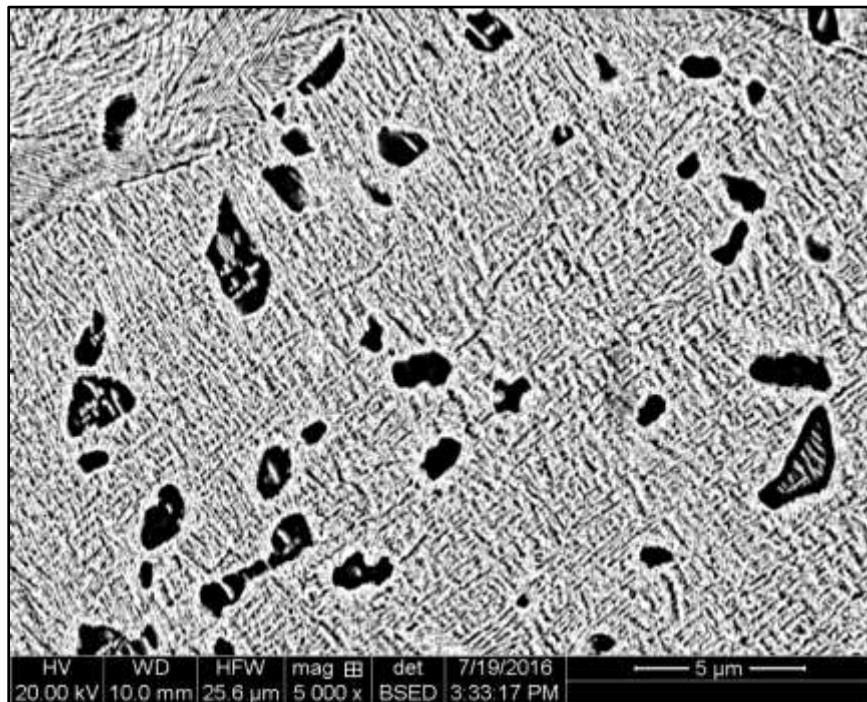


Figure 4-71: BSE image of heat treated extrusion 11 U-10Zr rod at 1500X

The uranium extruded product also showed microstructure artifacts from the extrusion process. In Figure 4-74, Figure 4-72, and Figure 4-73, the extrusion direction in the sample image is from left to right. In each image there are some small and large elongated grains in the extruded direction. Additionally, there are rows of smaller grains aligned in the extrusion direction. The large black spots are pores that are left over from impurities that were etched out during sample preparation. The very small black dots in Figure 4-74 are pores from over etching the sample. Additional uranium microstructure images can be seen in Appendix 7.

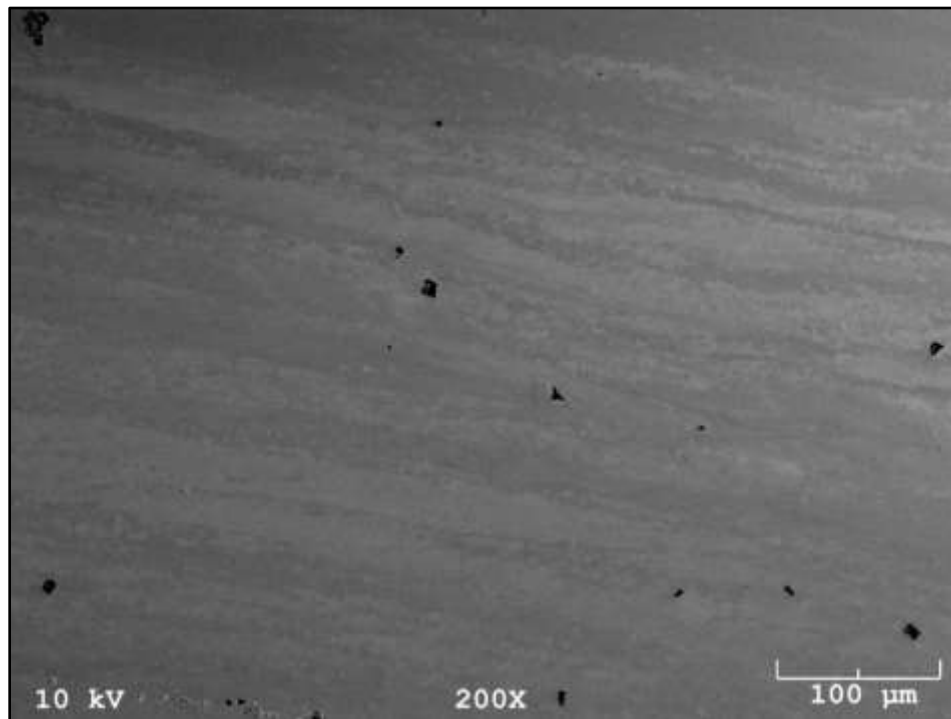


Figure 4-72: BSE image of extrusion 7 U tube at 200X

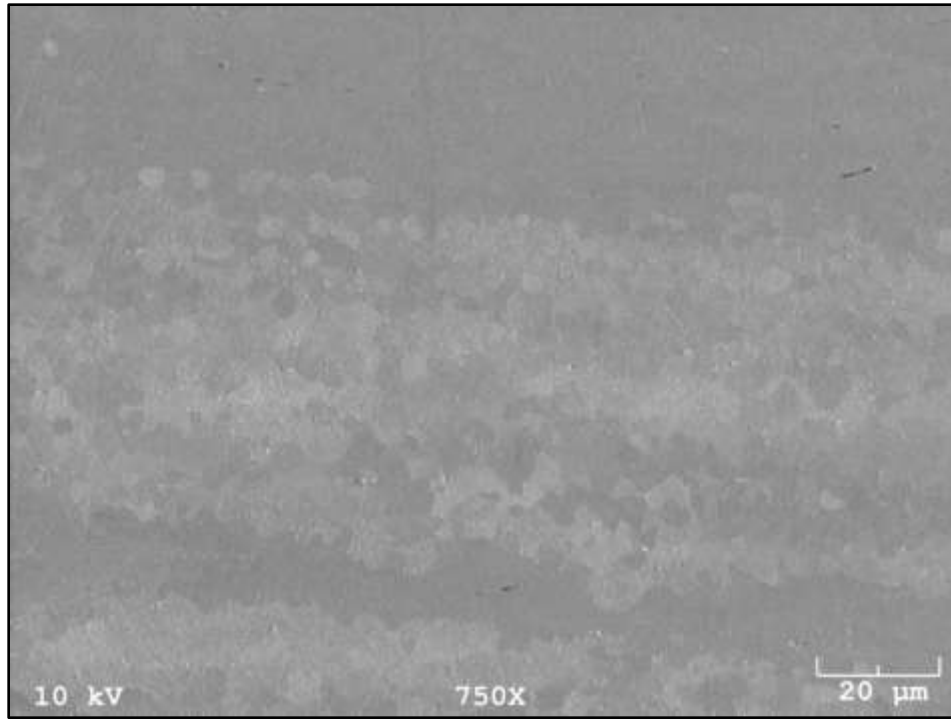


Figure 4-73: BSE image of extrusion 7 U tube at 750X

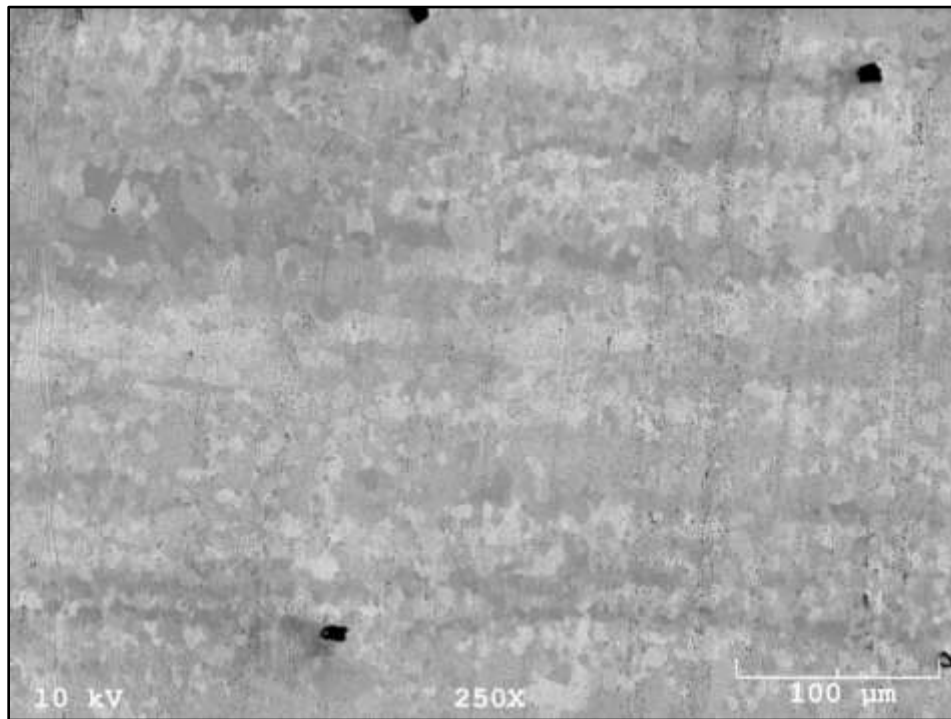


Figure 4-74: BSE image of extrusion 12 U rod at 250X

4.5 Neutron Diffraction Results

A sample from the U-10Zr extruded rod from extrusion 1 was used for texture measurements via neutron diffraction analysis at LANSCE. Three phases were studied during the texture measurements: α -U, β -U, and δ -UZr₂. Measurements were taken at 600°C, 650°C, 680°C, 700°C, and 800°C, during heating and cooling. These temperatures were chosen based off of the phase changes in the U-10Zr system.

The pole figures for α -U at multiple temperatures can be seen in Figure 4-75. The room temperature α -U pole figures indicate that the (100) and (110) poles are oriented in the extrusion direction. During heating at 200°C and at 600°C there is no change in texture observed. At 650°C, in the ($\alpha + \gamma$) phase field, the texture has become weak. After heating to 800°C and cooling the sample back down to 600°C the texture is completely lost. This is after the ($\alpha \rightarrow \beta \rightarrow \gamma \rightarrow \beta \rightarrow \alpha$) phase transformation cycle and this result was expected due to the crystal structure changes from one phase to another. This loss of α -U texture after this phase cycling has been previously observed in other extrusion sample studies. [40]

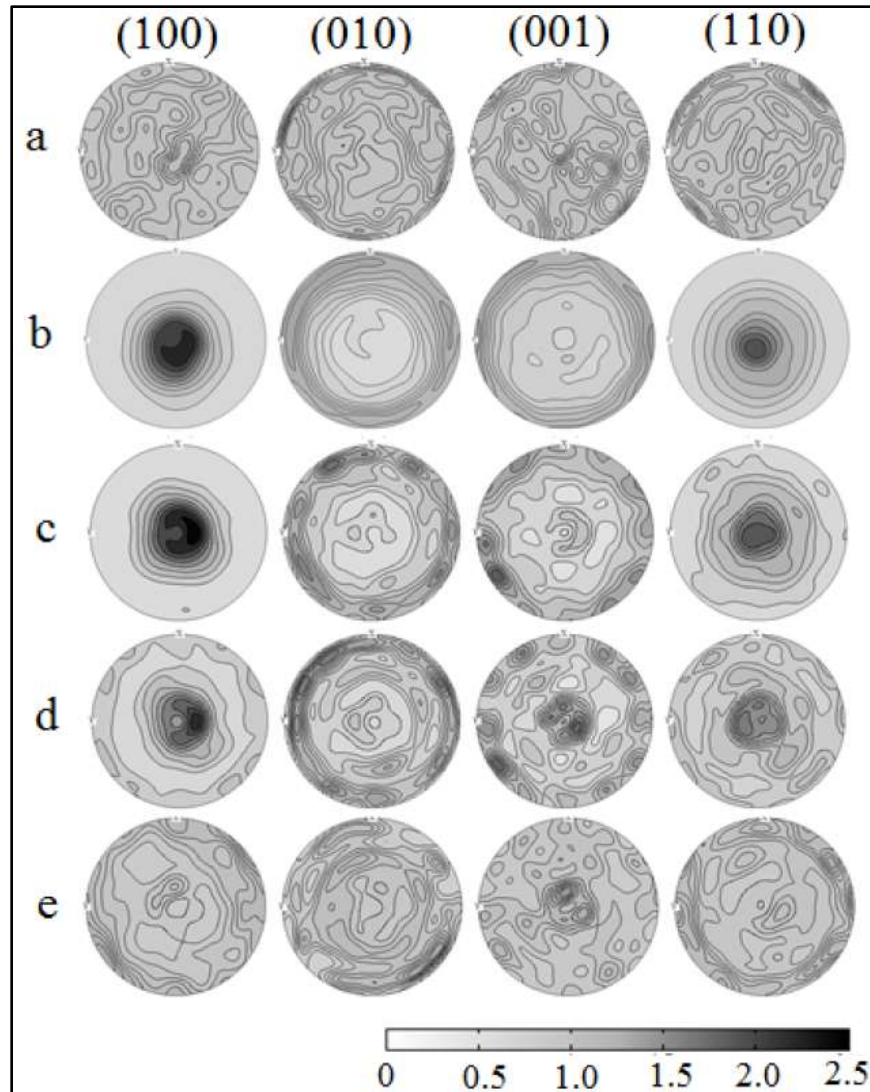


Figure 4-75: Pole figures of α -U: (a) as-cast alloy (b) extruded alloy at room temperature (c) at 600°C during heating (d) at 650°C during heating (e) at 600°C during cooling. Extrusion direction is at the center.

The pole figures for the δ phase in the as-cast sample are shown in Figure 4-76(a). It can be seen that it has a weak texture that developed during casting where the $(0001)_{\delta}$ poles are aligned parallel to the cylindrical billet axis. The pole figures for the δ phase in the extruded sample are shown in Figure 4-76(b-e). For the extruded sample, at room temperature, the $(0001)_{\delta}$ poles are oriented along the extrusion direction; which

indicates that there is a strengthening of the weak texture present in the as-cast sample. This texture is preserved at 200°C and 600°C during heating. After heating the sample to 800°C and cooling back to 600°C which is after the ($\delta \rightarrow \gamma \rightarrow \delta$) phase transformation cycle, the texture was analyzed again. It can be seen that the $(0001)_\delta$ texture is preserved which indicates a memory effect.

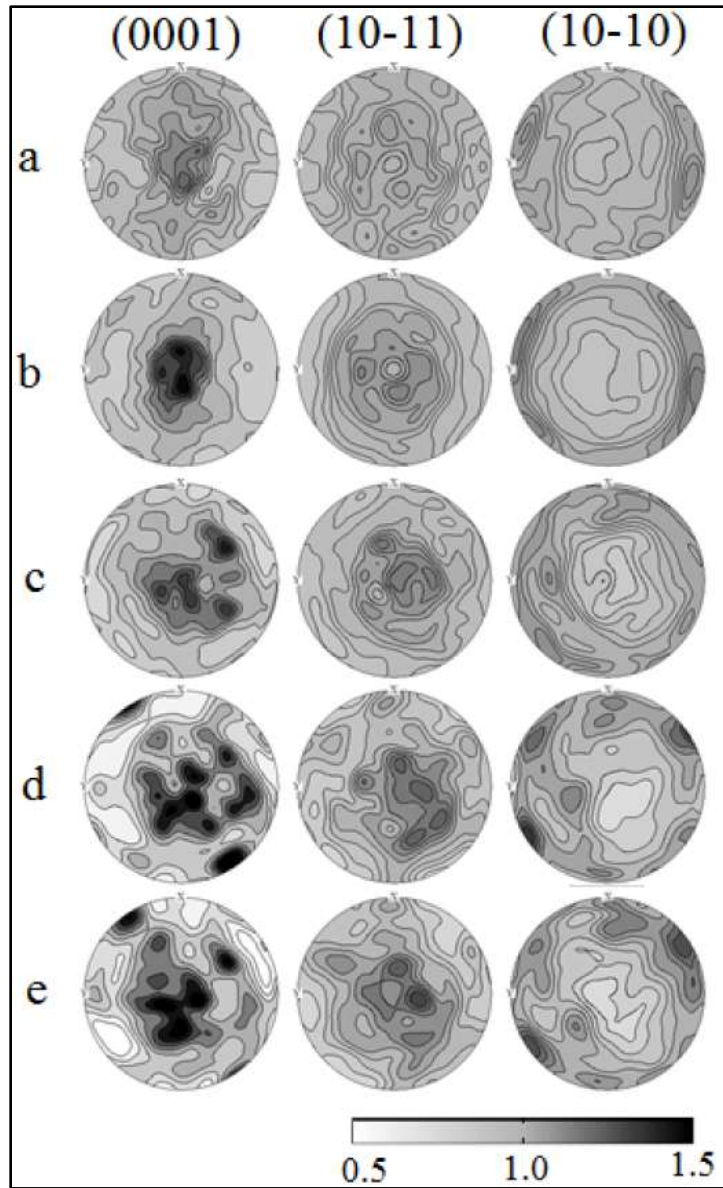


Figure 4-76: Pole figures of δ -UZr₂ (a) in the as-cast alloy (b) extruded alloy at room temperature (c) at 200°C (d) at 600°C during heating (e) at 600°C during cooling. Extrusion direction is at the center.

The pole figures in Figure 4-77 (a) show that the β -U phase has a random structure at 680°C after heating up past the ($\alpha \rightarrow \beta$) phase transition. The γ phase texture is shown at 650°C in the ($\alpha + \gamma$) phase field after the partial ($\delta \rightarrow \gamma$) transformation, 700°C, after the partial ($\beta \rightarrow \gamma$) transformation at which point the alloy is completely in

the γ phase, 800°C during heating, and at 700°C during cooling in Figure 4-77 (b), (c), (d), and (e) respectively. The texture in γ phase, although weak and difficult to discern from the α phase, can be observed at 650°C. It is seen that $(110)_\gamma$ and $(111)_\gamma$ poles are aligned in the extrusion direction. This becomes clearer when compared with the texture obtained at 700°C and 800°C, where the sample is entirely γ phase.

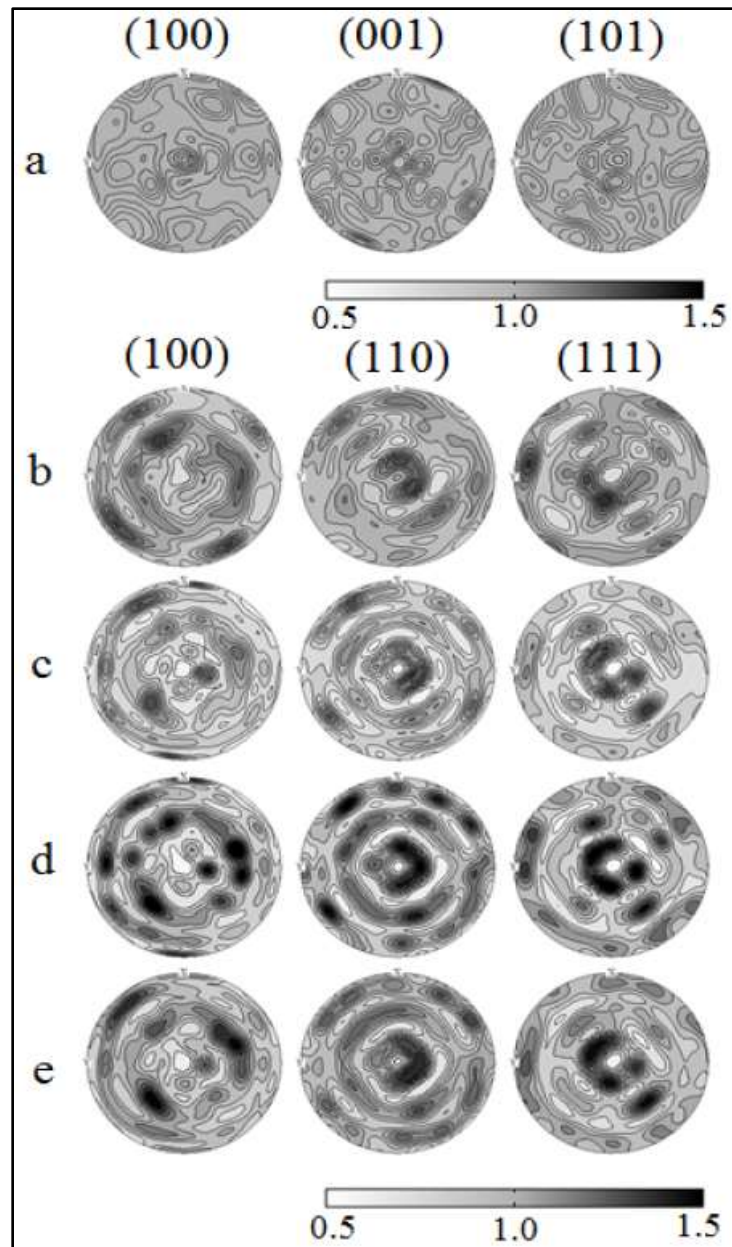


Figure 4-77: Pole figures of extruded sample for (a) β -U at 680°C (b) γ -U at 650°C during heating (c) γ -U at 700°C during heating (d) γ -U at 800°C during heating (e) γ -U at 700°C during cooling. Extrusion direction is at the center.

4.6 Thermal Conductivity of Uranium Pellets

The thermal diffusivity for each uranium HDH pellet was measured. The data was recorded every 10°C starting at 20 °C and ending at 300 °C. This data can be seen in Figure 4-78. In the plot each data set is labeled by the percent theoretical density for that pellet. The pellets are organized in the legend from highest density at the top to lowest density at the bottom. The diffusivity vs temperature data set for each density has the same general shape; the diffusivity increases slightly with temperature. However, there is a difference in the magnitude of the diffusivity in each data set. As the density is increased the diffusivity increases. This is not strictly true since the lowest measured diffusivity corresponds with 46.62 %TD rather than 45.52 %TD. This is most likely due to uncertainty in measurement of the density and thermal diffusivity.

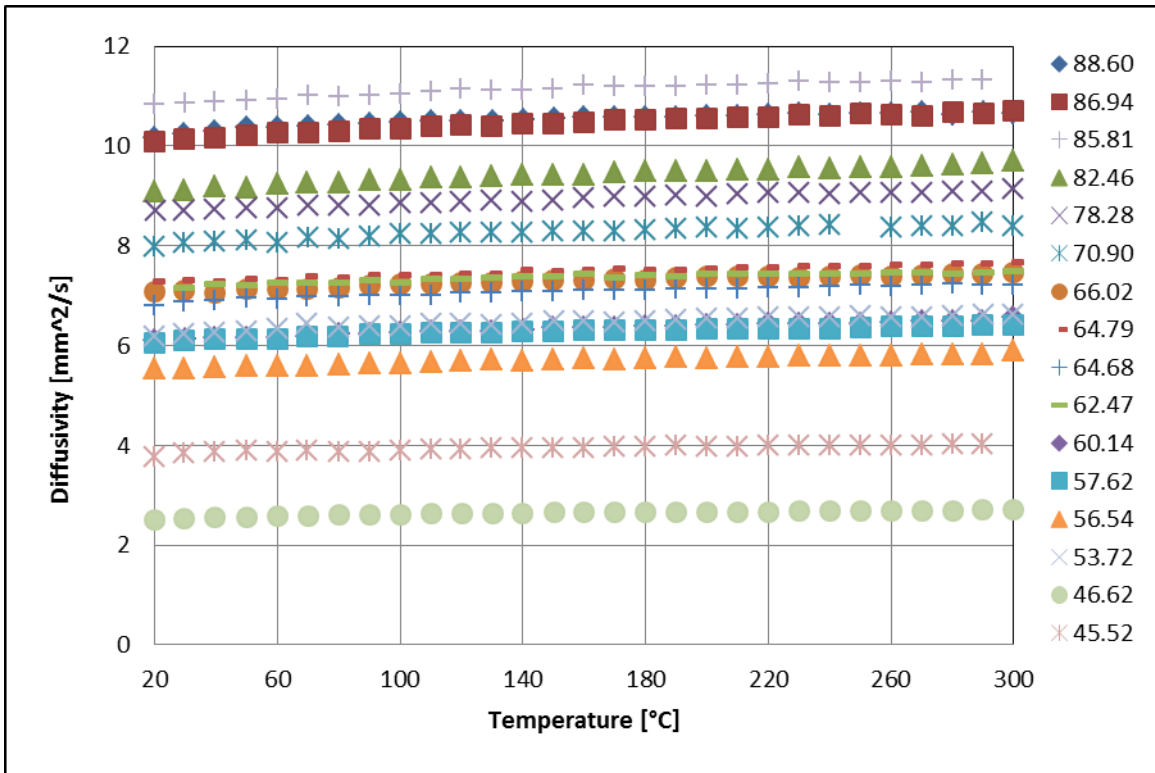


Figure 4-78: Thermal diffusivity of U HDH pellets

For further comparison, the thermal diffusivity of each U HDH pellet at 30°C was plotted vs %TD. This data can be seen in Figure 4-79. This plot also contains the thermal diffusivity of the uranium microsphere samples. The thermal conductivity at 30°C of the U HDH pellets and the U microspheres pellets is also plotted in the same fashion in Figure 4-80. In these 2 plots the highest density data point is actually a solid metal rod that was measured for a higher density comparison; the highest density HDH pellet is 88.60 %TD. In these plots it is clear that there is a linear relationship between percent theoretical density and the thermal diffusivity; additionally, such a relationship can be found between percent theoretical density and thermal conductivity.

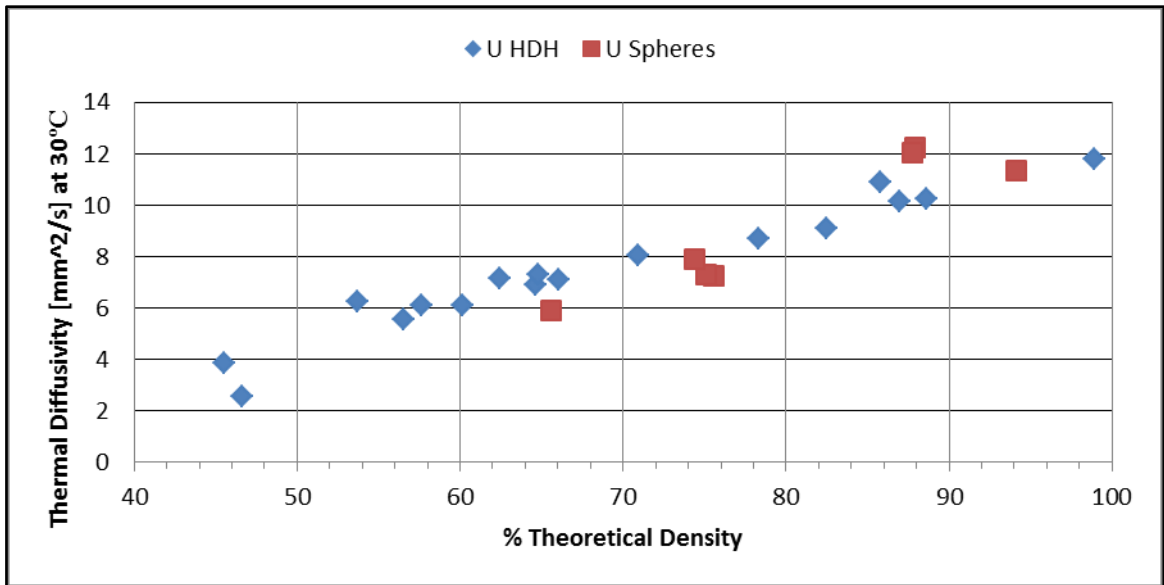


Figure 4-79: Thermal diffusivity of U HDH and U spheres pellets at 30°C

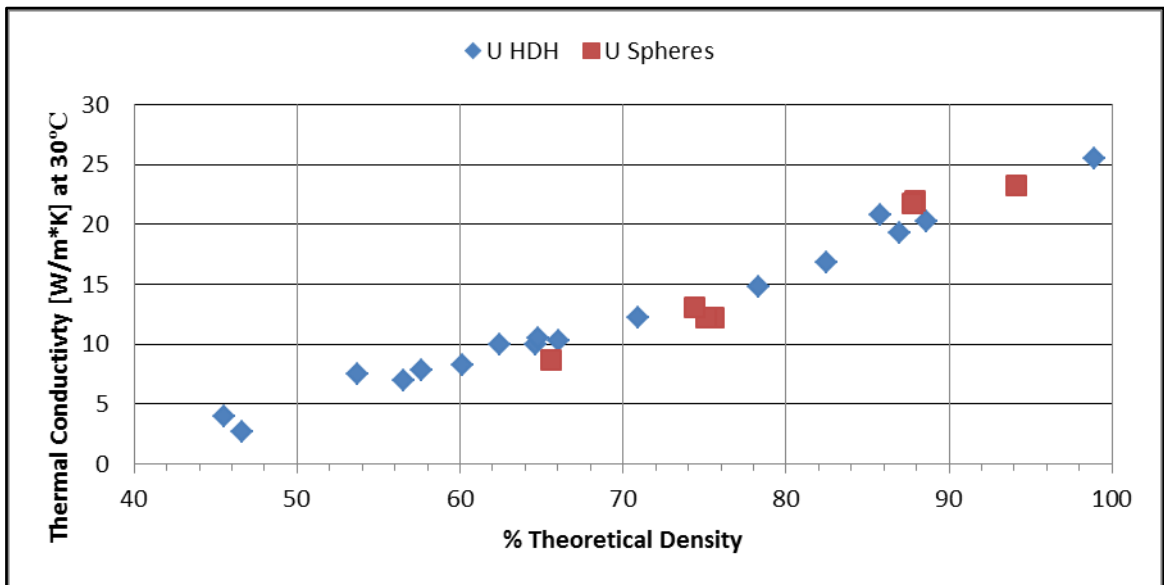


Figure 4-80: Thermal conductivity of U HDH and U spheres pellets at 30°C

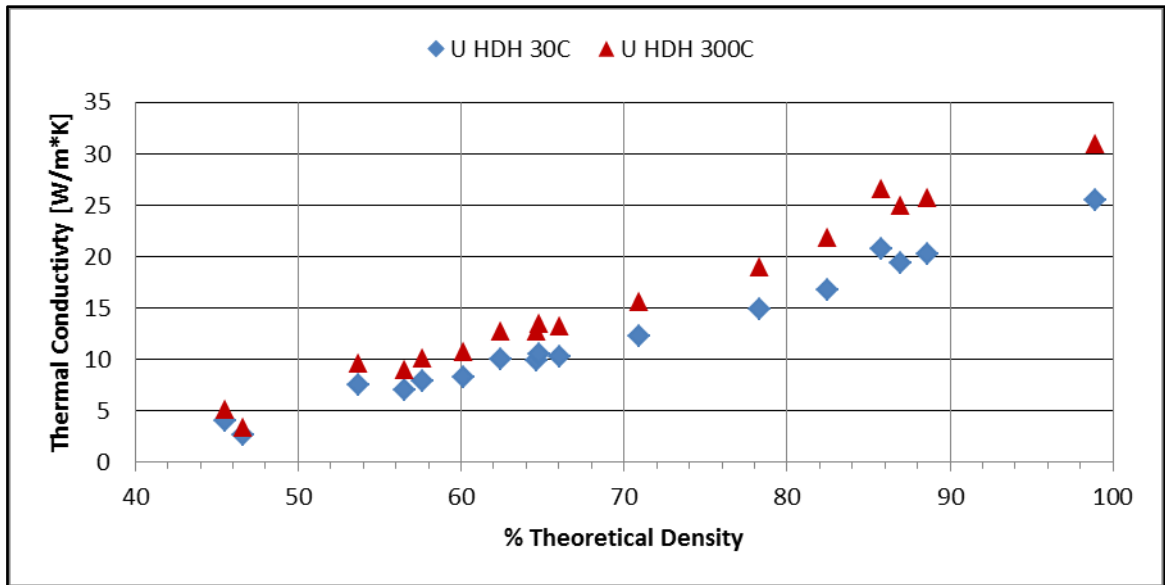


Figure 4-81: Thermal conductivity of U HDH pellets at 30 and 300°C

The thermal conductivity at 30°C and 300°C for the U HDH pellets are plotted together vs percent theoretical density in Figure 4-81. It is clear that there is still a linear relationship between the thermal property and the density at elevated temperatures. It also appears that the slope of this relationship increases with the increase in temperature.

4.7 Thermal Conductivity of U-5Zr Pellets

The thermal diffusivity for each U-5Zr HDH pellet was measured. The data is displayed in Figure 4-82 in the same way as the U HDH pellet data was displayed previously. The data behaves very similarly to the previous U HDH data. Each set that corresponds to a different density pellet has roughly the same shape, but as the density increases the magnitude of the diffusivity increases.

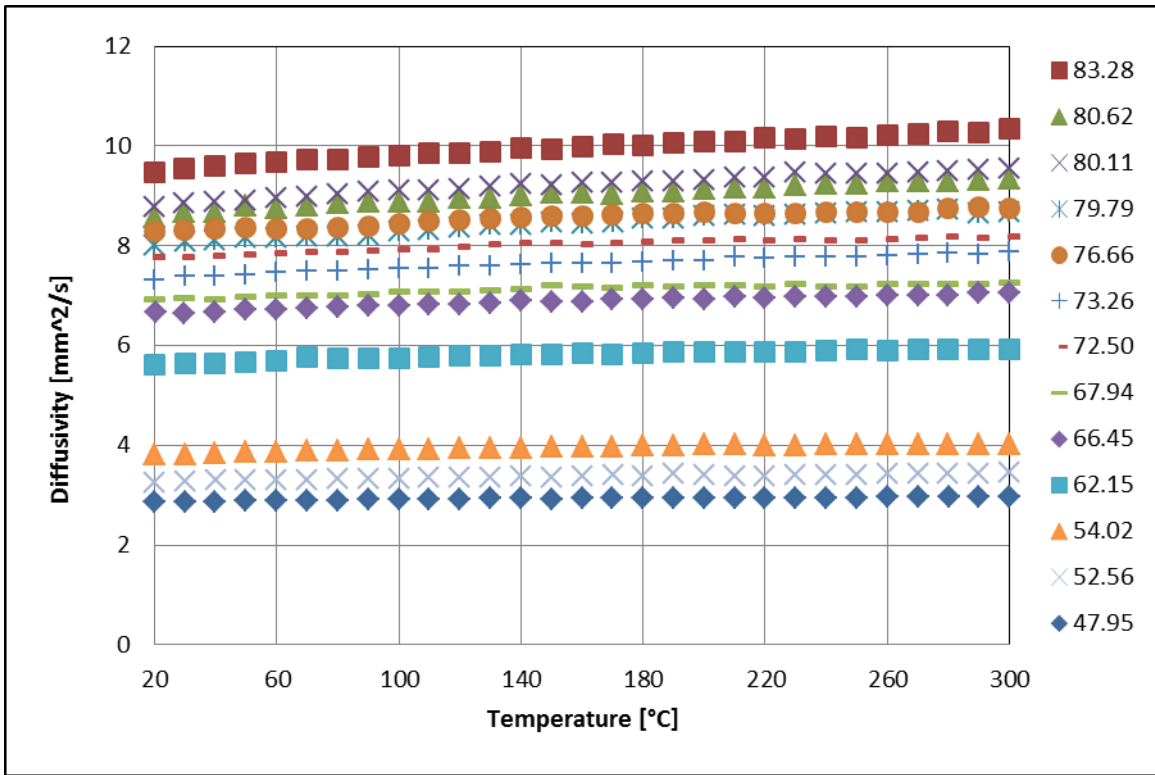


Figure 4-82: Thermal diffusivity of U-5Zr HDH pellets

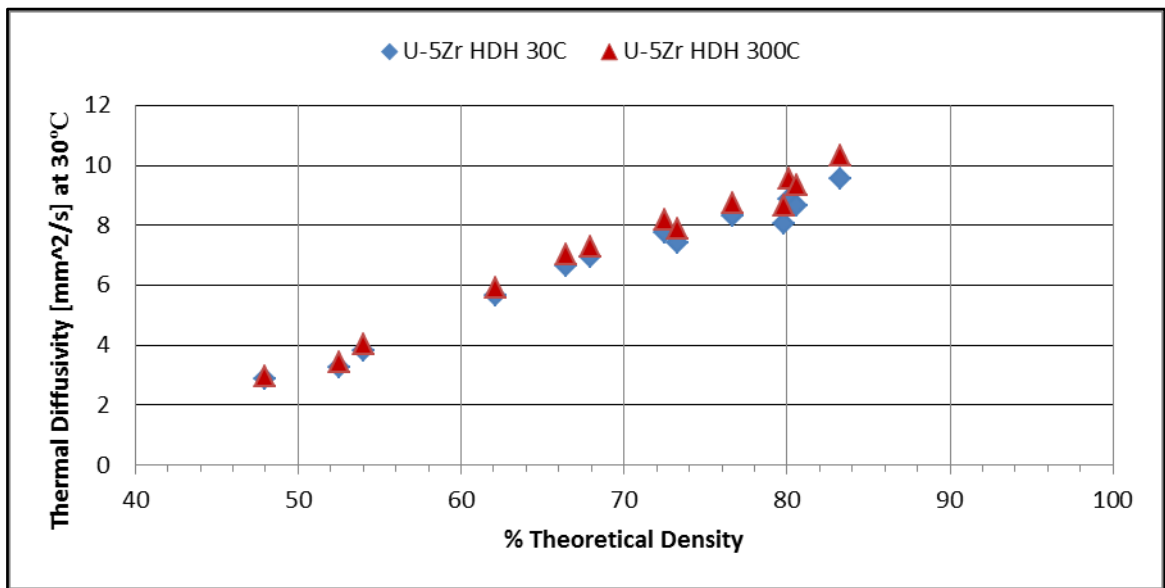


Figure 4-83: Thermal diffusivity of U-5Zr HDH pellets at 30 and 300°C

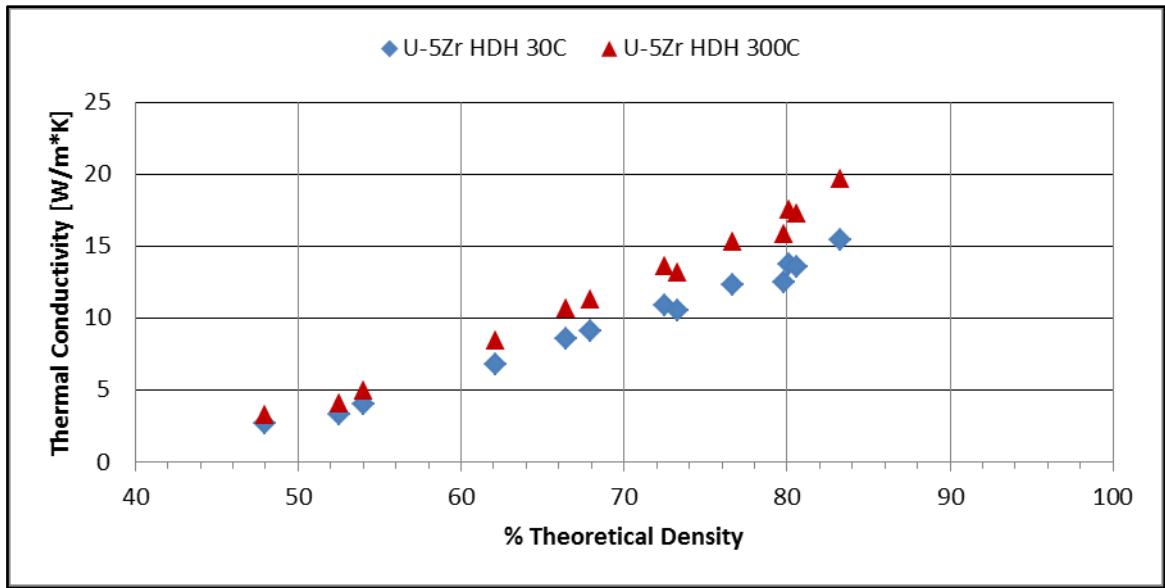


Figure 4-84: Thermal conductivity of U-5Zr HDH pellets at 30 and 300°C

The thermal diffusivity and thermal conductivity are plotted in Figure 4-83 and Figure 4-84 respectively. The data for 30°C and 300°C are included in each plot. As before, there is a clear linear relationship between the density and the thermal conductivity.

4.8 Thermal Conductivity of U-10Zr Pellets

The thermal diffusivity for each U-10Zr HDH pellet was measured. The data is displayed in Figure 4-85 in the same way as the U HDH and U-5Zr HDH pellet data were displayed previously. Again, each data set has roughly the same shape, but the magnitude increases as the density is increased. The higher density samples also have an increased slope.

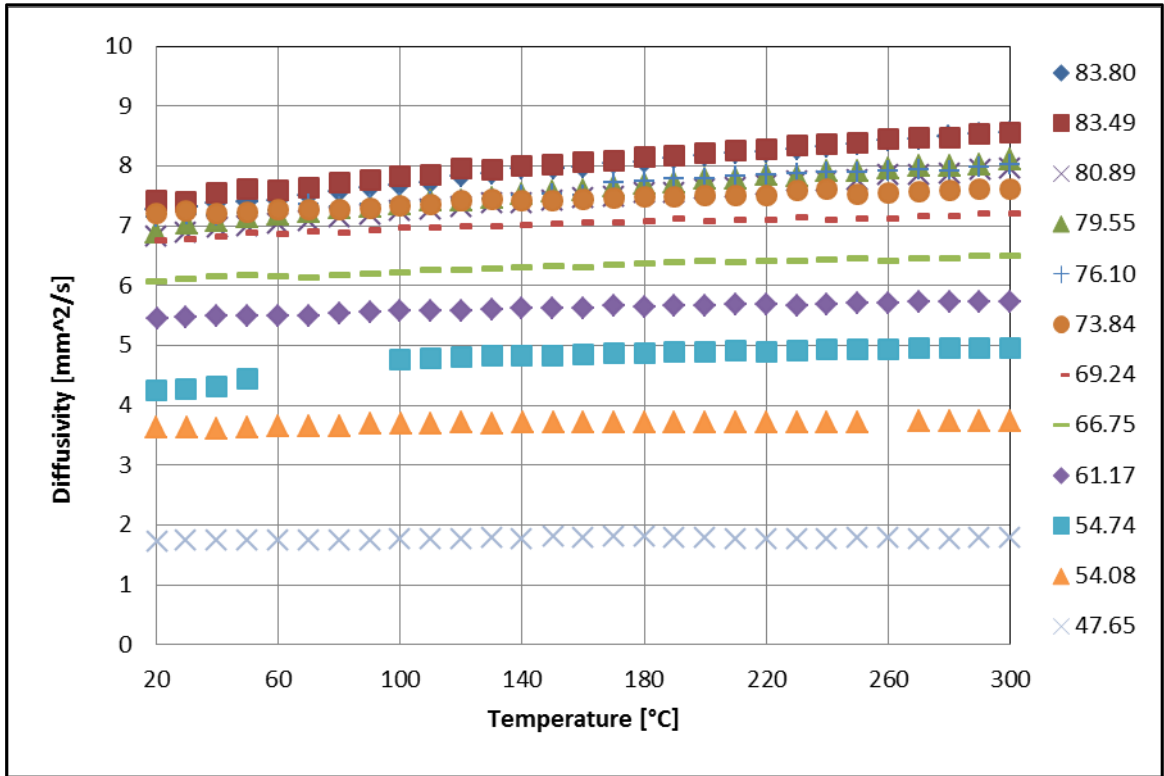


Figure 4-85: Thermal diffusivity of U-10Zr HDH pellets

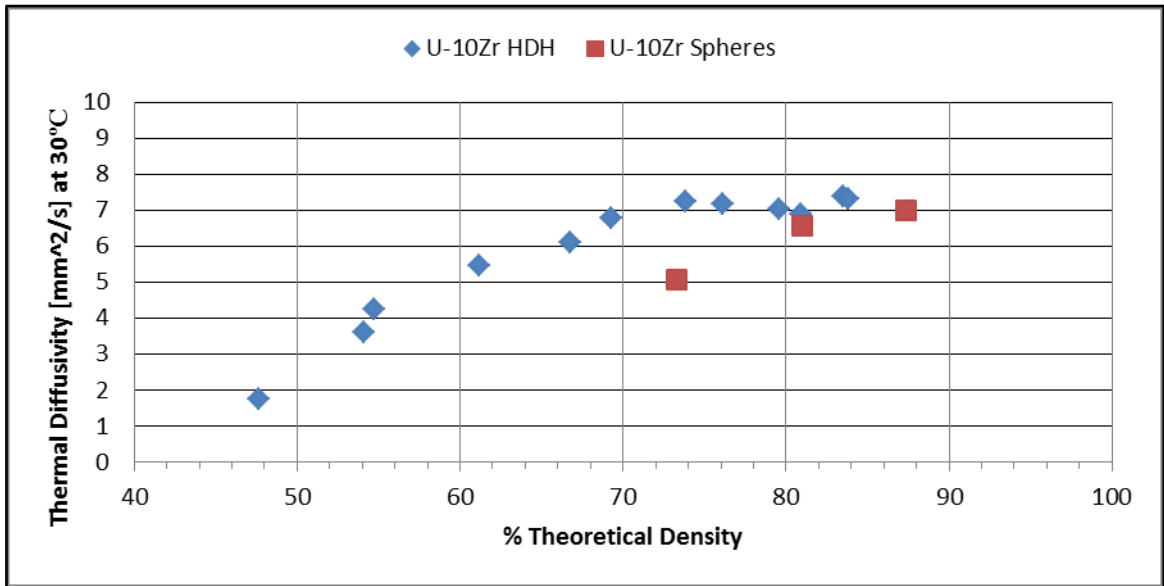


Figure 4-86: Thermal diffusivity of U-10Zr HDH and U-10Zr spheres pellets at 30°C

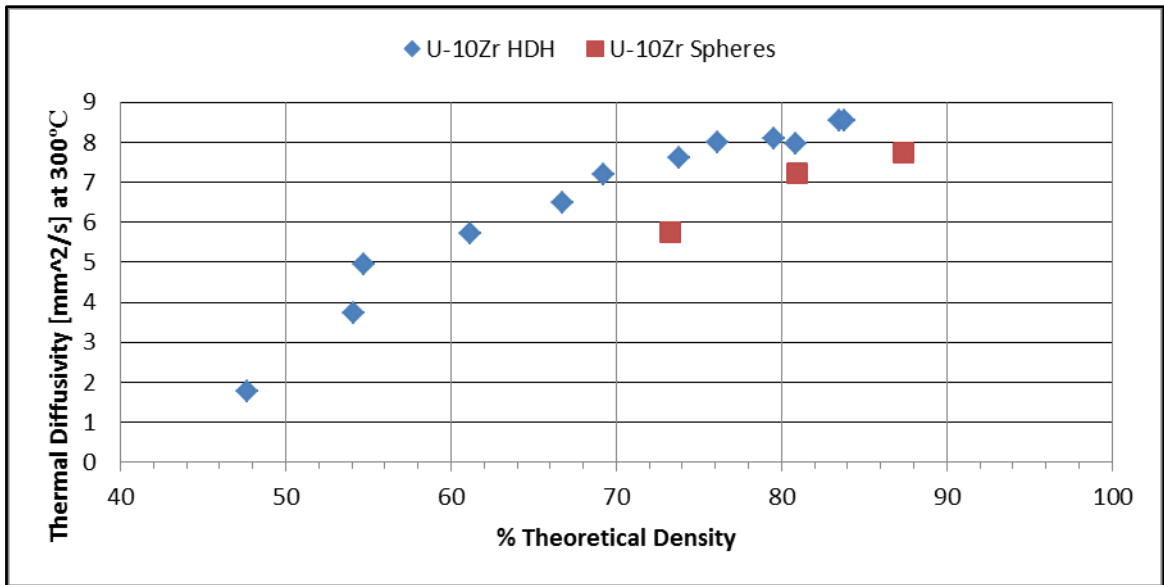


Figure 4-87: Thermal diffusivity of U-10Zr HDH and U-10Zr spheres pellets at 300°C

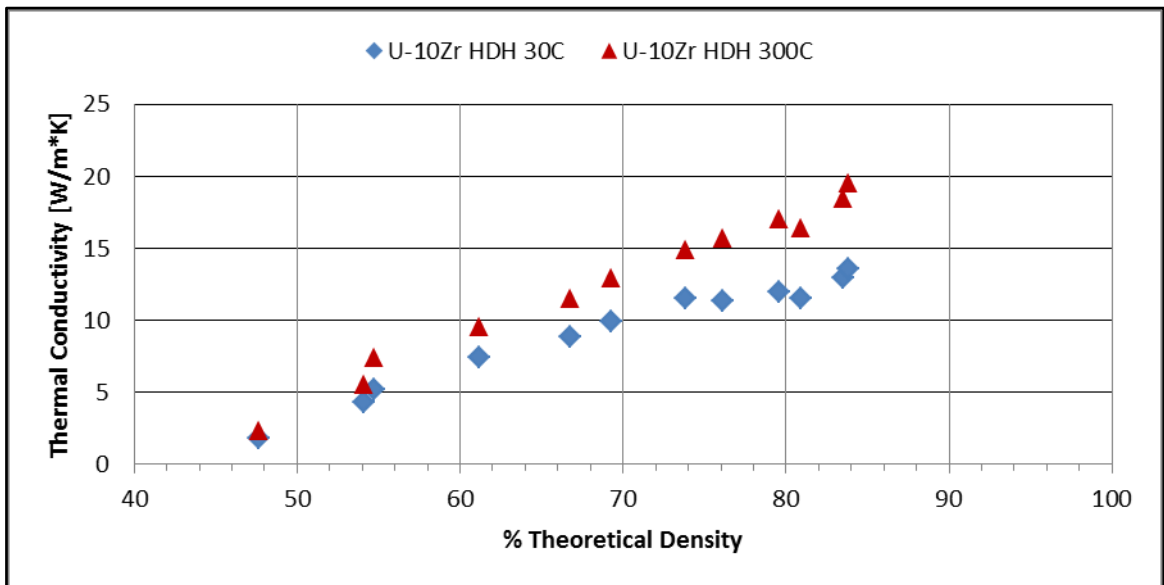


Figure 4-88: Thermal conductivity of U-10Zr HDH pellets at 30 and 300°C

4.9 Microstructure Analysis of Low Density Pellets

Pellets of many different densities were sectioned, polished, and imaged, for comparison of the microstructure and density. A list of the imaged pellets and their

densities can be seen in Table 4-1. Images of additional pellets as well as additional images of the pellets shown in this section can be seen in Appendix 5.

The uranium pellets were imaged with BSE only. The BSE image analysis was adequate to provide the desired information, which was pore distribution and general structure information. The U-10Zr and the U-5Zr pellets were imaged with BSE as well as EDX in order to also investigate the distribution of the zirconium relative to the uranium. However, the difference in *Z* number between uranium and zirconium results in zirconium being darker than uranium and relatively easy to see with BSE only.

The first section of images shown here are of U HDH samples. The image sets are shown with lowest density samples first. After the U HDH samples the next section is U spheres pellets followed by U-5Zr HDH, U-10Zr HDH, and lastly the U-1-Zr spheres pellets.

Table 4-1: List of LFA Pellets that were Analyzed with SEM

Material	%TD	Sample ID#	Figure Number
U HDH	45.5	26-182	Figure 4-89 - Figure 4-90
	53.7	31-32	Figure 4-91 - Figure 4-92
	57.6	31-33	Appendix 5
	60.1	31-31	Figure 4-93 - Figure 4-94
	62.5	31-30	Appendix 5
	64.8	31-29	Figure 4-95 - Figure 4-96
	70.9	17-1	Appendix 5
	87.0	26-184	Figure 4-97 - Figure 4-98
U Spheres	65.6	26-156	Figure 4-99 - Figure 4-101
	74.4	26-124	Appendix 5
	75.1	26-121	Figure 4-102
U-5Zr HDH	67.9	17-14	Figure 4-103 - Figure 4-104
	72.5	31-50A	Appendix 5
	80.6	31-63B	Figure 4-105 - Figure 4-106
U-10Zr HDH	54.7	17-5A	Figure 4-107 - Figure 4-108
	61.2	17-7B	Appendix 5
	76.1	17-9B	Figure 4-109 - Figure 4-110
	79.6	17-11B	Appendix 5
	83.5	17-11A	Figure 4-111 - Figure 4-112
	83.8	31-45	Appendix 5
U-10Zr Spheres	73.3	26-174	Appendix 5
	81.0	26-120	Appendix 5

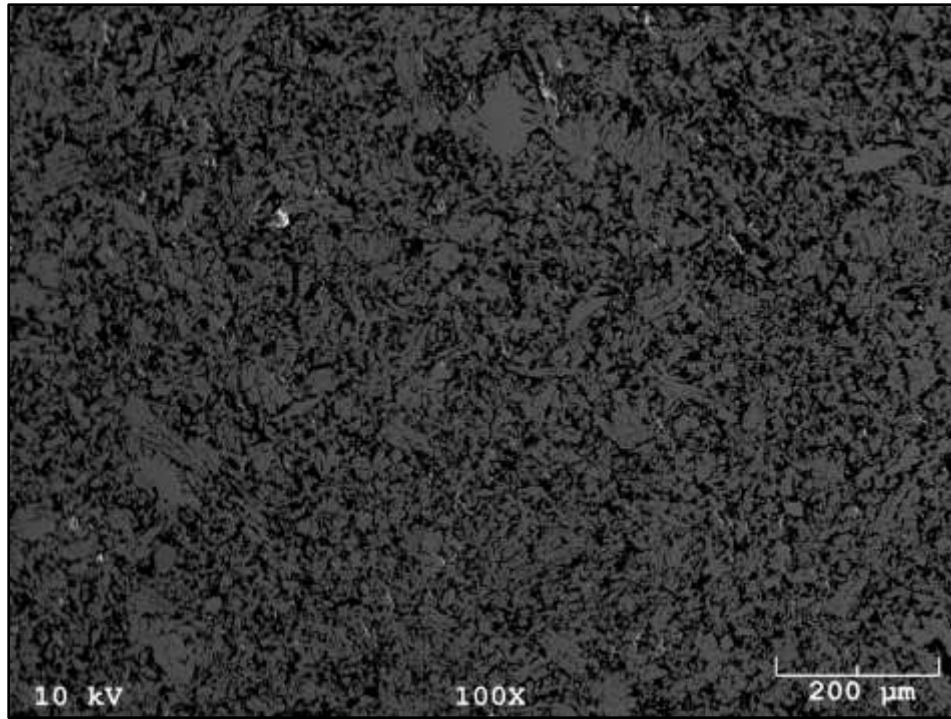


Figure 4-89: BSE image of 45.5 %TD U HDH pellet (26-182) at 100X

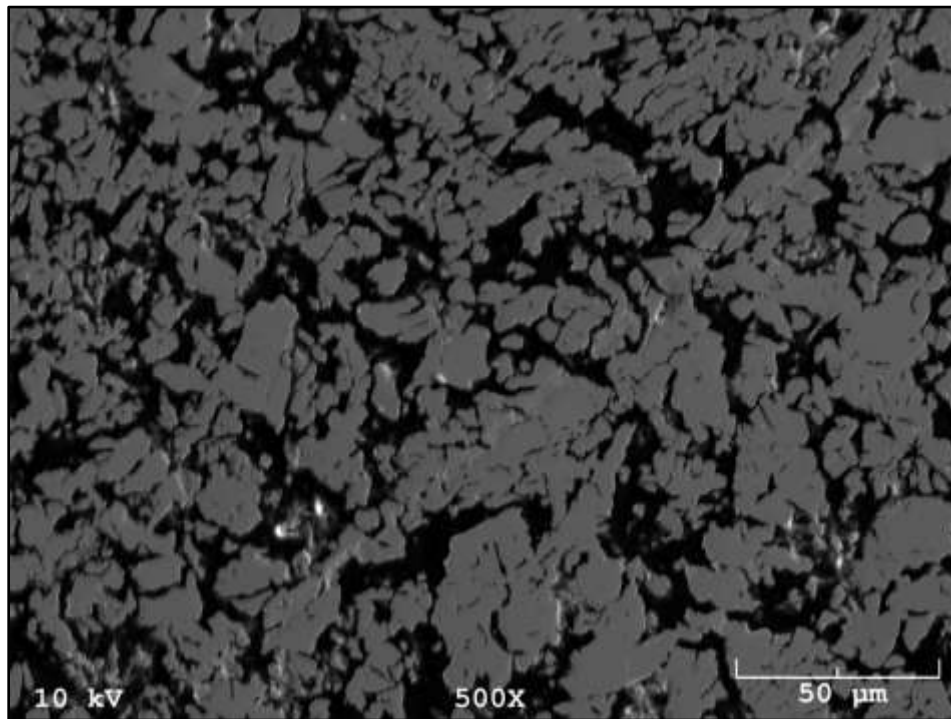


Figure 4-90: BSE image of 45.5 %TD U HDH pellet (26-182) at 500X

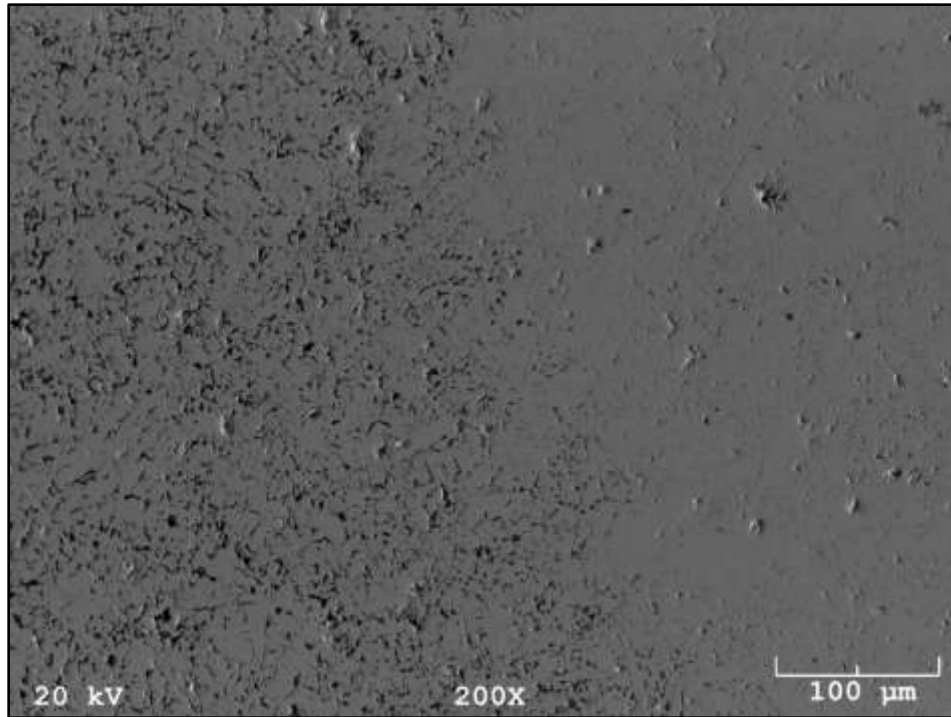


Figure 4-91: BSE image of 53.7 %TD U HDH pellet (31-32) at 200X

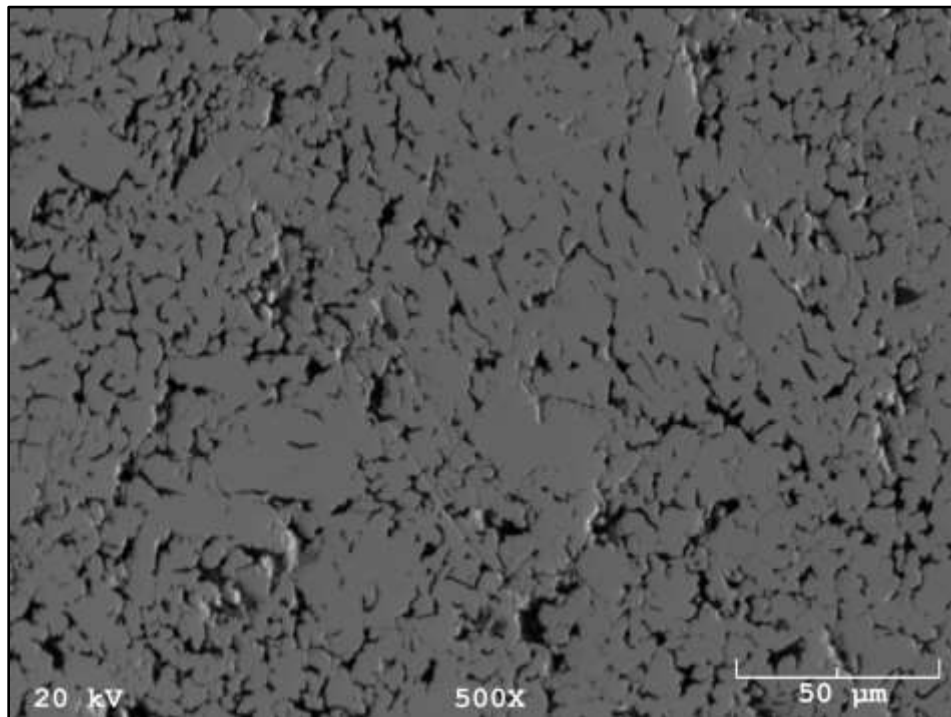


Figure 4-92: BSE image of 53.7 %TD U HDH pellet (31-32) at 500X

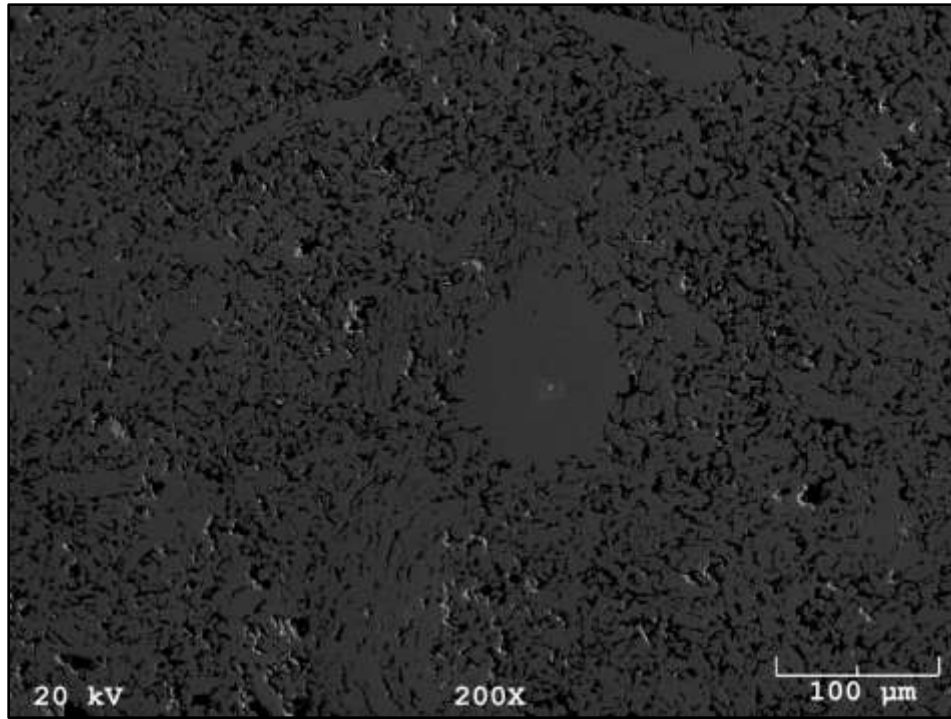


Figure 4-93: BSE image of 60.1 %TD U HDH pellet (31-31) at 200X

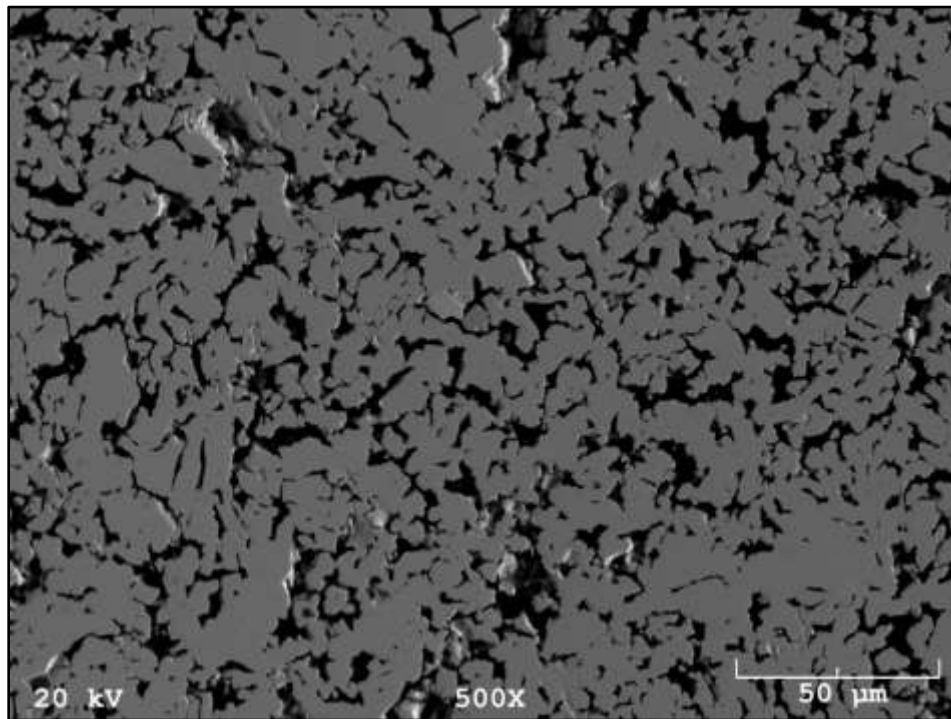


Figure 4-94: BSE image of 60.1 %TD U HDH pellet (31-31) at 500X

Sample 31-29 was a uranium HDH pellet. It was 64.8 %TD. This pellet was cut in half radially as opposed to axially like most of the other pellets. This was an important investigation to determine if the microstructure was homogenous or oriented differently. Figure 4-95 and Figure 4-96 show representative microstructure images for the sectioned sample. These images are very similar to the previous two sets of images. It was therefore determined that there were no significant differences between radial and axial cross sections and microstructure formations.

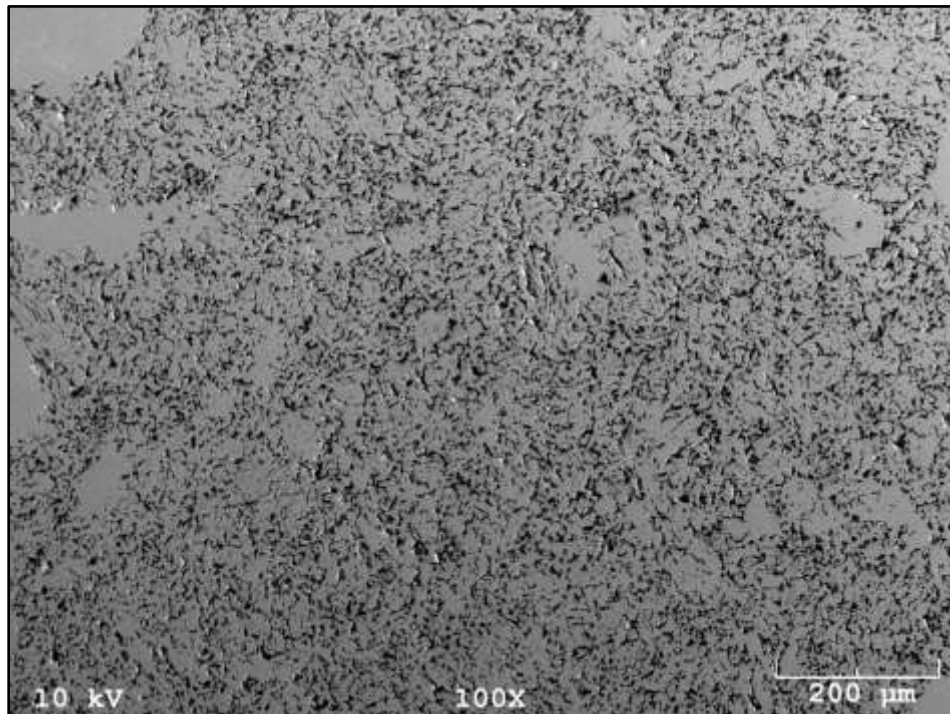


Figure 4-95: BSE image of 64.8 %TD U HDH pellet (31-29) at 100X

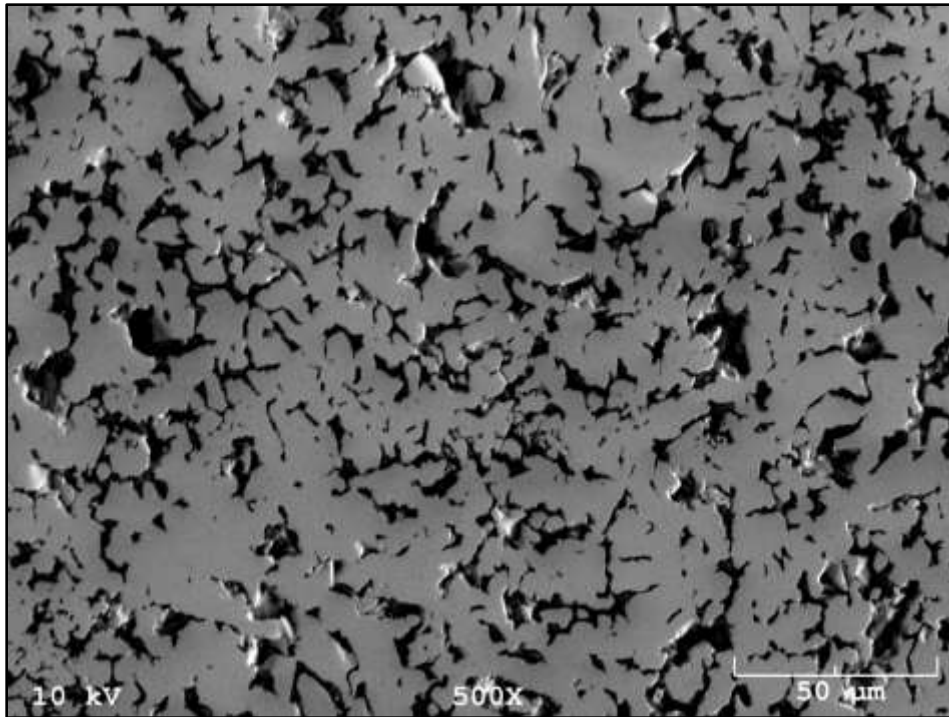


Figure 4-96: BSE image of 64.8 %TD U HDH pellet (31-29) at 500X

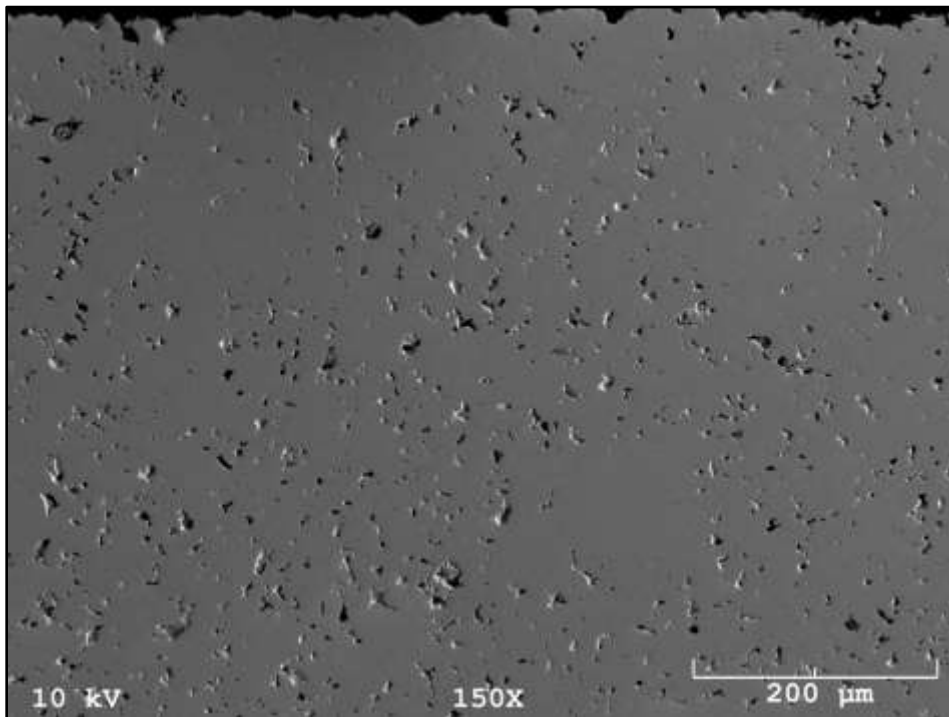


Figure 4-97: BSE image 1 of 87.0 %TD U HDH pellet (26-184) at 150X

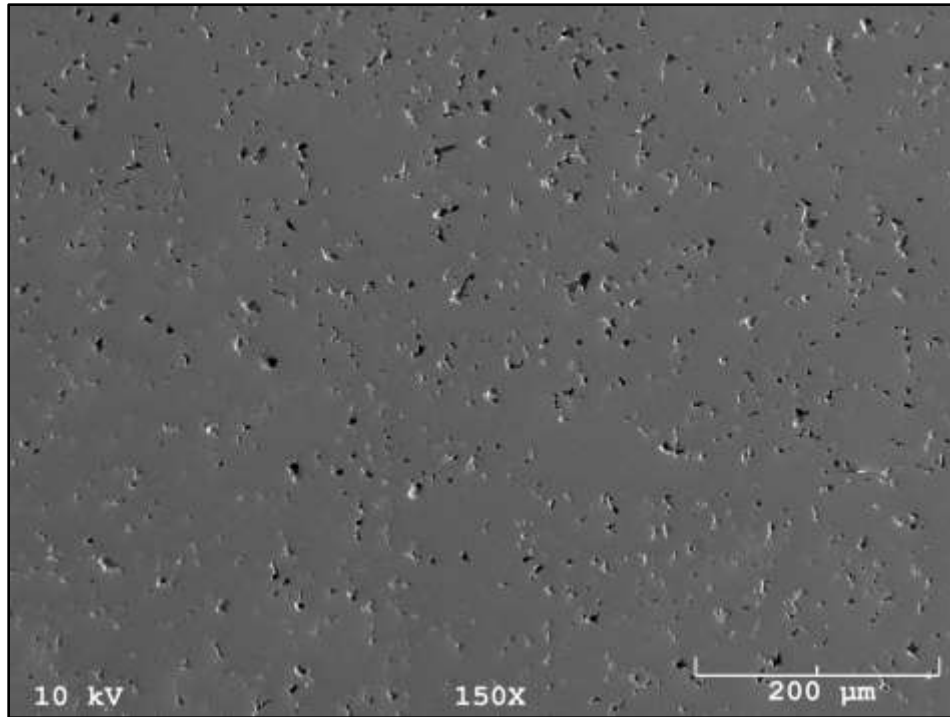


Figure 4-98: BSE image 2 of 87.0 %TD U HDH pellet (26-184) at 150X

These next two sets of images are of pellets that were made with uranium microspheres. Figure 4-99, Figure 4-100, and Figure 4-101, are of sample 26-156 which was 65.55 %TD. And Figure 4-102 is an image of sample 26-121 which had a percent theoretical density of 75.08. Figure 4-99 is an image of the sample surface. The dust-like particles on the surface of the pellets that can be seen in the images are remnants of the die lubricant used in the manufacturing of the pellets. Additionally, the epoxy can be clearly seen in between the microspheres in the cut face images. In Figure 4-101 and in Figure 4-102 small pores can be seen inside of each microsphere. However, in the higher density sample there are less of these pores in some areas due to the longer sintering time.

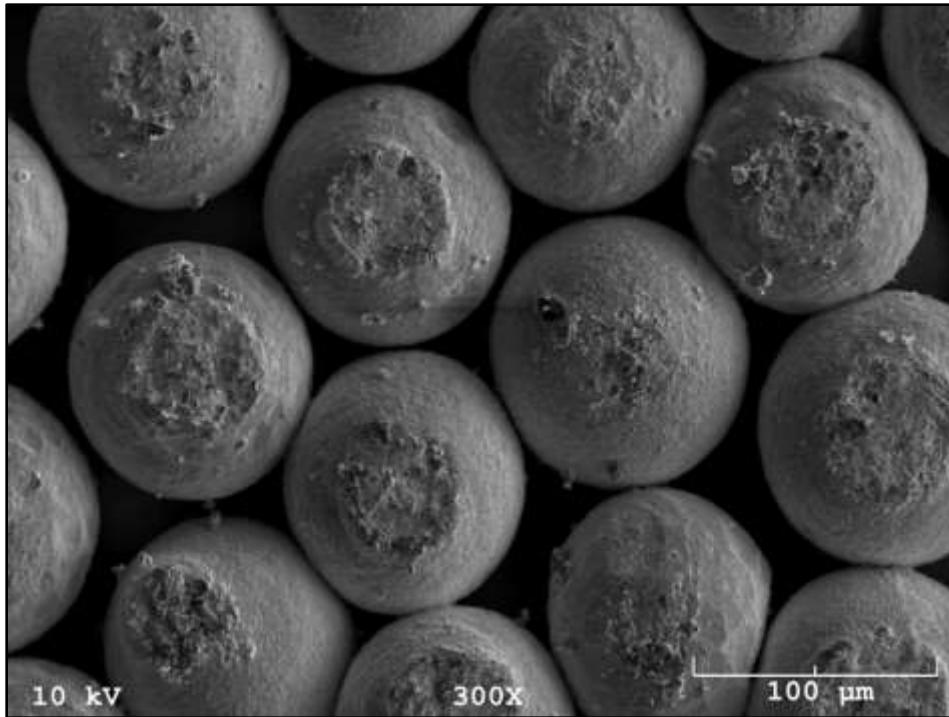


Figure 4-99: BSE image of 65.6 % TD U spheres pellet (26-156) at 300X

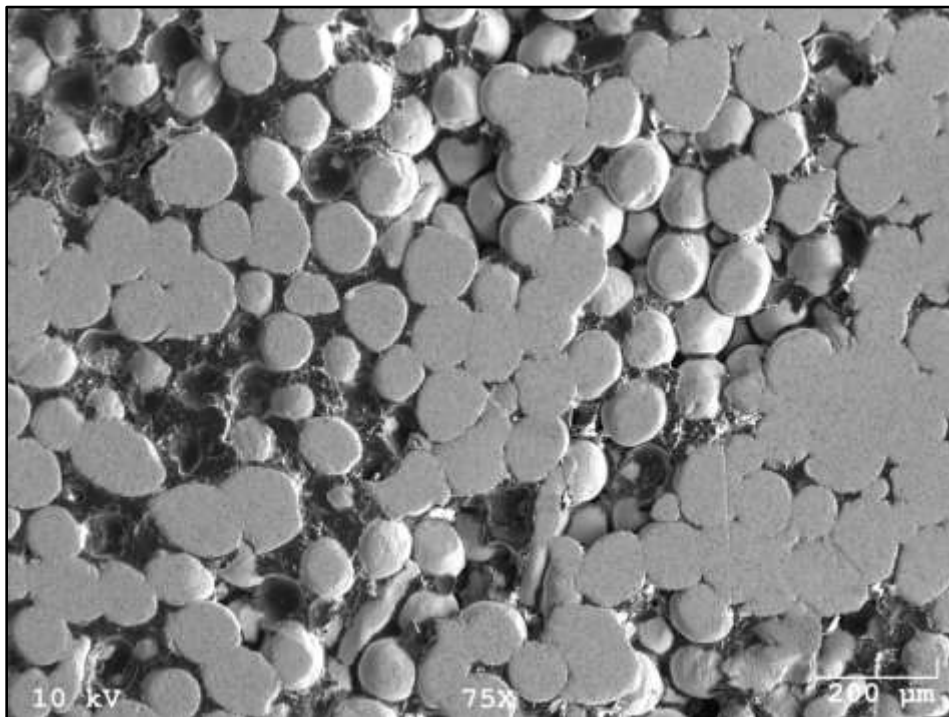


Figure 4-100: BSE image of 65.6 % TD U spheres pellet (26-156) at 75X

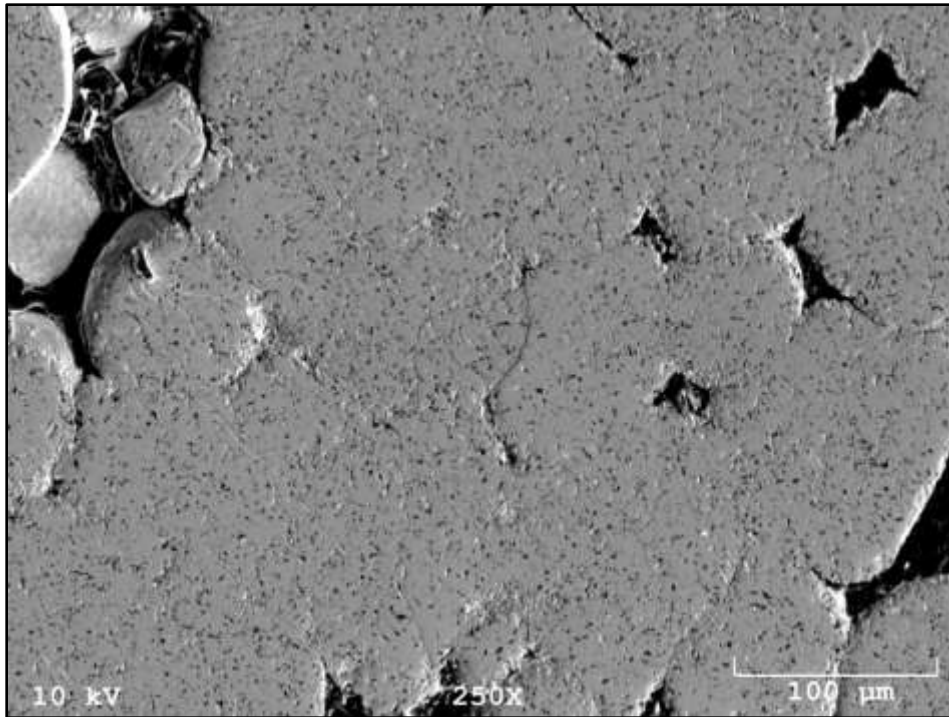


Figure 4-101: BSE image of 65.6 %TD U spheres pellet (26-156) at 250X

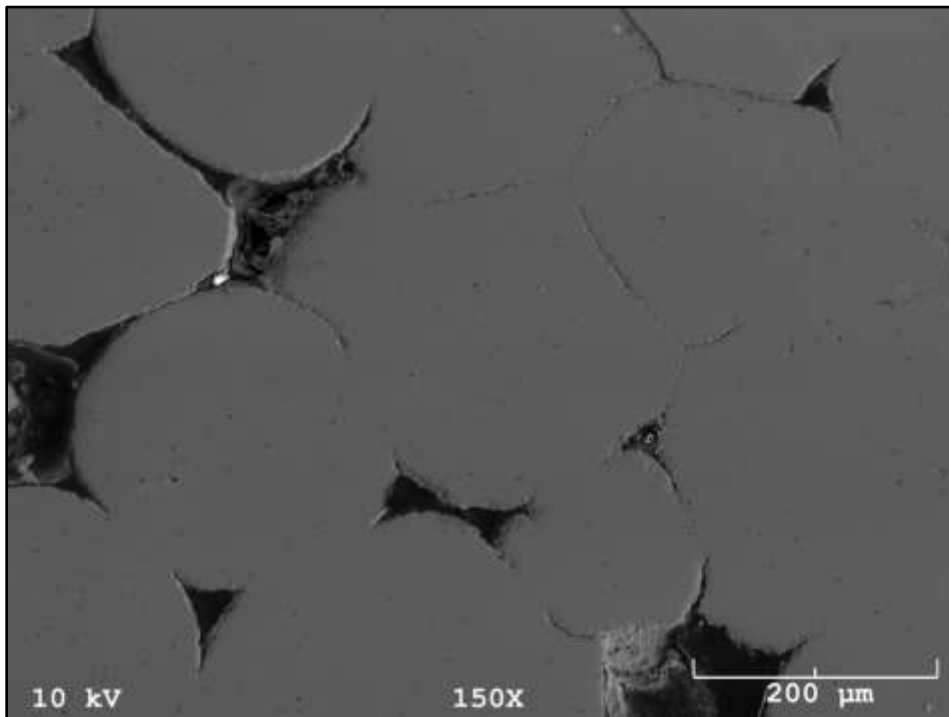


Figure 4-102: BSE image of 75.1 %TD U spheres pellet (26-121) at 150X

The U-5Zr HDH samples and the U-10Zr HDH samples look very similar with the only difference being the change in the amount of the zirconium. While it is only a 5 percent weight increase there is an obvious difference. Figure 4-103 and Figure 4-104 show sample 17-14 which was a U-5Zr HDH pellet with a percent theoretical density of 67.9. Figure 4-105 and Figure 4-106 show sample 31-63B which was a U-5Zr HDH sample with 80.6 %TD. The sample with the higher density and longer sintering time has smaller pores. Additionally, the zirconium is more diffused into the uranium. Both samples are very homogenous.

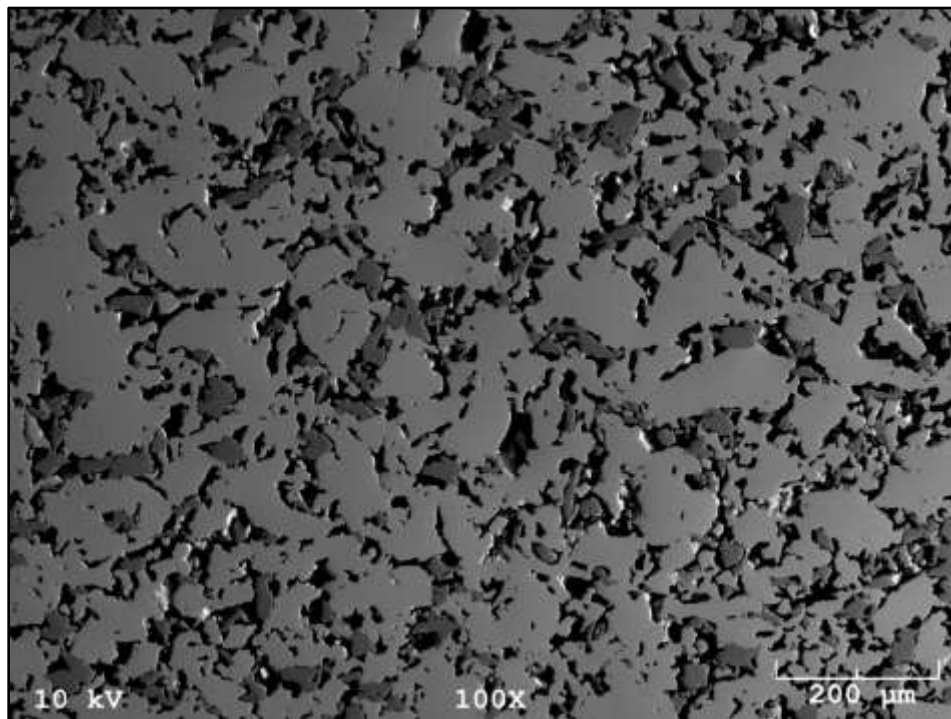


Figure 4-103: BSE image of 68.0 %TD U-5Zr HDH pellet (17-14) at 100X

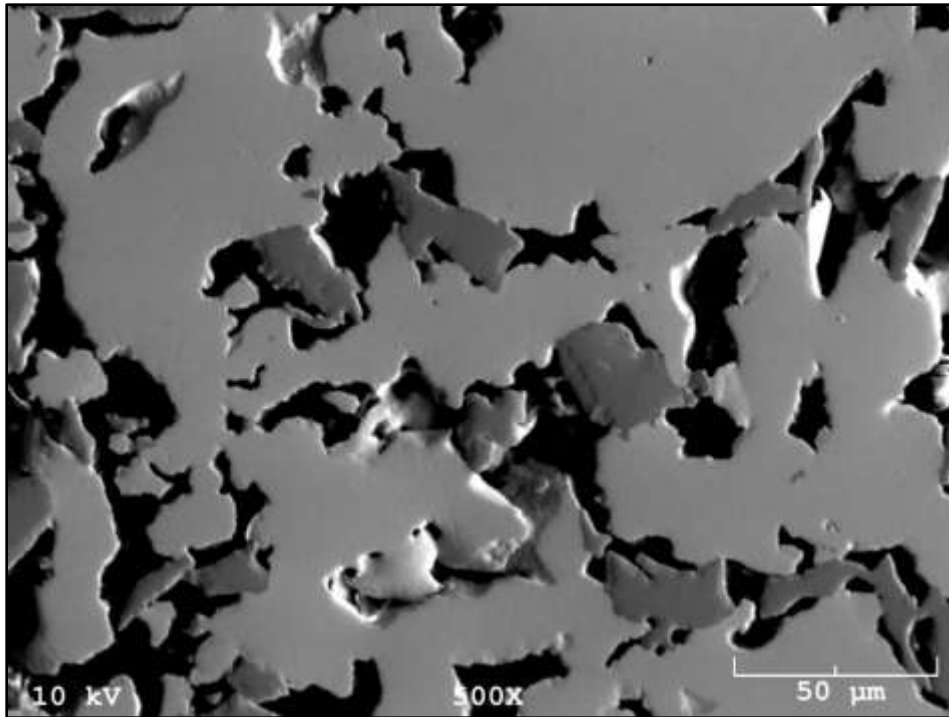


Figure 4-104: BSE image of 68.0 %TD U-5Zr HDH pellet (17-14) at 500X

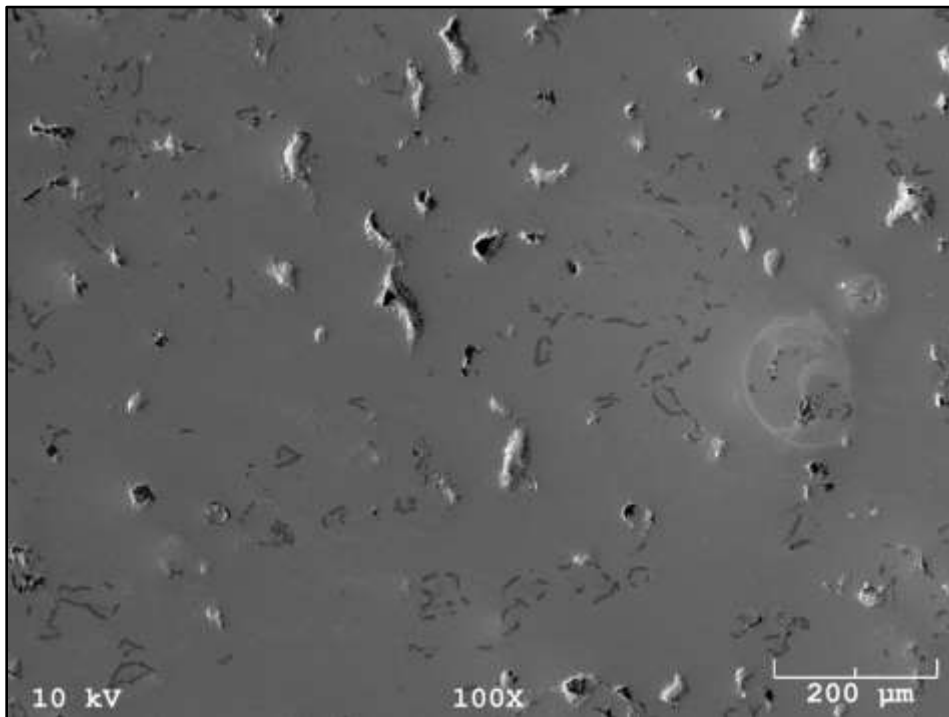


Figure 4-105: BSE image of 80.6 %TD U-5Zr HDH pellet (31-63B) at 100X

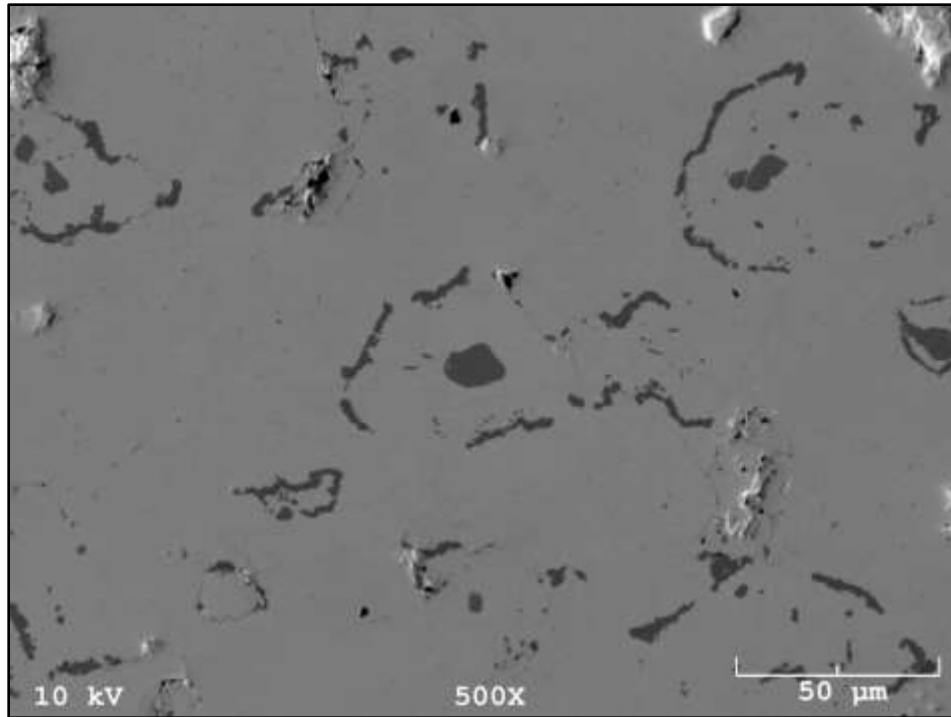


Figure 4-106: BSE image of 80.6 %TD U-5Zr HDH pellet (31-63B) at 500X

The next image sets are some of the U-10Zr HDH samples. These appear very similar to the U-5Zr HDH samples with the only difference being the increase in zirconium content. The difference in density between each image set is very clear. Additionally, the high density samples have an increase in zirconium mixing. The zirconium mixing and closing of the pores results in an interesting zirconium structure. There are long thin zirconium rich areas. These were most likely the boundaries between grains or pores.

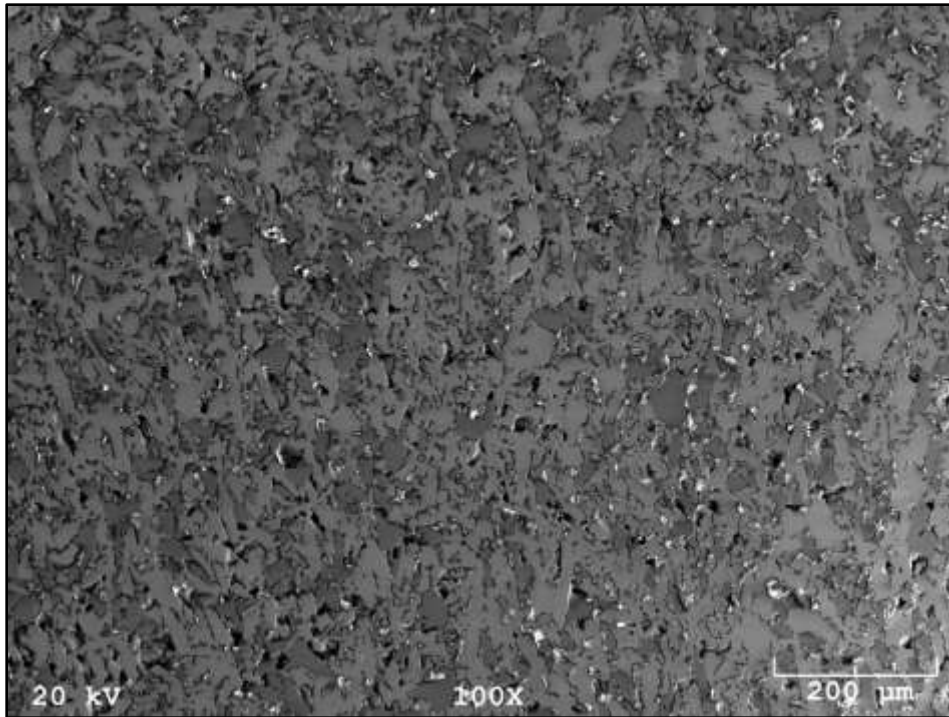


Figure 4-107: BSE image of 54.7 %TD U-10Zr HDH pellet (17-5A) at 100X

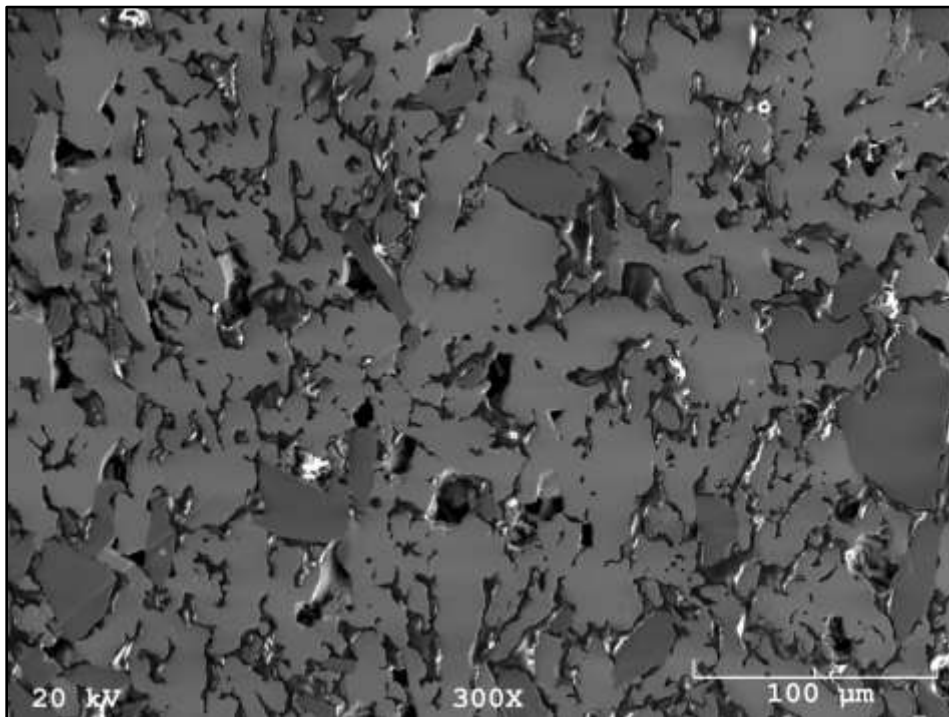


Figure 4-108: BSE image of 54.7 %TD U-10Zr HDH pellet (17-5A) at 300X

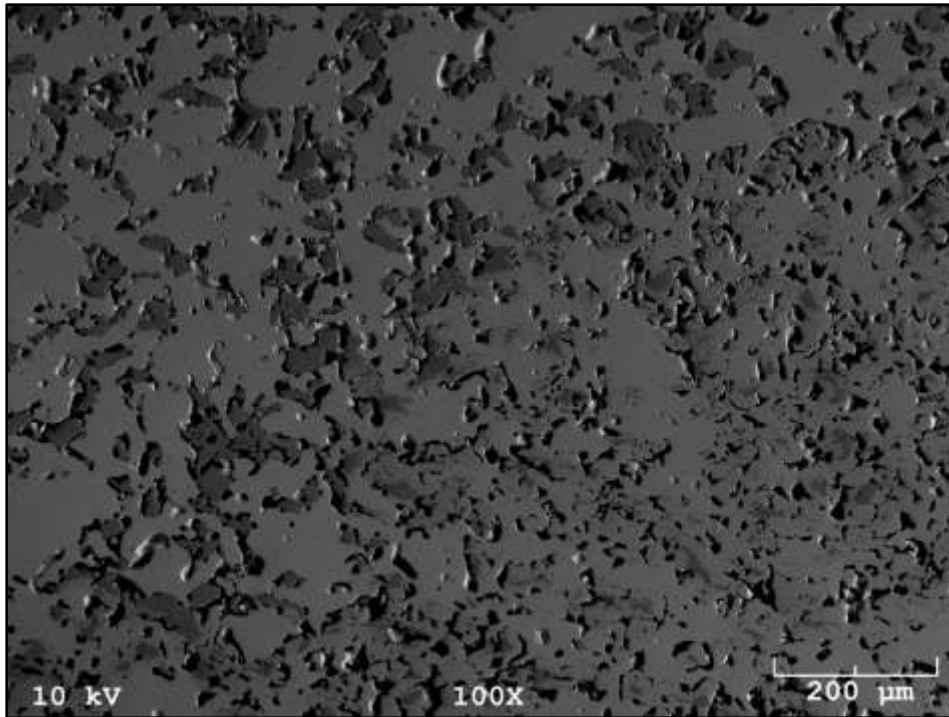


Figure 4-109: BSE image of 76.1 %TD U-10Zr HDH pellet (17-9B) at 100X

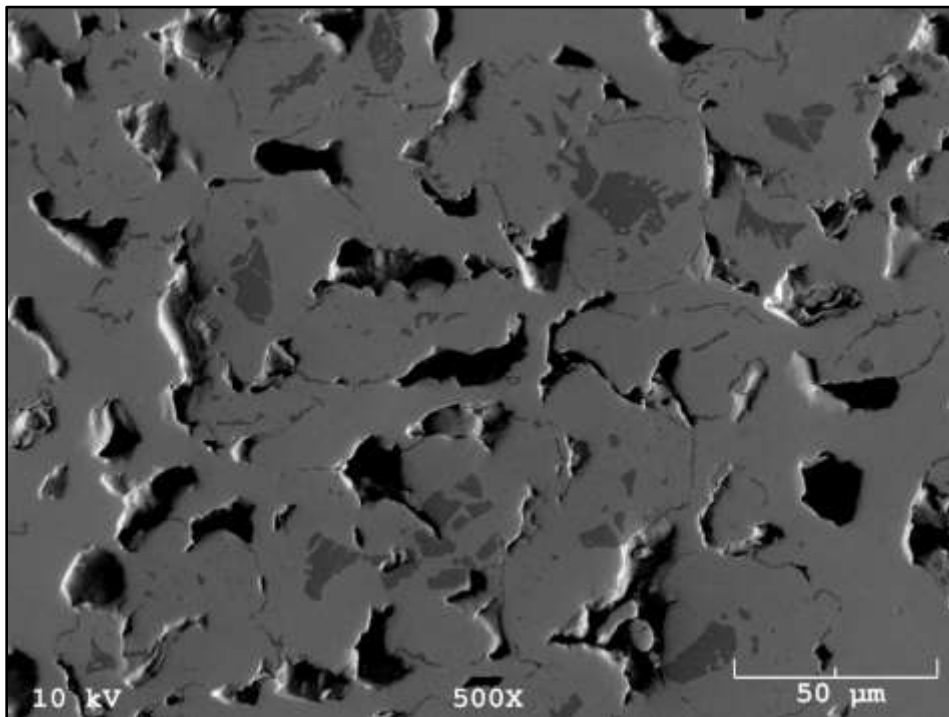


Figure 4-110: BSE image of 76.1 %TD U-10Zr HDH pellet (17-9B) at 500X

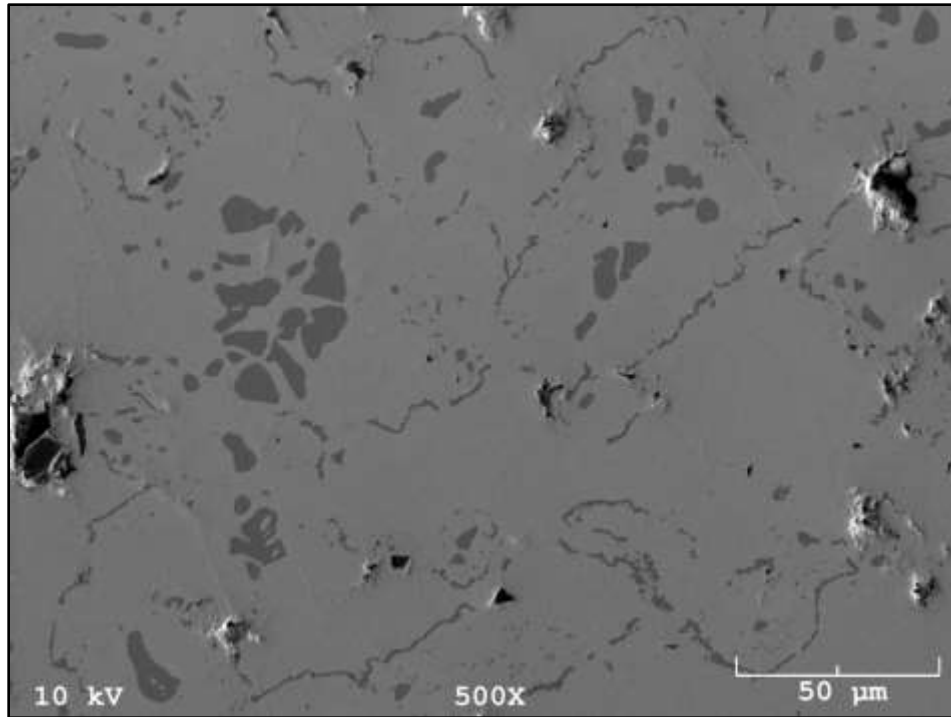


Figure 4-111: BSE image 1 of 83.5 %TD U-10Zr HDH pellet (17-11A) at 500X

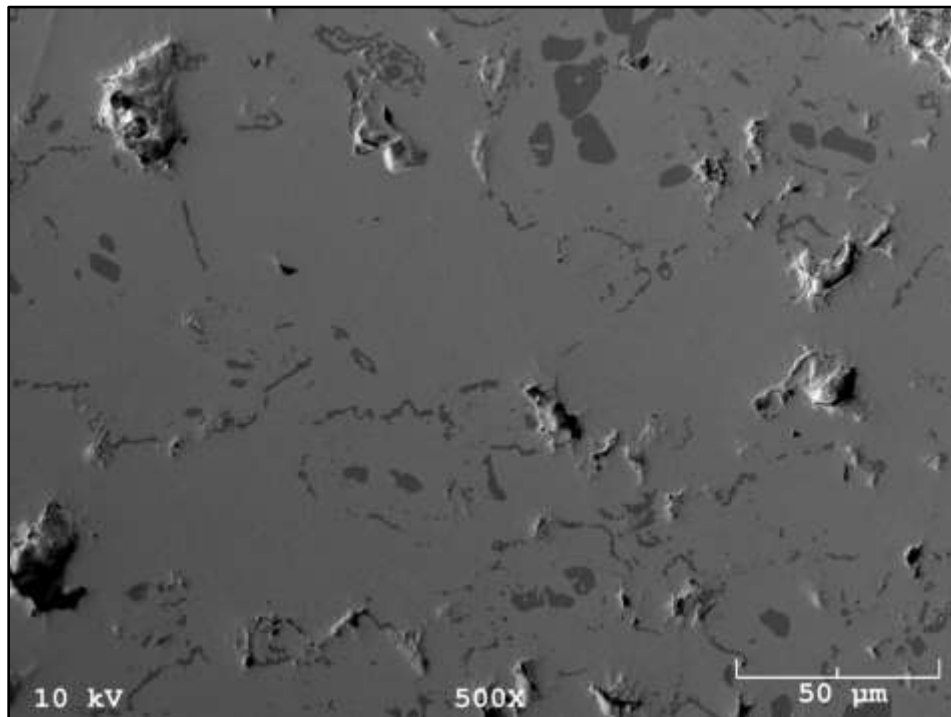


Figure 4-112: BSE image 2 of 83.5 %TD U-10Zr HDH pellet (17-11A) at 500X

5 DISCUSSION

5.1 Comments on the Extruded U and U-10Zr Products

Many of the extruded rods were slightly curved. It is presumed that the cause of the curvature was due to imprecise machining of tooling and misalignment of the holder and the die. Further, it is common to extrusion methods that a slight curve is present at the initial portion of the extruded material due to billet upsetting. [9] A larger billet would produce a longer extruded product and thus produce better, straighter results. An improvement in straightness is notable when comparing results from early extrusions and later extrusions.

The results of the tube extrusions were not ideal. This is almost entirely due to lack of precise machining of the uranium billets as well as the tooling sets. Uranium metal is not as easily machined as other metals due to its high density, strength, and pyrophoricity. Billets for tube extrusion should be machined with dedicated precision machinery, but that level of precision was not available for this project. The resulting uranium billets had central holes that were not perfectly centered and not aligned parallel to the billets sides. The ram mandrels broke in every tube extrusion. This was partially due to the billets, but also partially due to the tooling material and design. The mandrel should be made of a stronger material to help cope with lateral forces caused by the uranium metal during extrusions. The piercing of the billet method should be attempted in future research as a way to avoid the potential breaking of mandrels as well as eliminating the need for machining central holes in the billets.

On an industrial production scale utilizing large, perfectly machined tooling that is capable of handling larger billets, higher quality rods and tubes could be consistently extruded. For rods and tubes, post-extrusion rolling and straightening will be a necessary step after extrusion to have more control on final straightness and dimensions.

5.2 Observations from Extrusion Tooling Development

The extrusion tooling designs were modified and improved between almost every extrusion until the final few extrusions. The final tooling design can be seen in Figure 5-1 and Figure 5-2. Inspiration for tooling designs was drawn from large scale industrial designs. [9] [18] The early extrusion tooling sets fabricated for this work were oversimplified and lacked precision machining. The subsequent designs were better machined and became increasingly complex. The main issue with this design stage was that the ram would sometimes fail during an extrusion. The ram was made of H-13 and it would expand radially when compressed axially at the high temperatures. Once the ram had expanded it would then come into contact with the sides of the holder and the extrusion parts would seize and the process would stop. A secondary issue was that the alignment of the holder and the die opening was not consistently concentric, and while the final design did have close concentricity, it was not perfect.

The final design included a dummy block and a smaller diameter ram. Additionally, the ram and dummy block were made of C350 which was considerably stronger than H-13. This design and material change allowed the ram to resist radial deformation and not come into contact with the sides of the holder. This design also

included two set pins to ensure that the holder and die were properly aligned. This better alignment resulted in straighter rods. Extrusion tooling design and research was not a primary goal of this project, but it was a necessary step to gathering the extrusion data and it did reveal the vital importance of high quality tooling.

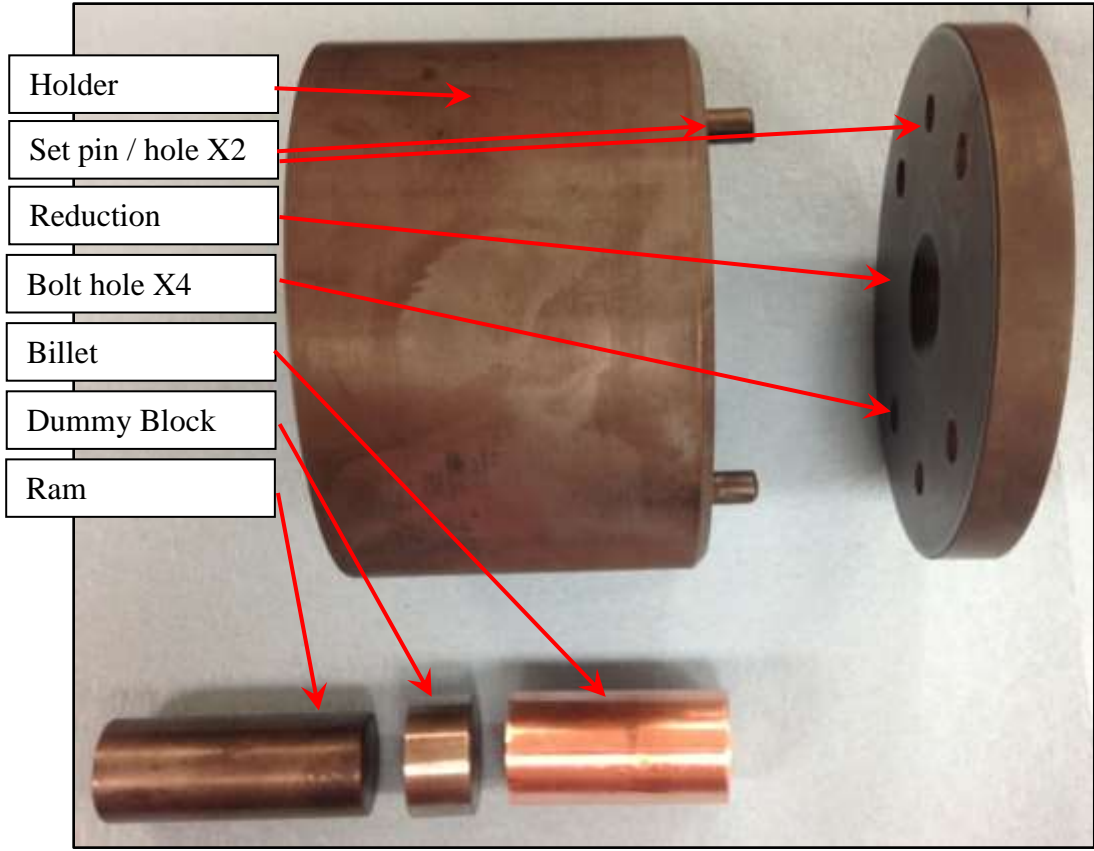


Figure 5-1: Final tooling design (side view)

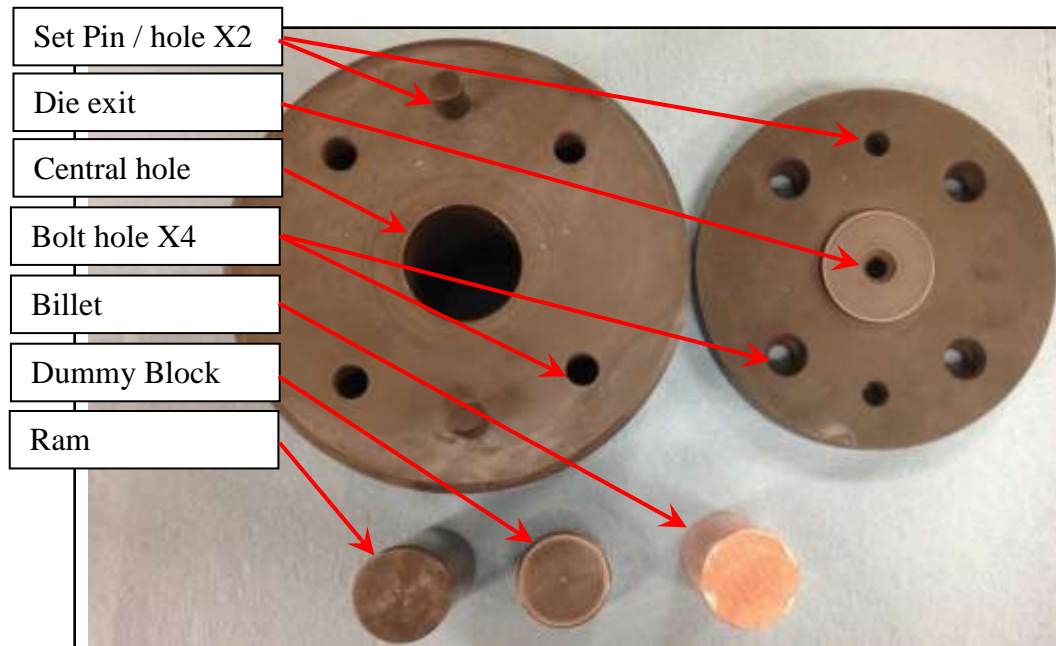


Figure 5-2: Final tooling design (bottom view)

5.3 Temperature Rise during Extrusion

In almost every extrusion the temperature was monitored at the billet and at the die. The die temperature was consistently lower than the billet temperature in each extrusion. This was due to the configuration of the tooling, the tooling support structure, and the heater. The tooling set sat directly on top of the tooling support structure and the die was in direct contact with the support structure. The heater which was placed around the tooling set also sat directly on top of the support structure. The support structure acted as a heat sink for the tooling set so it was consistently at a lower temperature than the billet which was farther away from the support.

In each extrusion, the temperature of the die increased during the extrusion. Temperature rise varied between 7 and 40 degrees Celsius. This rise was in part due to the billet which was at a slightly higher temperature than the die it was being forced

through. Additional temperature increase was due to the heat caused from deformation and friction. This temperature increase is of interest for future extrusion studies due to phase changes in the uranium system as well as the eutectic melting of uranium with iron.

5.4 Extrusion Constant

The extrusion constant for each extrusion was extracted from the force-displacement data recorded from each test that employed the load cell for force measurements and the LVDT for displacement. The calculated extrusion constants can be seen in Table 5-1. The extrusion constant was plotted vs. the reduction ratio and can be seen in Figure 5-3 for U-10Zr and Figure 5-4 for uranium. For both materials, as the reduction ratio increases the extrusion constant decreases. Additionally, as the temperature increases the extrusion constant decreases.

Table 5-1: Extrusion Experiments

ID#	Type	Material	T	RR	K
1	Rod	U-10Zr	600	11.1	64.64
2	Rod	U-10Zr	650	10.7	
3	Rod	U-10Zr	650	10.9	75.82
4	Rod	U-10Zr	550	11.3	101.13
5	Rod	U-10Zr	620	5.2	159.48
6	Rod	U-10Zr	620	15.4	83.35
7	Tube	U	600	10.1	65.85
8	Tube	U	600	10.1	104.99
9	Tube	U	600	13.3	55.01
10	Tube	U	600	5.0	108.90
11	Rod	U-10Zr	650	15.5	55.06
12	Rod	U	630	15.2	46.22
13	Rod	U-10Zr	650	15.3	60.98

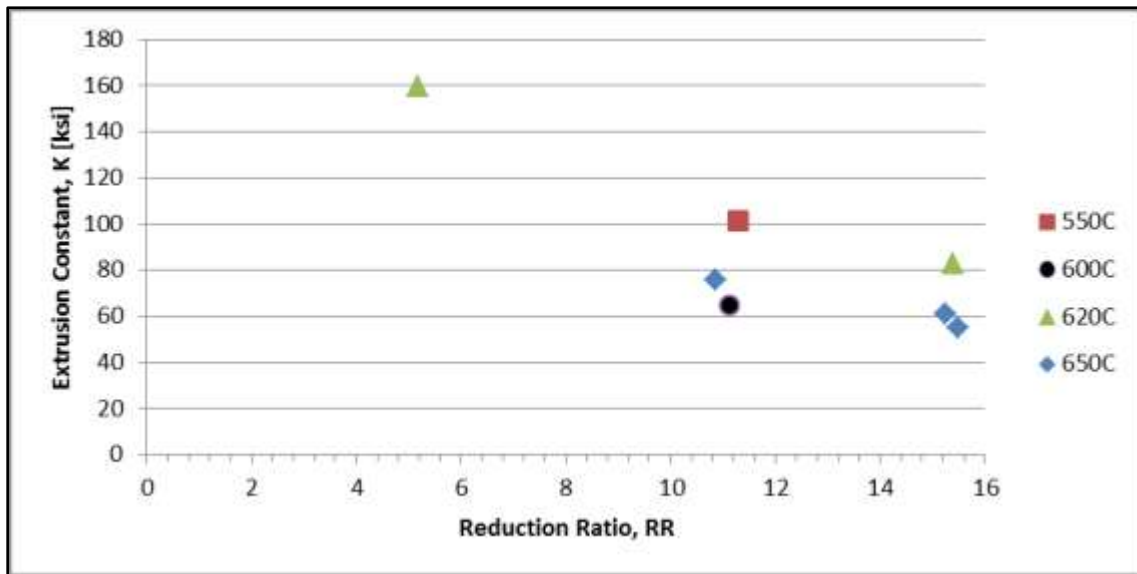


Figure 5-3: U-10Zr Extrusion constants plotted with the reduction ratio

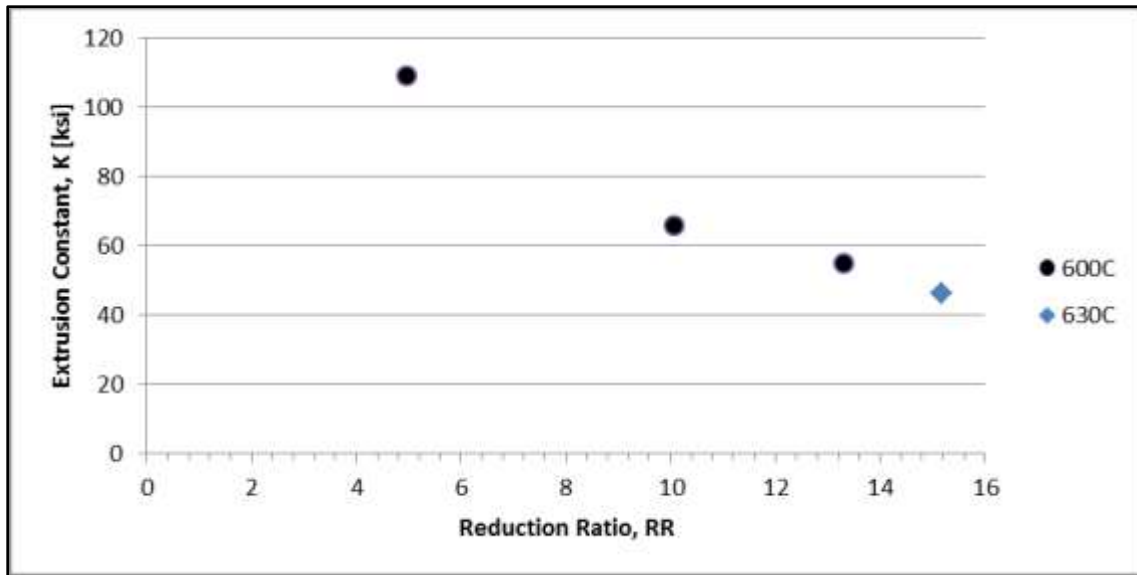


Figure 5-4: Uranium extrusion constants plotted with the reduction ratio

As previously mentioned, there is not much data regarding uranium extrusion engineering in literature. Even when there has been a record of the extrusion of uranium there are little to no specifics regarding the manufacturing process. The most reliable data gathered from literature has been reproduced below in Figure 5-5. This data is presented by Wilkinson in the book Uranium Metallurgy. However, there are no details associated with this data regarding the heating method, extrusion configuration, tooling, lubricant, or dimensions. Despite the lack of useful specific details this data is still helpful because it shows the same general trend for the extrusion constant as the data generated in this work. Further, the magnitude of the measured K-values is consistent with the literature values presented. The extrusion constants presented in Figure 5-5 include the data from Wilkinson as well as the constants generated in through this research. The U-10Zr data points are all black and each temperature has a different symbol. The uranium data points are all red and each temperature has a different symbol.

The Wilkinson uranium data has a different color and shape for each temperature as well as a line connecting the data points. [11]

The effect of temperature on the extrusion constant is more readily discerned in Figure 5-5 since there are more extrusions at each temperature. The extrusion constant generally decreases with increasing temperature. At higher reduction ratios the increase in temperature had less of an effect than it did at lower reduction ratios.

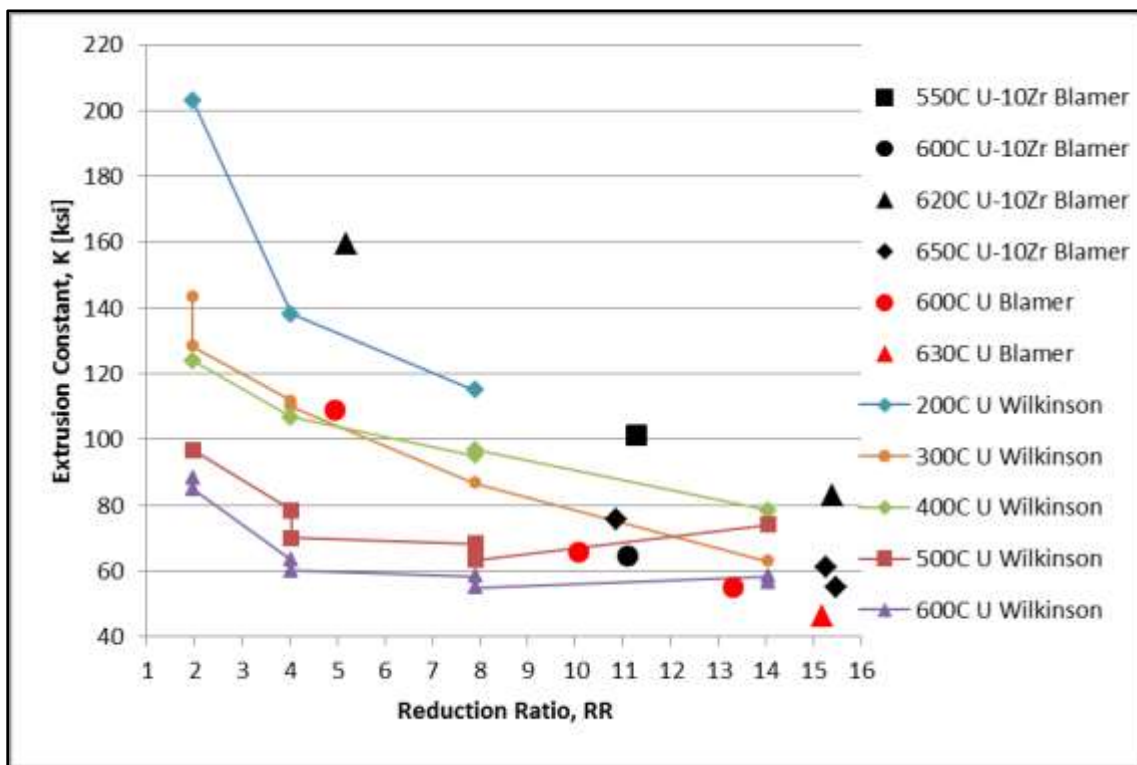


Figure 5-5: Uranium metal extrusion constants plotted with the reduction ratio [11]

5.5 Extruded Grain Structure

Extruded uranium and extruded U-10Zr both exhibited elongated grain structures. The uranium structure contained long rows of smaller grains oriented in the

direction of extrusion and some long grains stretched out in the direction of extrusion. This result is not surprising as it is well known that extruded metals can exhibit this structure. [41] [42] The extrusion 7 U tube sample and the extrusion 12 U rod sample both exhibited the same structure. The preparation of these samples for imaging required a carefully executed etching process. Over-etching resulted in small pores, and under-etching failed to reveal any grain structure at all. This grain structure may have an effect on initial fuel performance in a reactor loaded with extruded fuel. However, it is well known that grain structure and texture in uranium may be homogenized through the proper heat treatment. This could readily be done after extrusion but before putting the fuel into the reactor. [43] [44] [45] [42]

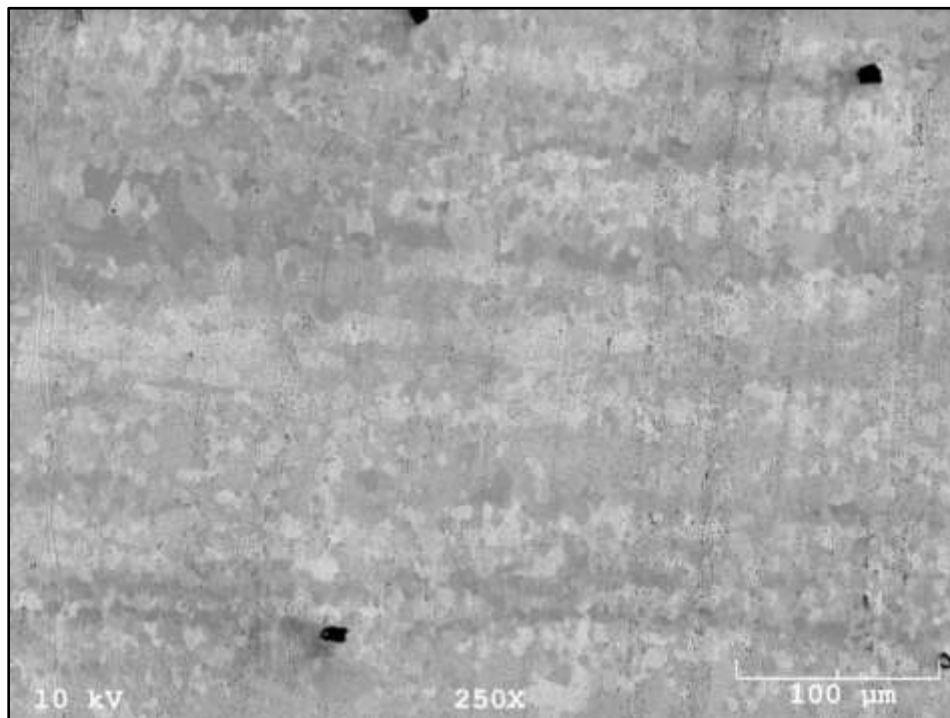


Figure 5-6: BSE image of extrusion 12 U rod at 250X, extrusion direction is horizontal

The study of the U-10Zr products revealed zirconium rich grains. These grains were present throughout all U-10Zr extruded product samples. These zirconium rich grains originate from zirconium acting as a gatherer of impurities in the U-10Zr system. These grains have been seen in many other research projects that involve the U-10Zr alloy. [14] The zirconium grains were not only elongated in the direction of extrusion, but they were also seemingly aligned in rows with other zirconium grains.

Further, the α -U + δ -UZr₂ phase grains exhibited slight elongation in the extrusion direction. The α + δ phase structure is more apparent in the extrusion 11 image set than it was in the other image sets because the polishing and etching were higher quality allowing for better focus with the SEM.

A section from extrusion 11 was examined using EBSD scans. However, no crystal patterns were found in the large zirconium grains. This implies that there was no significant crystal structure texture in those grains. Additionally, EDX maps of the zirconium grains show that they were not entirely zirconium as there was some small amount of uranium in them.

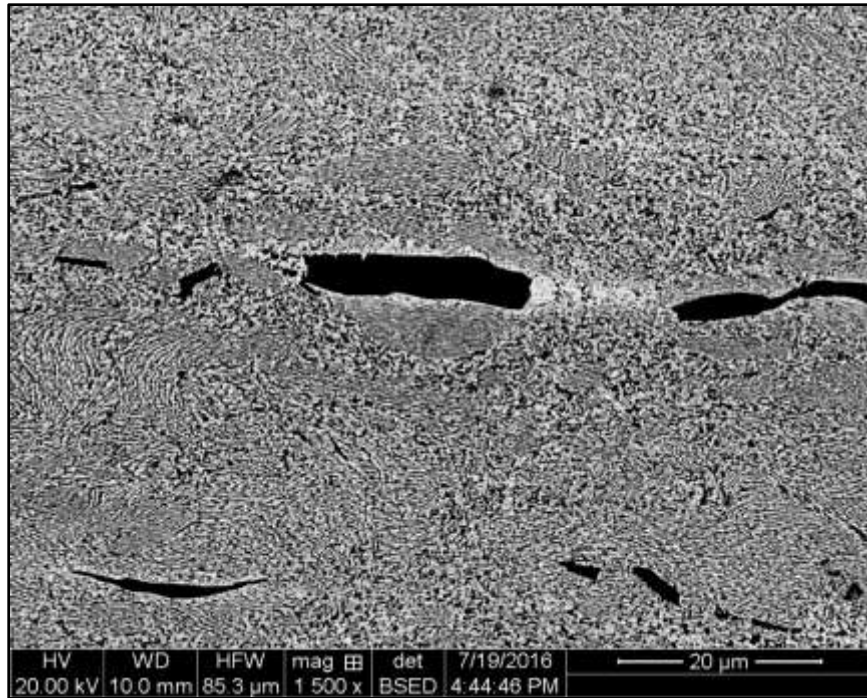


Figure 5-7: BSE image of extrusion 11 U-10Zr rod exhibiting α -U + δ -UZr₂

The extrusion 11 U-10Zr sample was heat treated and examined. The elongated zirconium grains were still present and displayed the same structure. The α -U + δ -UZr₂ phase bulk region underwent considerable restructuring. These grains no longer displayed an elongated structure. Additionally, the zirconium in this region exhibited Ostwald ripening behavior. The zirconium migrated from the bulk phase into the large zirconium grains and also congregated into smaller zirconium rich grains. Because of this, there was a zone around each large zirconium grain that had less zirconium as well as no small zirconium grains. The area between each large zirconium grain and outside of the zirconium free zone was dispersed with smaller zirconium grains. Around each of these smaller zirconium grains was the α -U + δ -UZr₂ phase.

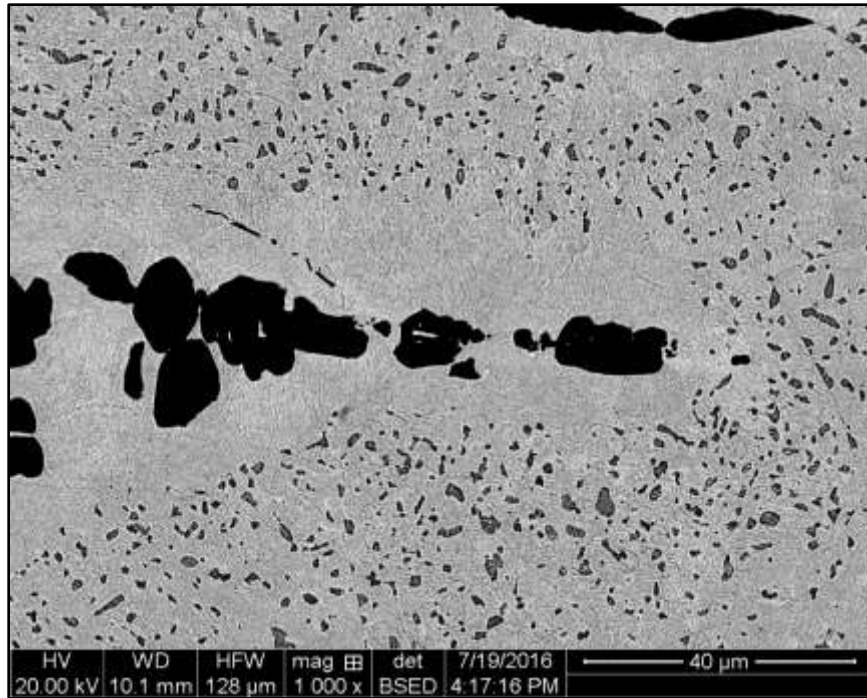


Figure 5-8: BSE image of extrusion 11 U-10Zr rod post heat treatment

5.6 Neutron Diffraction Analysis of Extruded U-10Zr

The neutron diffraction study results, described in Section 4.5, revealed texture in the extruded U-10Zr sample. The α -U phase structure that was present did not persist after heat treatment. This result was expected due to other studies of α -U texture. [46] There was no β -U texture present in the sample. This was expected because the β phase, which is tetragonal, has 30 atoms per unit cell, while the α phase, which is orthorhombic, has 4 atoms per unit cell and the ($\alpha \rightarrow \beta$) phase transformation involves a lot of shuffling of atoms. Moreover, no conclusive orientation relationship between the two phases has been observed. [40] The pole figures of α -U for (100) before and after heating can be seen Figure 5-9.

A unique result from the neutron diffraction study was the texture in $\delta\text{-UZr}_2$ phase which persisted through heat treatment to 800°C . This result has not been previously observed. The pole figures of $\delta\text{-UZr}_2$ for (0001) before and after heating can be seen Figure 5-10.

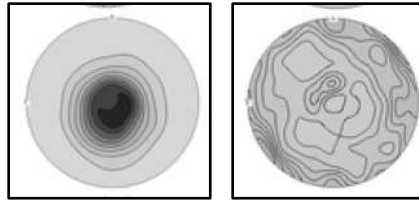


Figure 5-9: Pole figures of $\alpha\text{-U}$ (100): (left) extruded alloy at room temperature (right) at 600°C during cooling. Extrusion direction is at the center.

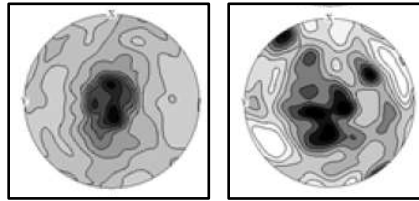


Figure 5-10: Pole figures of $\delta\text{-UZr}_2$ (0001): (left) extruded alloy at room temperature (right) at 600°C during cooling. Extrusion direction is at the center.

5.7 Thermal Conductivity of Low Density Pellets

The thermal conductivity vs percent theoretical density data for all three materials was fitted with both a linear and quadratic equation. This was done using the built in Microsoft Excel least squares functions. The coefficients of the equations can be seen in Table 5-2 and Table 5-3. The R^2 value for the linear fit for each material and both temperatures are all greater than 0.97. The increase in R^2 value when the fit is changed to a quadratic function is minimal. Plots of the linear fits at 30 and 300°C for

the thermal conductivity of U, U-5Zr, and U-10Zr, can be seen with the thermal conductivity data in Figure 5-11, Figure 5-12, and Figure 5-13.

Table 5-2: Linear Fit Coefficients

T [°C]	Material	R ²	X	1
30	U HDH	0.9811	0.4057	-15.7155
	U-5Zr HDH	0.9885	0.3561	-15.0774
	U-10Zr HDH	0.9708	0.2972	-11.3906
300	U HDH	0.9834	0.5057	-19.2064
	U-5Zr HDH	0.9872	0.4570	-19.5682
	U-10Zr HDH	0.9855	0.4337	-17.4423

Table 5-3: Quadratic Fit Coefficients

T [°C]	Material	R ²	X ²	X	1
30	U HDH	0.9864	0.0020	0.1213	-6.0721
	U-5Zr HDH	0.9908	0.0019	0.1107	-7.2263
	U-10Zr HDH	0.9882	-0.0042	0.8516	-29.3117
300	U HDH	0.9852	0.0014	0.2964	-12.1075
	U-5Zr HDH	0.9916	0.0033	0.0224	-5.6671
	U-10Zr HDH	0.9882	-0.0024	0.7506	-27.6875

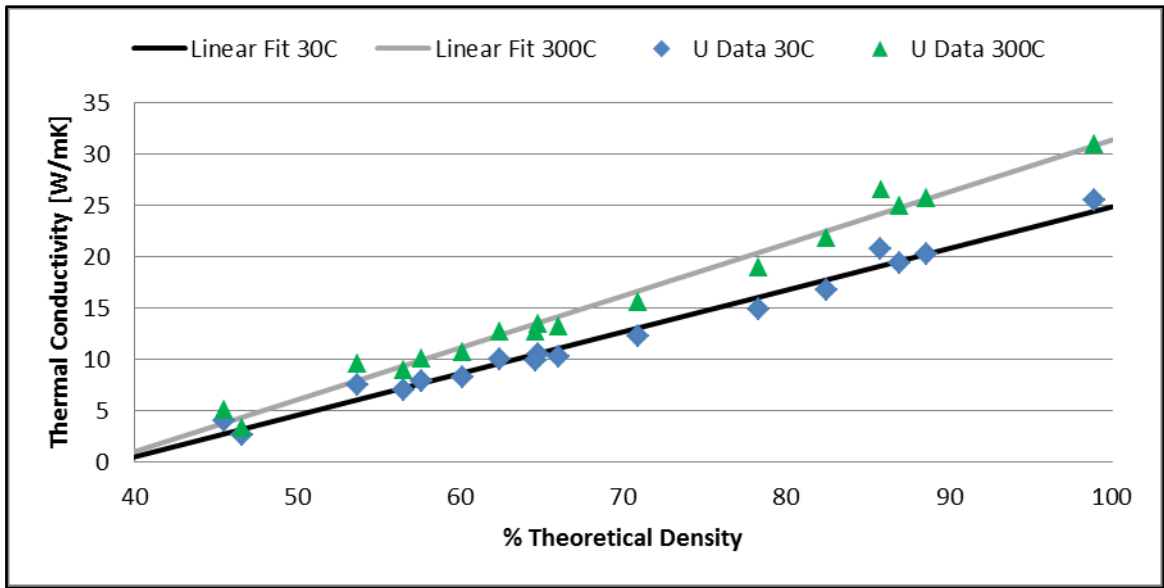


Figure 5-11: Linear fits of thermal conductivity of U at 30 and 300°C

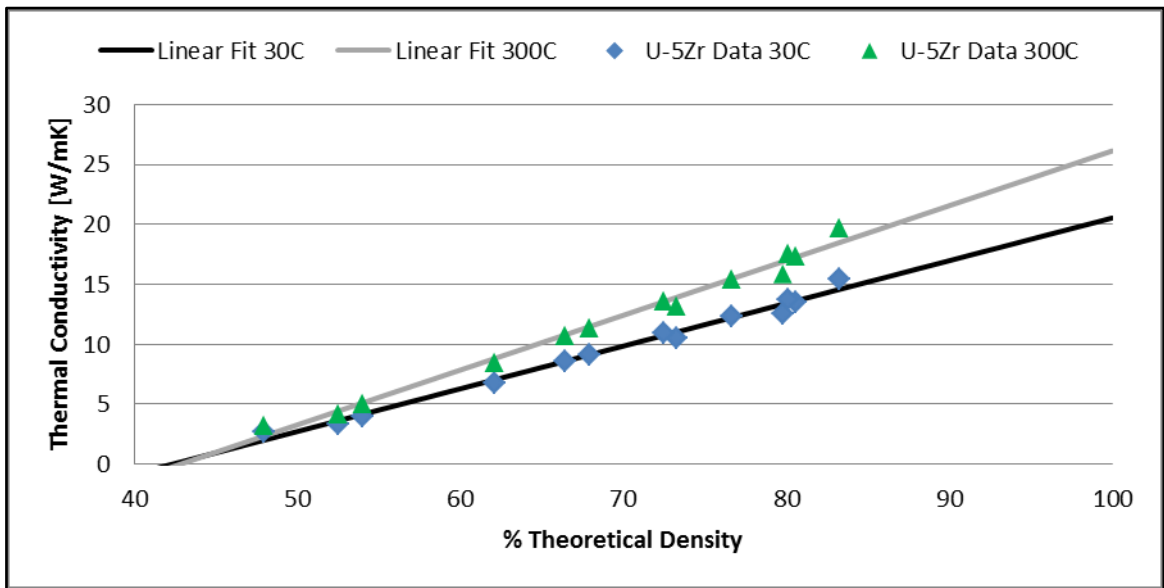


Figure 5-12: Linear fits of thermal conductivity of U-5Zr at 30 and 300°C

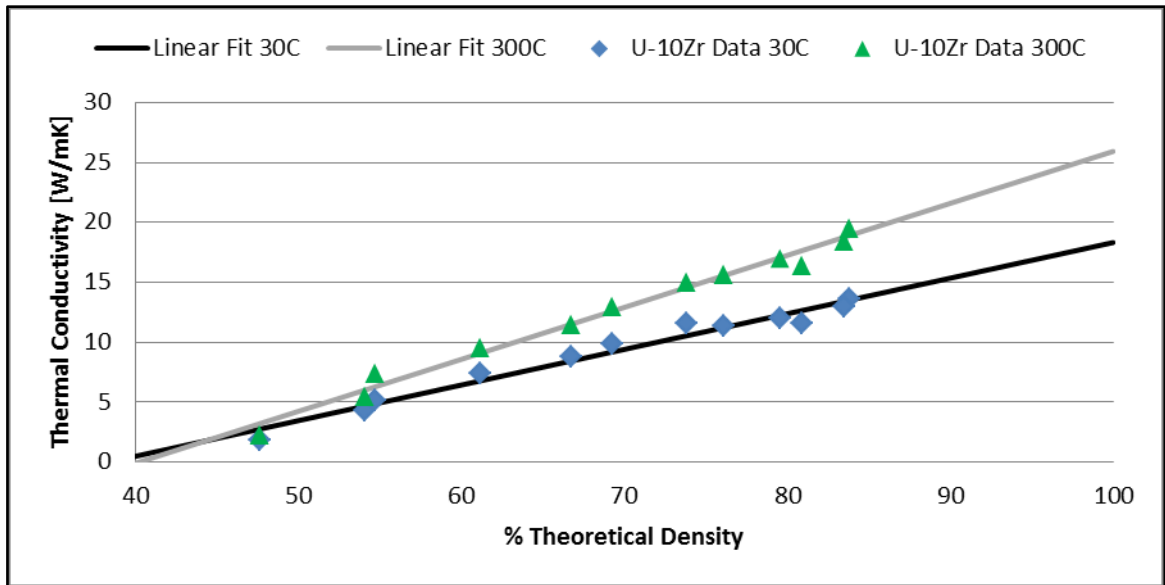


Figure 5-13: Linear fits of thermal conductivity of U-10Zr at 30 and 300°C

For each material, the higher temperature has a higher thermal conductivity. This is to be expected since that is the behavior of the thermal conductivity over a temperature increase for each of these materials. A plot of the theoretical thermal conductivity for 100% TD U, U-5Zr, and U-10Zr, can be seen in Figure 5-14. The gap in thermal conductivity between the high temperature and the low temperature samples becomes larger as the density increases. This implies that at lower densities the increase in temperature has less of an effect on thermal conductivity. Heat in metals is transferred by a combination of phonon and free electrons. The increase in porosity is most likely increasing the scattering of the phonons and free electrons. As temperature is increased phonons and free electrons increase thermal conductivity because the atomic vibration has increased and the average energy of the free electrons is also increased. This effect from the increase in temperature has less of an effect when the scattering is increased due to the increase in porosity. [23] [47]

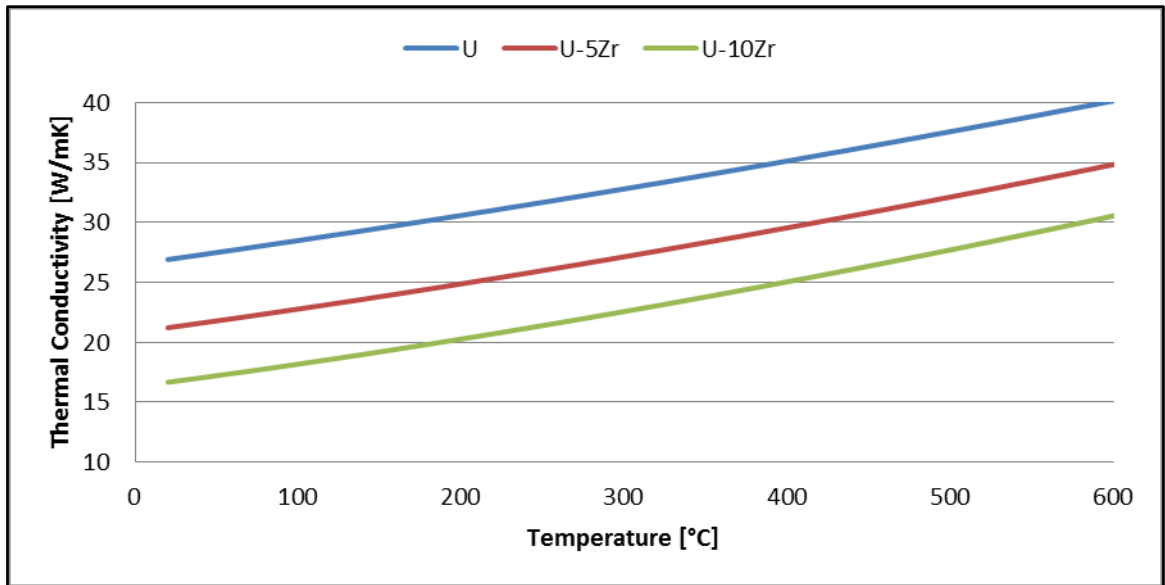


Figure 5-14: Theoretical thermal conductivity for U, U-5Zr, and U-10Zr [23]

The theoretical thermal conductivity for a 100% TD material and the value of the thermal conductivity calculated using the linear fit for 100% TD at 30 and 300°C for U, U-5Zr, and U-10Zr, can be seen in Table 5-4. In this table, the linear fit slightly underestimates the values for U and U-5Zr, but overestimates the value for U-10Zr. The slight inaccuracy of the U-5Zr and U-10Zr comparisons could be due to the highest data points being 84% TD. The highest data point for the U data was 89% TD. Another cause of the difference between the linear fit and the theoretical value for U-5Zr and U-10Zr may be that the theoretical value is derived from a perfectly mixed sample whereas the lower density samples of U-5Zr and U-10Zr were not well mixed. An additional cause may be that some of the pellets contained UO_2 due to the oxidation of the uranium metal. UO_2 has a significantly lower thermal conductivity than U and Zr. The theoretical thermal conductivity at 30°C of a pellet that is 10% UO_2 and 90% U is 25.14 W/mK. This value is very close to the value of 24.85 for the linear fit. For 300°C the theoretical

value of the oxidized mix is 30.07, which is not as close in value to the linear fit value of 31.36 W/mK.

Table 5-4: Comparison of theoretical values and linear fits

Material	K [W/mK] at 30 C			K [W/mK] at 300 C		
	Theoretical	Fit	% Diff	Theoretical	Fit	% Diff
U HDH	27.10	24.85	8.65%	32.80	31.36	4.58%
U-5Zr HDH	21.41	20.54	4.16%	27.14	26.13	3.87%
U-10Zr HDH	16.85	18.32	8.38%	22.57	25.93	12.94%

The thermal conductivity data points for U, U-5Zr, and U-10Zr, along with the linear fits for each data set were plotted with each thermal conductivity model that was previously discussed in the background section of this report. The thermal conductivity models use the theoretical thermal conductivity at 100% theoretical density of U, U-5Zr and U-10Zr. Additionally, the models assume the pores are filled with argon at atmospheric pressure. This assumption is reasonable because the pellets were made in an argon atmosphere and the LFA measurements were also made in an argon atmosphere.

The models for uranium can be seen in Figure 5-15. The models shown in this plot use the thermal conductivity of pure uranium metal, 27.10 W/mK. The EMT most closely replicates the behavior of the U HDH pellets as they increase in density. Figure 5-16 also shows the models with the U HDH data; however, these models use a thermal conductivity value of 25.14 W/mK. This value corresponds to a mixture of 90% uranium metal and 10% UO₂. The EMT model in Figure 5-16 more closely resemble the behavior of the U data than does the EMT model in Figure 5-15.

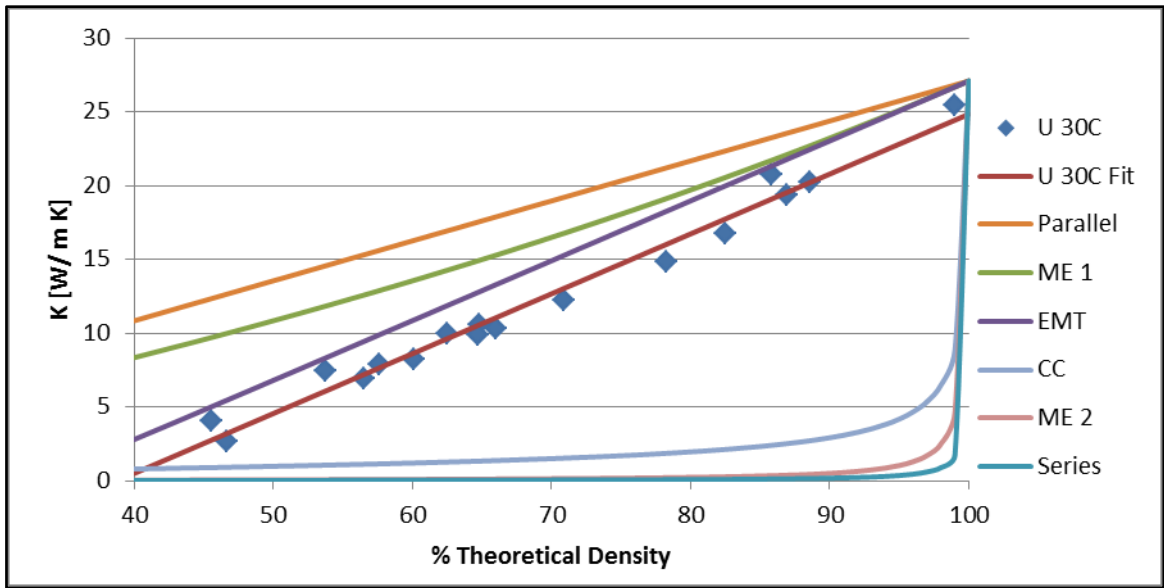


Figure 5-15: Thermal conductivity models for U at 30°C

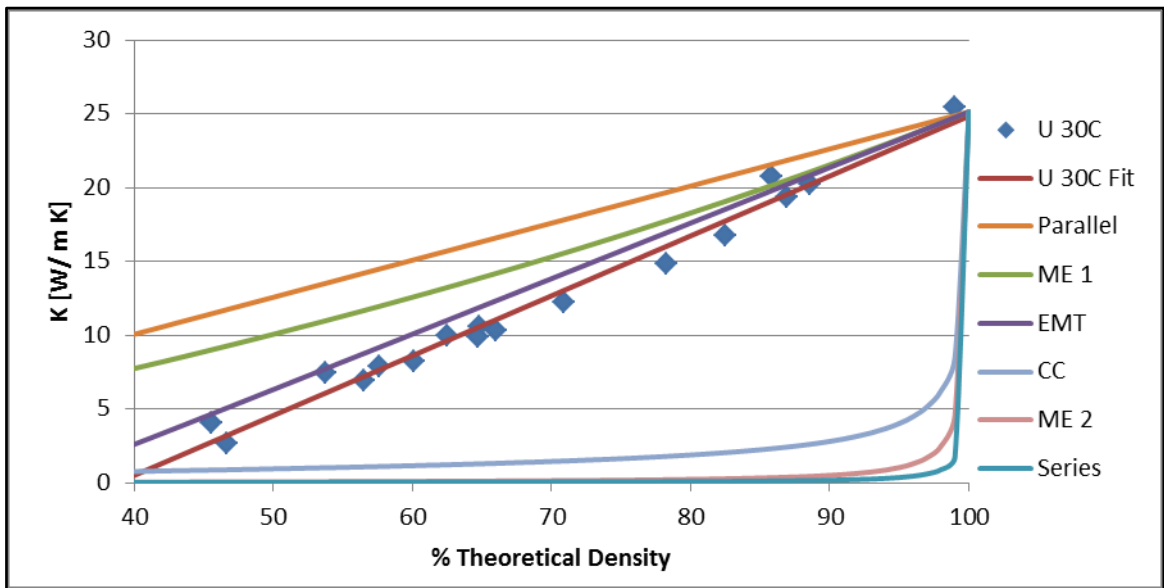


Figure 5-16: Thermal conductivity models for U-10UO₂ at 30°C

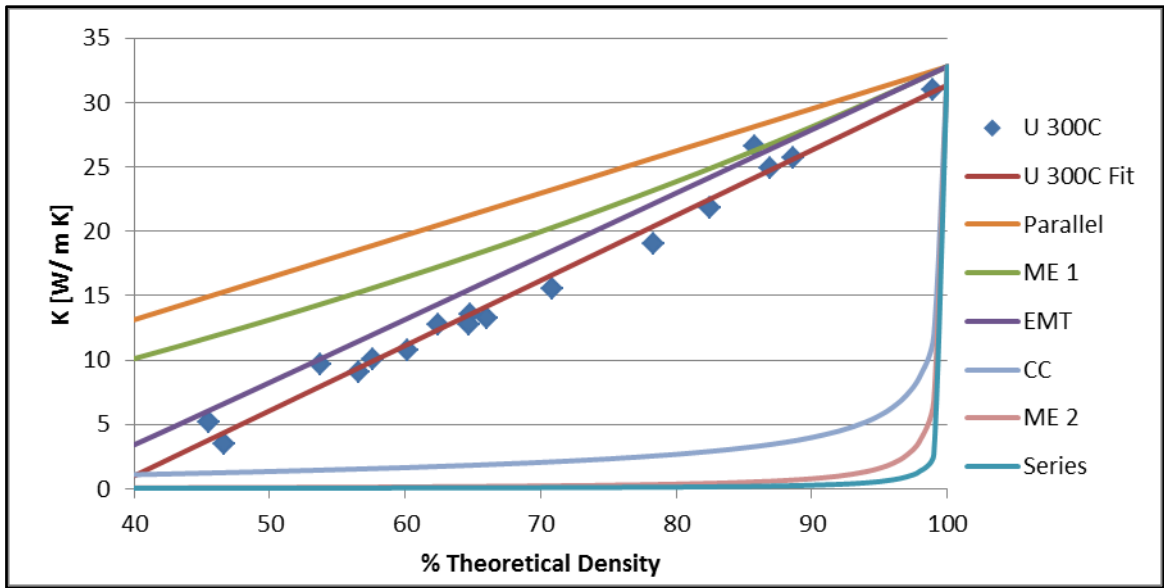


Figure 5-17: Thermal conductivity models for U at 300°C

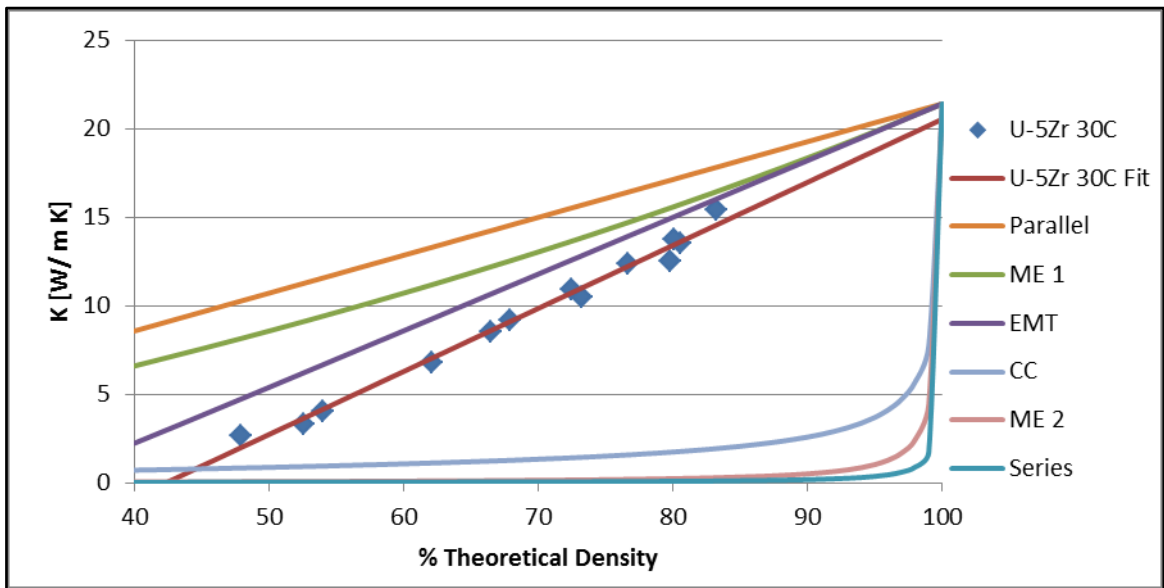


Figure 5-18: Thermal conductivity models for U-5Zr at 30°C

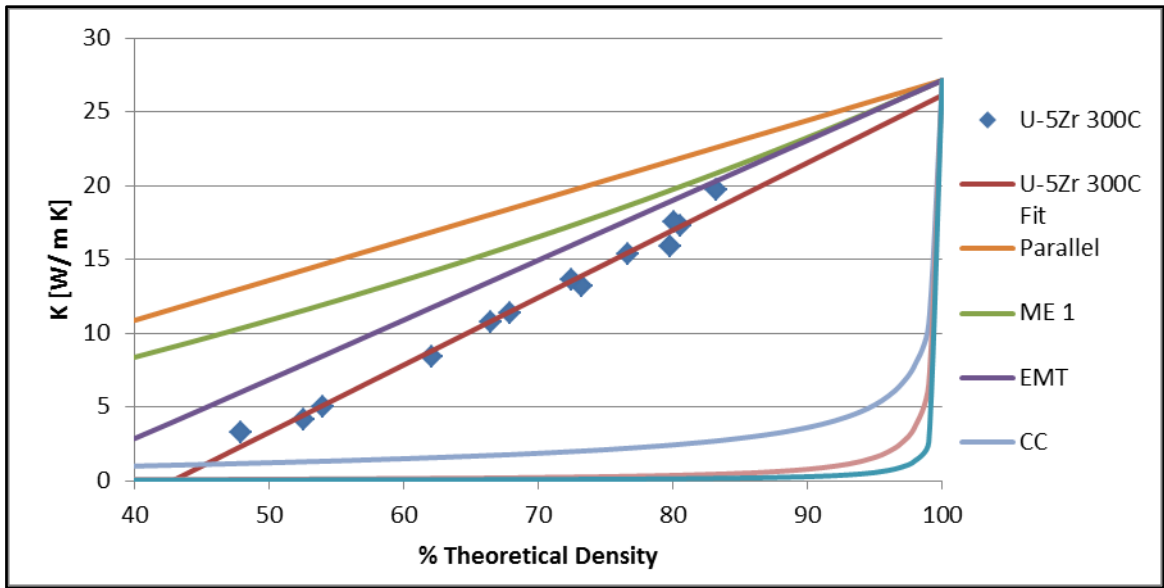


Figure 5-19: Thermal conductivity models for U-5Zr at 300°C

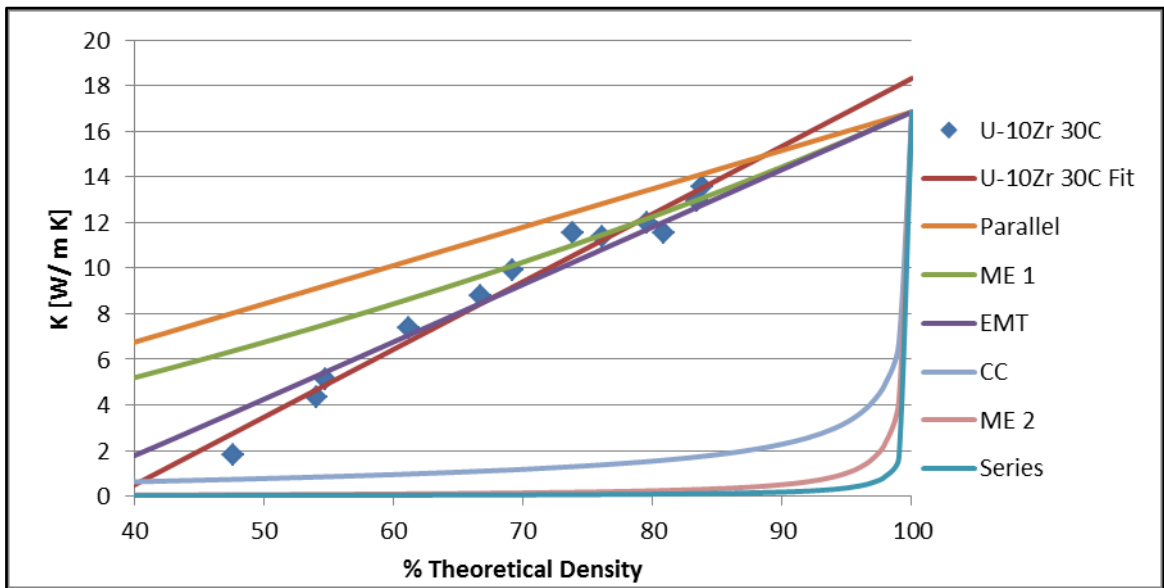


Figure 5-20: Thermal conductivity models for U-10Zr at 30°C

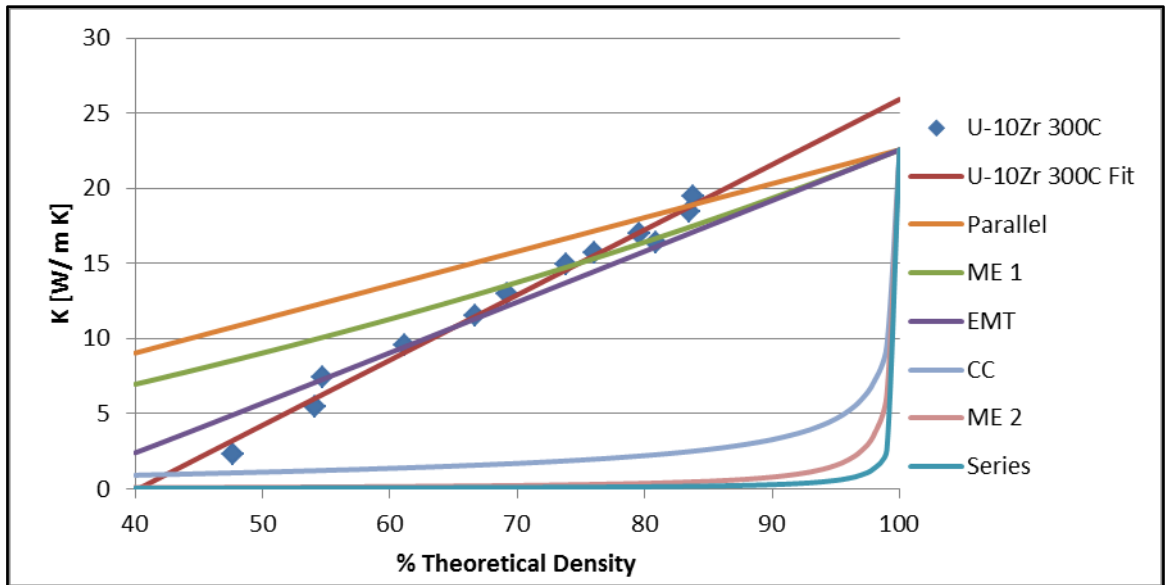


Figure 5-21: Thermal conductivity models for U-10Zr at 300°C

The theoretical models for U-5Zr, the U-5Zr data generated in this report, and the fit for that data are plotted together in Figure 5-18. Again, the EMT model is the model that most closely represents the experimentally generated data. The EMT is a slight overestimation. The difference in the fit and the model is greater at lower densities than at higher densities.

The theoretical models for U-10Zr, the U-10Zr data generated in this report, and the fit for that data are plotted together in Figure 5-20. In this case also, the EMT model is the model that most closely represents the experimentally generated data. However, in this case the linear fit overestimates the thermal conductivity for 100% dense material.

5.8 Microstructure of LFA Pellets

The microstructure of the LFA pellets was, in general, homogenous. However, some early pellets had a higher density region in the central area. This was determined to

be a side effect of the manufacturing process and it was corrected for later pellets. The cause was a slightly higher volume of powder being located in the center of the die before pressing. This can be thought of as a slight hill in the powder caused by pouring the powder in the center of the die. When this mound of powder was pressed down it created a slightly higher density region. This was corrected by tapping the side of the die to flatten out the powder distribution before pressing. The less homogenous pellets did not appear to have an effect on the linear trend of the data. This is likely due to the LFA equipment using a large portion of the surface of the pellet for the light flash.

Each time a pellet was created the manufacturing conditions were purposefully altered. As the sintering temperature was decreased the density of the pellet decreased. As the sintering time was shortened the density also decreased. Alternately, as the sintering time and temperature were increased the density increased. As the density of the pellet increased, the pore sizes decreased and the number of pores decreased. Additionally, the pressing pressure was varied slightly. Two pellets, one pressed at a high pressure and one at a low pressure resulted in the high pressure one having a higher green density. These two pellets sintered together under the same conditions resulted in the pellet with the higher green density having a higher final density. This was only for shorter sintering times; at long sintering times the densities were closer in value. Gathering sintering data was not the primary purpose of this investigation, but this data could be valuable for reproduction of low density pellets so all of the sintering data is organized in tables in Appendix 6.

The pores in the U HDH pellets varied in size but were, in general, around 20 um. At lower densities the pores were flake-like due to the powder used in the manufacturing process being flake-shaped. As the density increased the pores were more spherically shaped. Additionally, many of the smaller pores had closed. The pores did not have a preferential orientation.

The U-5Zr and U-10Zr low density pellets were sintered for short times and at low temperatures. Because of this, the zirconium was segregated from the uranium more than it would be in a melt cast alloy. As the pellets increased in density, the mixing of the zirconium into the uranium increased. The zirconium that was left that had not yet fully dispersed was left in long thin zirconium rich areas. The U-5Zr HDH and U-10Zr HDH pellet pores appeared similar to the U HDH pores. In both cases the pores shrank as the density increased. Despite the dispersion of the zirconium varying from the low density pellets to the high density pellets there did not appear to be an effect on the thermal conductivity.

The pore morphology created in this research project varied based on the density and sintering times. The higher density pellets that had longer sintering times had pores that were more spherical. The microstructures of those pellets were most like the morphology of irradiated nuclear fuel. An example of the pore morphology in irradiated U-10Zr nuclear fuel can be seen in Figure 5-24. The pores in the irradiate fuel are somewhat spherical or elongated but with rounded edges. They vary in size from small to large. Fuel that has a low smear density that undergoes irradiation will results in the interconnection of pores. While the lower density pellets created in this project had sharp

edges, the porosity was in general, interconnected. While the pellets in this report may not be a perfect simulation of swelled nuclear fuel, they certainly are similar in many aspects and the data generated is applicable to nuclear fuel.

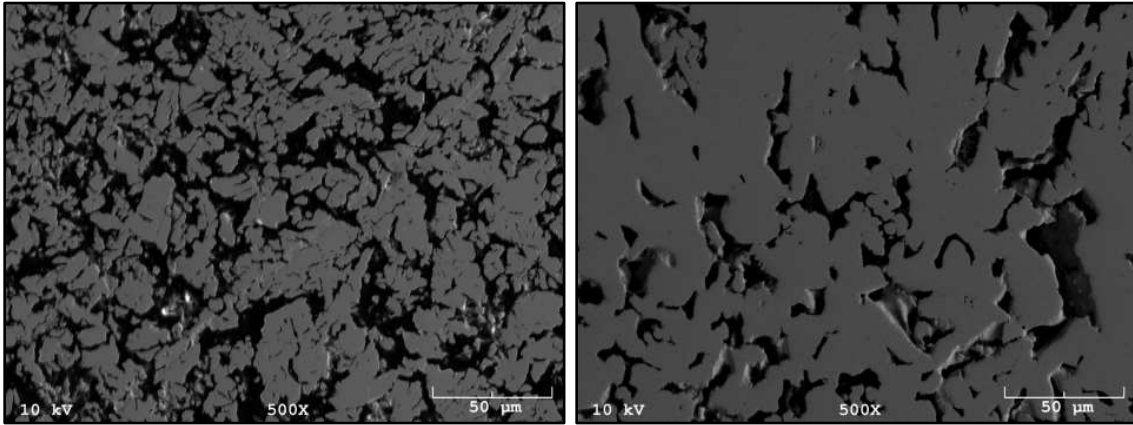


Figure 5-22: BSE images of U HDH pellets: (left) 45.5 %TD (right) 70.9 %TD

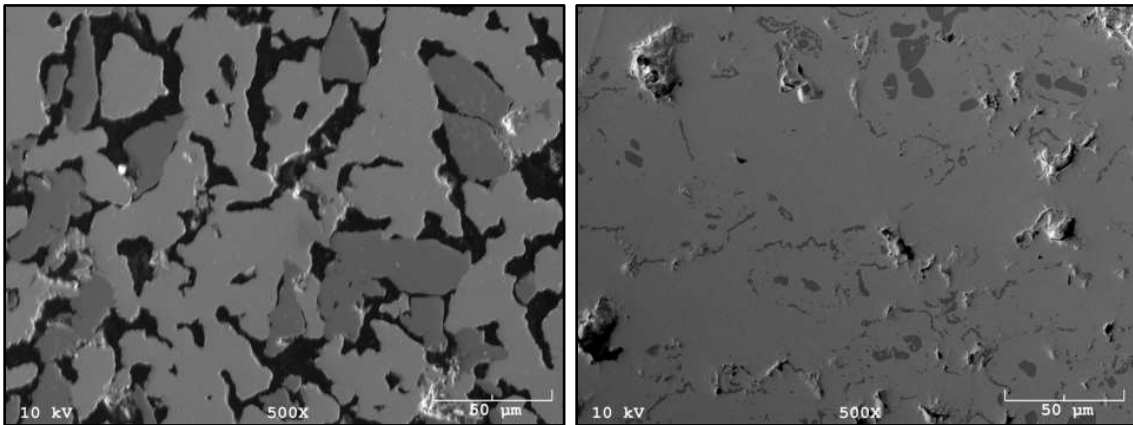


Figure 5-23: BSE images of U-10Zr HDH pellets: (left) 61.2%TD (right) 83.5%TD

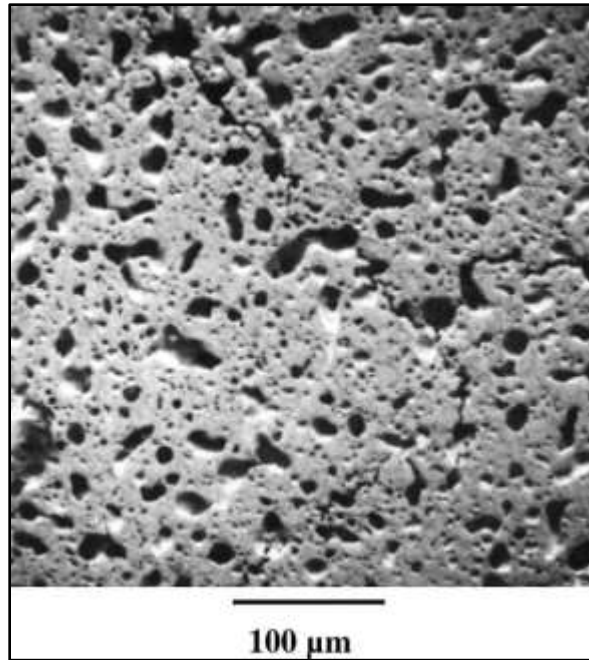


Figure 5-24: Fission gas pore morphology in irradiated U-10Zr fuel. Reprinted with permission from Elsevier.² [2]

² Reprinted from Journal of Nuclear Materials, 392, W. J. Carmack, D. L. Porter, Y. I. Chang, S. L. Hayes, M. K. Meyer, D. E. Burkes, C. B. Lee, T. Mizuno, F. Delage, J. Somers, Metallic fuels for advanced reactors, 139-150, Copyright (2009), with permission from Elsevier

6 CONCLUSION

This engineering investigation of the fabrication process for uranium alloy nuclear fuel forms was completed and the resulting alloys were characterized. The metal fuel alloys investigated in this project were uranium metal, uranium – 5 wt% zirconium (U-5Zr), and uranium – 10 wt% zirconium (U-10Zr). The unifying concept was the creation of low smear density metal fuel alloys and the quantification of processing and/or behavior characteristics. The physical fabricated forms included 1) dense, solid rods up to 10 cm long that could be used in low smear density nuclear fuel applications, 2) extruded tubes up to 10 cm long designed to begin fuel service in constant contact with cladding yet having a very low smear density, and 3) low density pellets ranging from ~45 to ~89 % TD to simulate low density fuel structures. The fabrication methods utilized above included hot uniaxial extrusion of rods and tubes and the cold pressing and sintering of representative pellets.

Uranium and U-10Zr solid metal rods and tubes were extruded at temperatures ranging from 550 to 650°C with extrusion ratios between 4 and 15. Part of the motivation for this portion of the work was to confirm literature values of the extrusion process variables. The process variables characterized during these tests include dynamic force profiles, extrusion ram motion, extrusion temperature, pre-extrusion billet dimensions, and extrusion die design. This information was used to empirically estimate extrusion constants (K), which ranged from 45 to 160 ksi over the course of this study. While the extrusion study was not comprehensive, historical process variables were confirmed to enable effective extrusion results and a self-consistent K data set was

generated. The extrusion constant, K , was found to decrease with increased temperature and with increased reduction ratio.

Future examination of extrusion of uranium and U-10Zr rods and tubes would benefit from high quality tolling sets and other equipment. The study should also include multiple extrusions with the same parameters to show reproducibility. Ideally, many temperatures and reduction ratios would also be examined. In this study the highest reduction ratio was only 15, an investigation of higher ratios would be informative.

The microstructures of the extruded products were studied using scanning electron microscopy (SEM) and neutron diffraction. The neutron diffraction studies were carried out at the Los Alamos Neutron Science Center on the time of flight diffractometer "HIPPO". The specimens exhibited elongated grains in the extrusion direction. The U-10Zr, which is known to have a multiphase structure consisting of isolated α zirconium in a matrix of α uranium plus δ -UZr₂, displayed aligned and elongated α zirconium grains. Neutron diffraction of the U-10Zr samples revealed texture in the α uranium as well as the δ -UZr₂. In the α uranium structure the (100) and (110) poles were oriented in the extrusion direction, and in the δ -UZr₂ structure the (0001) pole became preferentially aligned in the extrusion direction. Heat treatment of the U-10Zr samples to 800°C during neutron diffraction revealed the expected loss of texture within α uranium. However, this was not the case for δ -UZr₂, where the extrusion-induced texture remained after annealing.

To examine low density porous alloys, U, U-5Zr, and U-10Zr, powders were prepared and pellets were pressed and sintered with a range of densities from ~45 to ~89

%TD. In order to create a range of pellet densities, the pressing force was varied from 70 to 140 MPa (10 to 20 ksi), the sintering time was varied from 1 minute to 48 hours, and the sintering temperature was varied from 800 to 1100°C. The nominal pellet dimensions were 2.5 mm thick and 12 mm in diameter.

The powders used in the pellet processing were generated via two methods to create fine flaky powder and larger round microspheres. The first method started with solid uranium and used a hydride/de-hydride process to pulverize the metal and create powder with an average size of 40 μm . The second type of powder was generated using a rotating electrode system wherein U and U alloy microspheres ranging from 50 to 300 μm were manufactured.

The resulting alloy microstructures were characterized via scanning electron microscopy. The structures of the pellets were typically homogenous. The pores decreased in size and in number as the density was increased through increased sintering times and temperatures. The dispersion of the zirconium into the uranium also increased with increased sintering times and temperatures. The microstructures created were similar to the microstructures of fuel that has undergone irradiation swelling. Therefore, the porous pellets may be considered approximate analogs of fuel rods and tubes after swelling or of low-density porous fuel structures created specifically for implementation as low density nuclear fuel. Note that the data measured here represents a separate effect measurement focused on porosity and the data do not include the impact of effects due to irradiation and burnup-induced fission product accumulation.

In addition to microstructural measurements, the porosity-dependent thermal properties of the alloys were quantified by measuring the thermal diffusivity of all of the pellets in the temperatures range of 20 to 300°C. Thermal diffusivity was measured using a LFA 447 Nanoflash manufactured by Netzsch Instruments. As sample porosity increased, the variation of diffusivity with porosity was observed to decrease linearly over the entire sample set. Diffusivity values for uranium ranged from 10.7 mm²/s at 88.6 %TD and 300°C to 2.54 mm²/s at 46.6 %TD and 30°C. The low density samples provided first-of-a-kind data for these uranium fuel alloys and the behavior corresponded well with literature values for high density samples of the same materials.

The data from the low density pellets was used to create an empirical model to relate the density and thermal conductivity for U, U-5Zr, and U-10Zr. Six structural models for heat transfer in a porous medium were investigated. The predicted values from the effective medium theory model were found to correlate well with the empirical relationship developed for each material that was investigated. This model will assist in future attempts of simulation of nuclear fuel for nuclear reactors.

Future work related to the thermal conductivity of porous U, U5Zr, and U-10Zr, should include thermal diffusivity measurements at higher temperatures to be more relevant to reactor operating temperatures and accident scenarios. Additionally, a large number of samples and a wide range of densities should be studied to have a representative data set.

REFERENCES

- [1] K. Weaver, "A Once-Through Fuel Cycle for Fast Reactors," *Journal of Engineering for Gas Turbines and Power*, vol. 132, 2010.
- [2] W. J. Carmack, "Metallic fuels for advanced reactors," *Journal of Nuclear Materials*, vol. 392, pp. 139-150, 2009.
- [3] L. C. Walters, "Thirty years of fuels and materials information from EBR-II," *Journal of Nuclear Materials*, vol. 270, pp. 39-48, 1999.
- [4] G. L. Hofman, "Metallic Fast Reactor Fuels," *Progress in Nuclear Energy*, vol. 31, pp. 83-110, 1997.
- [5] C. Trybus, J. E. Sanecki and S. P. Henslee, "Casting of Metallic Fuel Containing Minor Actinides," *Journal of Nuclear Materials*, vol. 204, pp. 50-55, 1993.
- [6] T. Ogata, "Chapter 3.01: Metal Fuel," in *Comprehensive Nuclear Materials*, Waltham, MA, Elsevier, 2012, pp. 1-40.
- [7] J. Aris, "Maching of Uranium and Uranium Alloys," *Metals Handbook*, vol. 16, pp. 874-878, 1990.
- [8] J. Hurst and A. Read, "Maching Depleted Uranium," Oak Ridge Y-12 Plant, Oak Ridge, Tennessee, 1972.
- [9] M. Bauser, G. Saucer and K. Siegert, *Extrusion*, 2nd ed., Materials Park, Ohio: ASM International, 2006.
- [10] D. Burkes, "A US perspective on fast reactor fuel fabrication technology and

experience part I: metal fuels and assembly design," *Journal of Nuclear Materials*, vol. 389, pp. 458-469, 2009.

- [11] W. Wilkinson, *Uranium Metallurgy*, New York: John Wiley & Sons, 1962.
- [12] R. I. Sheldon and D. E. Peterson, "The U-Zr (Uranium-Zirconium) system," *Bulletin of Alloy Phase Diagrams*, vol. 10, no. 2, pp. 165-171, 1989.
- [13] Chubb, Muehlenkamp and Schwoppe, "A Hot-Hardness Survey of the Zirconium-Uranium System," Battelle Memorial Institute, Columbus, Ohio, 1953.
- [14] A. Bauer, "An Evaluation of the Properties and Behavior of Zirconium-Uranium Alloys," Battelle Memorial Institute, Columbus, Ohio, 1959.
- [15] Yamada and Yamanaka, "Mechanical Properties of (U,Ce)O₂," *Journal of Alloys and Compounds*, Vols. 271-273, pp. 697-701, 1998.
- [16] J. K. Fink, "Thermophysical Properties of Uranium Dioxide," *Journal of Nuclear Materials*, vol. 279, no. 1, pp. 1-18, 2000.
- [17] G.-Y. Huang and B. D. Wirth, "First-principles study of bubble nucleation and growth behaviors in alpha U-Zr," *Journal of Physics: Condensed Matter*, vol. 24, 2012.
- [18] P. K. Saha, *Aluminum Extrusion Technology*, Materials Park: ASM International, 2000.
- [19] L. Cornwall, K. Hartwig and R. Goforth, "The equal channel angular extrusion process for materials processing," *Materials Characterization*, vol. 37, no. 5, pp. 295-300, 1996.

- [20] F. Lenel, *Powder Metallurgy: Principles and Applications*, 1st ed., Princeton, NJ: Metal Powder Industries Federation, 1980.
- [21] R. German, *Sintering Theory and Practice*, New York: John-Wiley & Sons, 1996.
- [22] M. Waldron and B. Daniell, *Sintering*, London: Heyden & Son Ltd, 1978.
- [23] Y. S. Kim and G. L. Hofman, "AAA Fuels Handbook," Argonne National Laboratory, Argonne, Illinois, 2003.
- [24] Chen and Saxena, "Thermal conductivity of argon in the temperature range 350 to 2500 K," *Molecular Physics*, vol. 29, no. 2, pp. 455-466, 1975.
- [25] J. Wang, J. K. Carson, M. F. North and D. J. Cleland, "A new approach to modelling the effective thermal conductivity of heterogeneous materials," *International Journal of Heat and Mass Transfer*, vol. 49, pp. 3075-3083, 2006.
- [26] J. Wang, J. K. Carson, M. F. North and D. J. Cleland, "A new structural model of effective thermal conductivity for heterogeneous materials with co-continuous phases," *International Journal of Heat and Mass Transfer*, vol. 51, pp. 2389-2397, 2008.
- [27] O. Wiener, "Die theorie des Mischkorpers fur das Feld der Statonaren Stromung. I. Die Mittelwertsatze fur Kraft, Polarisation und Energie, Der Abhandlungen der Mathematisch-Physischen Klasse der Konigl, Sachsischen Gesellschaft der Wissenschaften," vol. 32, pp. 509-604, 1912.
- [28] Carson, Lovatt, Tanner and Cleland, "Thermal conductivity bounds for isotropic, porous materials," *Internation Journal of Heat and Mass Transfer*, vol. 48, pp.

2150-2158, 2005.

- [29] R. J. Jansen, "Drilling Uranium Billets on a Leblond-Carlstedt Rapid Borer," Technical Division National Lead Company of Ohio, Cincinnati, Ohio, 1963.
- [30] H. Hausner and J. Zambrow, "The Powder Metallurgy of Uranium," *Nuclear Science and Engineering*, vol. 1, no. 1, pp. 92-101, 1956.
- [31] D. Garnetti, *Uranium Powder Production via Hydride Formation and Alpha Phase Sintering of Uranium and Uranium-zirconium Alloys for Advanced Nuclear Fuel Applications*, College Station, TX: Texas A&M University, 2009.
- [32] C. Thompson, *A Rotating Electrode System for the Generation of Metal Alloy Microspheres*, College Station, TX: Texas A&M University, 2012.
- [33] B09.04, "ASTM B962-15, Standard Test Methods for Density of Compacted or Sintered Powder Metallurgy (PM) Products Using Archimedes' Principle," ASTM International, West Conshohocken, PA, 2015.
- [34] Takahashi, Yamamoto and Ohsato, "Heat Capacities of uranium-zirconium alloys from 300 to 1100 K," *Journal of Nuclear Materials*, vol. 167, pp. 147-151, 1989.
- [35] J. A. Cape and G. W. Lehman, "Temperature and Finite Pulse-Time Effects in the Flash Method for Measuring Thermal Diffusivity," *Journal of Applied Physics*, vol. 34, 1963.
- [36] A. M. Kelly, R. D. Field and D. J. Thoma, "Metallographic Preparation Techniques for U-6wt%Nb," *Journal of Nuclear Materials*, vol. 429, pp. 118-127, 2012.
- [37] L. L. S. V. H. R. Wenk, *Nuclear Instruments and Methods in Physics Research*

Section A: Accelerators, Spectrometers, Detectors and Associated Equipment, vol. 515, pp. 575-588, 2003.

- [38] L. L. S. C. V. H. R. Wenk, *Powder Diffraction*, vol. 25, pp. 283-296, 2010.
- [39] H. S. R. Hielscher, *Journal of Applied Crystallography*, vol. 41, pp. 1024-1037, 2008.
- [40] A. Goldberg and T. B. Massalski, "Phase Transformations in the Actinides," in *Proceedings of the Fourth International Conference on Plutonium and Other Actinides*, Santa Fe, NM, 1970.
- [41] J. R. Davis, *Copper and Copper Alloys*, Materials Park, OH: ASM International, 2001.
- [42] L. G. Wexlin, "Elevated-Temperature Mechanical Properties of Uranium With Various Processing Histories," Clearinghouse for Federal Scientific and Technical Information, Springfield, VA, 1968.
- [43] Saller, Dickerson and Murr, "Uranium Alloys for High-Temperature Application," Batteller Memorial Institute, Columbus, Ohio, 1956.
- [44] H. H. Chiswik, A. E. Dwight and L. T. Lloyd, "Advances in the Physical Metallurgy of Uranium and its Alloys," in *Second United Nations International Conference on the Peaceful Uses of Atomic Energy*, Lemont, Illinois, 1958.
- [45] Carloni and Lewis, "Effect of Transfer Time on the Recrystallization Behavior of Beta-Cooled Uranium," Research Department, Bridgeport Brass Company, Bridgeport, Connecticut, 1959.

- [46] R. Anderson, D. Carpenter and S. Rogers, Phase and texture analysis of the alpha-phase extruded uranium-2. 4 weight percent niobium alloy, 1981.
- [47] W. D. Callister, Material Science and Engineering An Introduction, 7th ed., John Wiley & Sons, 2007.
- [48] D. Keiser, "ANL-NT-240," 2006.
- [49] R. Pahl, C. Lahm and S. Hayes, *Journal of Nuclear Materials*, vol. 204, 1993.
- [50] S. Irukuvarghula, B. Blamer, S. Ahn, S. Vogel, A. Losko and S. McDevitt, "Texture evolution during annealing of hot extruded U-10wt%Zr alloy by in situ neutron diffraction," *Journal of Nuclear Materials*, 2017.

APPENDIX 1

CERTIFICATIONS

This appendix includes copies of the certifications of compliance and accuracy for data collection equipment used in this project: load cell, thermocouples, thermocouple data logger, calipers, and 200 gram weight standard.

Certificate of Compliance
LOAD CELL CENTRAL
216 MAIN ST.
MONROETON, PA.
1-800-LOADCELL

The material and parts supplied on this order conform to the applicable specifications and drawings. Inspection and/or test equipment used on these materials are in current calibration and are traceable to the National Institute of Standards. Documentation in the form to support this certification are on file and available for review upon request.

Load Cell model Number/Capacity: LCC SCS3-200K 200,000LB S/N: 42671
Indicator Model Number: WEIGTRHSENSE OM-232-10 S/N: 60081
F.S. MV Output: 3 OHM Resistance: 350
Standard Model/Cap/Serial No. REVERE S/N BX1523 Cal. Date: 01/12/11
NIST Traceable No: REPORT# BX1523A1211
Ambient Temperature: 76° Relative Humidity: 48%

<u>STD FORCE (LBS)</u>	<u>% OF F.S.</u>	<u>INDICATOR (LBS)</u>
0	0	0
40000	20	39990
80000	40	79980
120000	60	119970
160000	80	159950
200000	100	199970
0	0	0


Certified By:  Date: 10/01/2012
Calibration Date: 10/01/2012 Due Date: 10/01/2013

Figure A1-1: Certificate of compliance for the load cell used in this project


CERTIFICATE OF CALIBRATION/COMPLIANCE			
Serial # :	42671	Wired :	
Model # :	SCS3-200K	Excitation + :	A & B
Capacity :	200K	Excitation - :	C & D
Actual Full Scale :	3.0003 MV/V	Signal + :	F
Zero Balance :	1.0 % FS	Signal - :	E
Linearity : ±	.10%	Sense + :	
Hysteresis : ±	.08%	Sense - :	
Input Resistance :	350	Safe Overload :	150% of Capacity
Output Resistance :	350	Insulation Res. : >	5000 Megohms @ 50 VD
Compensated From : 0 Thru 110 deg F			
The reference part was built in conformance with applicable specifications and drawings. Calibration was performed using traceable standards from National Institute of Standards and Technology.			
Technician:		Date:	10/2/2012
	Garry Case		

Figure A1-2: Certificate of calibration for the load cell used in this project

Certificate of Calibration

Customer: TEXAS A&M UNIVERSITY
Customer P.O.: BB082312
W.O. Number: 209926596
Test Item: KMQSS-040U-24
Lot Number: N/A
Report Number: OM-120911614
A.R. Number: 209-4913

Cal-3

Omega Engineering, Inc. certifies that the above instrumentation has been calibrated and tested to **meet or exceed** the published specifications. This calibration and testing was performed using instrumentation and standards that are traceable to the **National Institute of Standards and Technology**. Calibration has been performed in compliance with ISO 10012-1, ISO 9001, ANSI/NCSL Z540-1-1994, ANSI MC 96.1 and ASTM E 230. This Certificate/Report shall not be reproduced, except in full, without written consent of Omega Engineering Inc.

CALIBRATION INFORMATION

Calibration Date:	9/11/12	Temperature:	22 C
Calibration Due:	Per System Application	Relative Humidity:	35%
Procedure Used:	QAP-2100		
System Uncertainty:	The maximum calibration uncertainty is calculated to be 0.3 C in the range of -80 C to 500 C and 0.55 C in the range of 500 C to 1350 C.		

STANDARDS USED FOR CALIBRATION

Model Number	Serial Number	Cal Due Date	NIST Numbers
AGILENT 34401A	US36127770	29-NOV-12	775585-6256307:1299497961
DP251	1287-022-459	22-MAR-13	CAL103220
TRC-III	I-0017	04-OCT-12	OM-120210102
GE T100-450-S (PRP-4)	4827B-01	25-OCT-12	CAL107461



Metrology Technician:



Quality Assurance Inspector:

Page 1 of 2

Figure A1-3: Certificate of calibration for a thermocouple used in this project page 1

Probe Number	Nominal Temperature	Actual Test Temperature	Indicated Temperature
1	100 C	100.04 C	99.24 C
1	200 C	200.05 C	199.75 C
1	400 C	400.09 C	399.34 C

Figure A1-4: Certificate of calibration for a thermocouple used in this project page 2

Certificate of Calibration

Customer: TEXAS A&M UNIVERSITY
Customer P.O.: BB011513
W.O. Number: 301905886
Test Item: KMQSS-040U-24
Lot Number: N/A
Report Number: OM-130213084
A.R. Number: N/A

Cal-3

Omega Engineering, Inc. certifies that the above instrumentation has been calibrated and tested to **meet or exceed** the published specifications. This calibration and testing was performed using instrumentation and standards that are traceable to the **National Institute of Standards and Technology**. Calibration has been performed in compliance with ISO 10012-1, ISO 9001, ANSI/NCSL Z540-1-1994, ANSI MC 96.1 and ASTM E 230. This Certificate/Report shall not be reproduced, except in full, without written consent of Omega Engineering Inc.

CALIBRATION INFORMATION

Calibration Date: 2/13/13
Calibration Due: Per System Application
Procedure Used: QAP-2100
System Uncertainty: The maximum calibration uncertainty is calculated to be 0.3 C in the range of -80 C to 500 C and 0.55 C in the range of 500 C to 1350 C.

Temperature: 22 C
Relative Humidity: 35%

STANDARDS USED FOR CALIBRATION

Model Number	Serial Number	Cal Due Date	NIST Numbers
AGILENT 34401A	US36127770	29-NOV-13	775685-6450303:1331459975
TRC-III	I-0012	19-MAR-13	OM-120210102
FLUKE 2562	B11094	22-MAR-13	B2312024
FLUKE 5609	01513	22-MAR-13	B2305016



Metrology Technician:



Quality Assurance Inspector:

Page 1 of 2

Figure A1-5: Certificate of calibration for a thermocouple used in this project page 1

Continued Report Number: OM-130213084

Probe Number	Nominal Temperature	Actual Test Temperature	Indicated Temperature
1	100 C	100.01 C	99.48 C
1	200 C	200.01 C	200.05 C
1	400 C	400.00 C	400.29 C

Figure A1-6: Certificate of calibration for a thermocouple used in this project page 2

Certificate of Calibration

Customer: TEXAS A&M UNIVERSITY
Customer P.O.: BB082312
Instrument: Omega HH306A
Work Order Number: 208904829
Description: DIGITAL THERMOMETER
Serial Number: 120403691
Equipment I.D.#: 208904829
A.R. Number:

Cal-3

Omega Engineering, Inc. hereby certifies that the above instrumentation has been calibrated and tested to **meet or exceed** the published specifications. This calibration and testing was performed using instrumentation and standards that are traceable to the **National Institute of Standards and Technology**. Omega Engineering, Inc. is in compliance with ISO 10012-1, ISO 9001 and ANSI/NCSL Z540-1-1994. This certificate shall not be reproduced, except in full, without the written consent of Omega Engineering, Inc.

CALIBRATION INFORMATION

Cal Date: 28-Aug-12 Temperature: 22 C ± 5 C
Cal Due Date: 28-Aug-13 Humidity: Below 80%

Absolute Uncertainty: 0.1 C

Comments:

Pass: Y Technician: Canrobert Antoine Seals OK: Yes
Procedure: QAP-2100 Certificate #: 121757

STANDARDS USED FOR CALIBRATION

Asset Number	Description	NIST Traceable Number	Cal. Date	Due Date
01010	Fluke 5700A Multicalibrator	775585-6255307:1343110085	10-Aug-12	10-Feb-14
01158	Omega TRCIII Ice Point Cell	OM-120210102	22-Aug-12	29-Aug-12


Metrology Technician:


Quality Assurance Inspector:

Figure A1-7: Certificate of calibration for the thermocouple data logger used in this project page 1

Calibration Results

Customer:	TEXAS A&M UNIVERSITY	Result:	PASS
P.O. Number:	BB082312	Cal Date:	28-Aug-12
Work Order #:	208904829	Cal Due Date:	28-Aug-13
Instrument:	Omega HH306A	Technician:	Canrobert Antoine
Description:	DIGITAL THERMOMETER	Temperature:	22 °C ± 5 °C
Serial Number:	120403691	Humidity:	Below 80%
Equipment I.D.#:	208904829	Condition F/L:	FOUND-LEFT
A.R. Number:		Procedure:	QAP-2100
		Certificate #:	121757

Standards Used

Asset #	Description	NIST Traceable Number	Cal Date	Due Date
01010	Fluke 5700A Multicalibrator	775585-6255307:1343110085	10-Aug-12	10-Feb-14
01158	Omega TRCIII Ice Point Cell	OM-120210102	22-Aug-12	29-Aug-12

Test Data

Test Description	True Value	Test Result	Lower limit	Upper limit	
Thermocouple Input 1					
-100.0 DegreeKC		-100.0	-101.2	-98.8	Pass
750 DegreeKC		749	747	753	Pass
1360 DegreeKC		1359	1356	1364	Pass
Thermocouple Input 2					
-100.0 DegreeKC		-100.0	-101.2	-98.8	Pass
750 DegreeKC		749	747	753	Pass
1360 DegreeKC		1360	1356	1364	Pass

End of Test Data

Figure A1-8: Certificate of calibration for the thermocouple data logger used in this project page 2



Certificate of Calibration



NAME & ADDRESS: MC MASTER GARR SUPPLY CO. ATLANTA, GA.	CONDITION: NEW
CODE NUMBER: 500-195-20	DESCRIPTION: DIGIMATIC CALIPER
SERIAL NUMBER: 11377604	CONTROL NO.: 576037
I.D. No.: N/A	RANGE: 0.000" - 4.000"

RANGE (inches)	OUTSIDE ERROR (inches)	INSIDE ERROR (inches)
1.000	0.0000	0.0000
2.000	0.0000	0.0000
4.000	0.0000	0.0000

DEPTH ERROR: 0.0000"
STEP ERROR: 0.0000"

Measurement uncertainty: ± (200 + 10L) µm where L= Nominal length in inches.
This uncertainty represents an expanded uncertainty expressed at approximately the 95% confidence level using a coverage factor of k=2.
Procedure used: CLTM-7 REV. D. "As-found" = "As-left" data.

This is to certify that the gages listed have been compared with Mitutoyo Masters, which are traceable to the National Institute of Standards and Technology, at a measuring temperature of 20° C ± 1.00° C, RH 30% to 50%.

Calibrated by: [Signature] Date: NOVEMBER 17, 2011 NIST Number: Test No. 48528223-00
Jerry Wieland, Calibration Technician Date put in to service:

THIS CERTIFICATE SHALL NOT BE REPRODUCED EXCEPT IN FULL WITHOUT THE WRITTEN PERMISSION OF THE MITUTOYO CALIBRATION LAB.
MITUTOYO AMERICA CORP. CALIBRATION LAB., 2025 TONNE ROAD, ELK GROVE VILLAGE, IL 60007
PHONE (847) 593-7750 - FAX (847) 593-7758

Page 1 of 1

Figure A1-9: Certificate of calibration for the calipers used in this project

STATEMENT OF ACCURACY

We certify that the weight/weight set listed below meets the specifications for the type and class listed.

Weight Range: 200g
 Serial Number: 1000044561
 Date: 10-10-11

Type I II

Class:
 Ultra Class
 ANSL/ASTM 0 1 2 3 4 5 6 7
 OIML E1 E2 F1 F2 M1 M2
 NIST Class F

Date Weight(s) placed into service by customer: _____

Material/Density at 20°C:
 Stainless Steel 7.85g/cm³
 Stainless Steel 7.95g/cm³
 Stainless Steel 8.03g/cm³
 Aluminum 2.7g/cm³
 Cast Iron 7.2g/cm³

TROEMNER
 201 Wolf Dr. • P.O. Box 87
 Thorofare, NJ 08086-0087 USA
 Phone: (856) 686-1600
 Fax: (856) 686-1601
 http://www.troemner.com
 Email: troemner@troemner.com

TROEMNER
 LABORATORIES

Joseph Moran
 Joseph Moran
 DC Metrology Manager

Wilbert D. Abele
 Wilbert D. Abele
 President

6-059-BF (Rev 9/10)

Figure A1-10: Certificate of calibration for the weight standard used in this project

APPENDIX 2

BILLET DETAILS

This appendix has a table of the billets created for use in extrusions. The first column shows which extrusion the billet was used in. The next 2 columns are the masses of the initial material used in the melt. The next column is the exact weight percent based on the masses in the previous 2 columns. The next three columns are the height, diameter, and mass of the billet at the time of the extrusion. The mass at the time of extrusion is less for several reasons. Before extrusion, the billet is sanded and pickled in nitric acid as mentioned in previous sections. Additionally, for some extrusions the top of the billet was cut off.

Table A2-1: Details of Billets Used in Extrusion Experiments

Ext#	U [g]	Zr [g]	Wt% Zr	H [in]	D [in]	Billet Mass [g]
1	73.06	8.19	10.08%	0.63	0.76	72.76
2	76.28	8.46	9.98%	0.61	0.78	81.03
3	86.58	9.64	10.02%	0.63	0.77	82.41
4	68.85	7.12	9.37%	1.25	0.52	70.00
5	93.39	10.55	10.15%	0.97	0.76	103.14
6	93.30	10.28	9.92%	0.67	0.90	102.77
7	96.15	0.00	0.00%	0.77	0.72	83.93
8	100.13	0.00	0.00%	0.78	0.74	87.84
9	104.33	0.00	0.00%	0.56	0.91	95.78
10	67.00	0.00	0.00%	1.06	0.51	50.84
11	134.69	15.00	10.02%	0.92	0.91	146.08
12	144.30	0.00	0.00%	0.77	0.91	144.10
13	114.89	12.72	9.97%	0.86	0.90	127.25

APPENDIX 3

EXTRUSION TOOLING DESIGNS

This appendix contains drawings of some tooling designs. The dimensions shown are specific to a particular extrusion and slight adjustments may have been made between extrusions. Additionally, the dimensions and tolerances listed were the as machined dimensions. There is a small dimensional change at the time of heat treatment as well as small errors that may have been during machining. The first set of drawings presented in this appendix detail the final extrusion tooling design. This design and these dimensions were used in extrusion 11, 12, and 13. Some other tooling drawings shown were used for multiple extrusions as well.

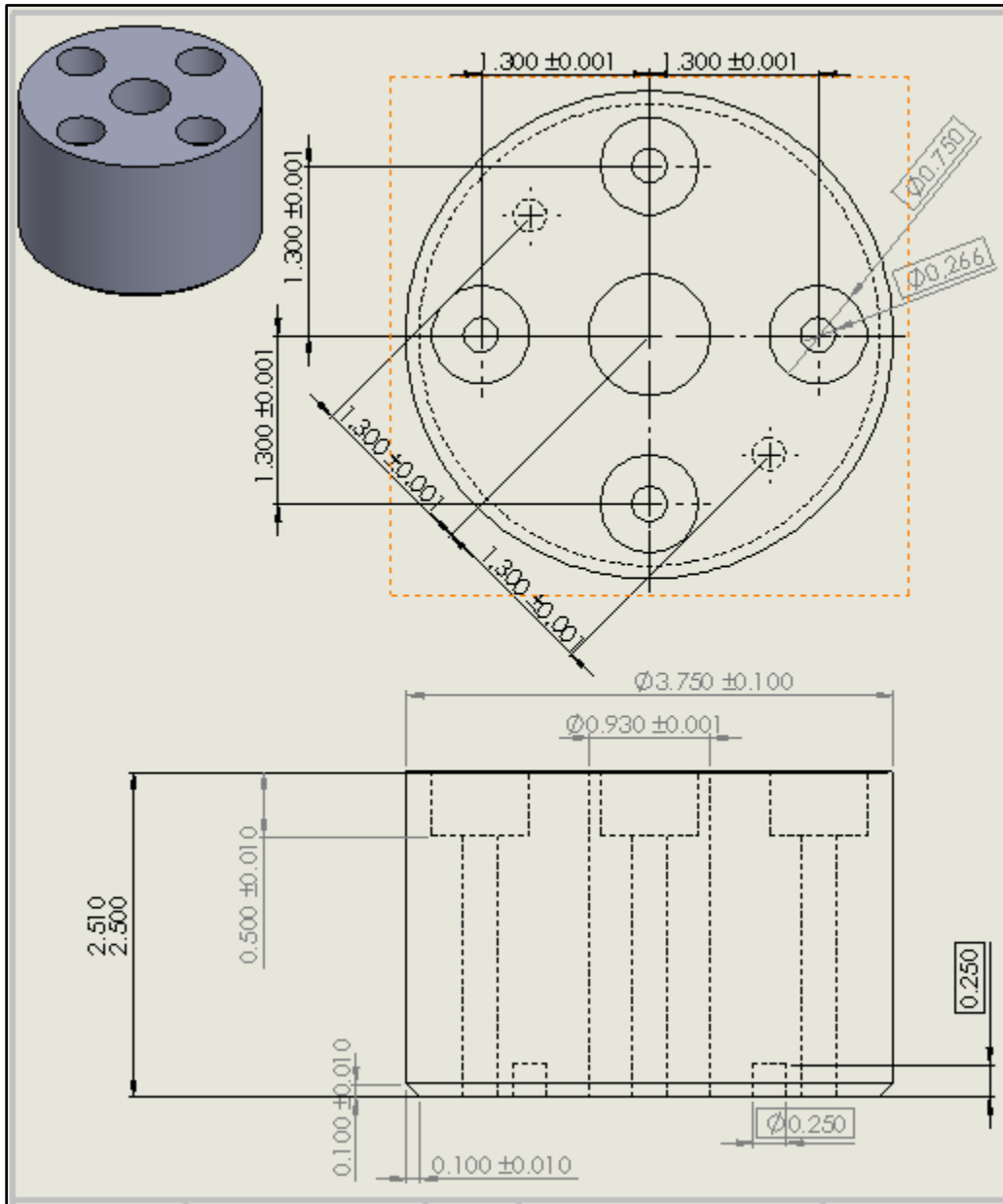


Figure A3-1: Final rod extrusion tooling design - holder

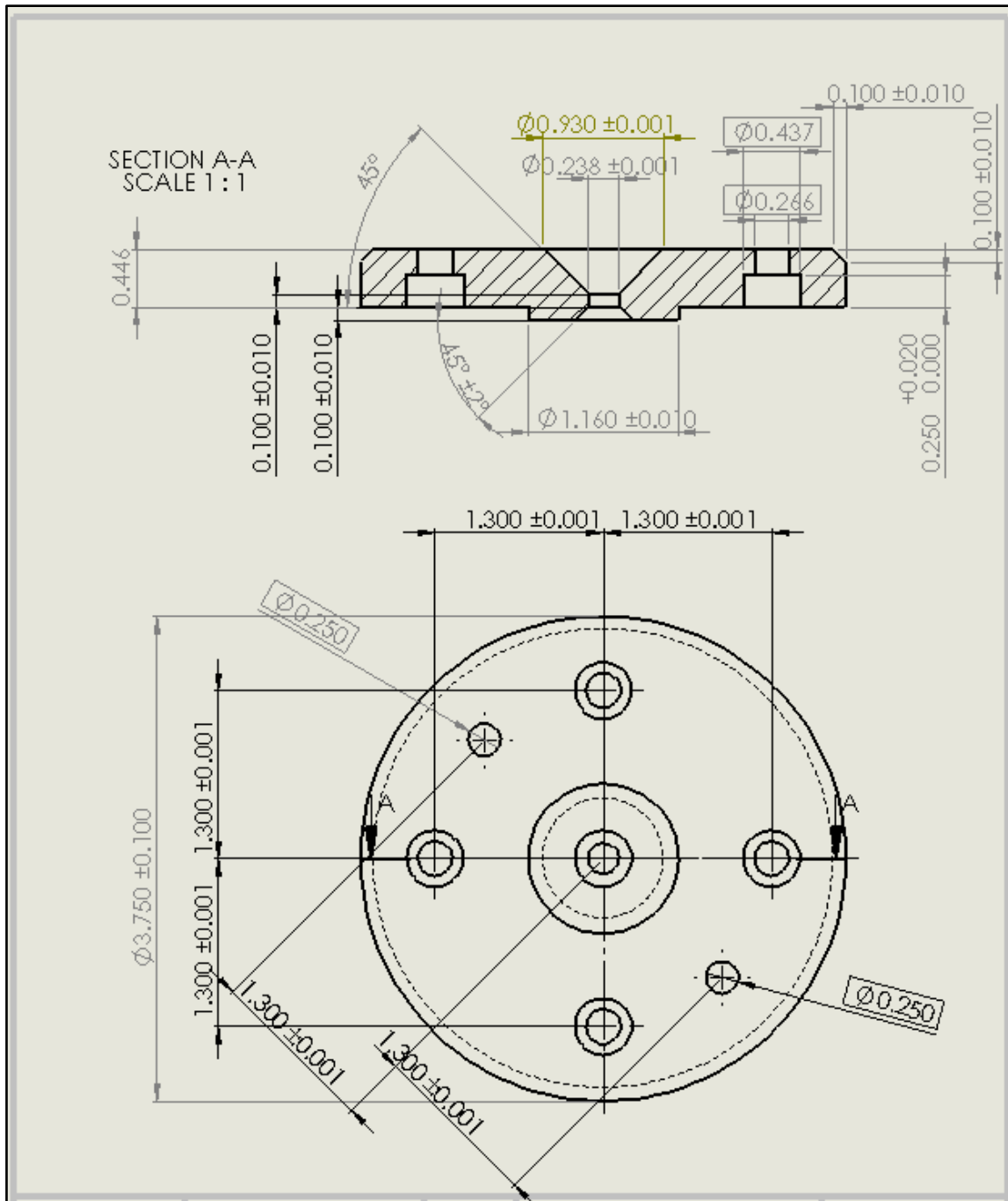


Figure A3-2: Final rod extrusion tooling design - die

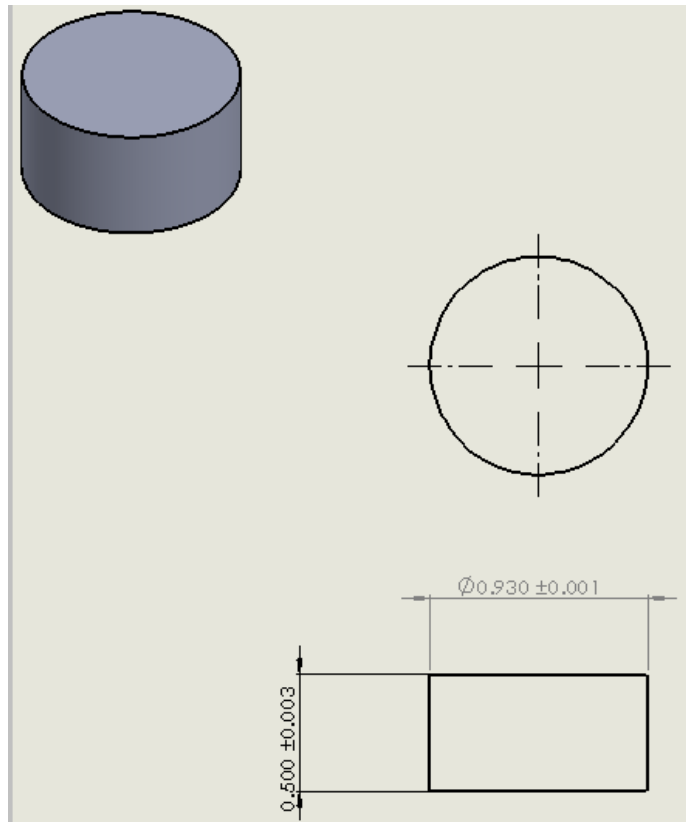


Figure A3-3: Final rod extrusion tooling design – dummy block

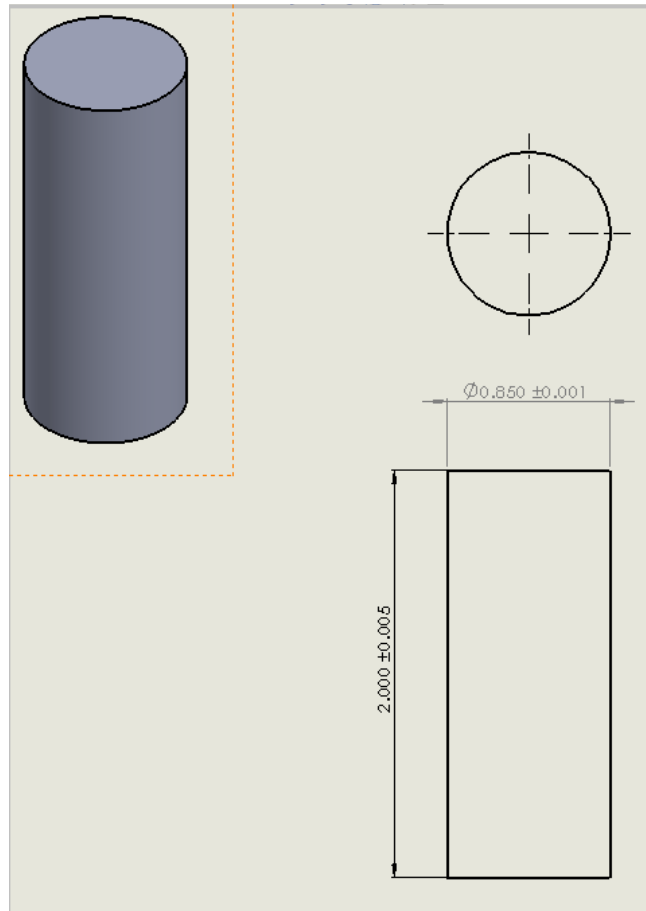


Figure A3-4: Final rod extrusion tooling design – ram

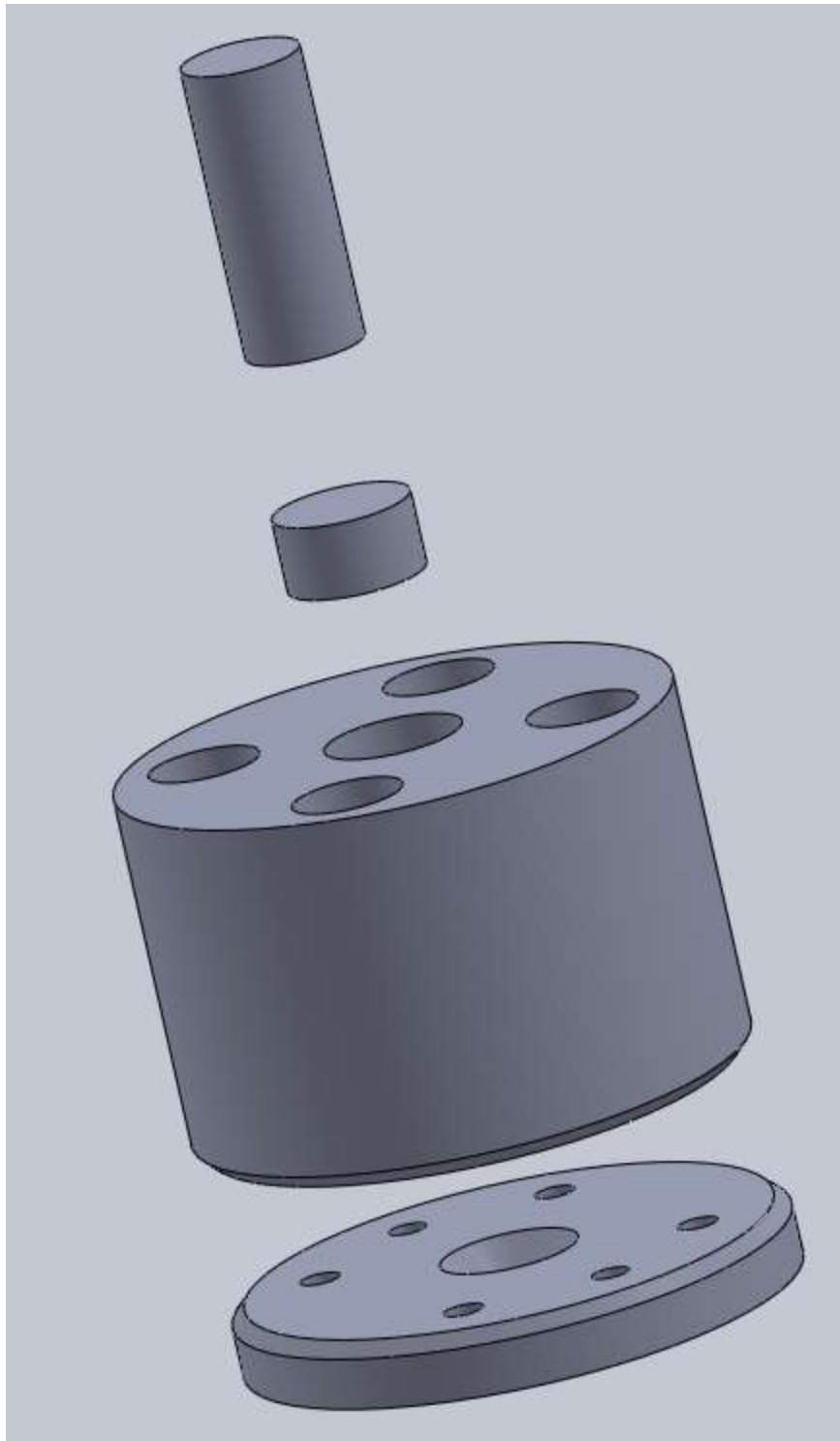


Figure A3-4: Final rod extrusion tooling design – assembly of parts

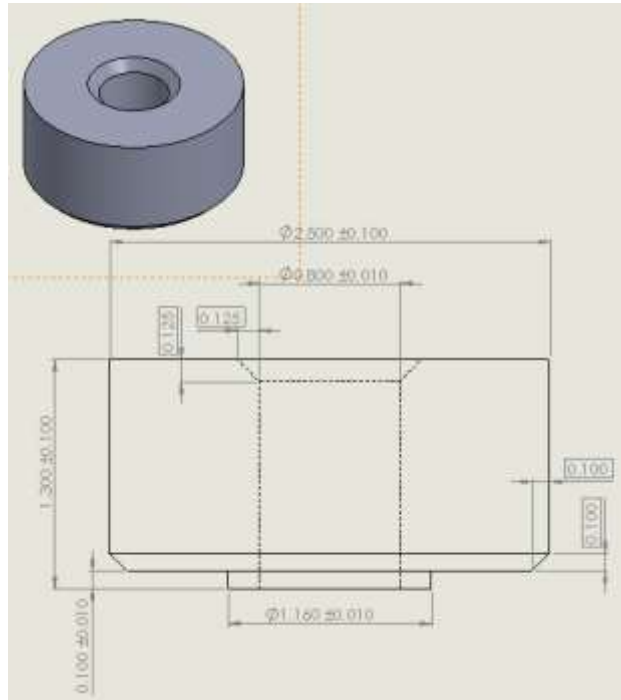


Figure A3-5: U-10Zr extrusion 1 – holder

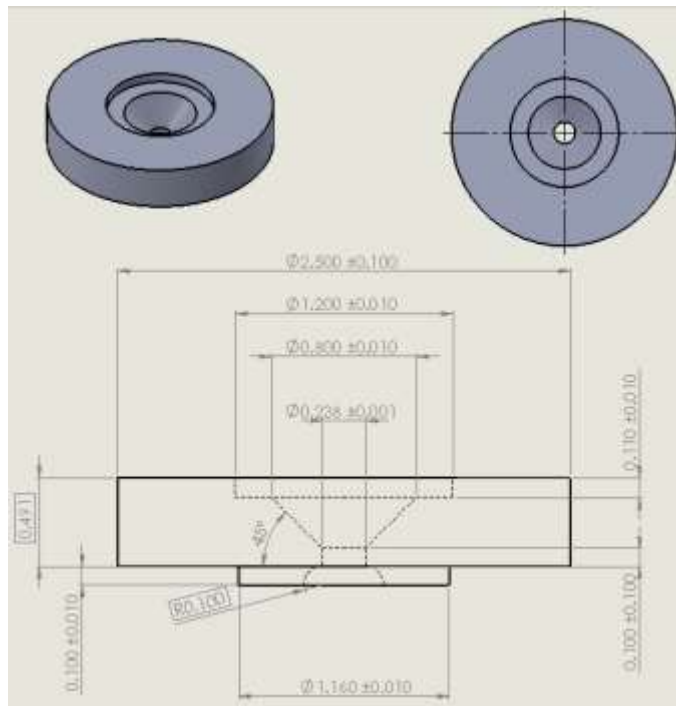


Figure A3-6: U-10Zr extrusion 1 – Die

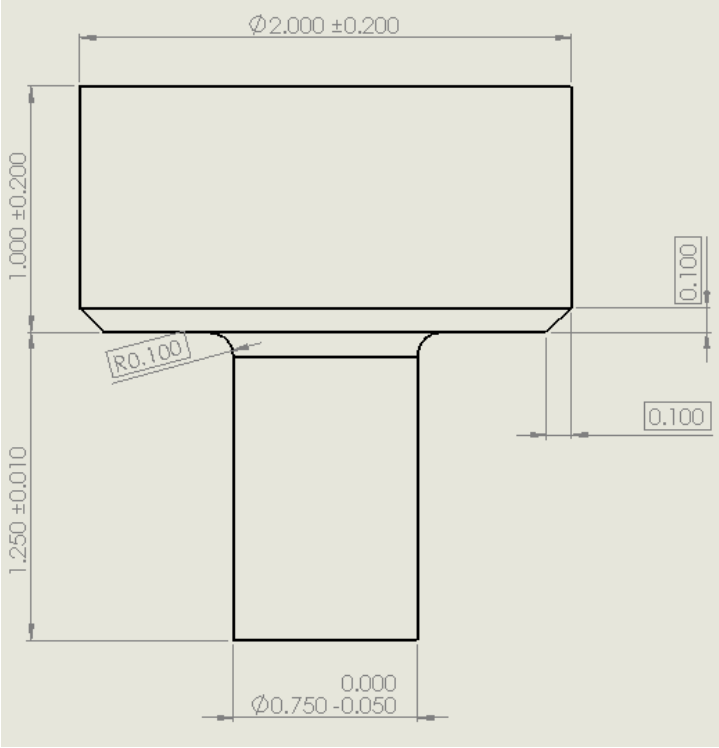


Figure A3-7: U-10Zr extrusion 1 – ram

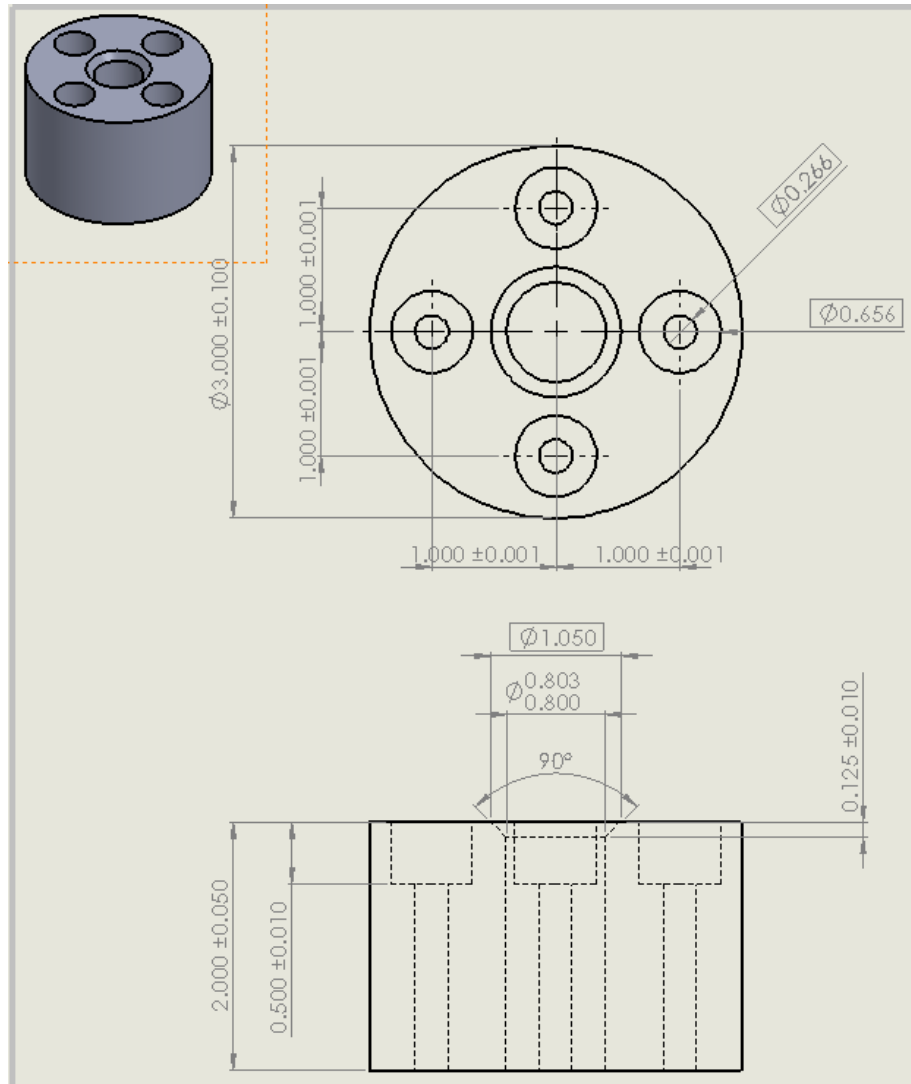


Figure A3-8: U-10Zr extrusion 2 – holder

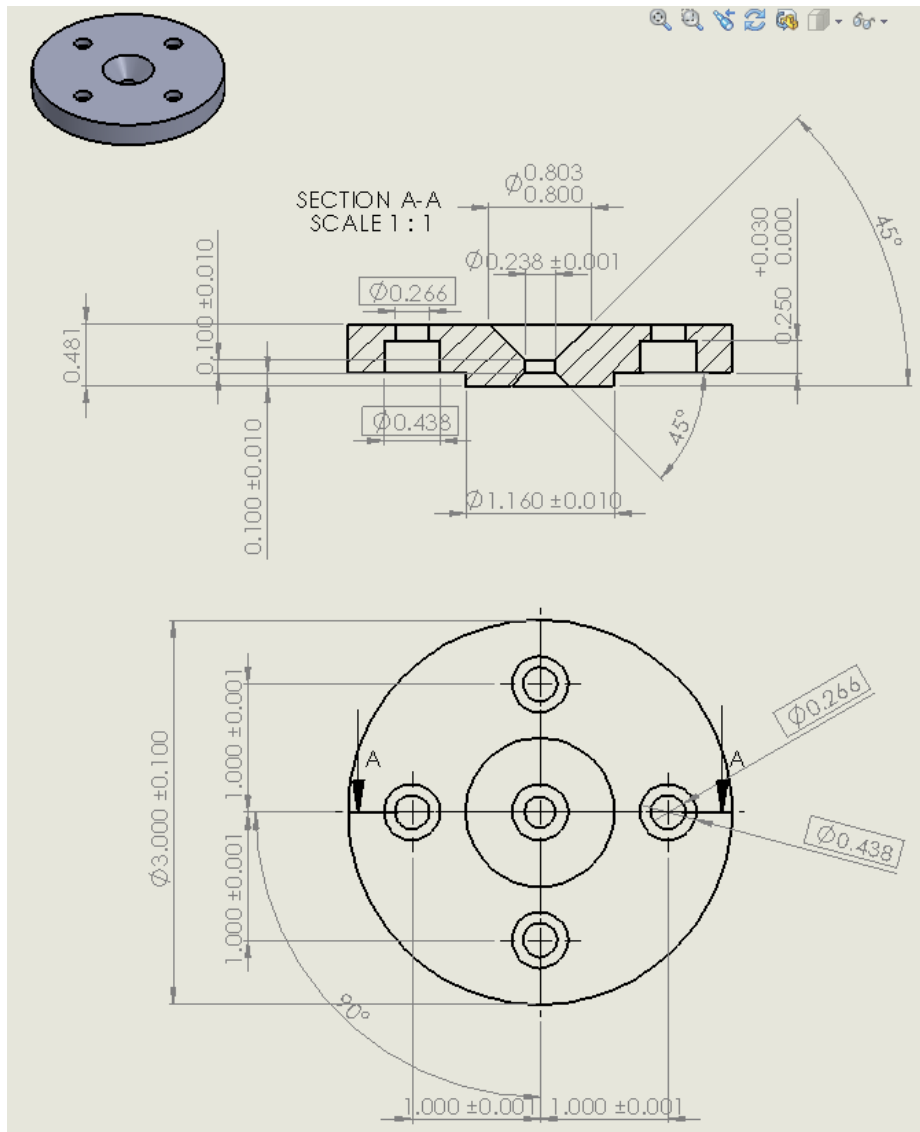


Figure A3-9: U-10Zr extrusion 2 – die

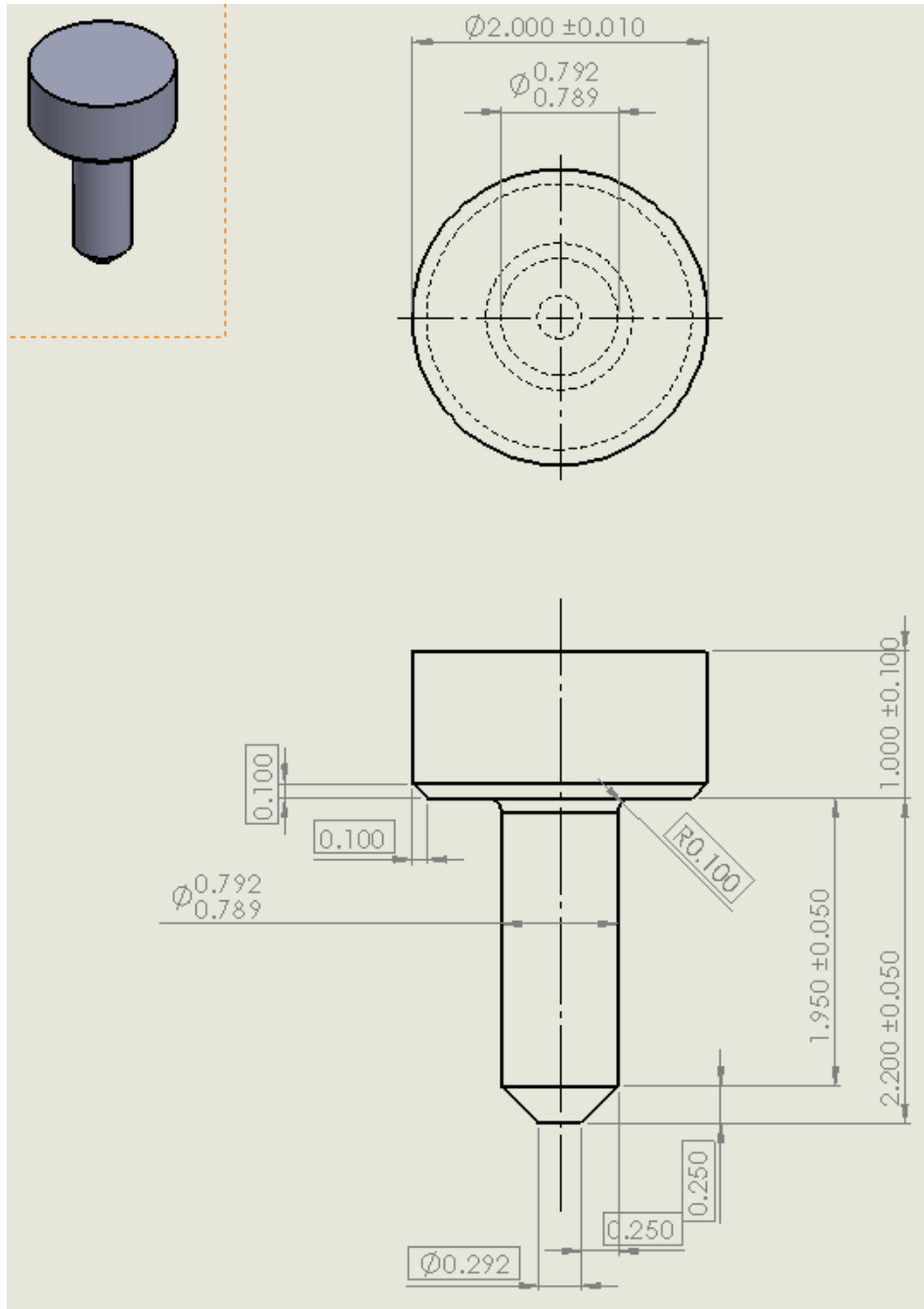


Figure A3-10: U-10Zr extrusion 2 – ram

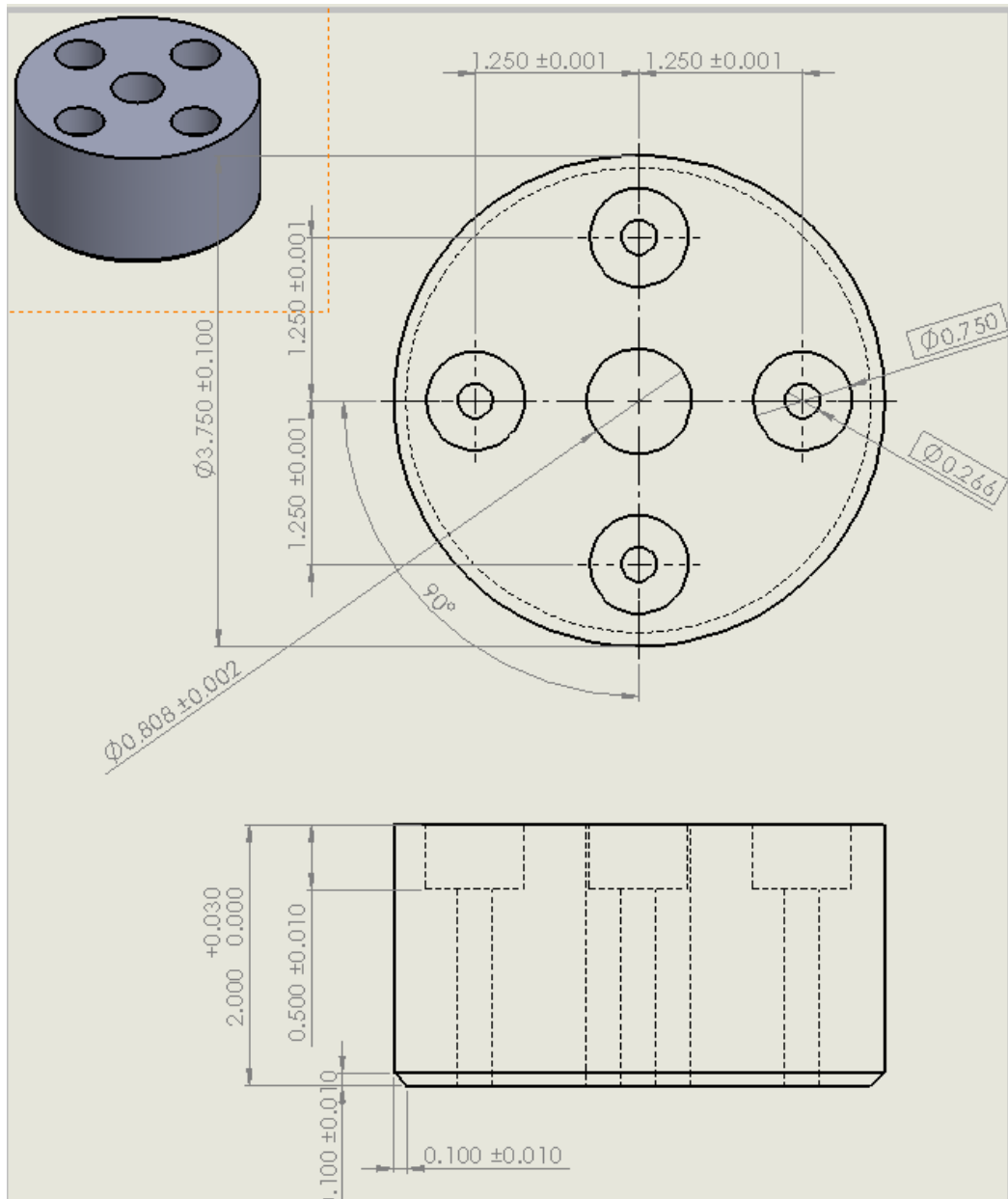


Figure A3-11: U-10Zr extrusion 3 – holder

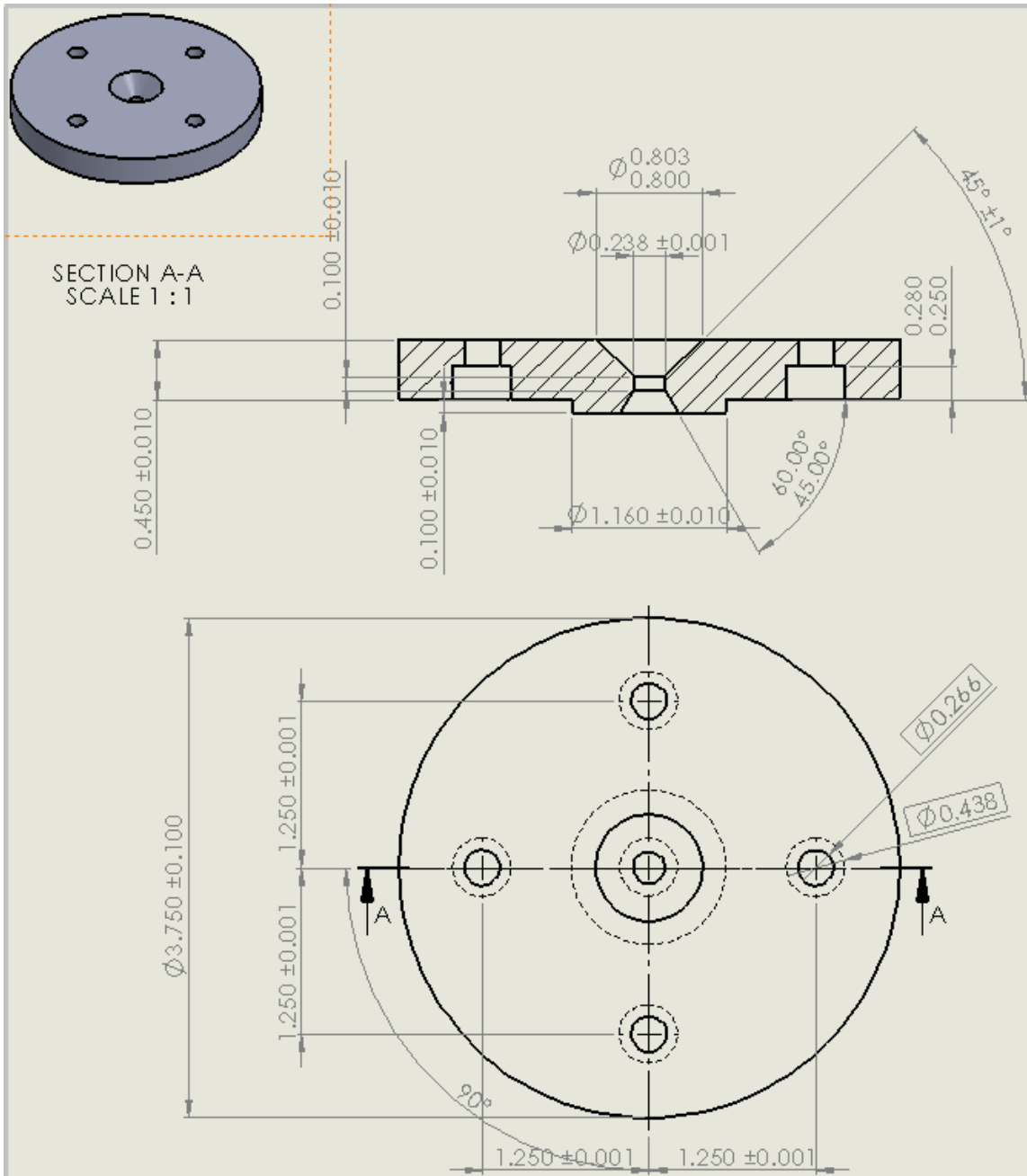


Figure A3-12: U-10Zr extrusion 3 – die

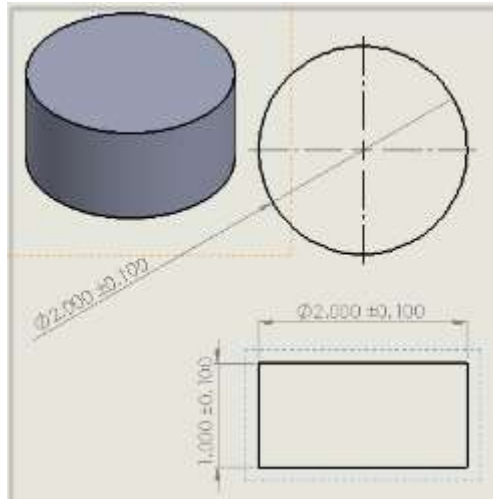


Figure A3-12: used in many extrusions – ram top

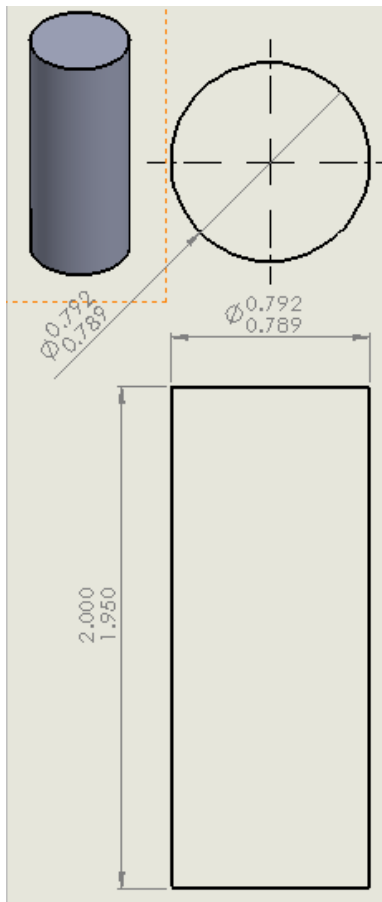


Figure A3-13: U-10Zr extrusion 3 – ram

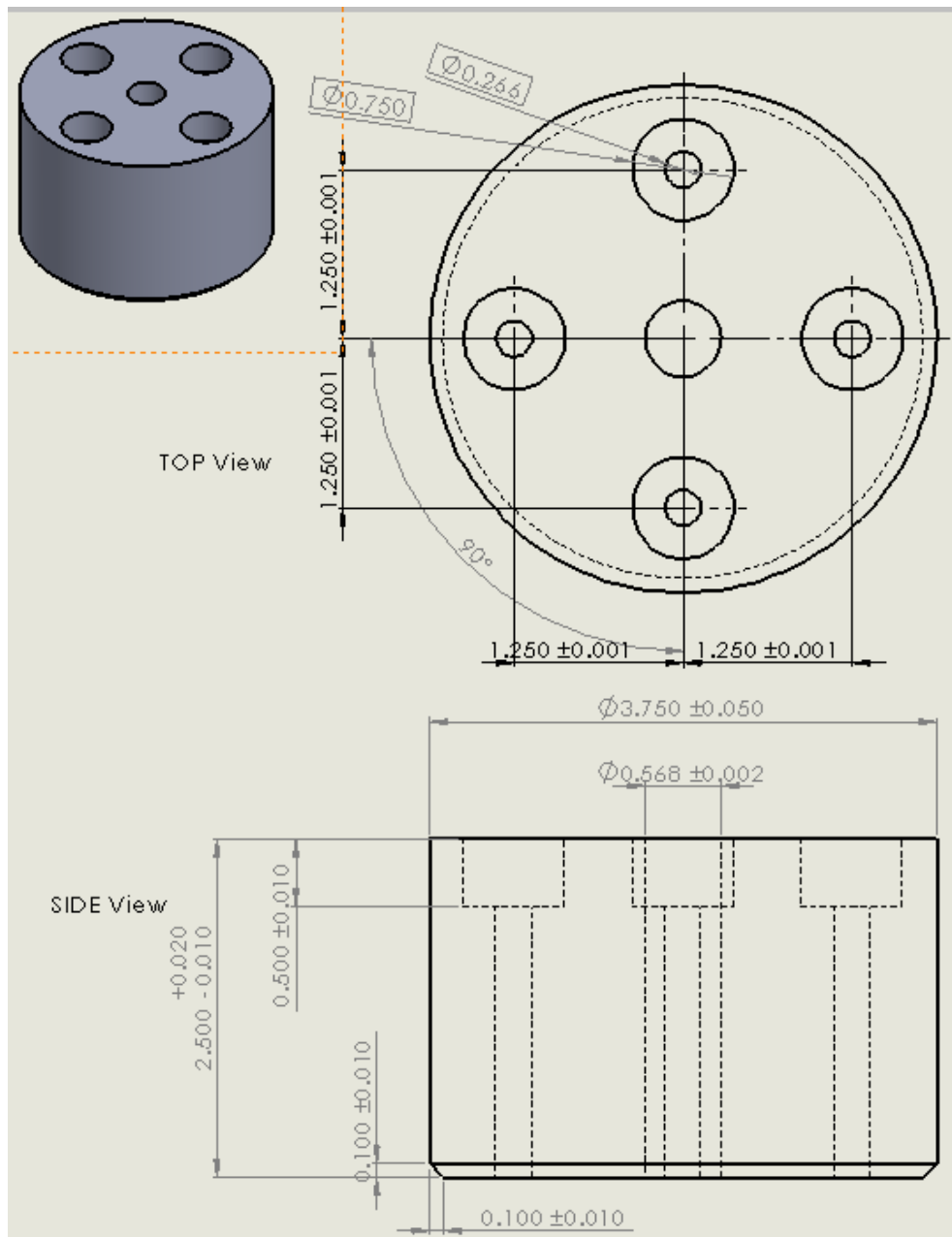


Figure A3-14: U-10Zr extrusion 5 – holder

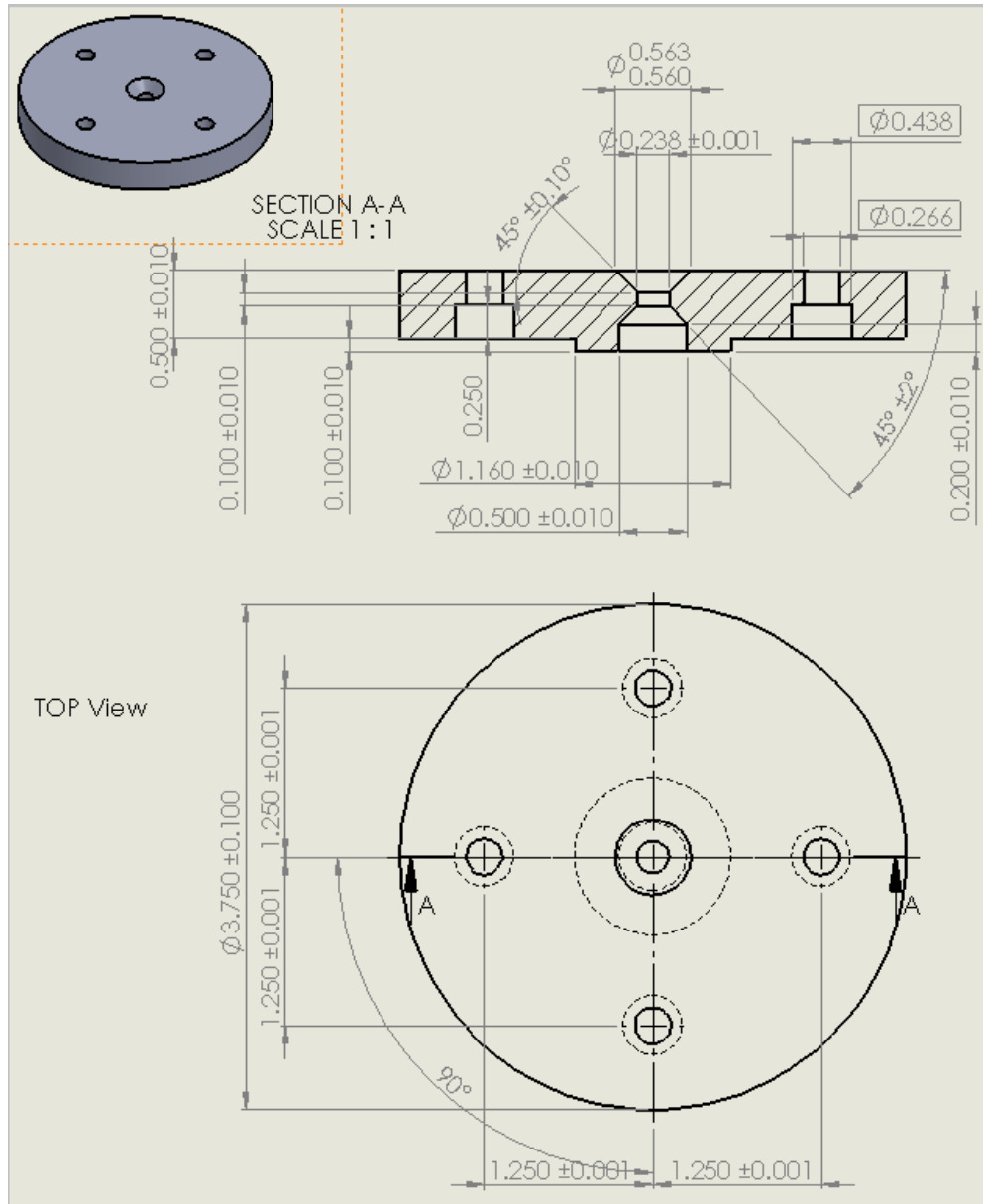


Figure A3-15: U-10Zr extrusion 5 – die

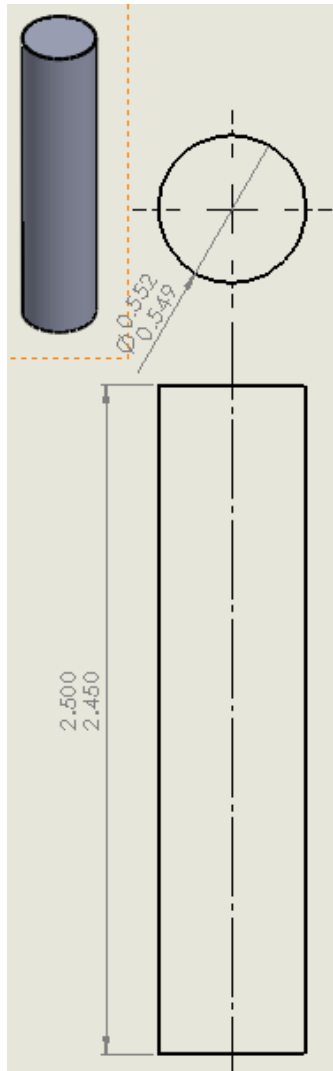


Figure A3-16: U-10Zr extrusion 5 – ram

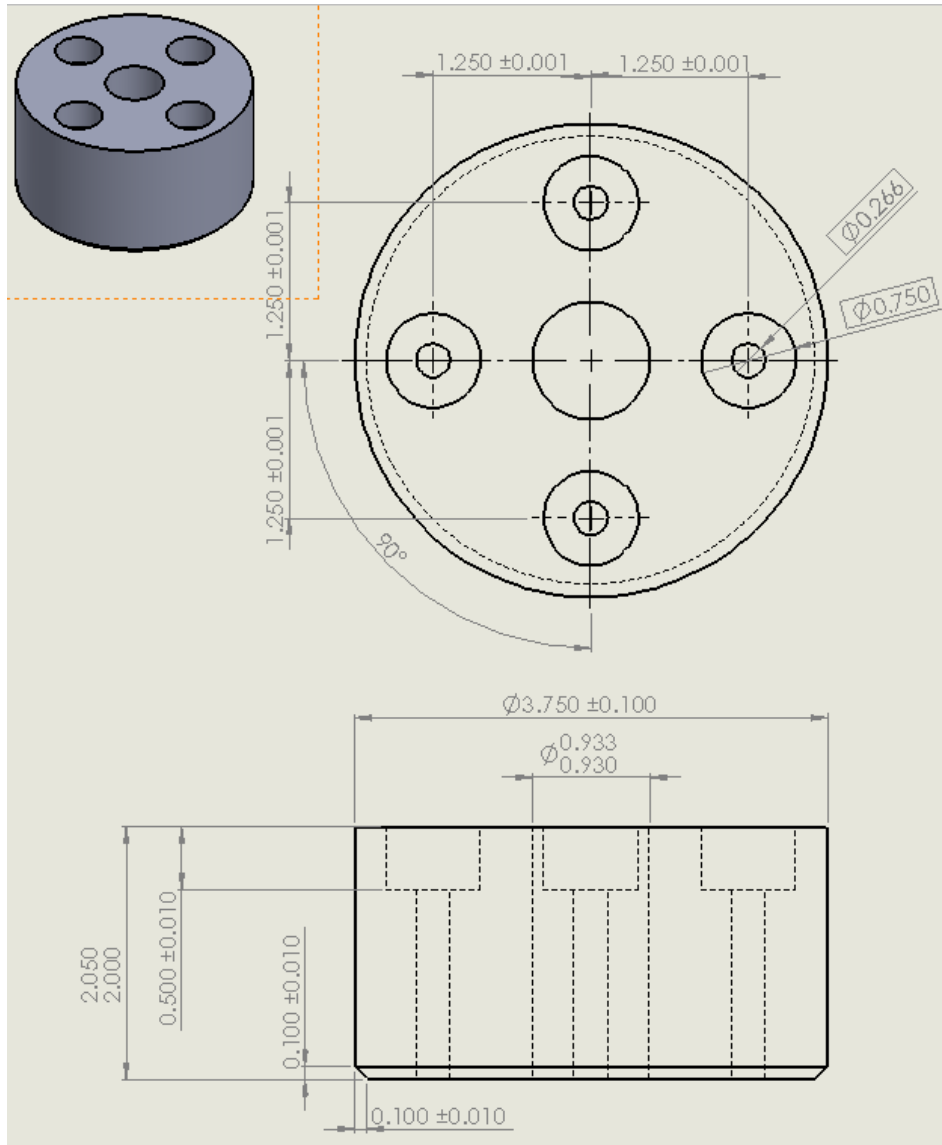


Figure A3-17: U-10Zr extrusion 6 – holder

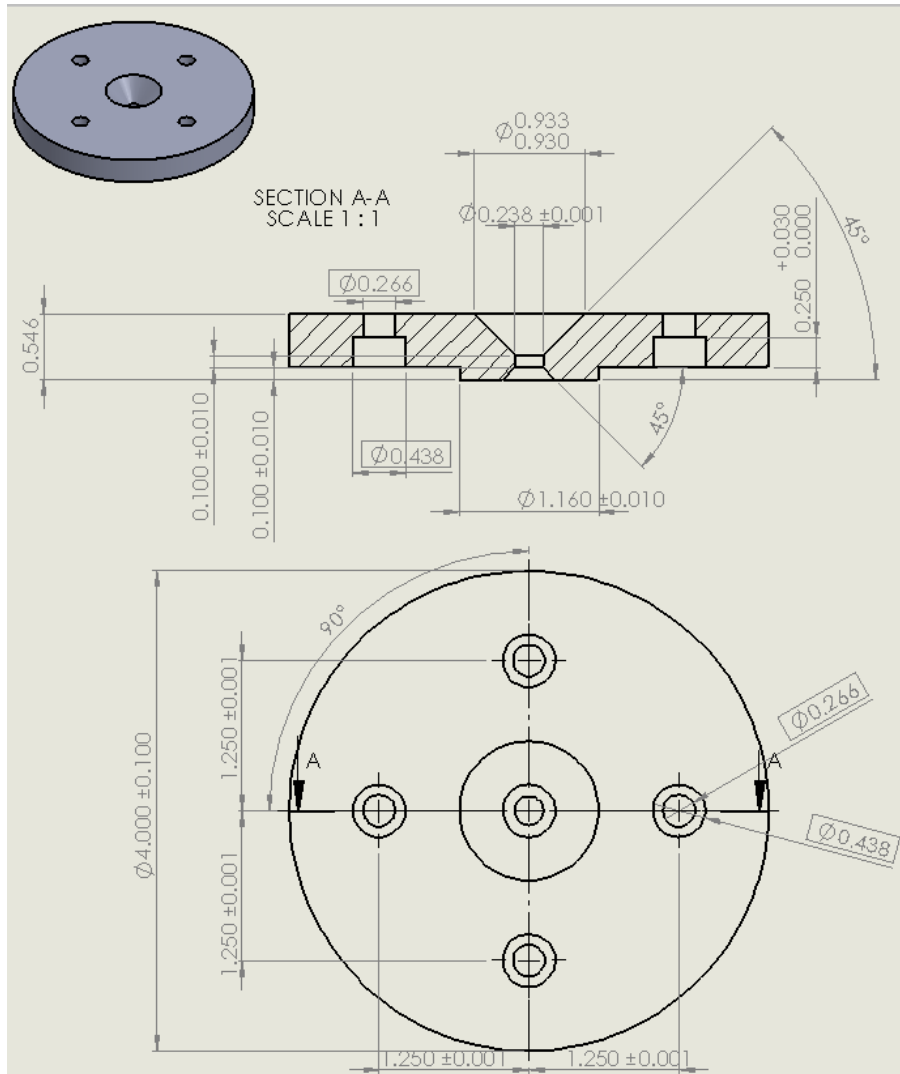


Figure A3-18: U-10Zr extrusion 6 – die

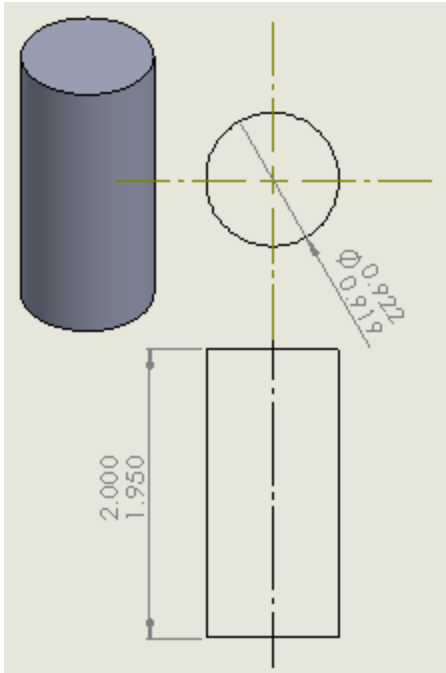


Figure A3-19: U-10Zr extrusion 6 – ram

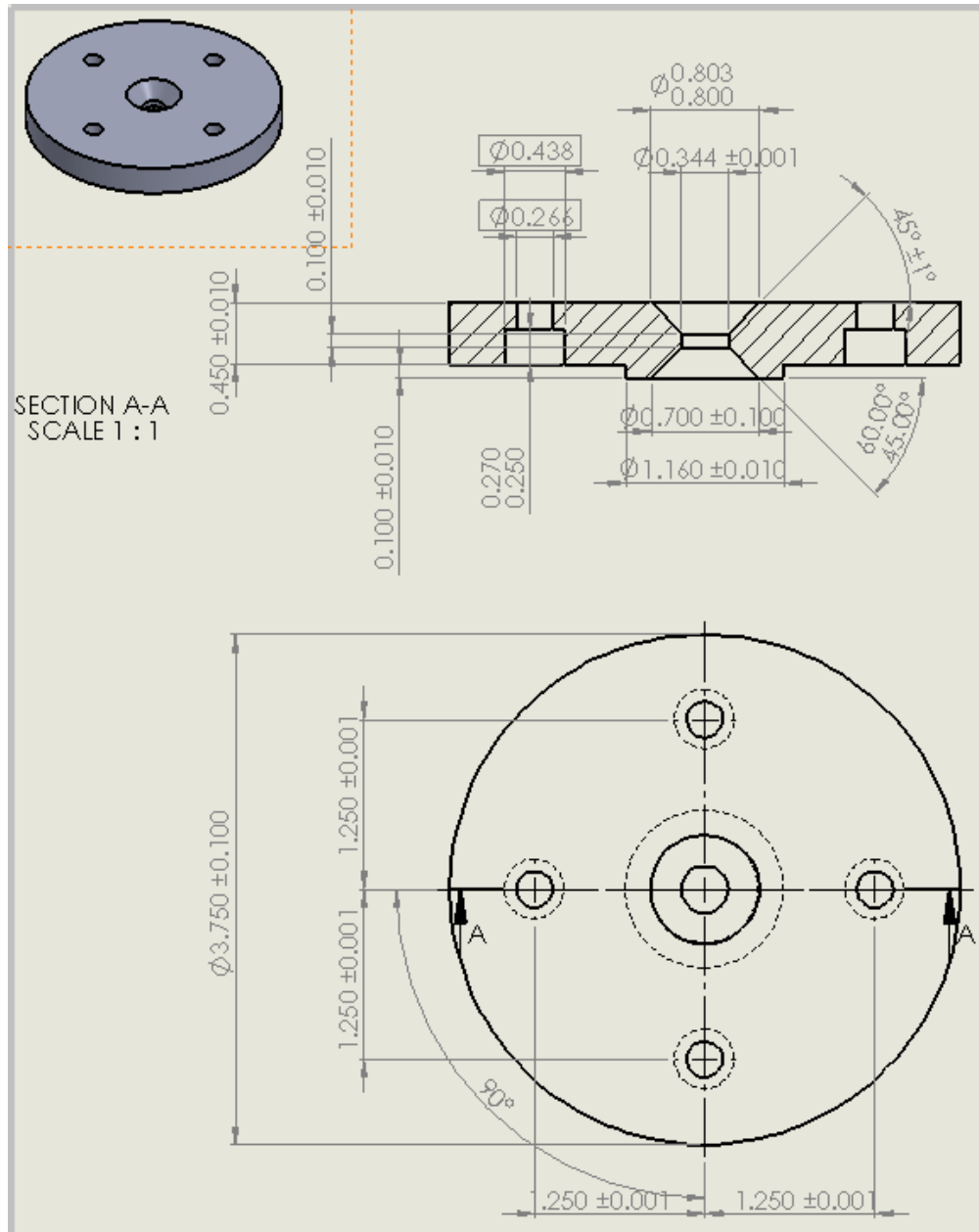


Figure A3-20: U extrusion 7 – die

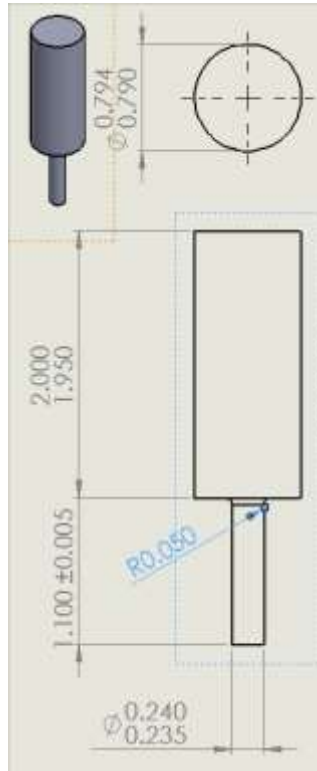


Figure A3-21: U extrusion 7 – ram

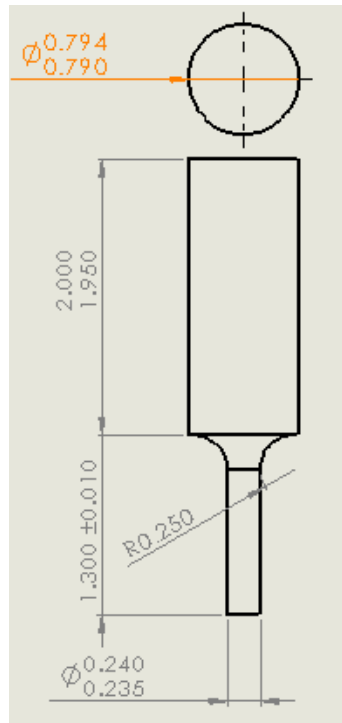


Figure A3-22: U extrusion 8 – ram

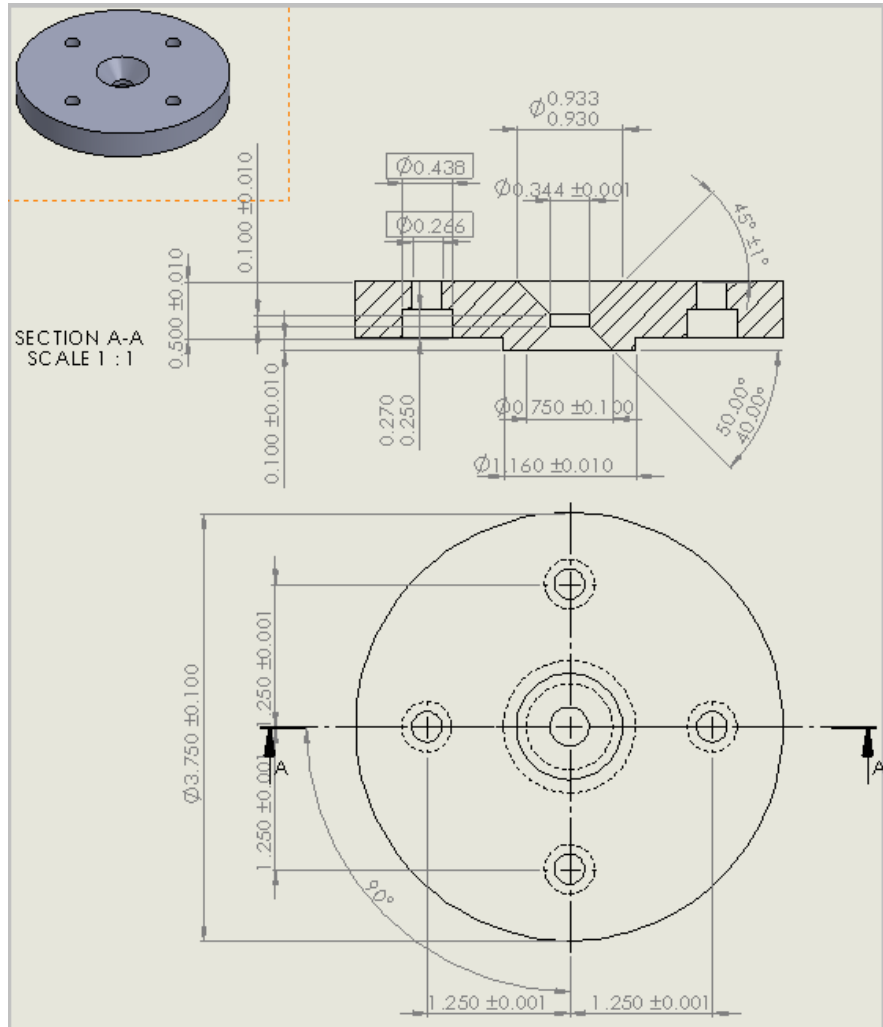


Figure A3-23: U extrusion 9 – die

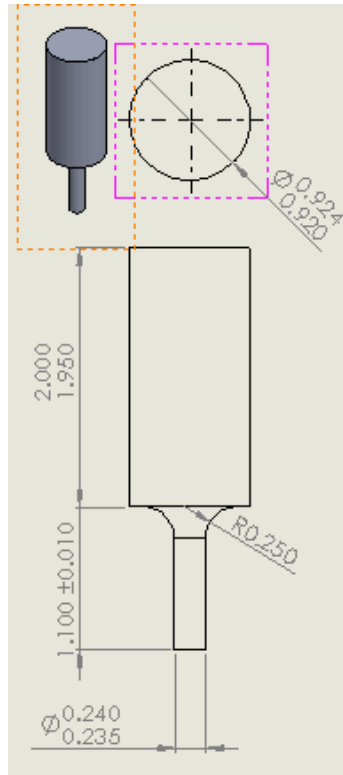


Figure A3-24: U extrusion 9 – ram

APPENDIX 4

LFA INERT ATMOSPHERE HOLDERS

Before the inert atmosphere LFA sample holders were used, they were cleaned and the seals were inspected to be in good operating condition. At the start of the project and several times throughout, the LFA sample holders were checked with a standard. The standard used was Pyroceram 9606 with ID#7513. The standard was coated in graphite and tested in a regular holder in the LFA. It was then tested again in the inert atmosphere holder. These data sets were then compared to literature values for the standard to ensure that the LFA and the holders were all in good working condition and the data produced from the experiments would be reliable. The data collected with the standard can be seen below in Figure A4-1.

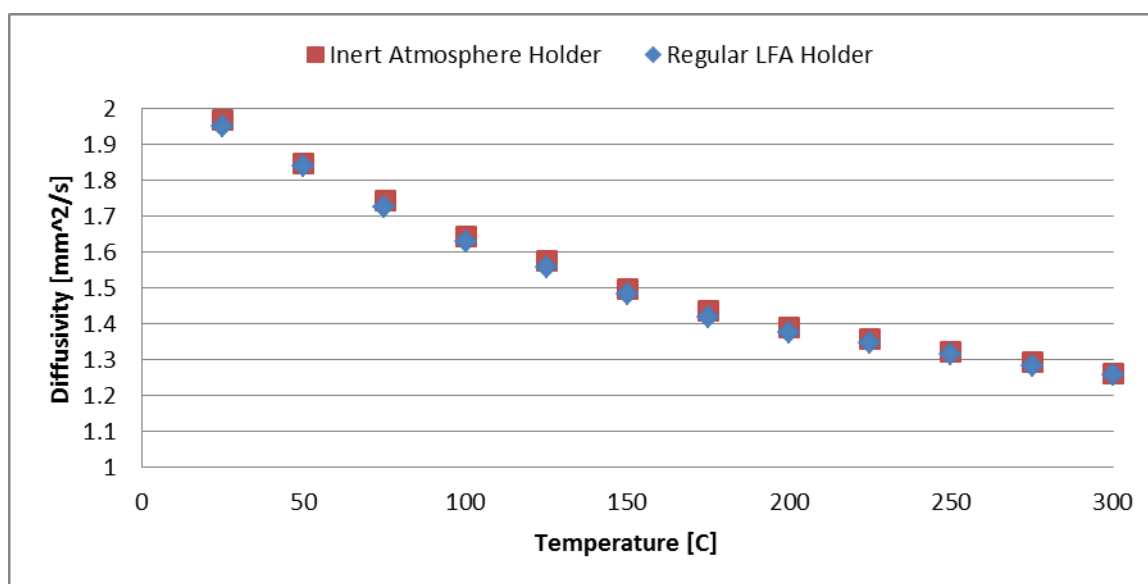


Figure A4-1: Comparison of standard data for LFA sample holders

APPENDIX 5

IMAGES OF LOW DENSITY PELLETS

Table A5-1: List of imaged LFA Pellets and figure reference numbers

Material	%TD	ID#	Figure
U HDH	45.5	26-182	A5-1 to A5-3
	53.7	31-32	A5-4 to A5-5
	57.6	31-33	A5-6 to A5-9
	60.1	31-31	A5-10
	62.5	31-30	A5-11 to A5-12
	64.8	31-29	A5-13
	70.9	17-1	A5-14 to A5-15
	86.9	26-184	A5-16
U spheres	65.6	26-156	A5-17-A5-19
	74.4	26-124	A5-20 to A5-21
	75.1	26-121	A5-22 to A5-23
U-5Zr HDH	68.0	17-14	A5-24 to A5-26
	72.5	31-50A	A5-27 to A5-29
	80.6	31-63B	A5-30 to A5-31
U-10Zr HDH	61.2	17-5A	A5-32
	66.8	17-7B	A5-33 to A5-34
	76.1	17-9B	A5-35 to A5-37
	79.6	17-11B	A5-38 to A5-40
	83.5	17-11A	A5-41 to A5-42
	83.8	31-45	A5-43 to A5-44
U-10Zr Spheres	73.3	26-174	A5-45 to A5-47
	81.0	26-120	A5-48 to A5-50

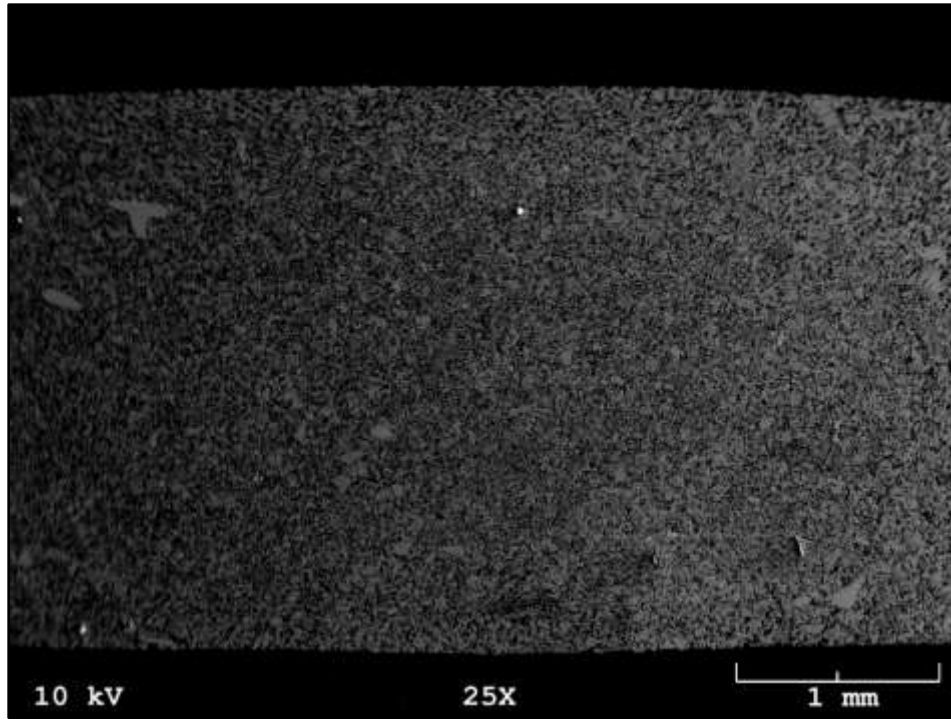


Figure A5-1: 45.5 %TD U HDH pellet (26-182) at 25X

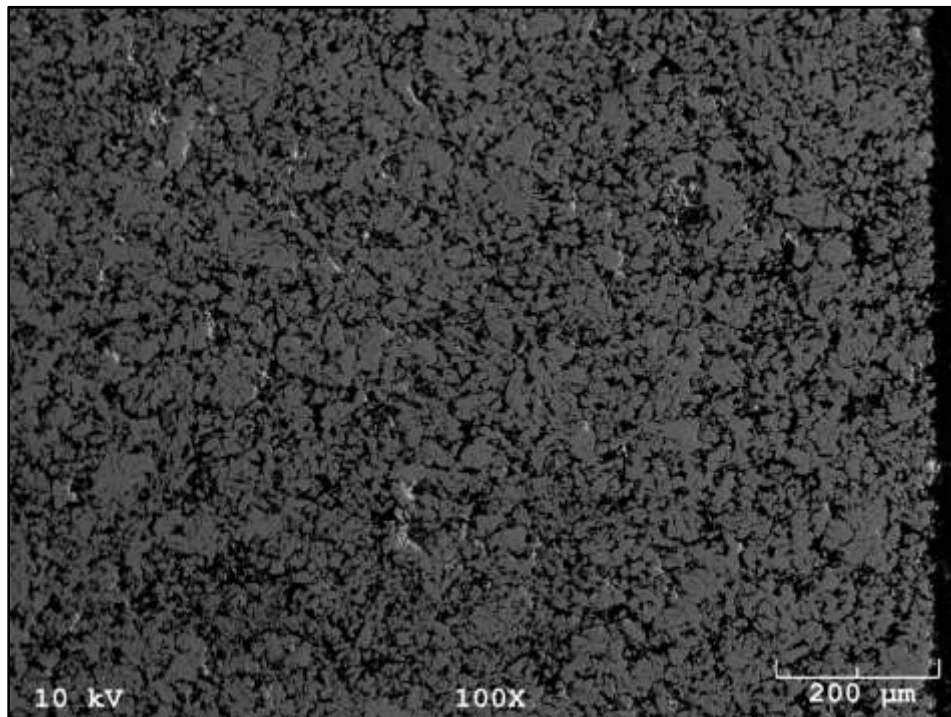


Figure A5-2: 45.5 %TD U HDH pellet (26-182) at 100X

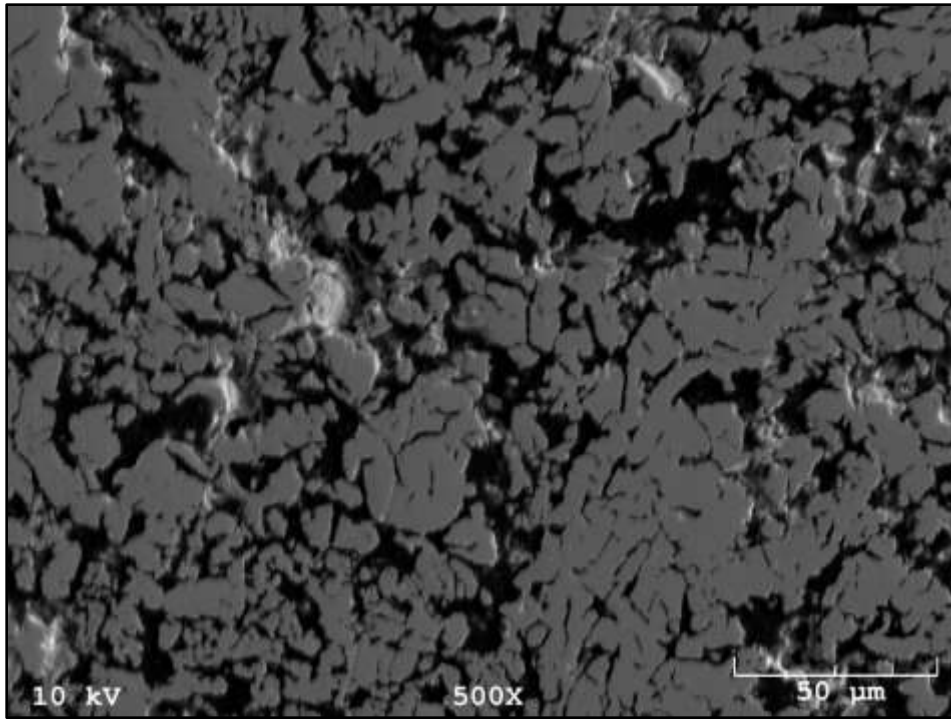


Figure A5-3: 45.5 %TD U HDH pellet (26-182) at 500X

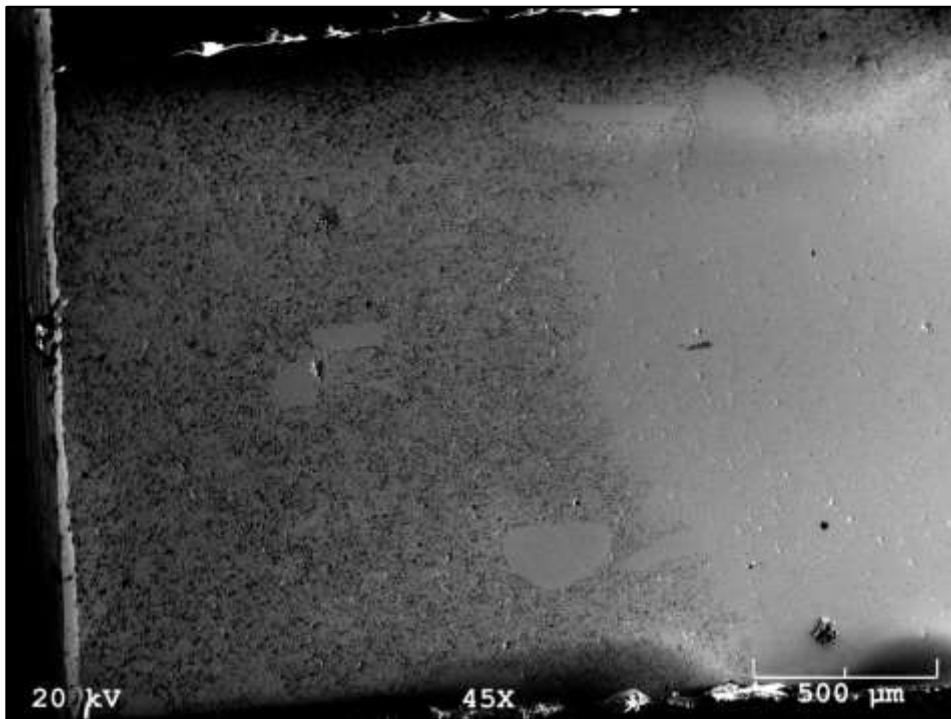


Figure A5-4: 53.7 %TD U HDH pellet (31-32) at 45X

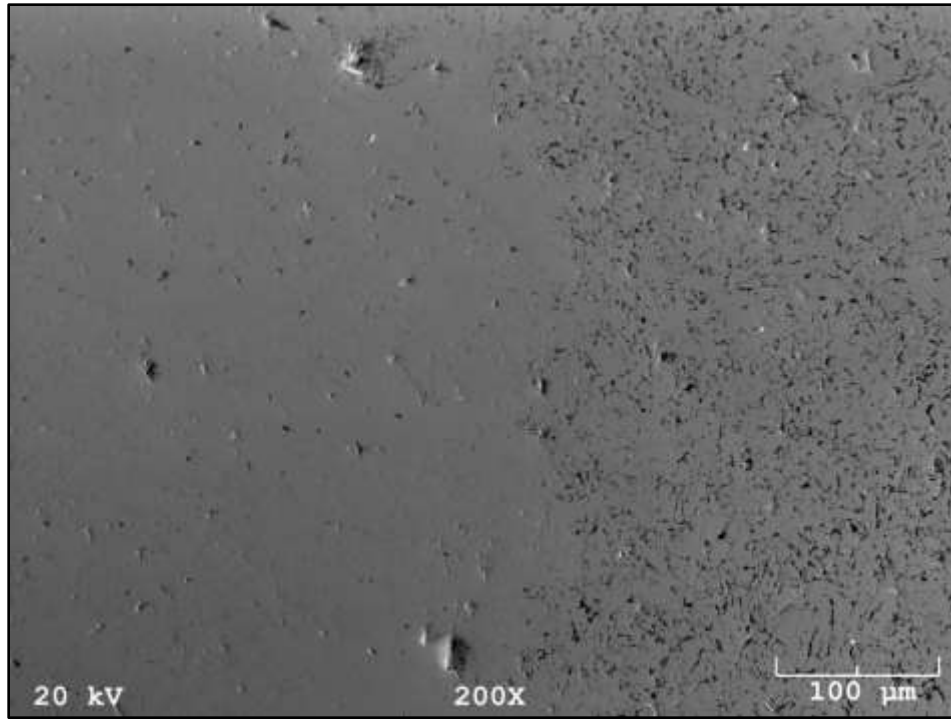


Figure A5-5: 53.7 %TD U HDH pellet (31-32) at 200X

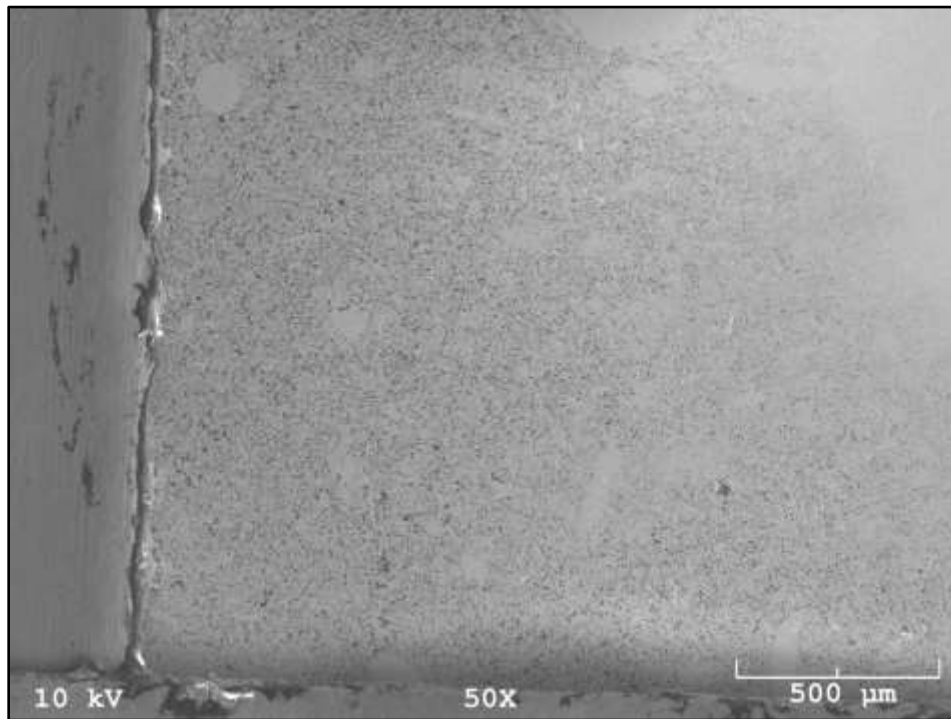


Figure A5-6: 57.6 %TD U HDH pellet (31-33) at 50X

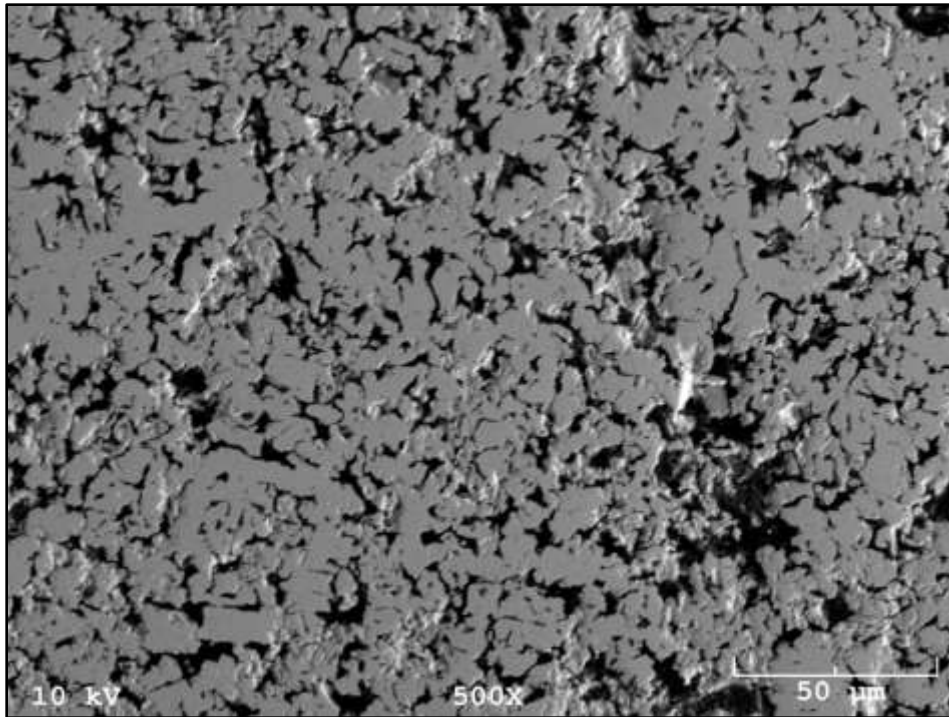


Figure A5-7: 57.6 %TD U HDH pellet (31-33) at 500X

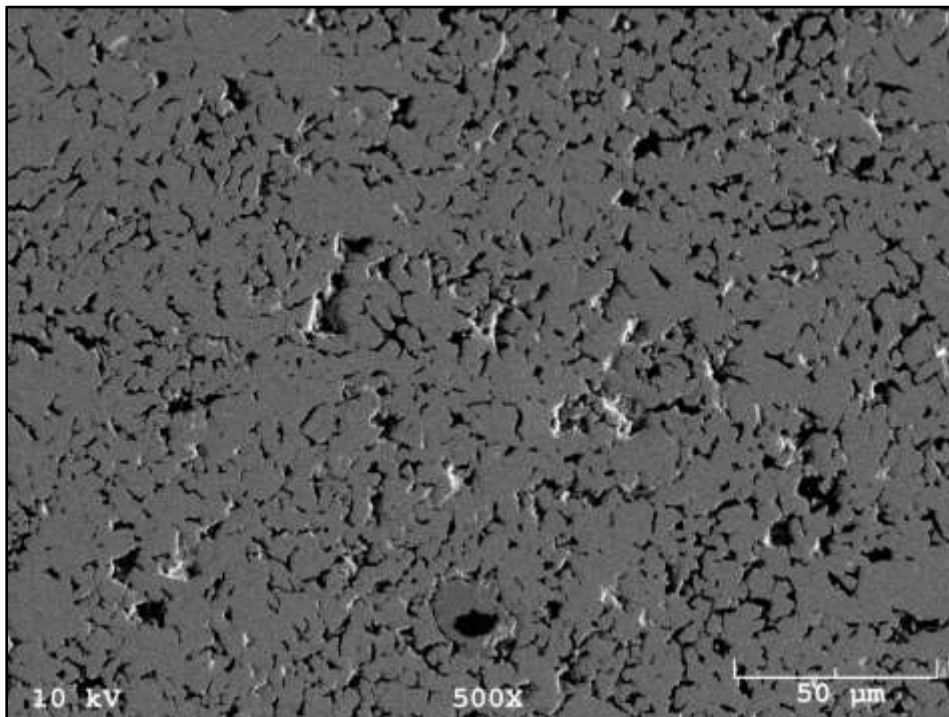


Figure A5-8: 57.6 %TD U HDH pellet (31-33) at 500X

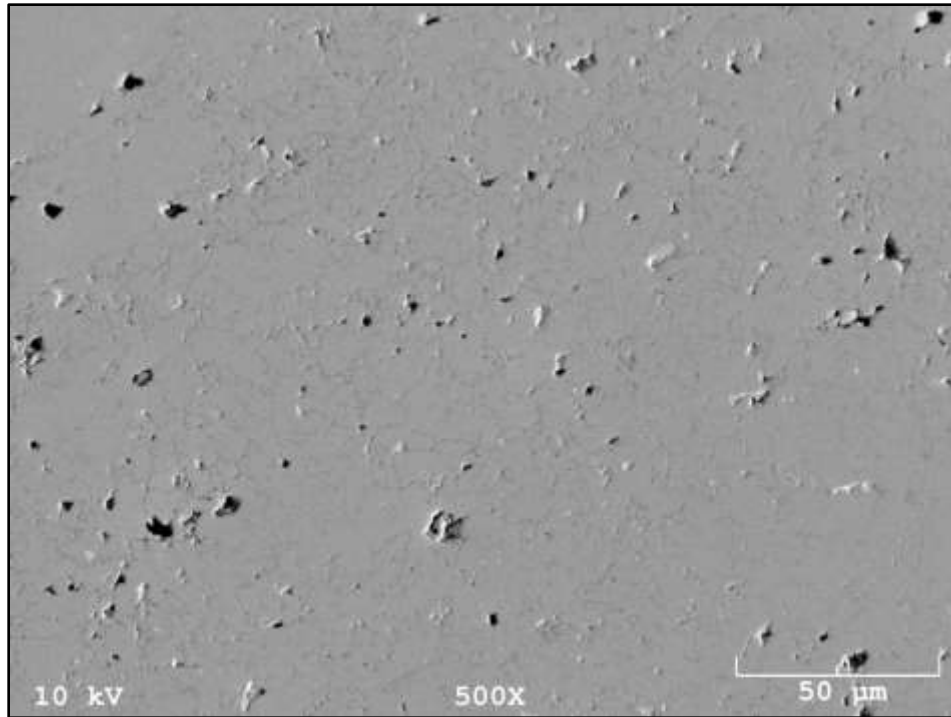


Figure A5-9: 57.62 %TD U HDH pellet (31-33) at 500X

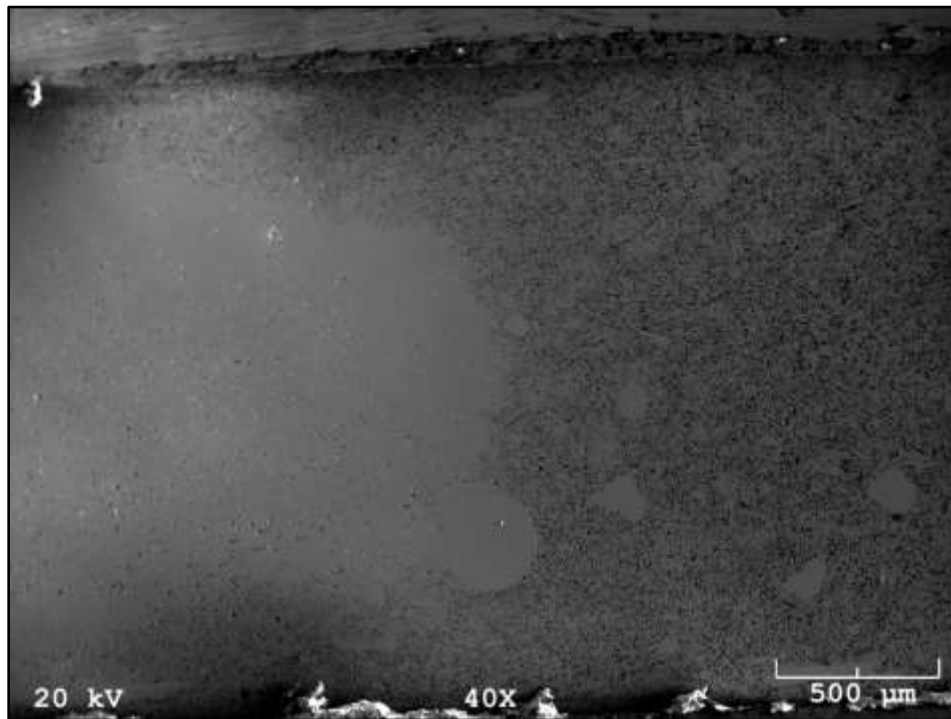


Figure A5-10: 60.1 %TD U HDH pellet (31-31) at 40X

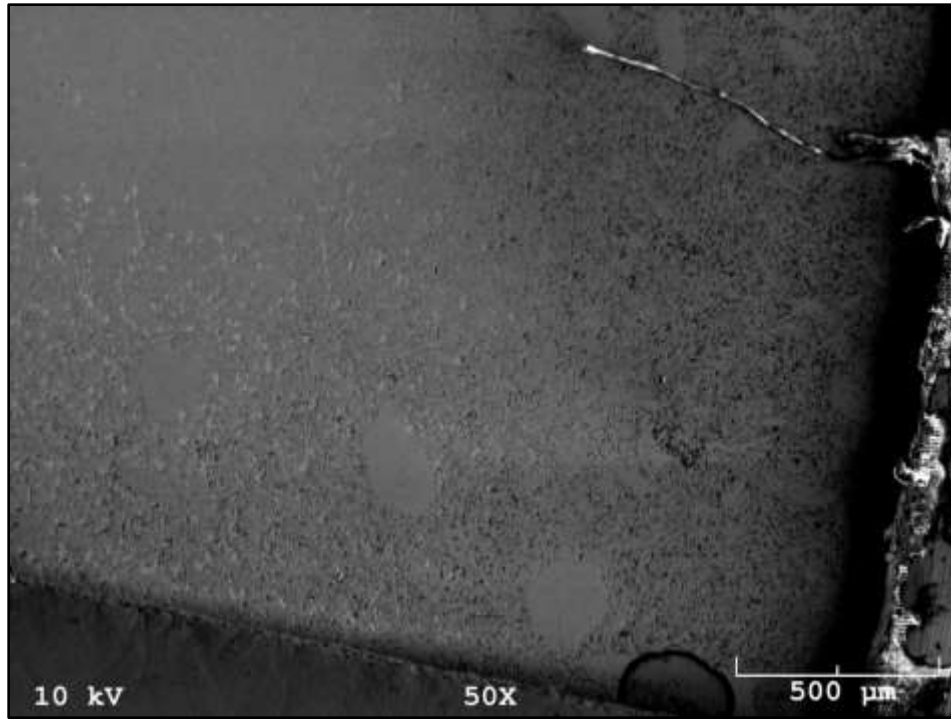


Figure A5-11: 62.5 %TD U HDH pellet (31-30) at 50X

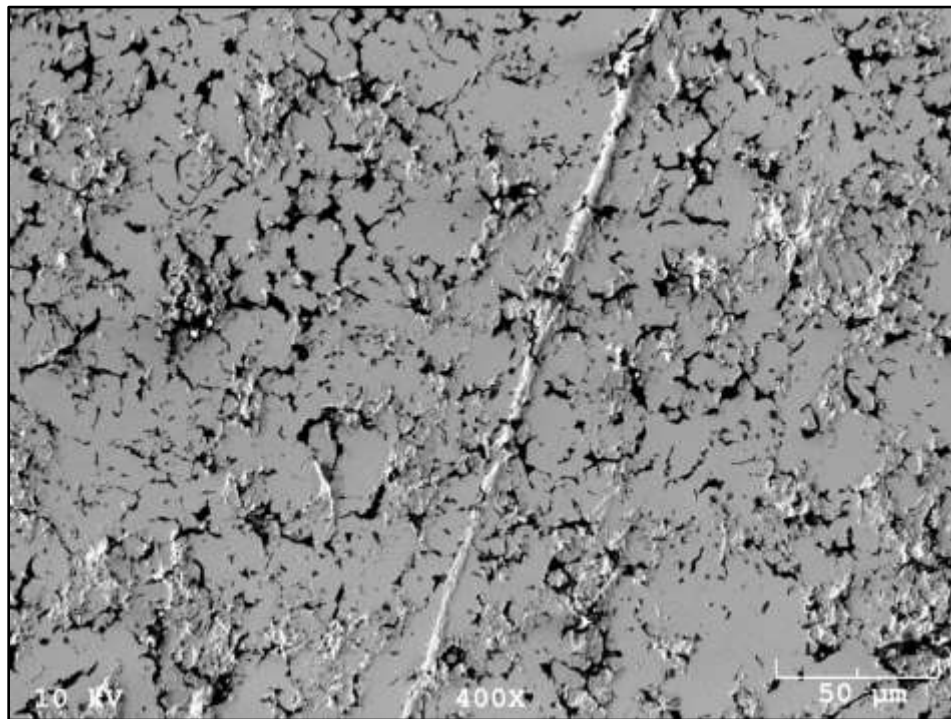


Figure A5-12: 62.5 %TD U HDH pellet (31-30) at 400X

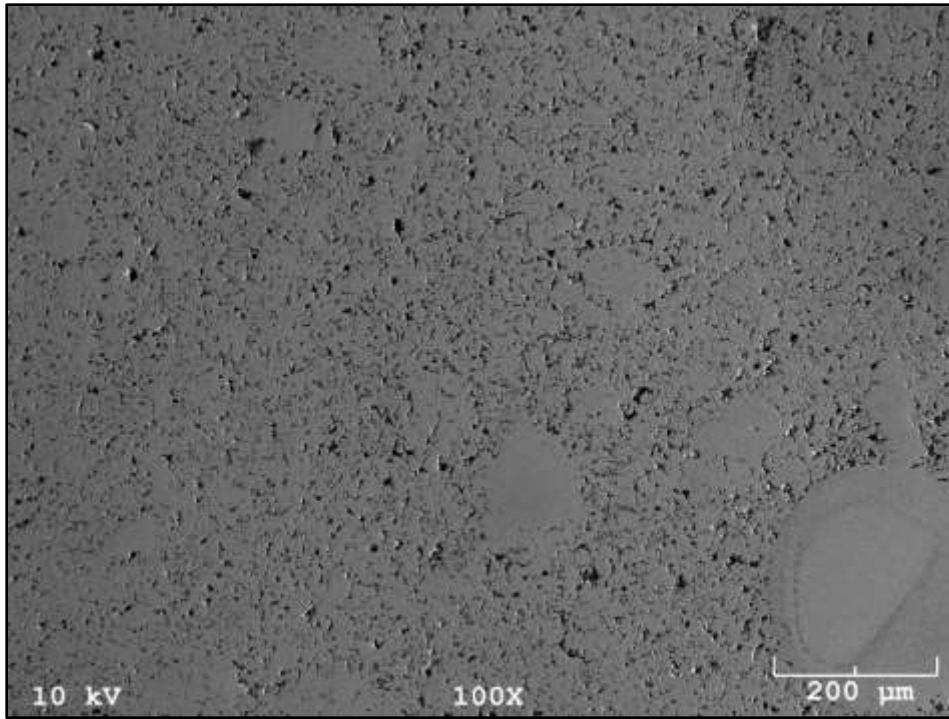


Figure A5-13: 64.8 %TD U HDH pellet (31-29) at 100X

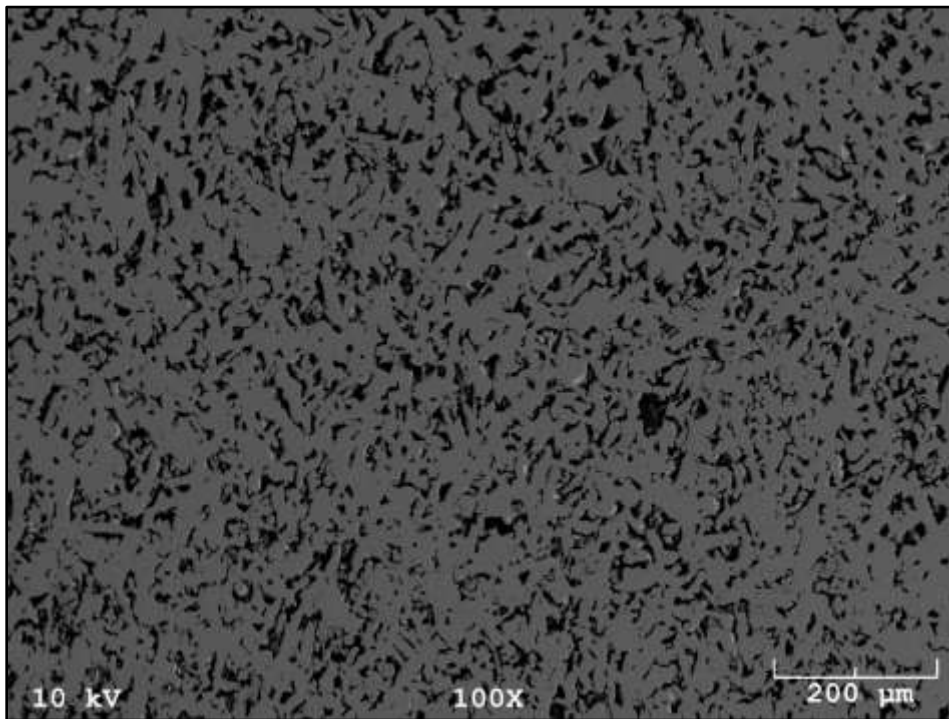


Figure A5-14: 70.9 %TD U HDH pellet (17-1) at 100X

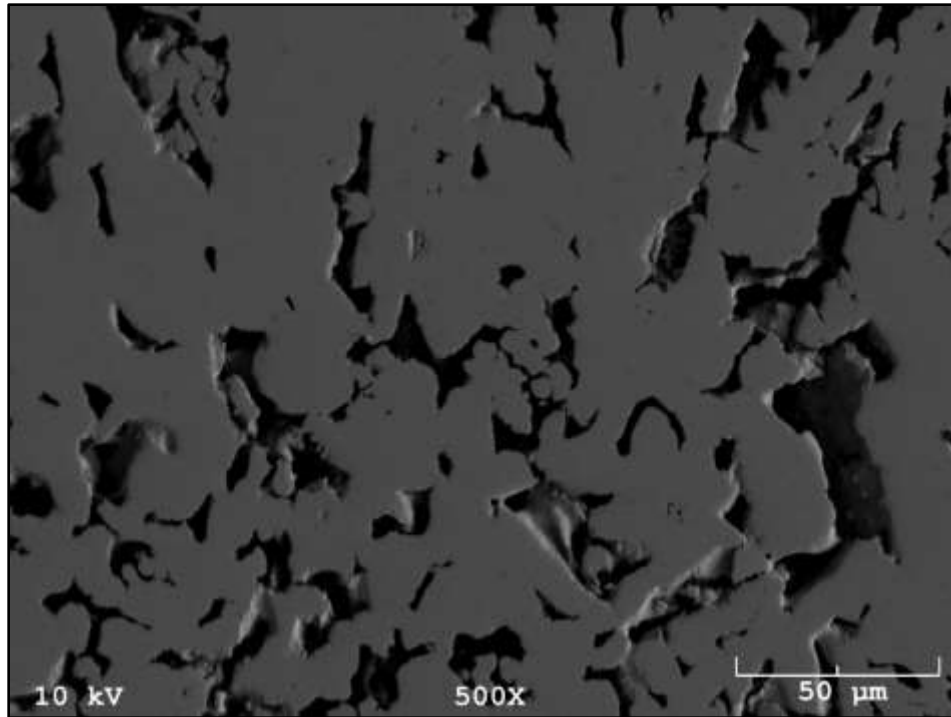


Figure A5-15: 70.9 %TD U HDH pellet (17-1) at 500X

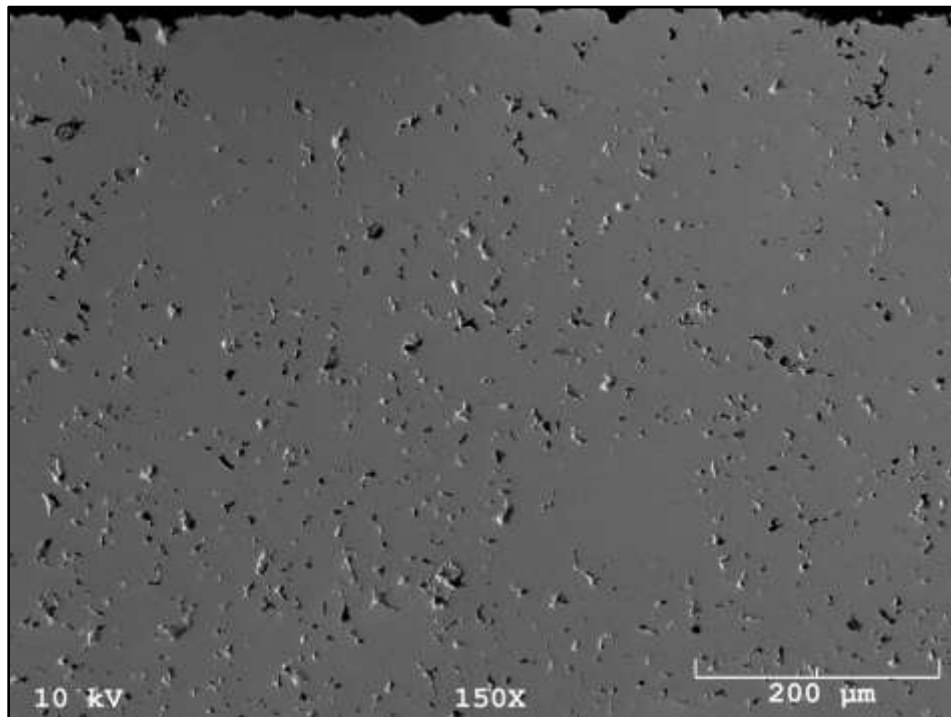


Figure A5-16: 87.0 %TD U HDH pellet (26-184) at 150X

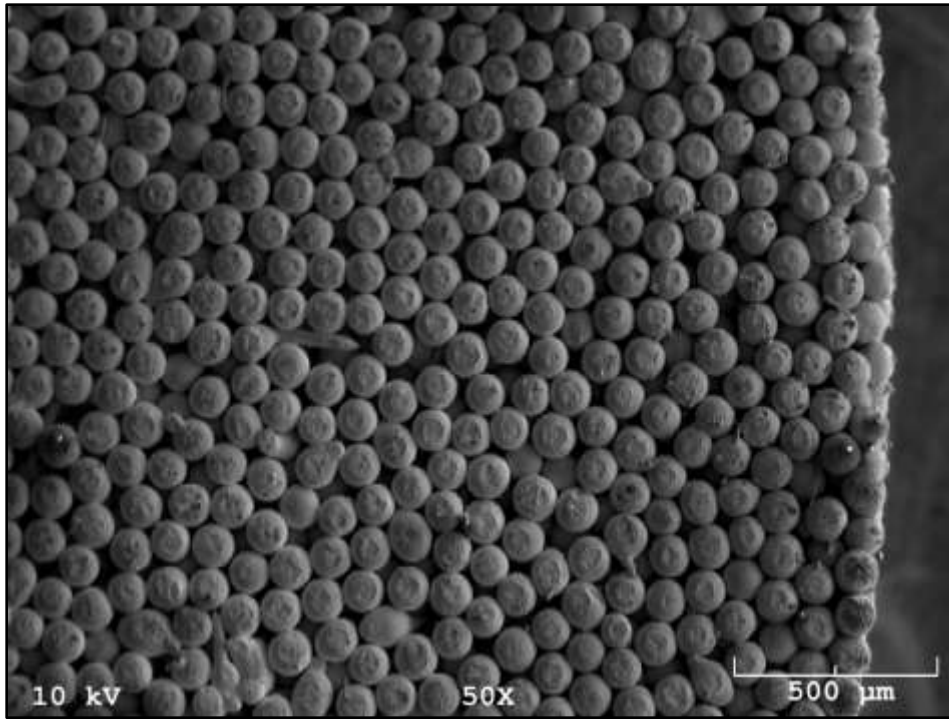


Figure A5-17: 65.55 %TD U spheres pellet (26-156) at 50X (surface)

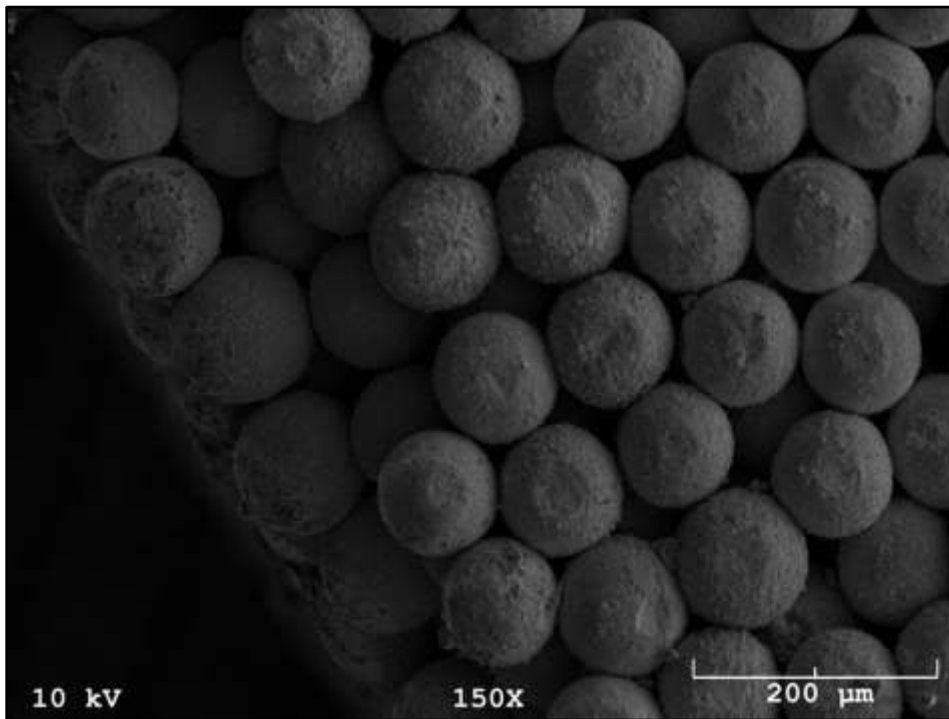


Figure A5-18: 65.55 %TD U spheres pellet (26-156) at 150X (surface edge)

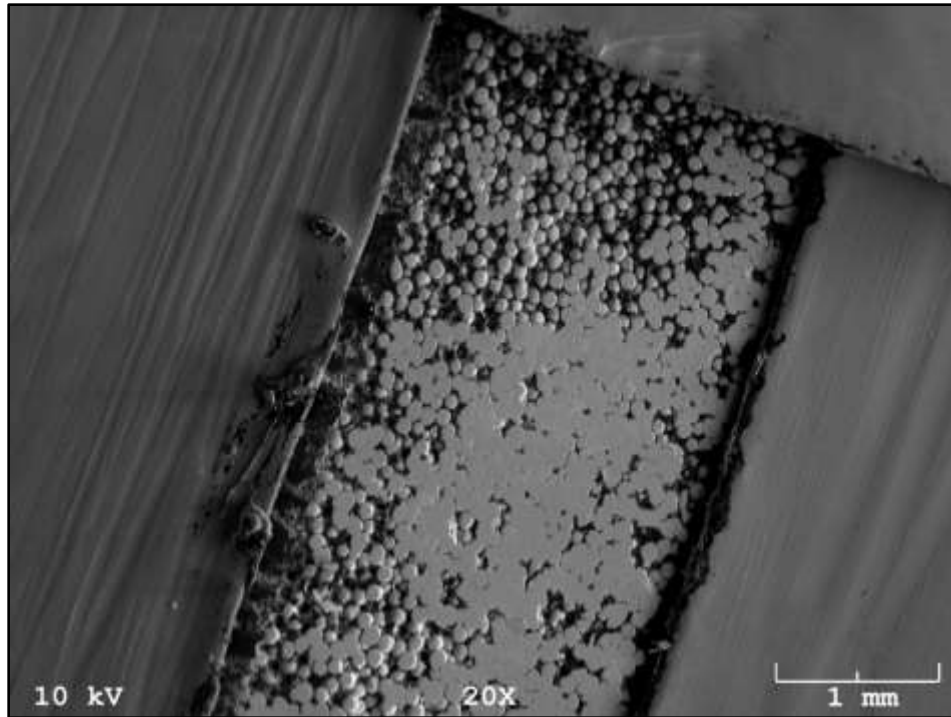


Figure A5-19: 65.55 %TD U spheres pellet (26-156) at 20X

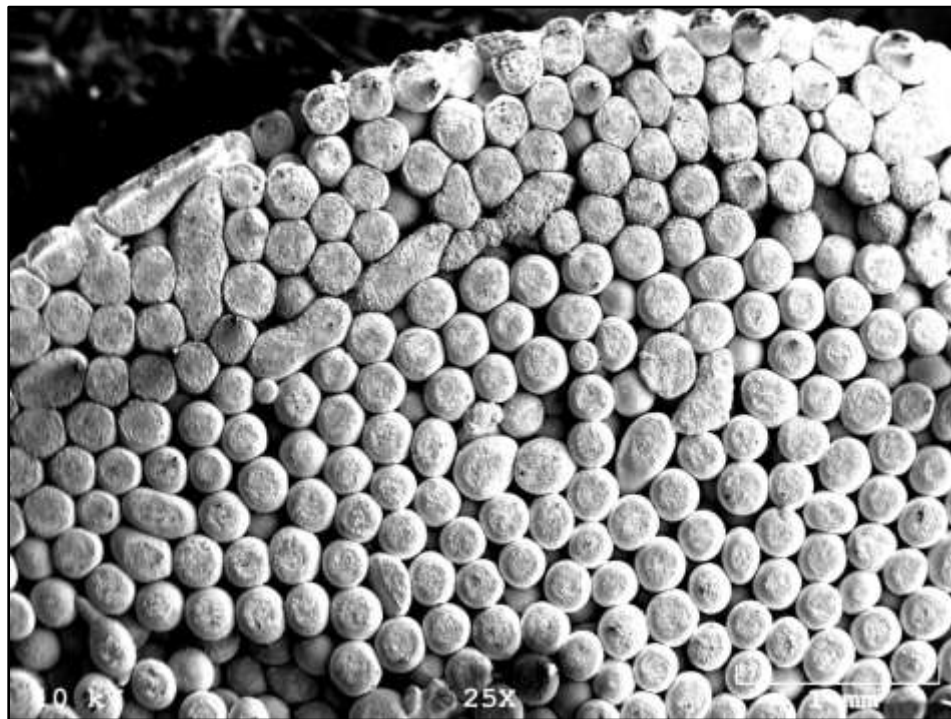


Figure A5-20: 74.35 %TD U spheres pellet (26-124) at 25X (surface)

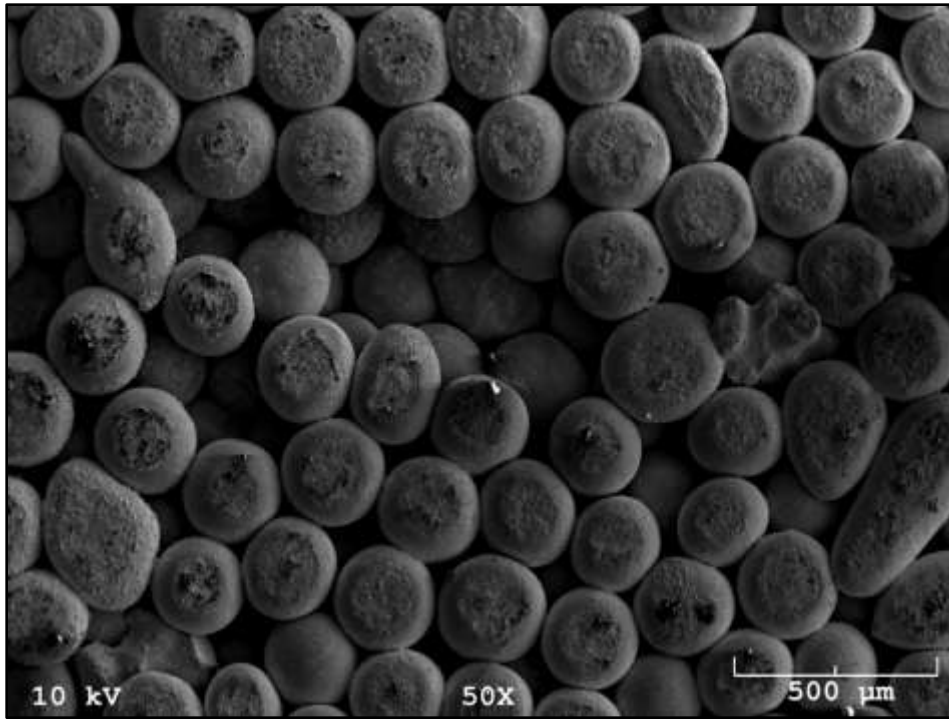


Figure A5-21: 74.35 %TD U spheres pellet (26-124) at 50X (surface)

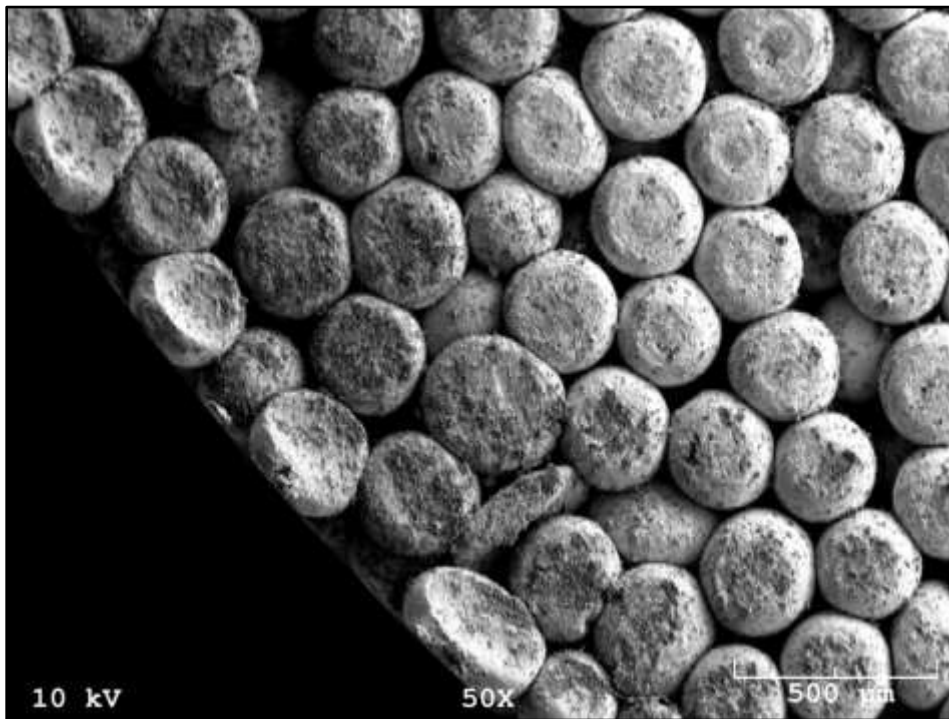


Figure A5-22: 75.08 %TD U spheres pellet (26-121) at 50X (surface edge)

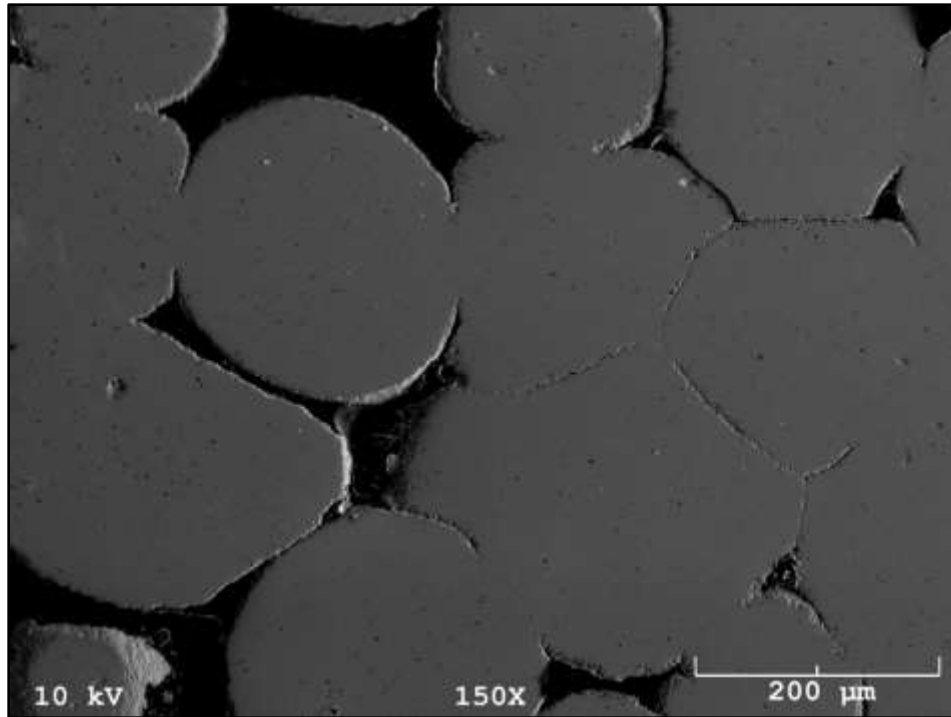


Figure A5-23: 75.08 %TD U spheres pellet (26-121) at 150X

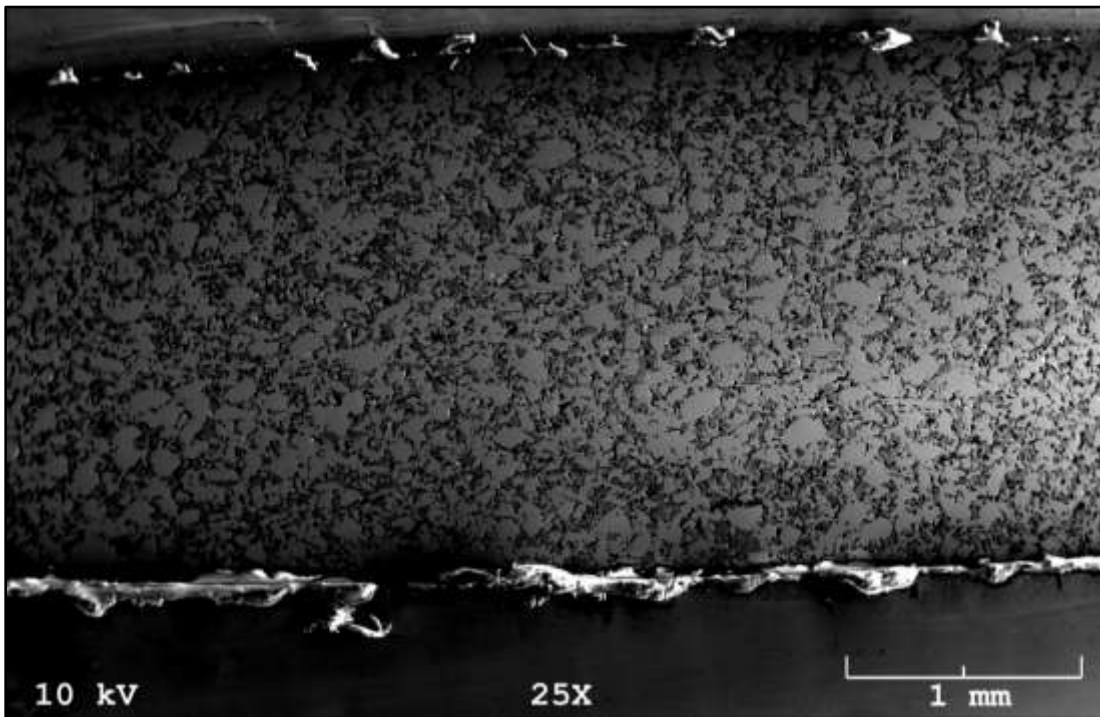


Figure A5-24: 67.94%TD U-5Zr HDH pellet (17-14) at 25X

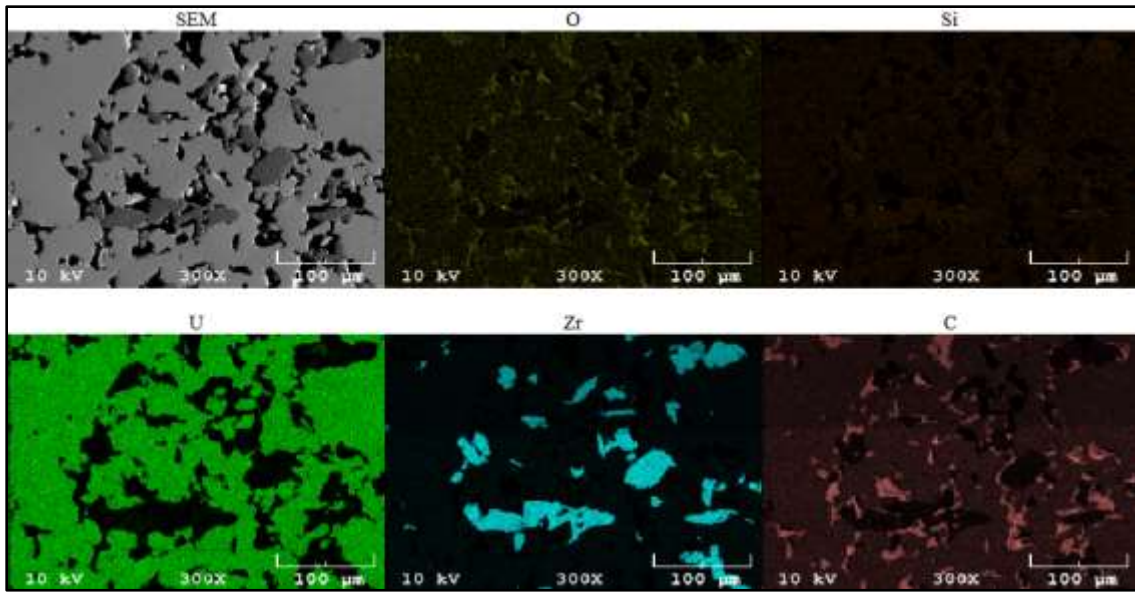


Figure A5-25: EDX mapping of 67.94%TD U-5Zr HDH pellet (17-14) at 300X

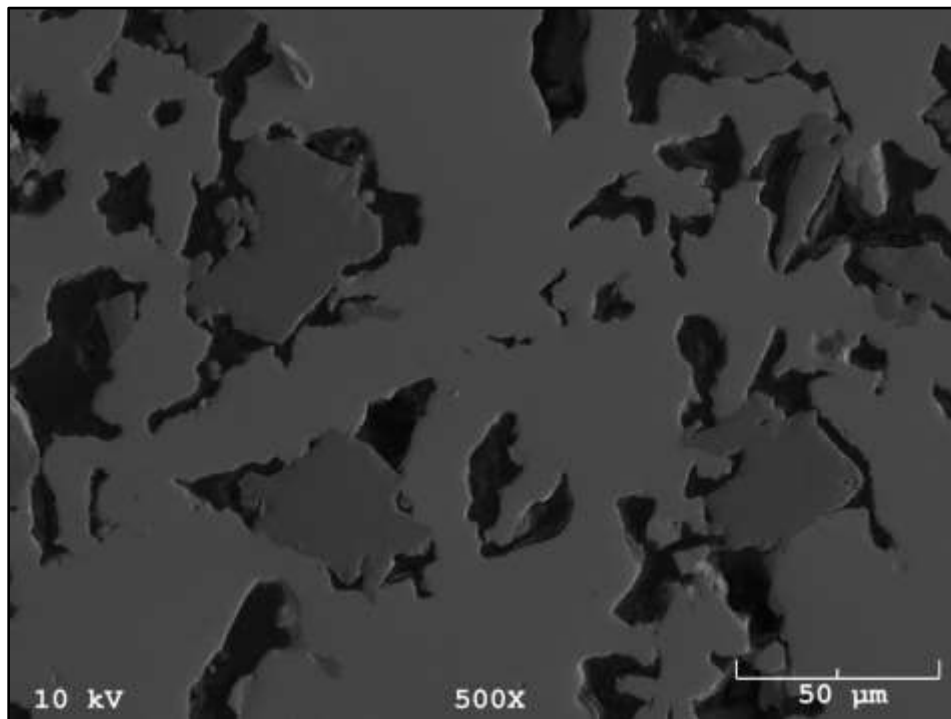


Figure A5-26: 67.94%TD U-5Zr HDH pellet (17-14) at 25X

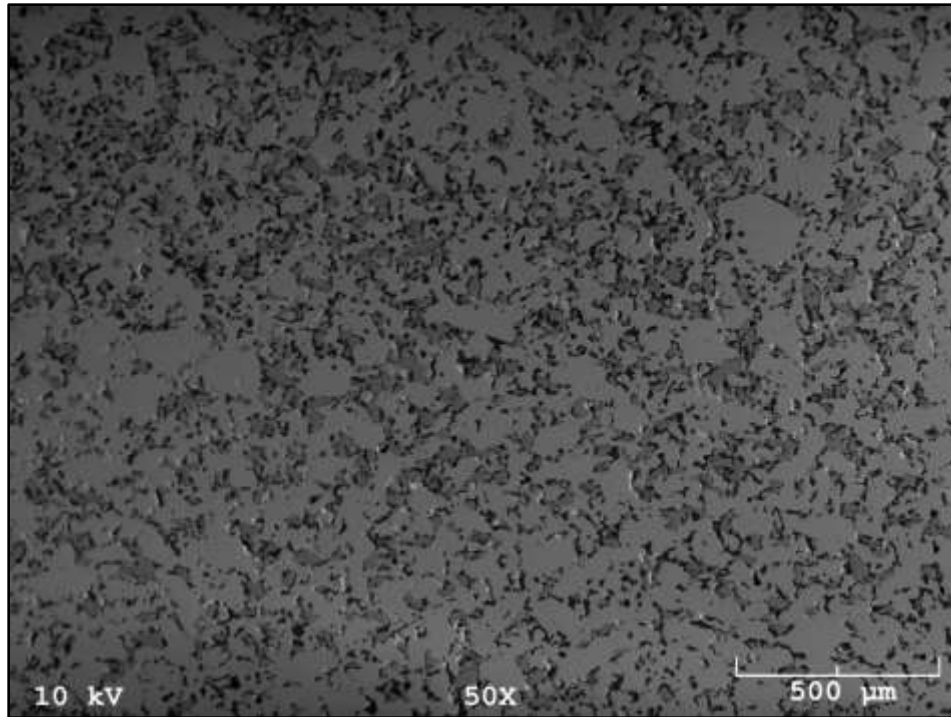


Figure A5-27: 72.5% TD U-5Zr HDH pellet (31-50A) at 50X

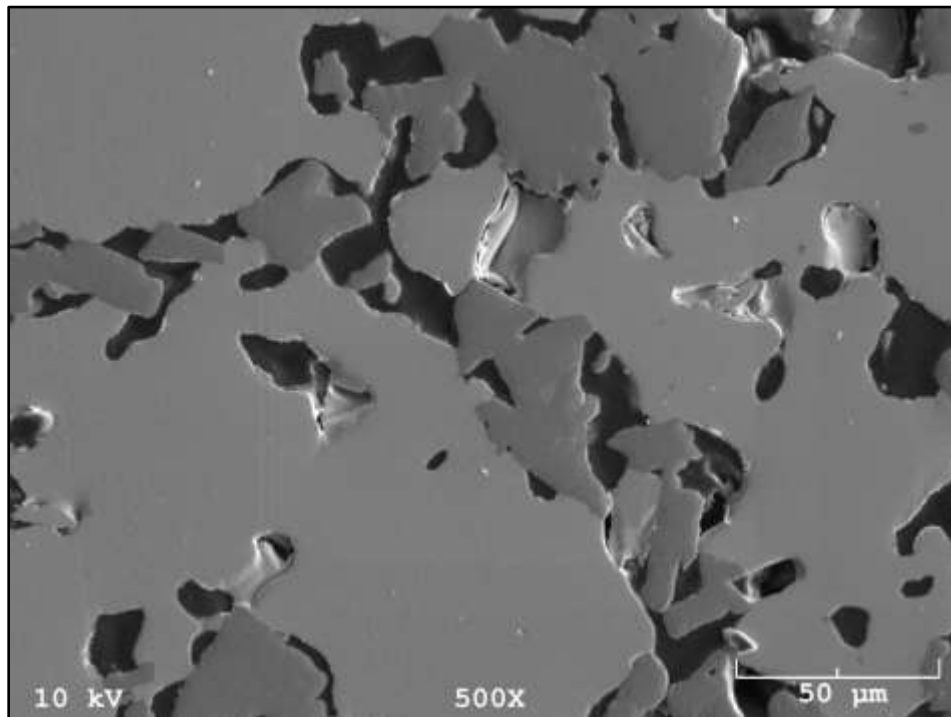


Figure A5-28: 72.5% TD U-5Zr HDH pellet (31-50A) at 500X

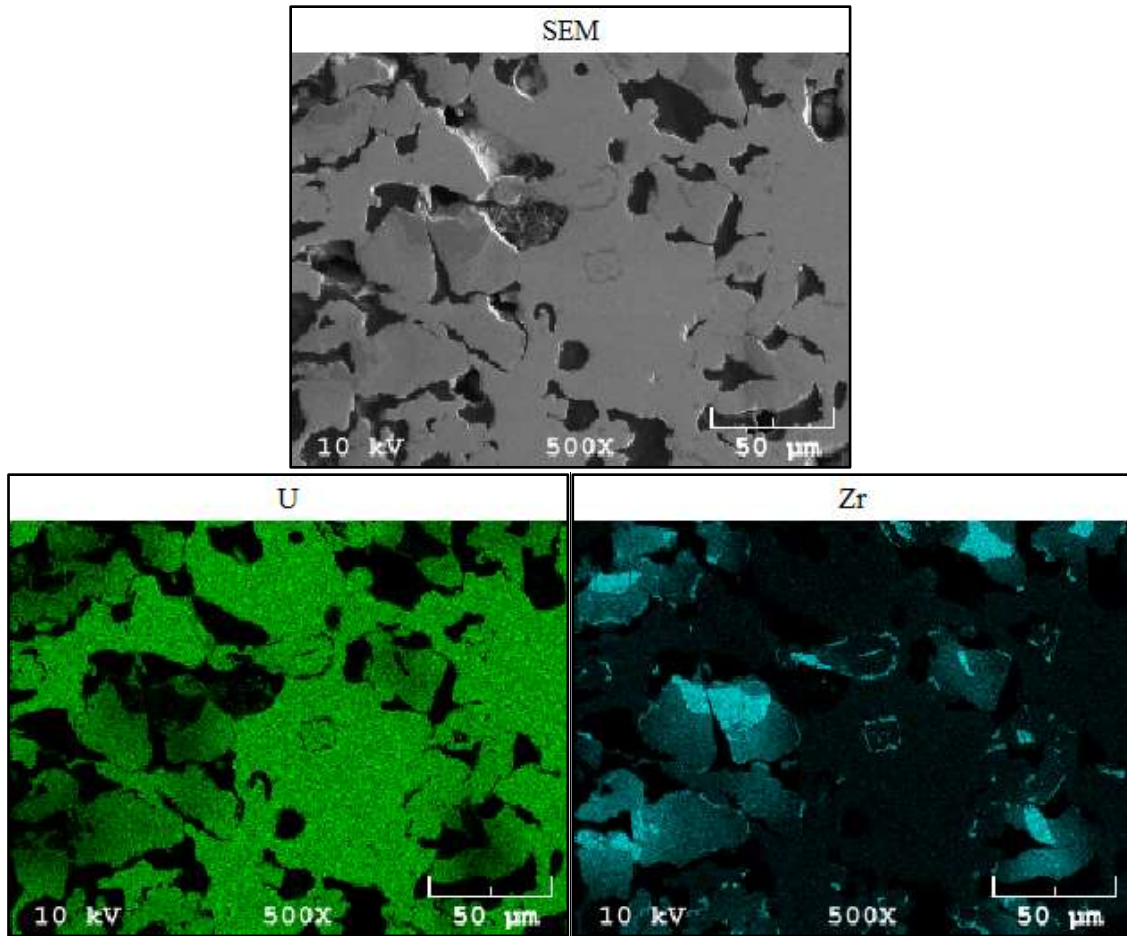


Figure A5-29: 72.5%TD U-5Zr HDH pellet (31-50A) at 500X

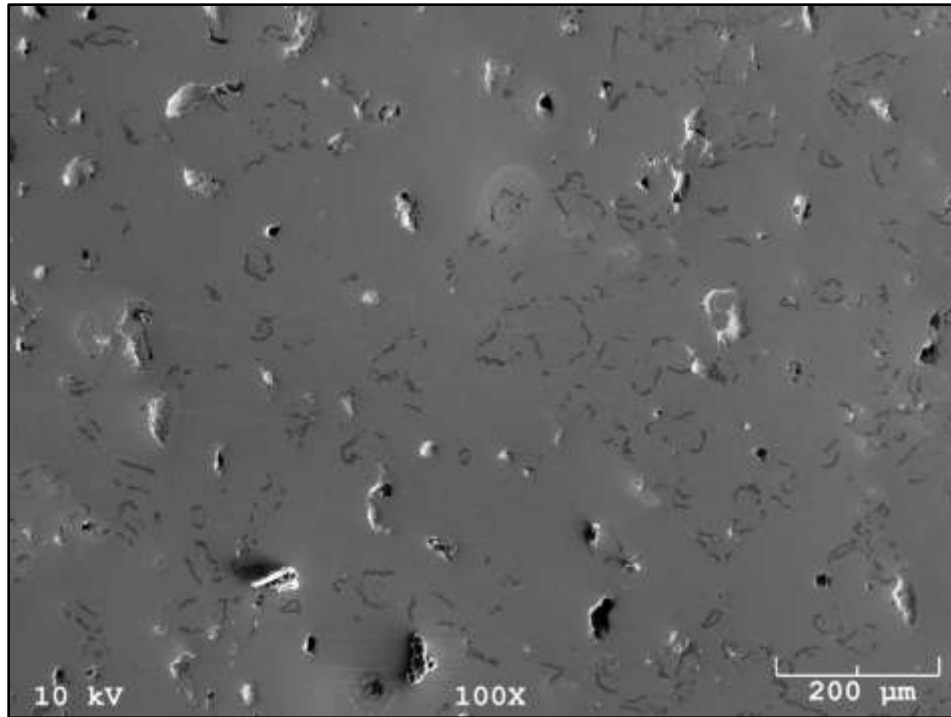


Figure A5-30: 80.6% TD U-5Zr HDH pellet (31-63B) at 100X

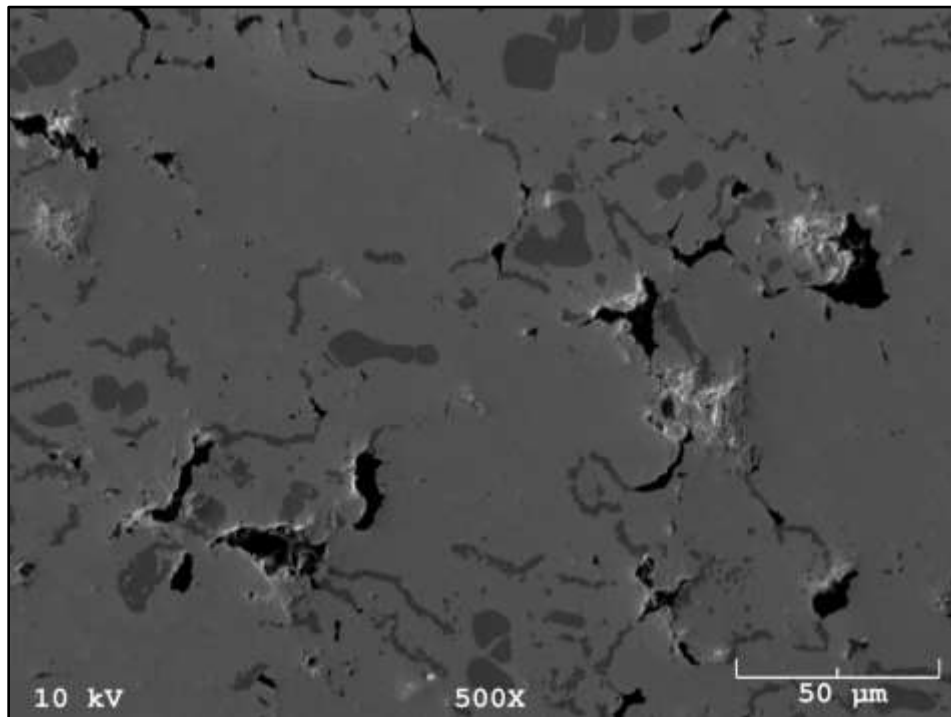


Figure A5-31: 80.6% TD U-5Zr HDH pellet (31-63B) at 500X

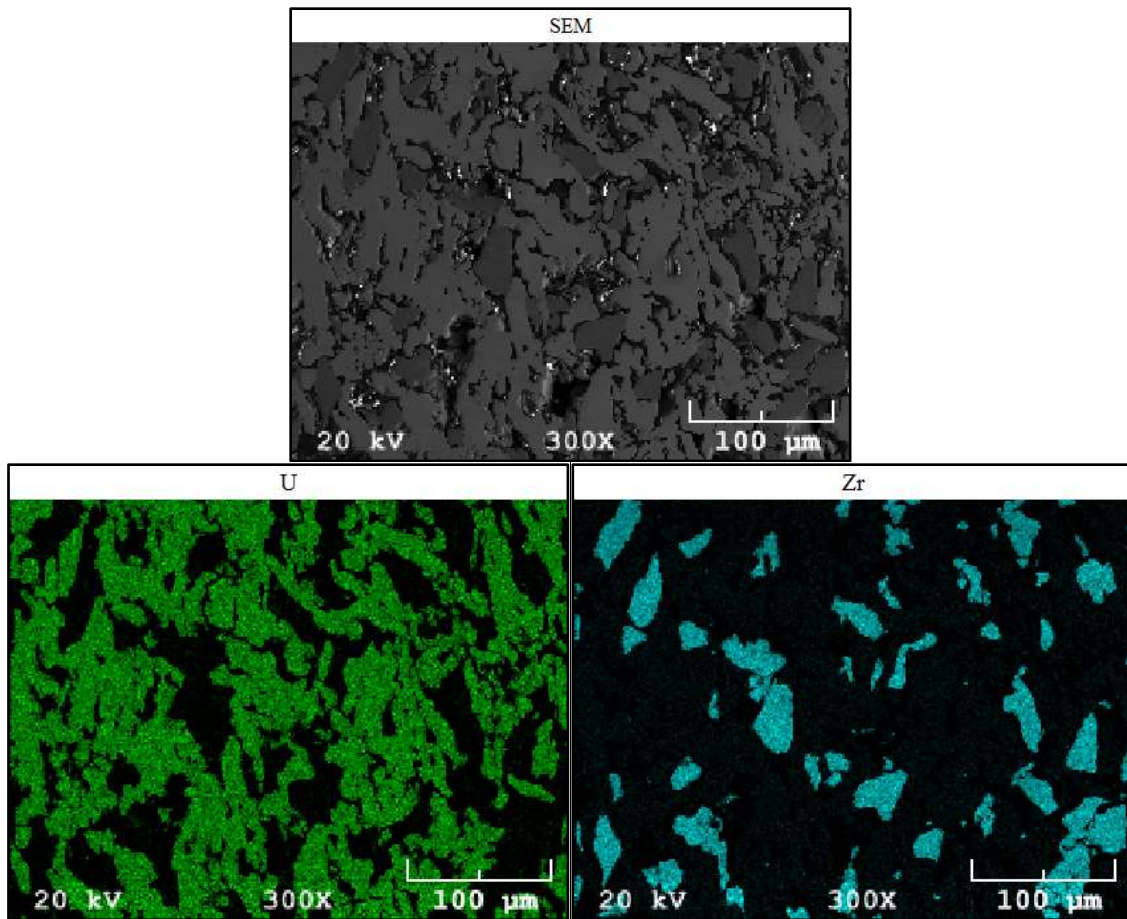


Figure A5-32: 54.74%TD U-10Zr HDH pellet (17-5A) at 300X

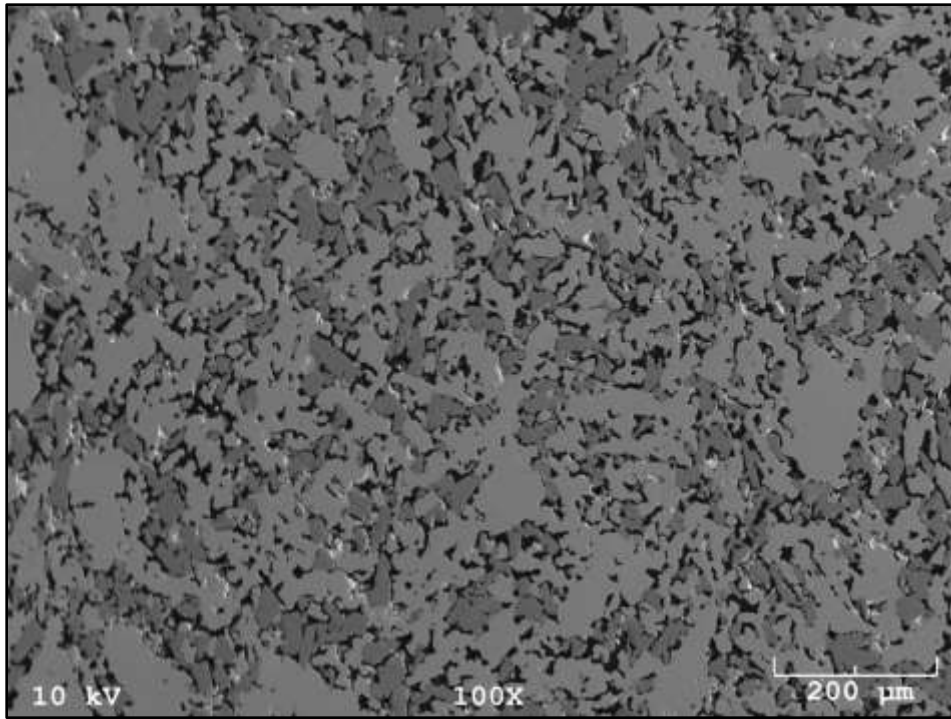


Figure A5-33: 61.2% TD U-10Zr HDH pellet (17-7B) at 100X

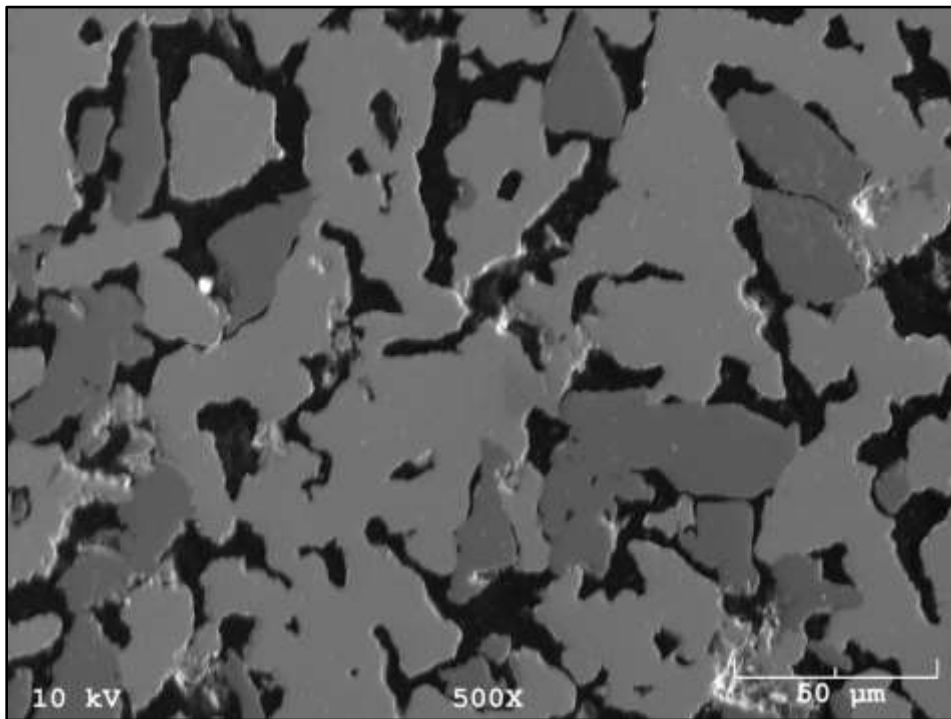


Figure A5-34: 61.2% TD U-10Zr HDH pellet (17-7B) at 500X

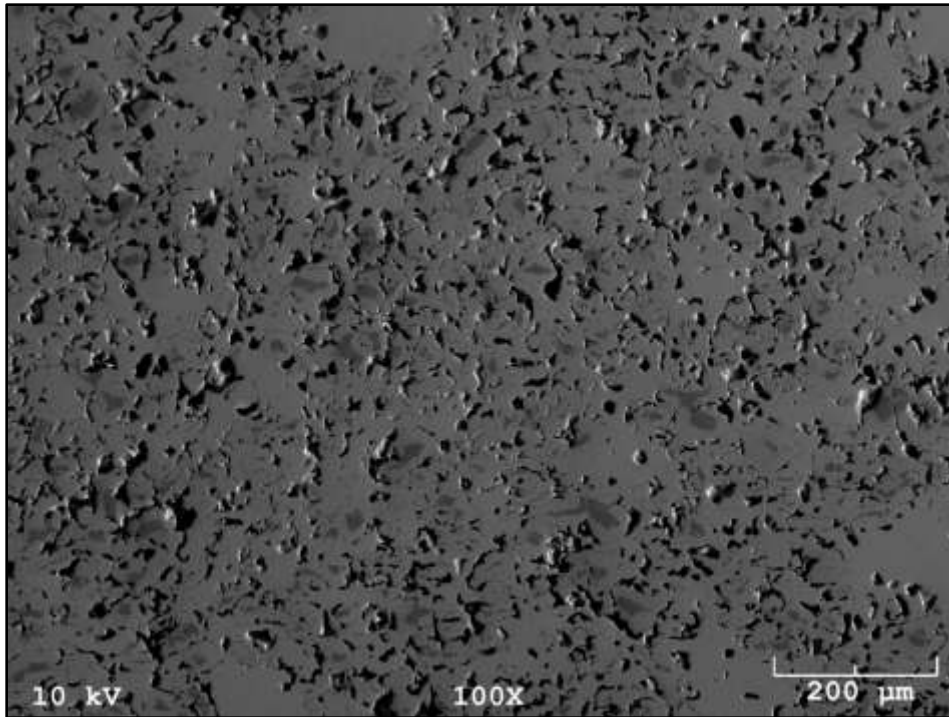


Figure A5-35: 76.1%TD U-10Zr HDH pellet (17-9B) at 100X

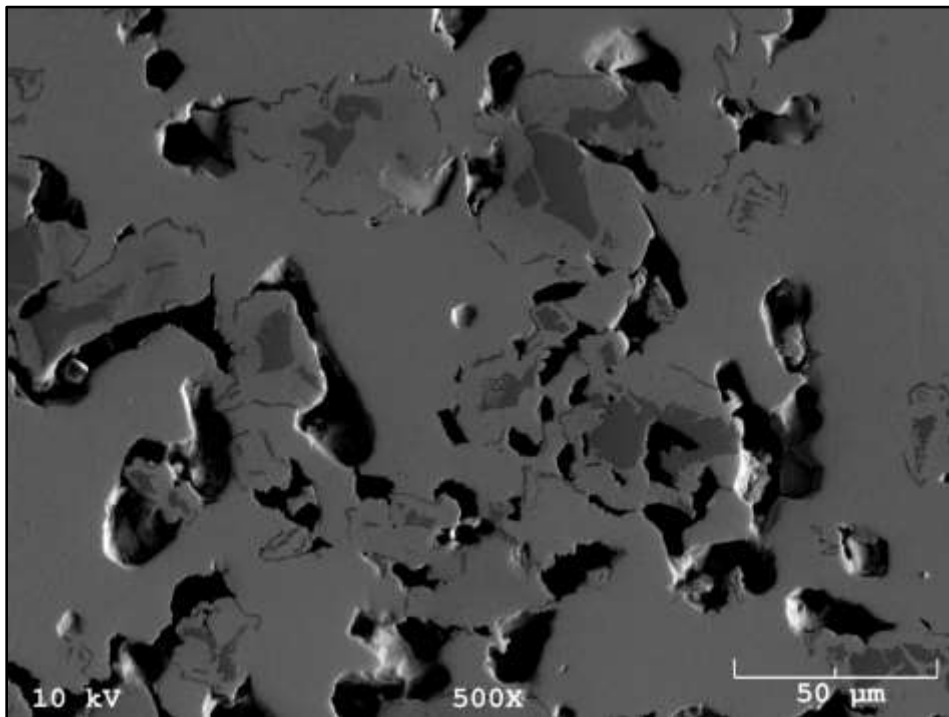


Figure A5-36: 76.1%TD U-10Zr HDH pellet (17-9B) at 500X

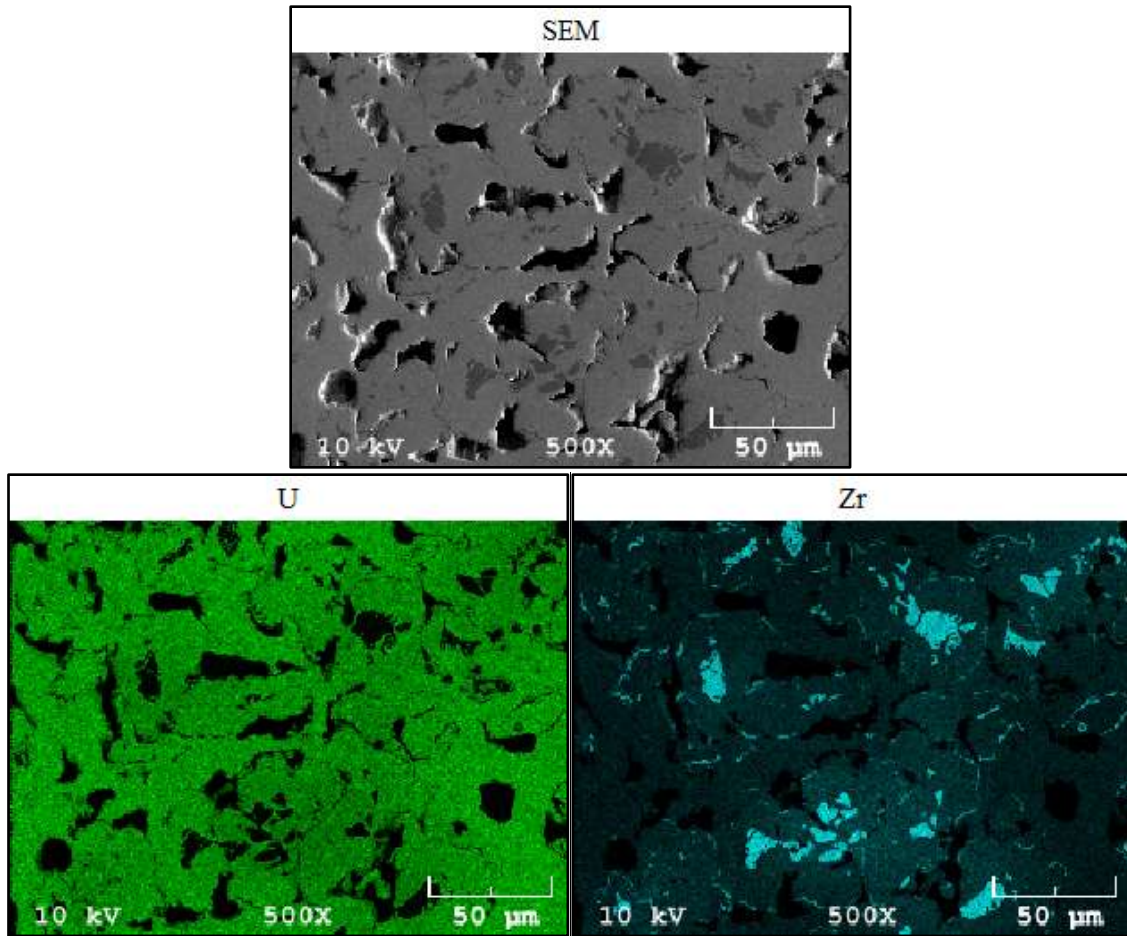


Figure A5-37: 76.1%TD U-10Zr HDH pellet (17-9B) at 500X

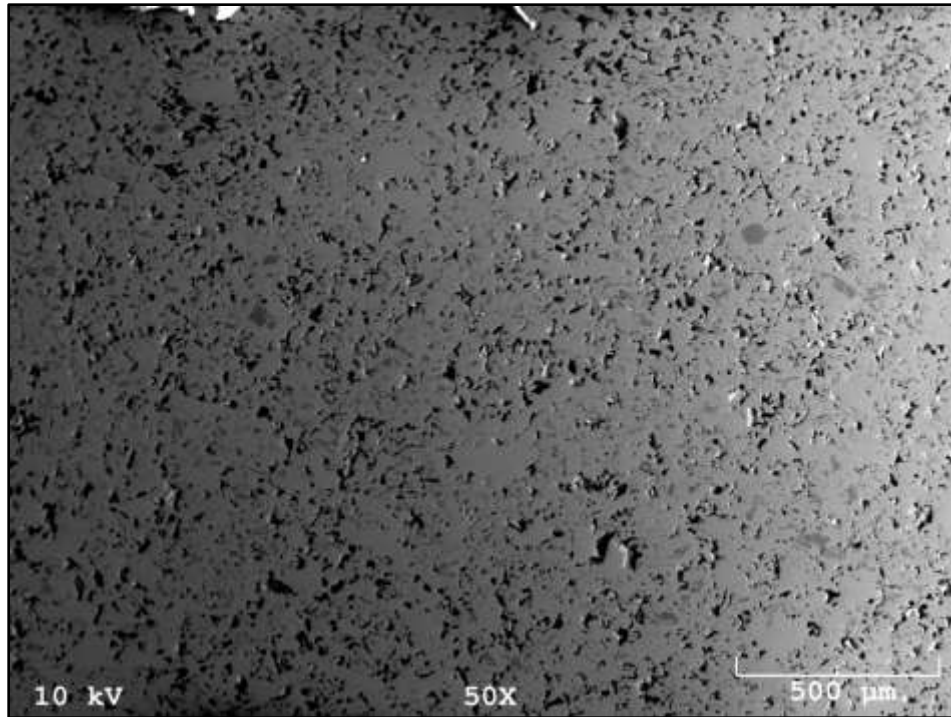


Figure A5-38: 79.55% TD U-10Zr HDH pellet (17-11B) at 50X

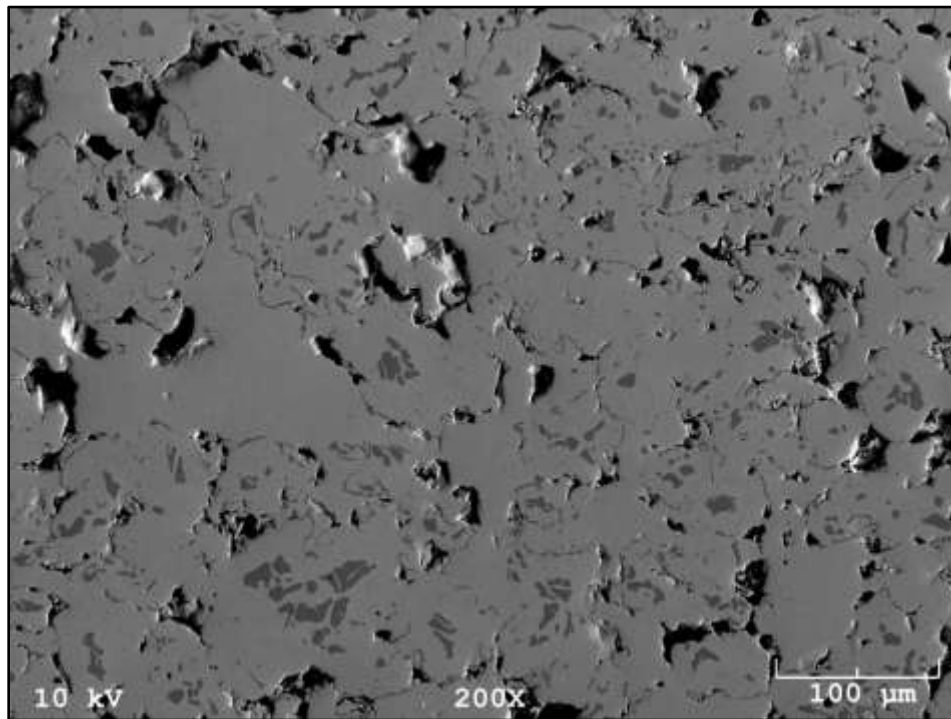


Figure A5-39: 79.55% TD U-10Zr HDH pellet (17-11B) at 200X

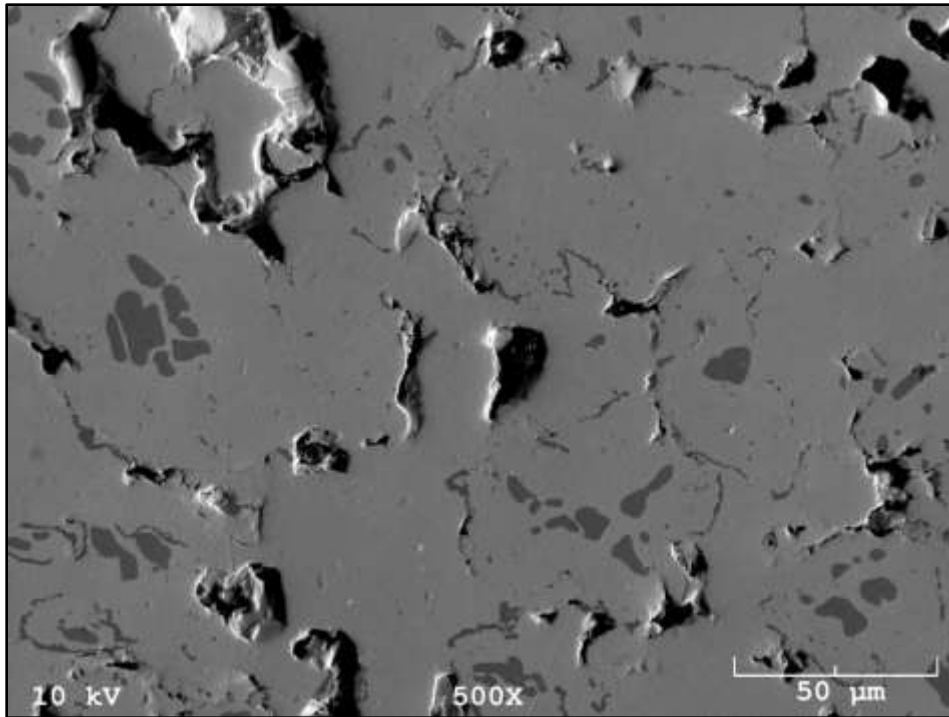


Figure A5-40: 79.55%TD U-10Zr HDH pellet (17-11B) at 500X

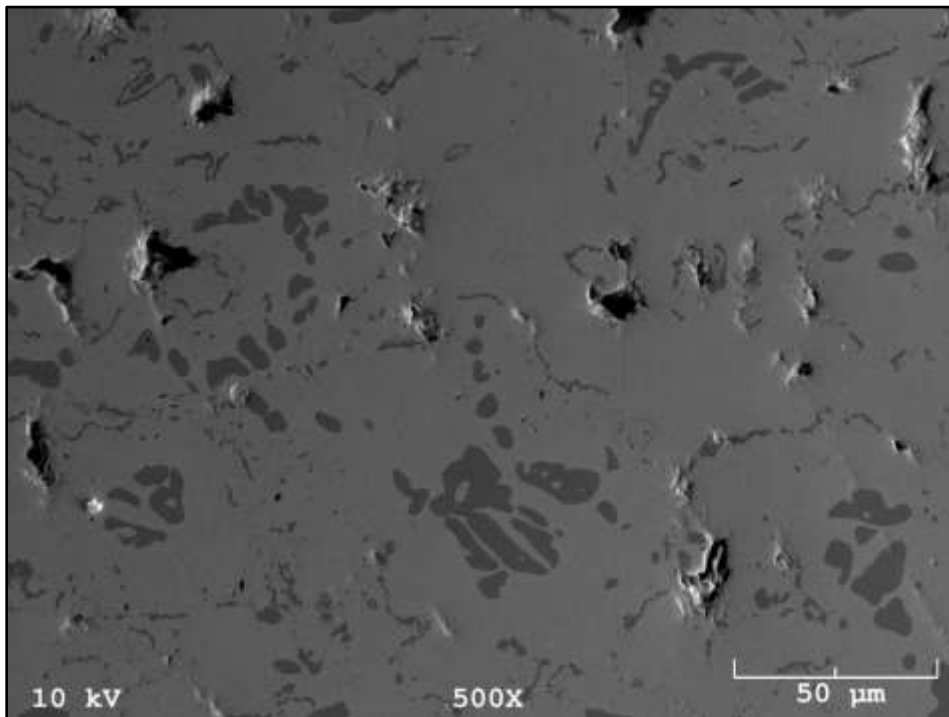


Figure A5-41: 83.49%TD U-10Zr HDH pellet (17-11A) at 500X

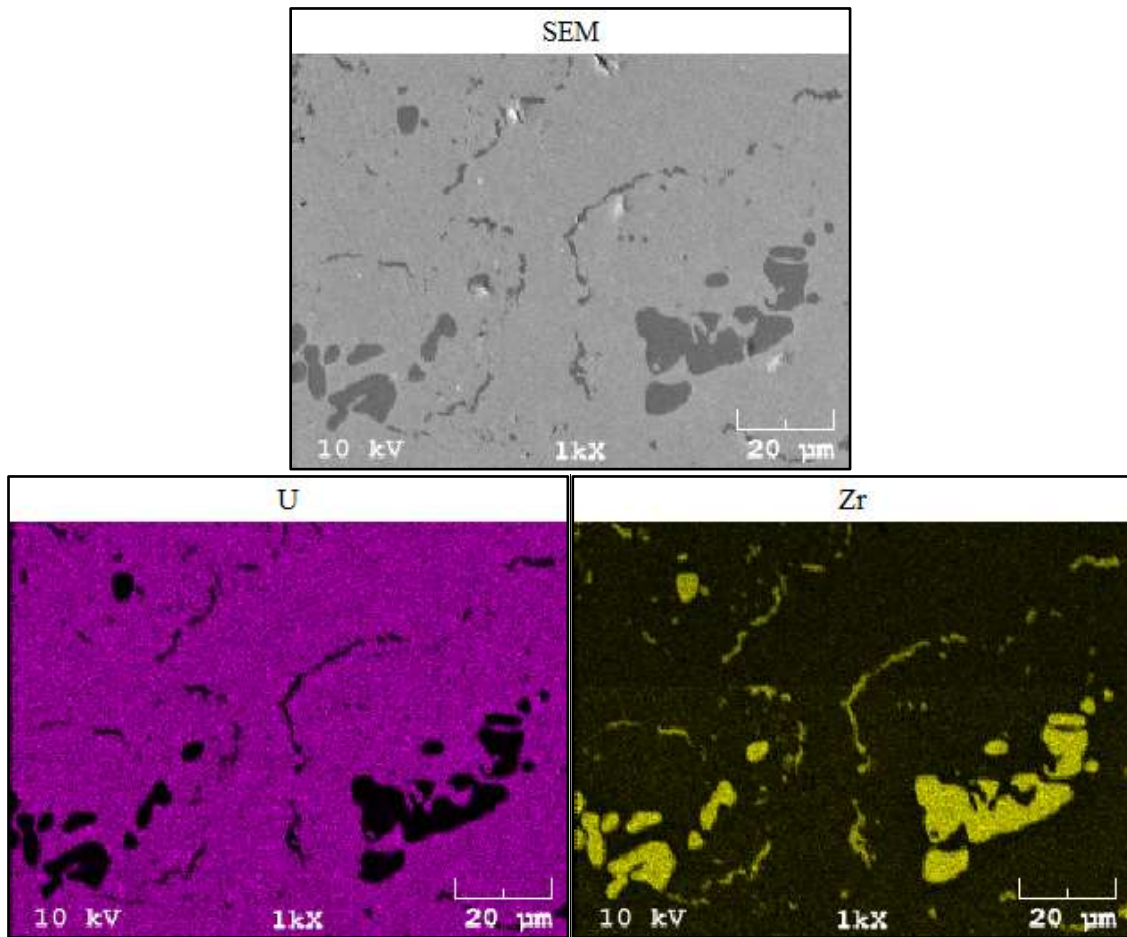


Figure A5-42: 83.49% TD U-10Zr HDH pellet (17-11A) at 1000X

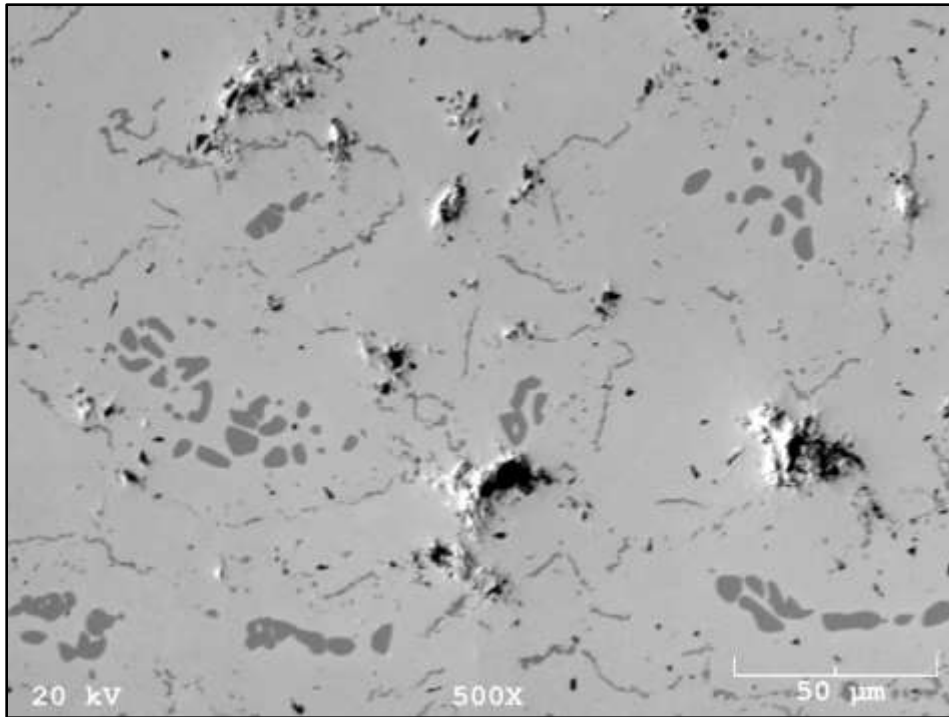


Figure A5-43: 83.8%TD U-10Zr HDH pellet (31-45) at 500X

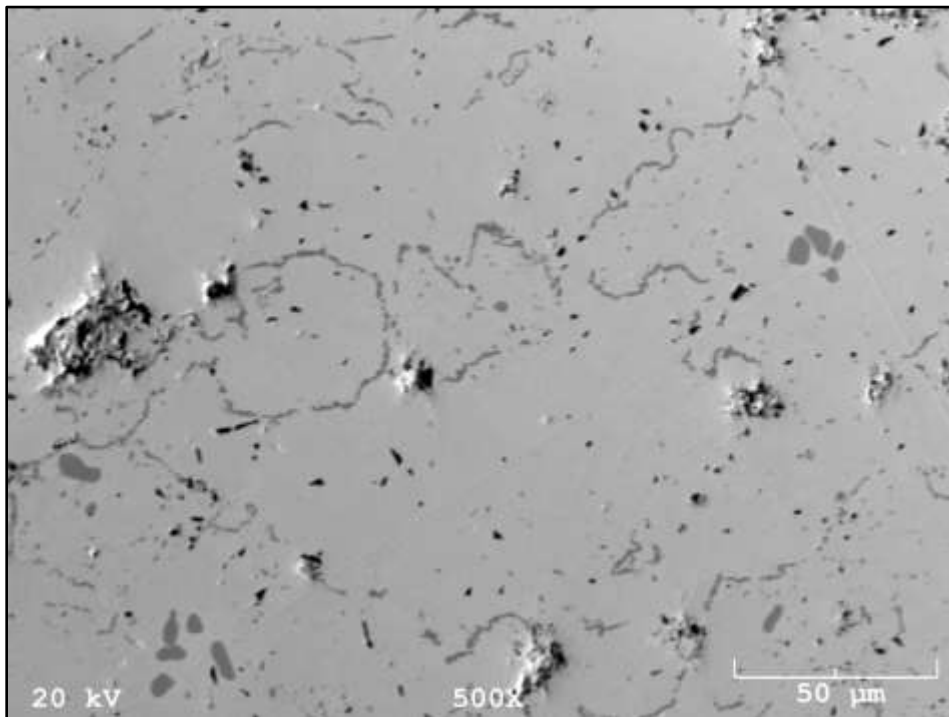


Figure A5-44: 83.8%TD U-10Zr HDH pellet (31-45) at 500X

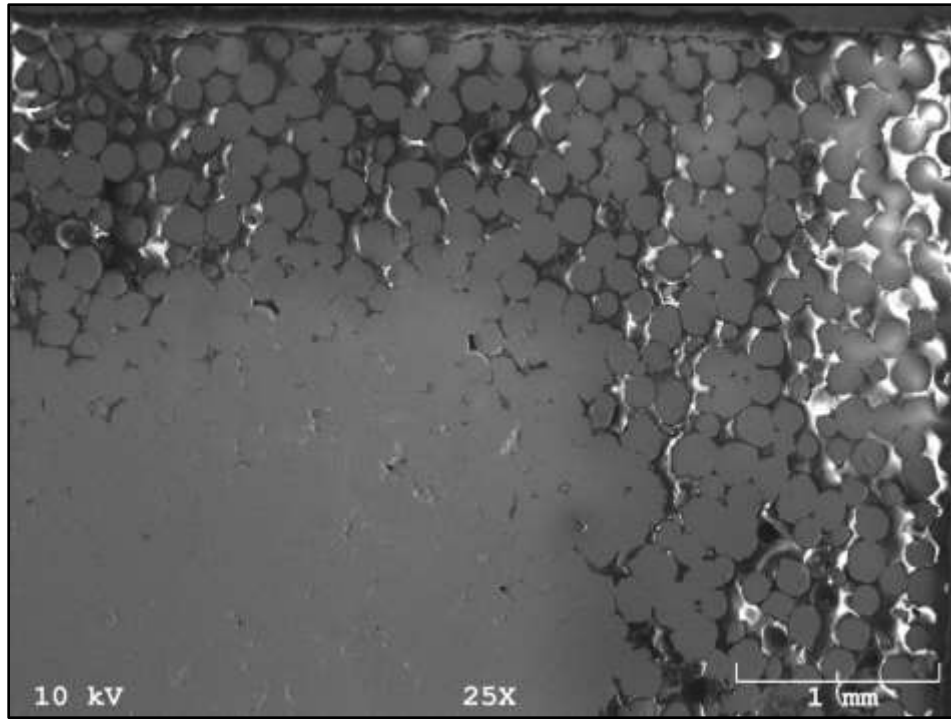


Figure A5-45: 73.25% TD U-10Zr spheres pellet (26-174) at 25X

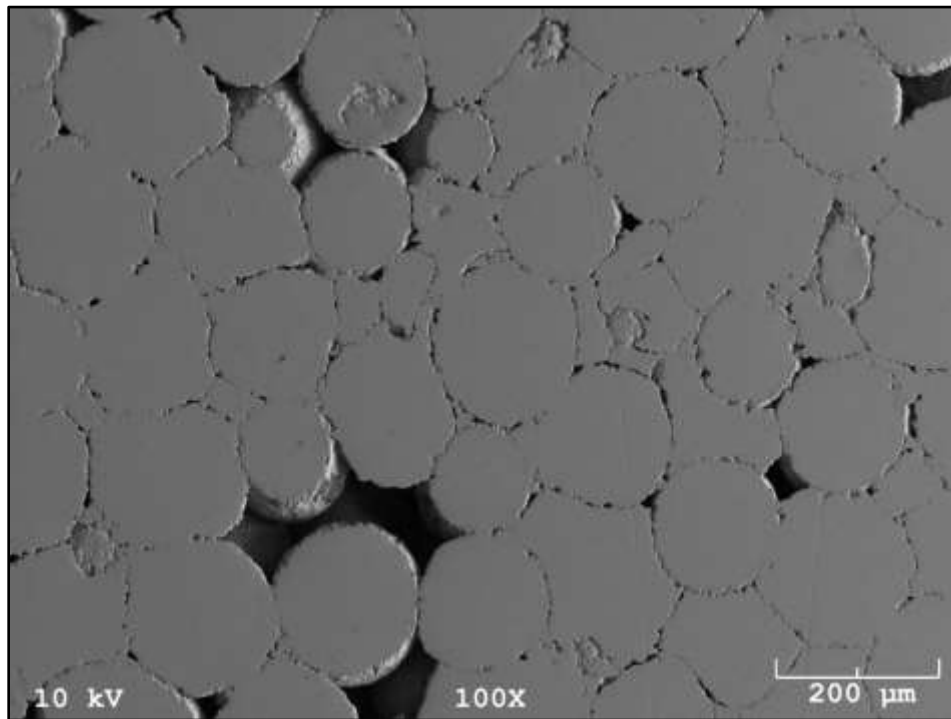


Figure A5-46: 73.25% TD U-10Zr spheres pellet (26-174) at 100X

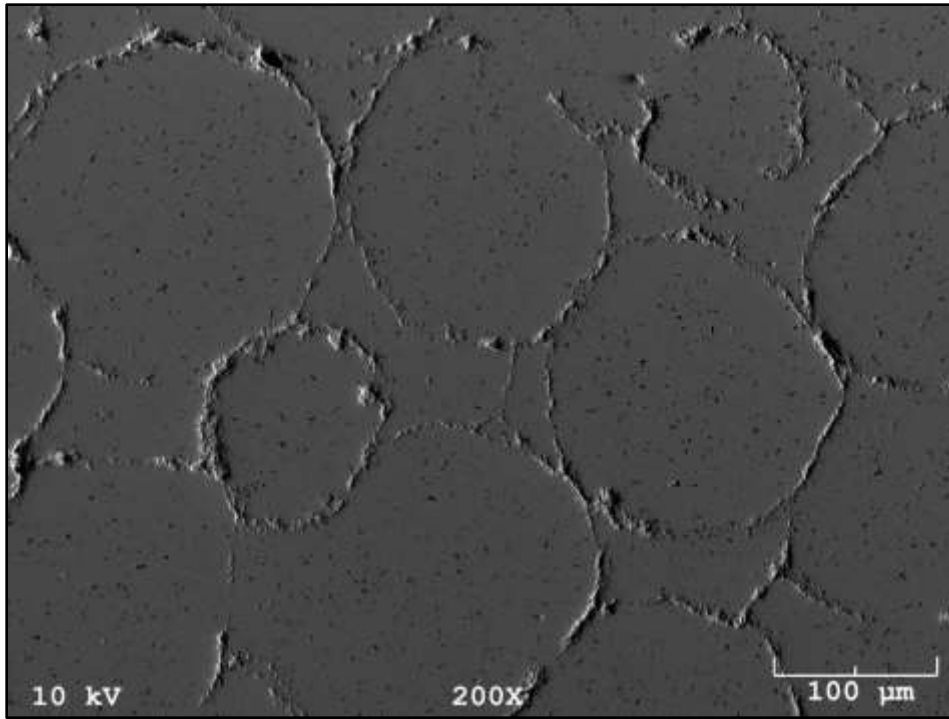


Figure A5-47: 73.25% TD U-10Zr spheres pellet (26-174) at 200X

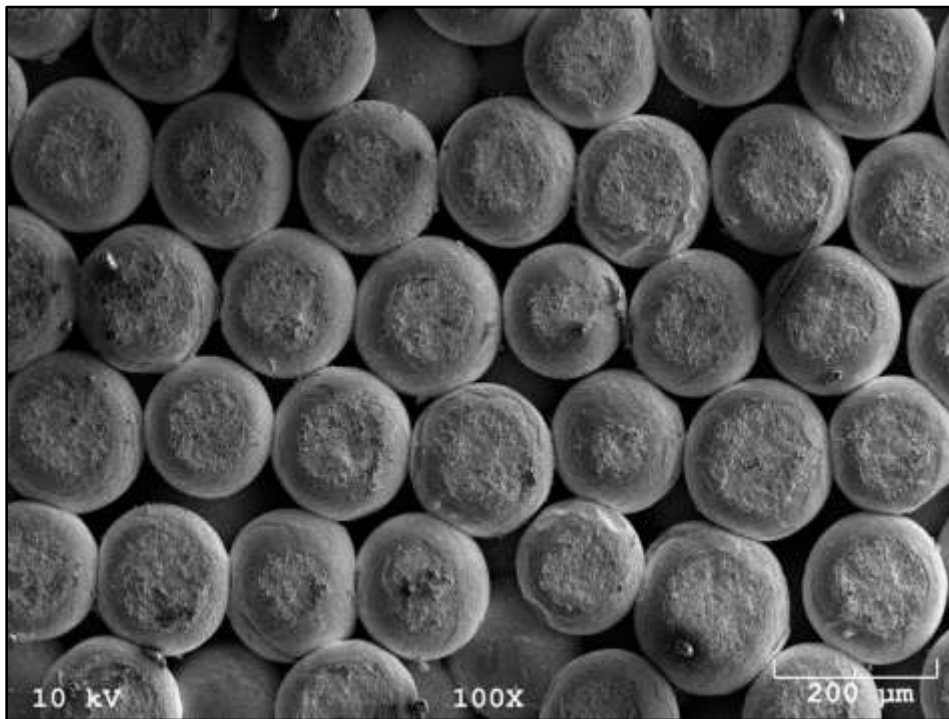


Figure A5-48: 80.96% TD U-10Zr spheres pellet (26-120) at 100X (surface)



Figure A5-49: 80.96% TD U-10Zr spheres pellet (26-120) at 200X (surface)

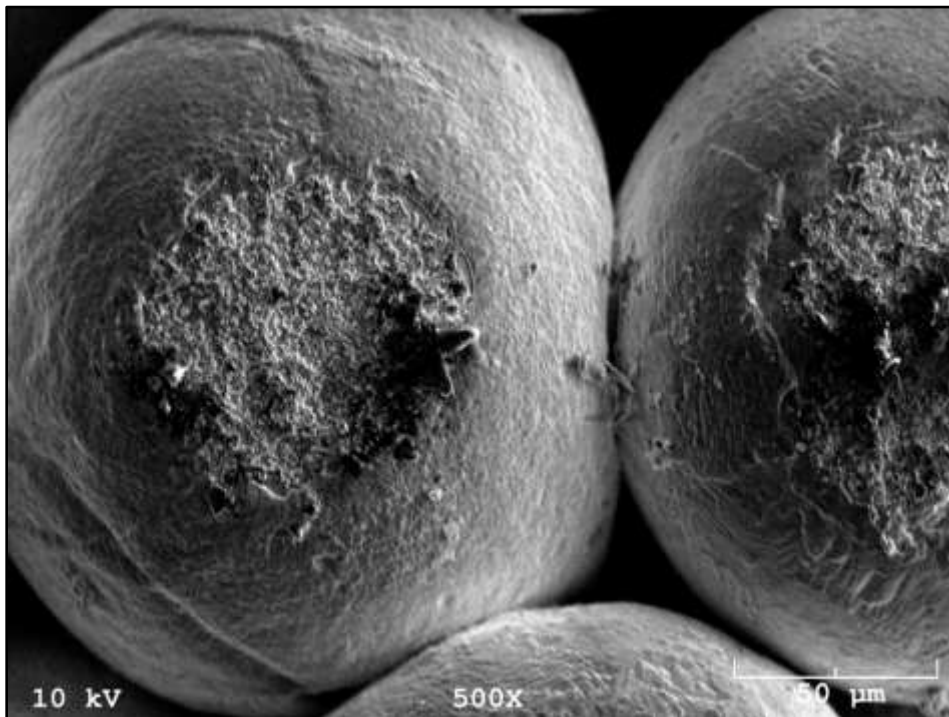


Figure A5-50: 80.96% TD U-10Zr spheres pellet (26-120) at 500X (surface)

APPENDIX 6

SINTERING DATA FOR LFA PELLETS

This appendix contains the sintering data pertaining to the pellets that were used to gather data from the LFA experiments. There were other pellets that were not included for various reasons because they were either deemed not reliable for LFA experiments or the pellet was damaged or destroyed. In each table the samples are listed in order of increasing density. The data included the percent theoretical density, the geometric density, the Archimedes density, the force used in the pressing process, the sintering time, the sintering temperature, the green pellet density, and the sample identification number. The tables in order from A6-1 to A6-5 are U HDH, U spheres, U-5Zr HDH, U-10Zr HDH, and U-10Zr spheres.

Table A6-1: Sintering data for U HDH pellets

%TD	Geometric	Archimedes	Press	Sinter	Sinter	Green	Sample
	Density	Density	Force	Time	Temperature	Density	ID#
	g/cm ³	g/cm ³	Lb	hr	°C	g/cm ³	
45.52	8.99	8.69	2000	0.33	814	7.47	26-182
46.62	8.58	8.90	2000	0.02	800	7.67	31-68
53.72	10.26		2000	0.50	850	7.89	31-32
56.54	10.75	10.80	2000	0.25	850	8.06	26-180
57.62	10.88	11.01	2000	0.50	850		31-33
60.14	11.49		2000	1.00	850	8.04	31-31
62.47	11.93		2000	2.00	850	8.13	31-30
64.68	12.35		2000	12.00	850		1-192
64.79	12.37	12.37	2000	4.00	850	8.26	31-29
66.02	12.42	12.61	2000	4.00	900	7.93	31-42
70.90	13.00	13.54	2000	2.00	950	7.93	17-1
78.28	14.60	14.95	6000	2.00	950	9.68	17-2
82.46	15.80	15.75	5000	4.00	950	8.95	26-189
85.81	15.27	16.39	15000	12.00	950	11.64	31-44
86.94	16.35	16.60	5000	12.00	950	9.22	26-184
88.60		16.92	4000	6.00	1100		31-77B

Table A6-2: Sintering data for U spheres pellets

%TD	Geometric	Archimedes	Press	Sinter	Sinter	Green	Sample
	Density	Density	Force	Time	Temperature	Density	ID#
	g/cm ³	g/cm ³	Lb	hr	°C	g/cm ³	
65.55	12.52			24.00	860		26-156
75.08	14.34			24.00	907		26-121
75.60	14.44			4.00	860		1-173
87.73	15.47	16.76		6.00	950		26-188
87.88	15.37	16.78		48.00	950		26-179
94.12	17.52	17.98		24.00	950		26-183

Table A6-3: Sintering data for U-5Zr HDH pellets

%TD	Geometric	Archimedes	Press	Sinter	Sinter	Green	Sample
	Density	Density	Force	Time	Temperature	Density	ID#
	g/cm ³	g/cm ³	Lb	hr	°C	g/cm ³	
47.95	9.00	8.42	2000	0.33	870	7.65	17-31B
52.56	9.11	9.23	2000	0.02	861	7.87	17-22B
54.02	9.33	9.49	2000	0.02	850	7.54	17-18B
62.15	10.47	10.91	2000	1.28	947		31-51
66.45	11.07	11.67	2000	0.25	950	7.60	17-20
67.94	11.75	11.93	2000	2.75	950	7.80	17-14
72.50	11.98	12.73	2000	1.03	965		31-50A
73.26	12.50	12.86	2000	3.00	950	7.63	31-55
74.06	12.75	13.00	2000	4.00	950	7.80	17-16B
76.66	12.76	13.46	5000	1.03	965		31-50B
79.79	13.41	14.01	3000	6.00	950	8.09	17-21
80.11	13.21	14.07	4000	6.00	1000	7.75	31-60
80.62	13.45	14.16	6000	24.00	1000	7.77	31-63B
83.28	13.56	14.62	6000	12.00	1000	8.17	31-61

Table A6-4: Sintering data for U-10Zr HDH pellets

%TD	Geometric	Archimedes	Press	Sinter	Sinter	Green	Sample
	Density	Density	Force	Time	Temperature	Density	ID#
	g/cm ³	g/cm ³	Lb	hr	°C	g/cm ³	
47.65	7.77	7.63	2000	0.33	823	7.41	17-29
54.08	8.61	8.66	2000	0.02	861	7.26	17-22A
54.74	8.77		2000	0.25	900	7.03	17-5A
61.17	9.80		5000	0.25	900	8.06	17-5B
66.75	10.44	10.69	2000	1.00	900	7.07	17-7B
69.24	10.57	11.09	2000	3.00	900	7.05	17-9A
73.84	11.54	11.83	5000	1.00	900	8.33	17-7A
76.10	11.50	12.19	5000	3.00	900	8.15	17-9B
79.55	12.34	12.74	2000	12.00	950	7.14	17-11B
80.89	12.15	12.96	5000	12.00	900	8.21	17-10B
82.64	12.04	13.24	2000	12.00	900	7.13	17-10A
83.49	12.70	13.37	5000	12.00	950	8.13	17-11A
83.80	12.42	13.42	15000	12.00	950		31-45

Table A6-5: Sintering data for U-10Zr spheres pellets

%TD	Geometric	Archimedes	Press	Sinter	Sinter	Green	Sample
	Density	Density	Force	Time	Temperature	Density	ID#
	g/cm ³	g/cm ³	Lb	hr	°C	g/cm ³	
73.25	11.74			4.00	900		1-174
80.96	12.97			24.00	963		26-120
87.40	12.90	14.00		24.00	950		31-47

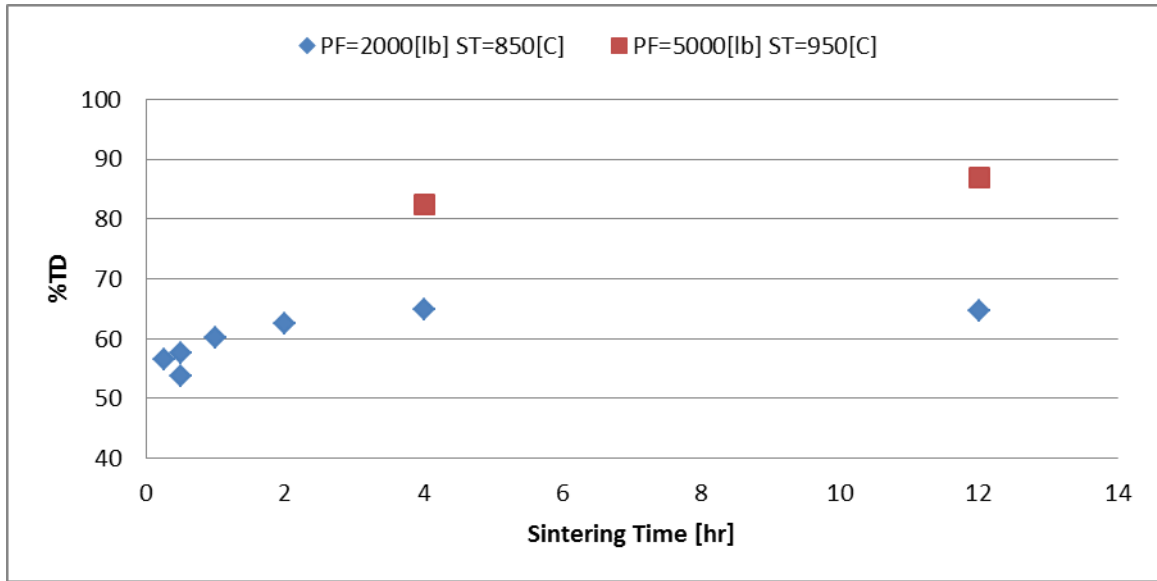


Figure A6-1: Sintering data for U HDH pellets at two different pressing forces and two different sintering temperatures

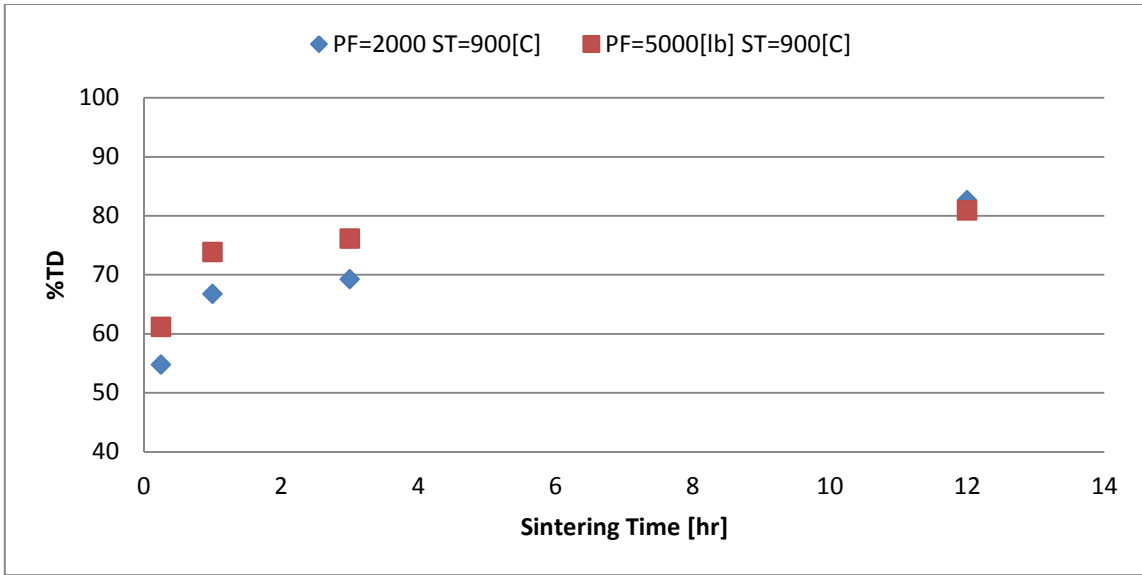


Figure A6-2: Sintering data for U-10Zr HDH pellets at two different pressing forces

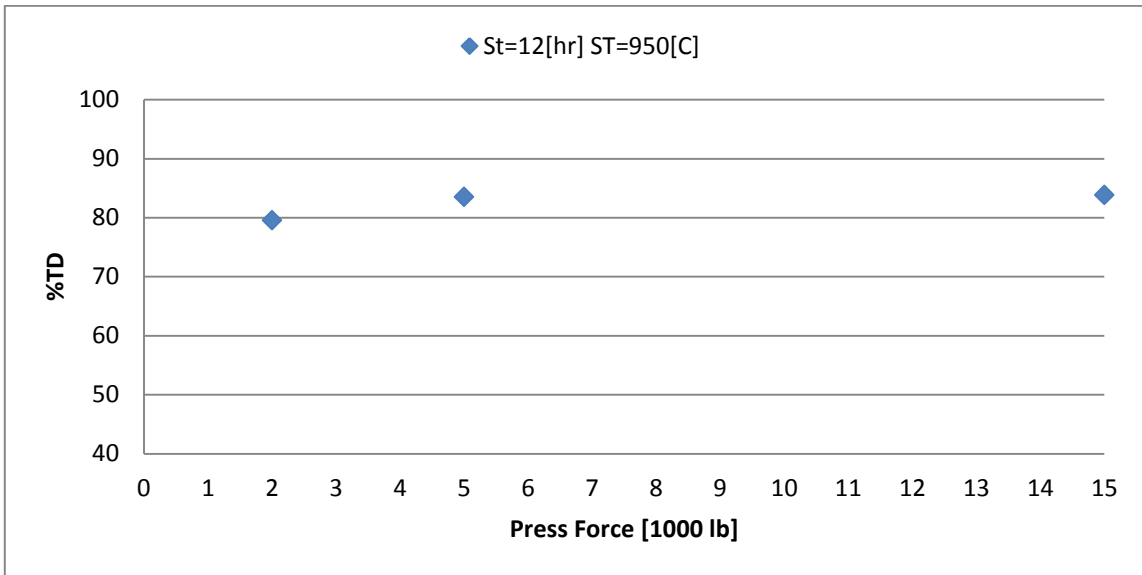


Figure A6-3: Sintering data for U-10Zr HDH pellets at 3 different pressing forces

APPENDIX 7

IMAGES OF EXTRUDED PRODUCTS

This appendix contains additional images of the microstructure of the extruded products. The images are presented with uranium samples first, followed by U-10Zr samples. Furthermore, the samples are in order of extrusion.



Figure A7-1: BSE image of extrusion 7 U tube

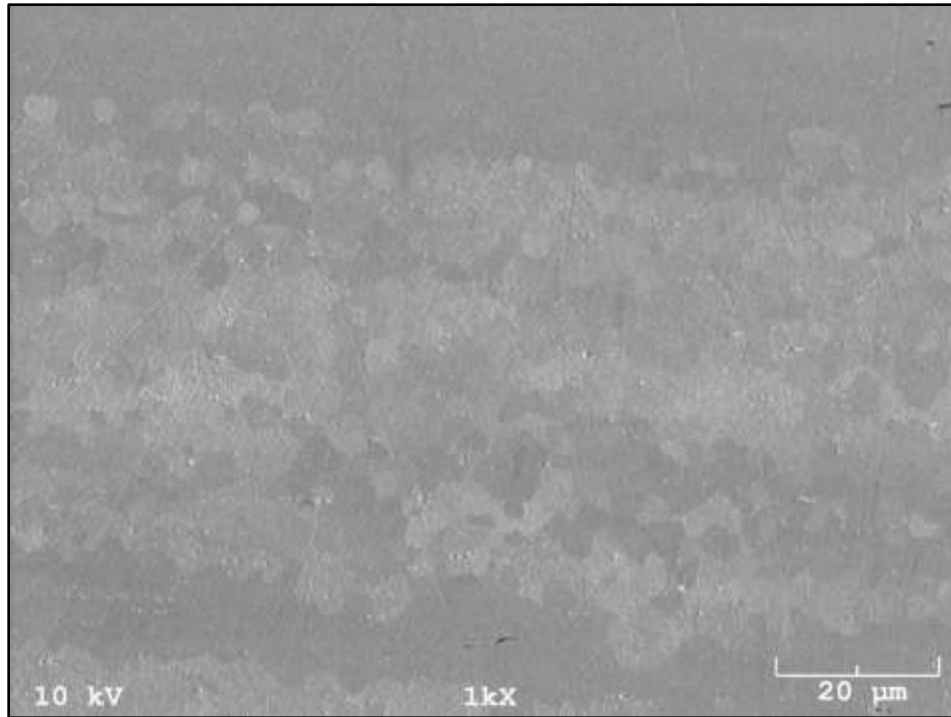


Figure A7-2: BSE image of extrusion 7 U tube (higher magnification of Figure A7-1)

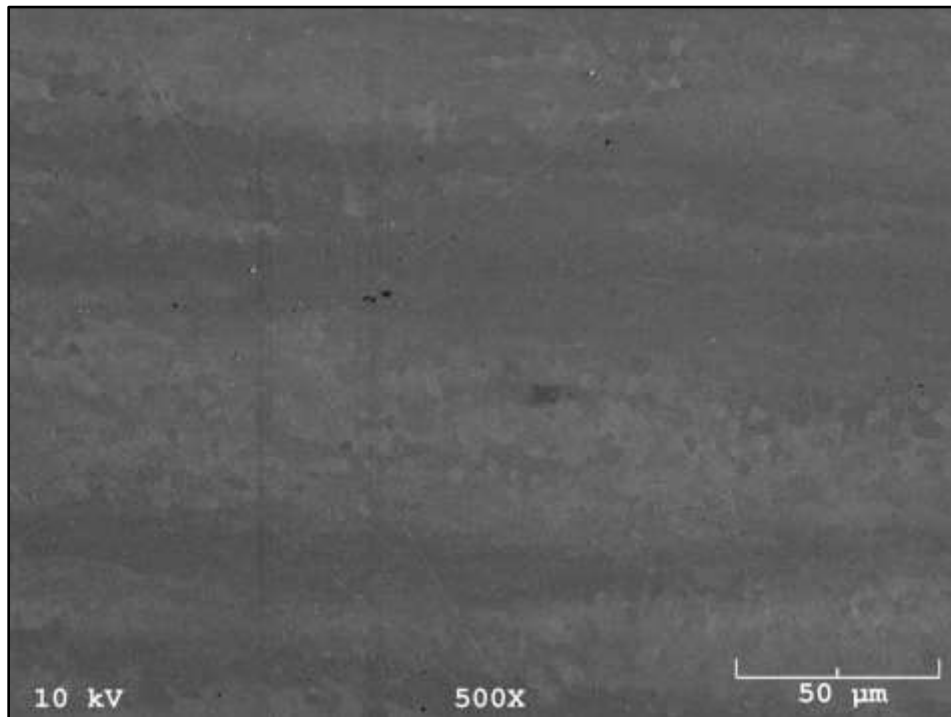


Figure A7-3: BSE image of extrusion 7 U tube

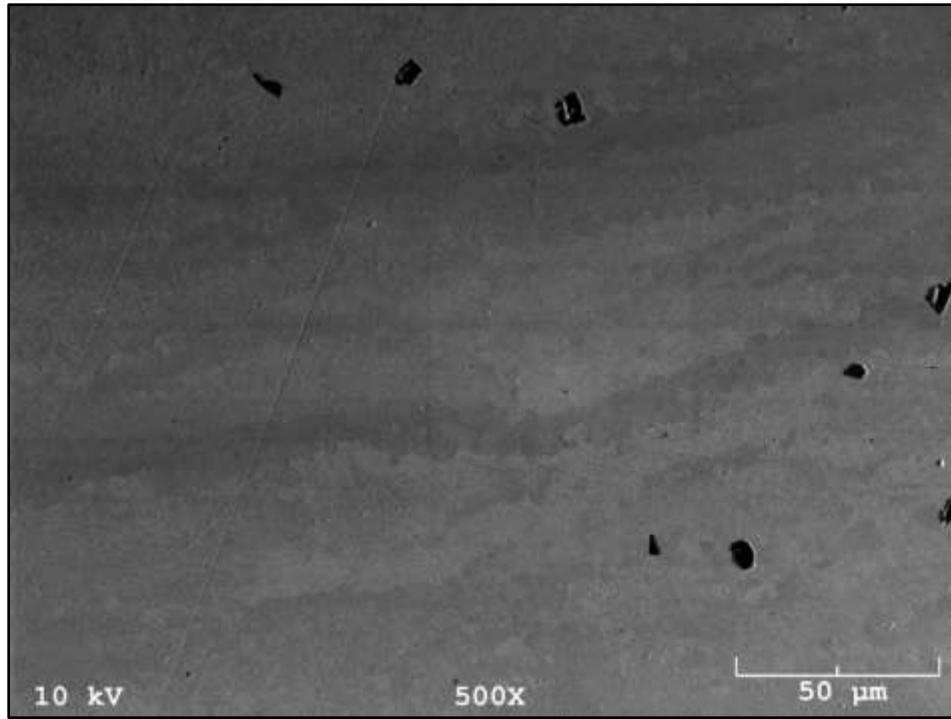


Figure A7-4: BSE image of extrusion 7 U tube

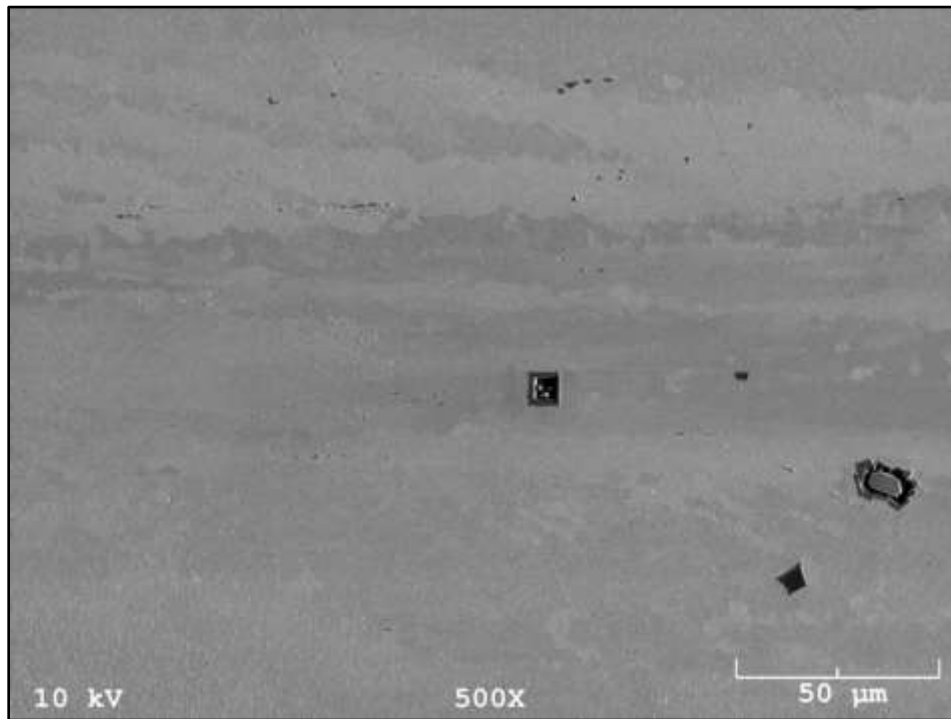


Figure A7-5: BSE image of extrusion 7 U tube

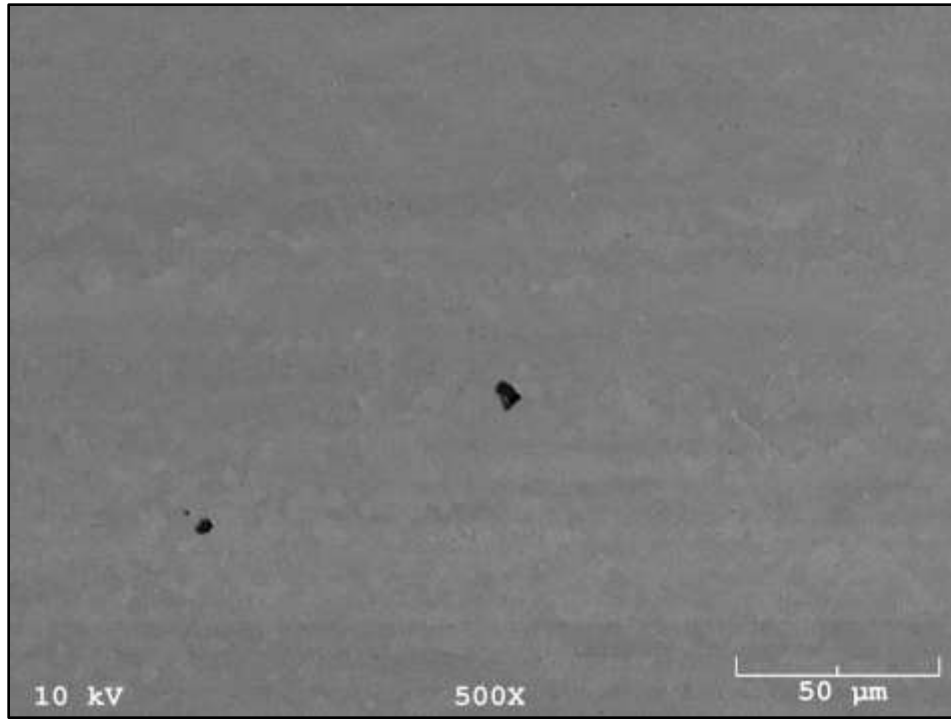


Figure A7-6: BSE image of extrusion 7 U tube

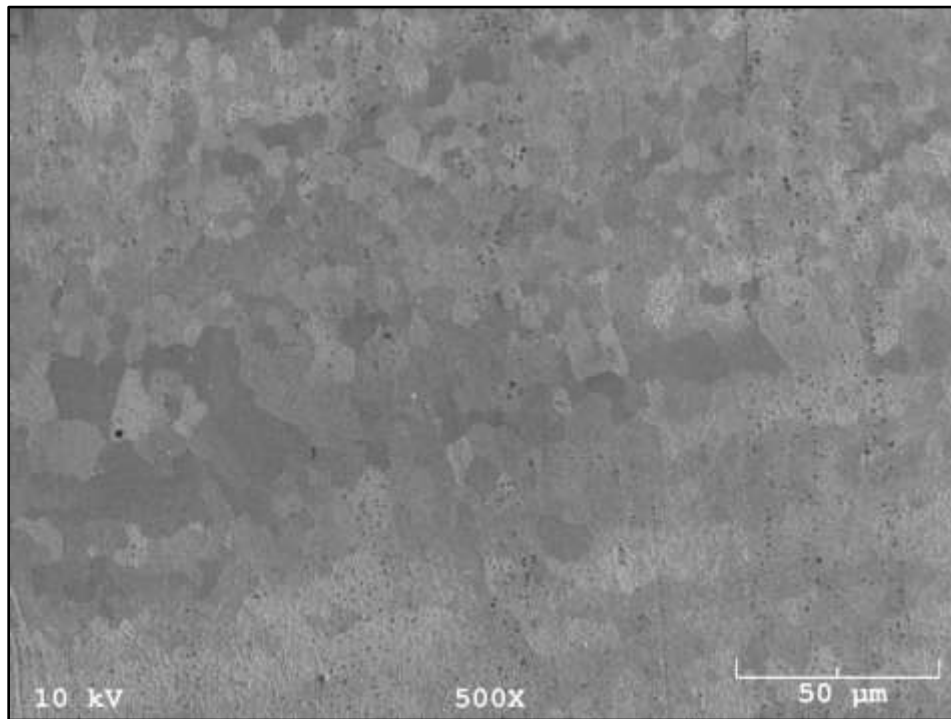


Figure A7-7: BSE image of extrusion 12 U rod

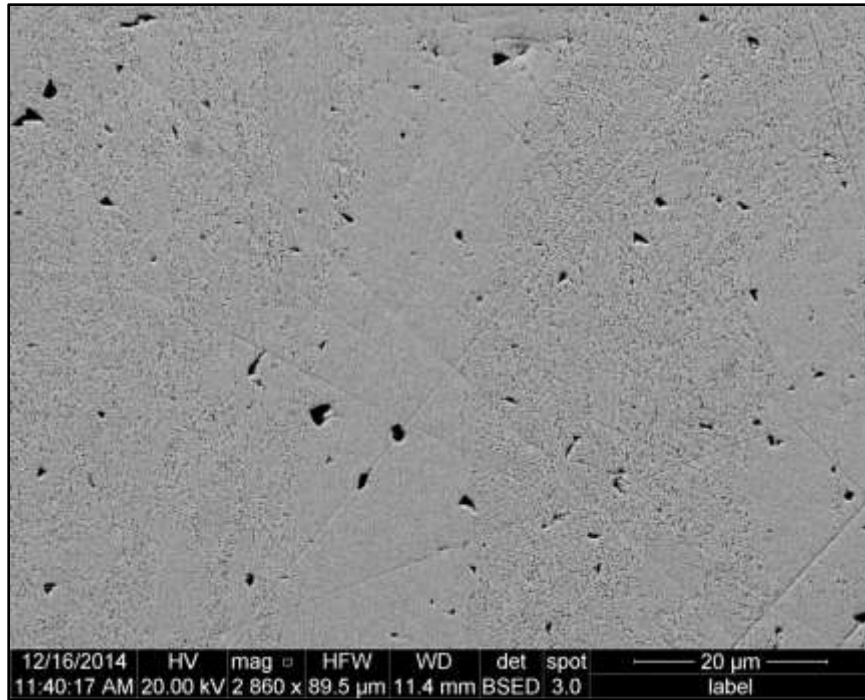


Figure A7-8: BSE image of extrusion 1 U-10Zr rod

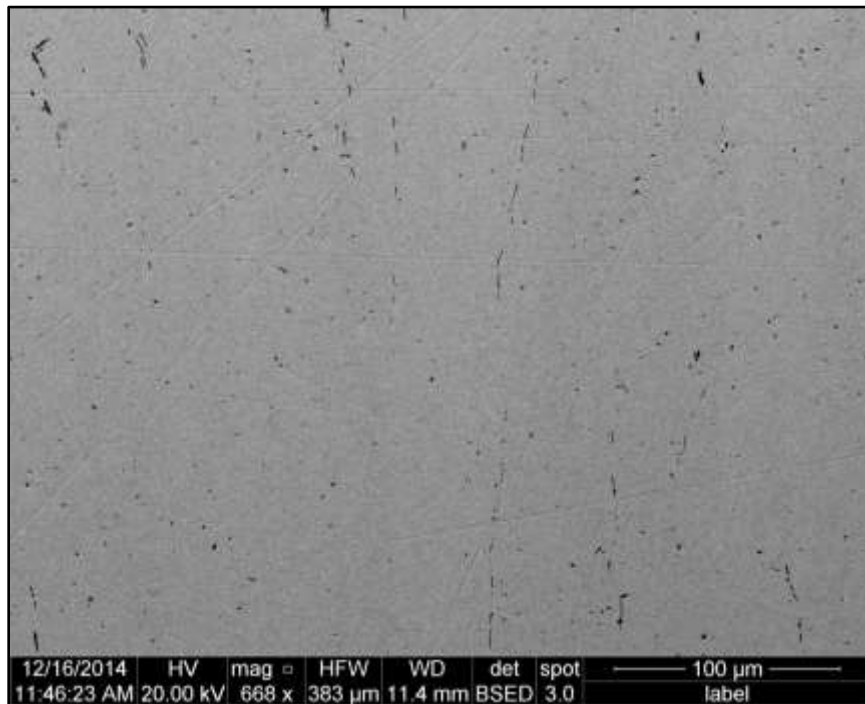


Figure A7-9: BSE image of extrusion 1 U-10Zr rod

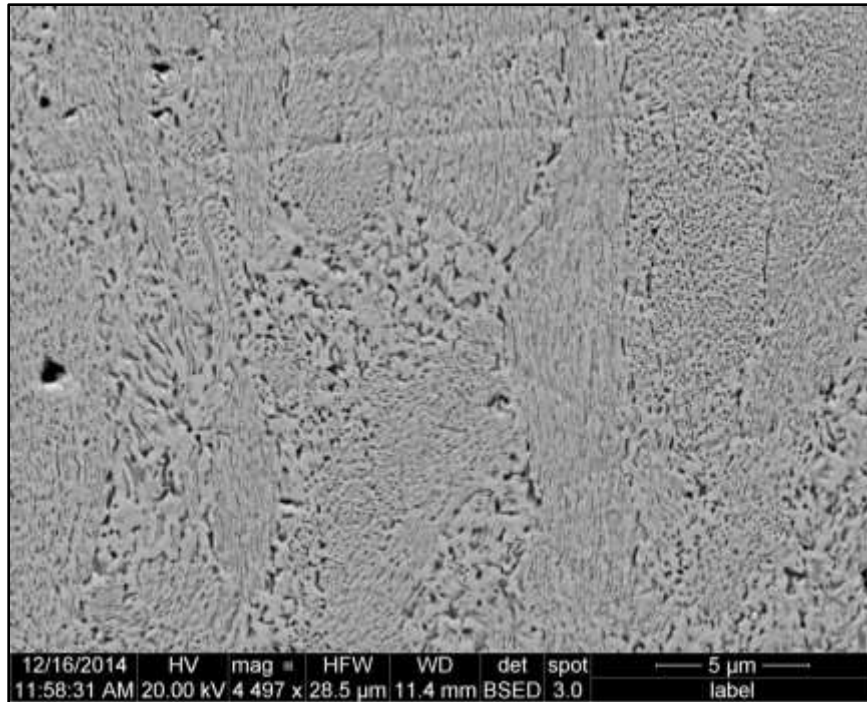


Figure A7-10: BSE image of extrusion 1 U-10Zr rod

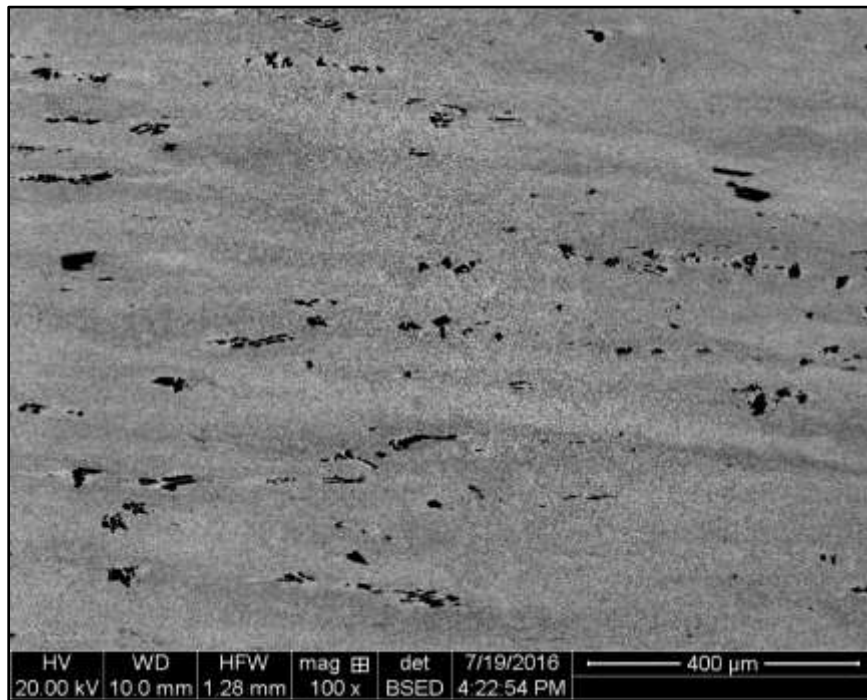


Figure A7-11: BSE image of extrusion 11 U-10Zr rod

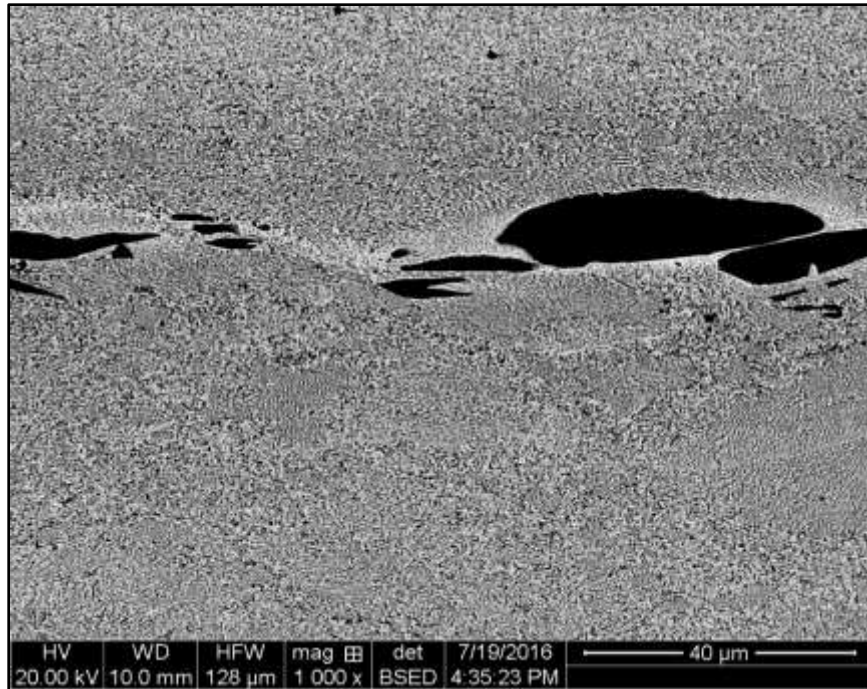


Figure A7-12: BSE image of extrusion 11 U-10Zr rod



Figure A7-13: BSE image of extrusion 11 U-10Zr rod

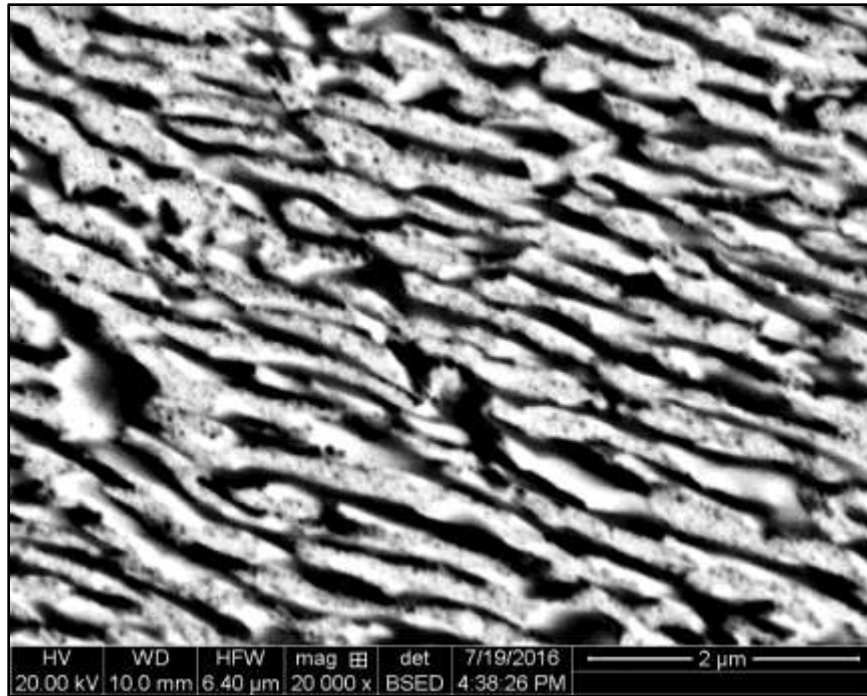


Figure A7-14: BSE image of extrusion 11 U-10Zr rod

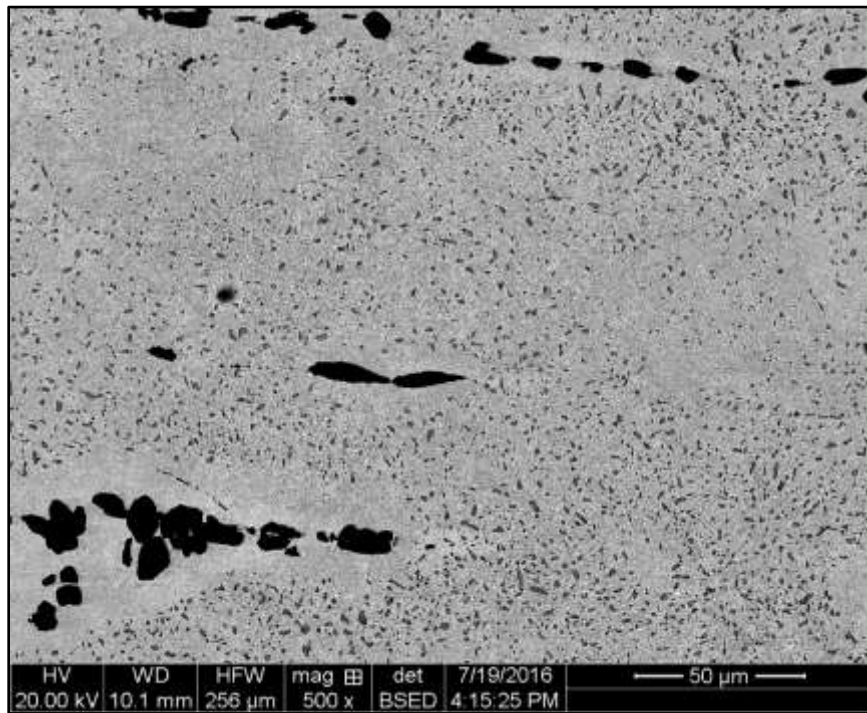


Figure A7-15: BSE image of heat treated extrusion 11 U-10Zr rod

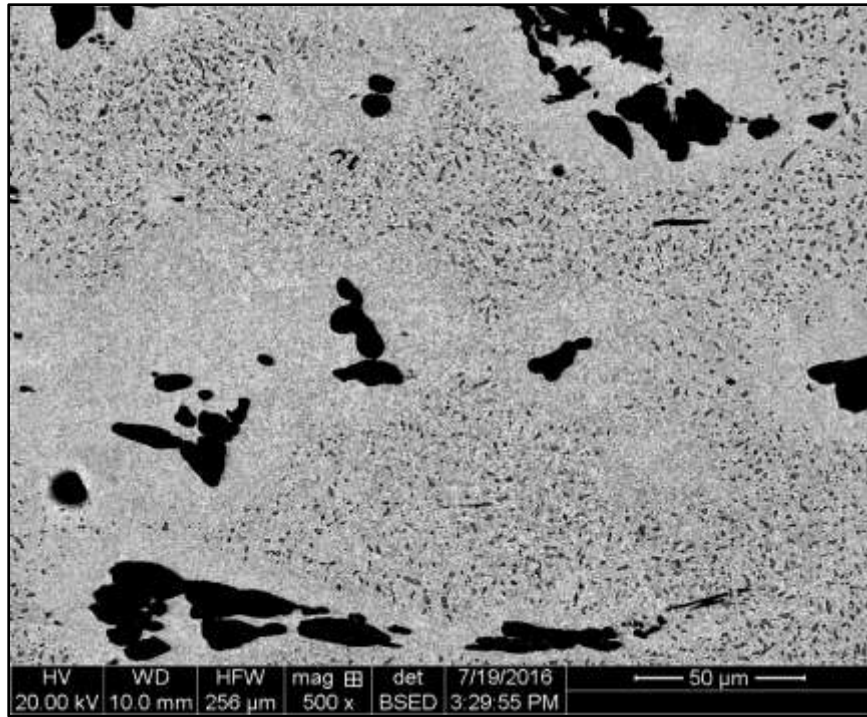


Figure A7-16: BSE image of heat treated extrusion 11 U-10Zr rod

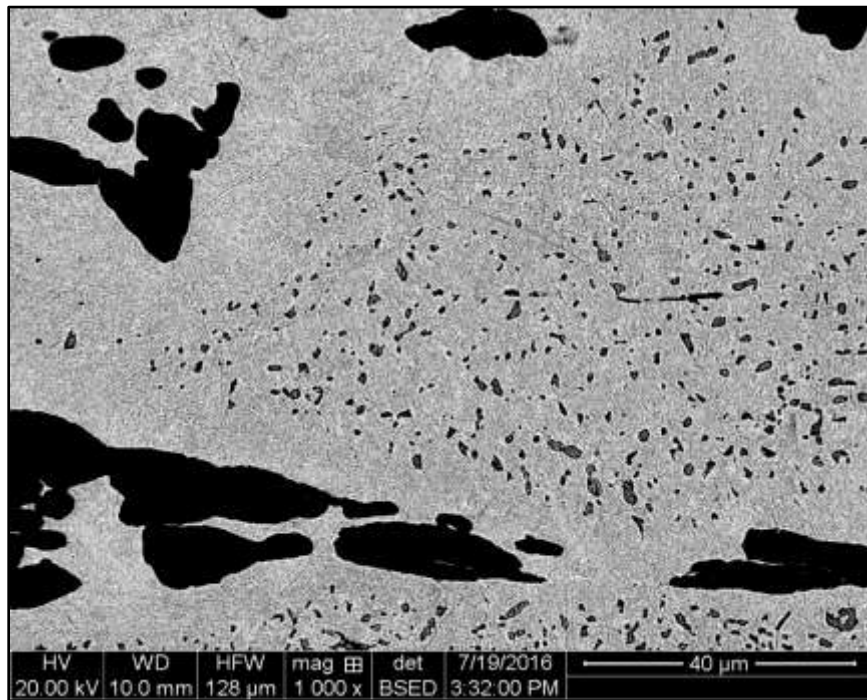


Figure A7-17: BSE image of heat treated extrusion 11 U-10Zr rod

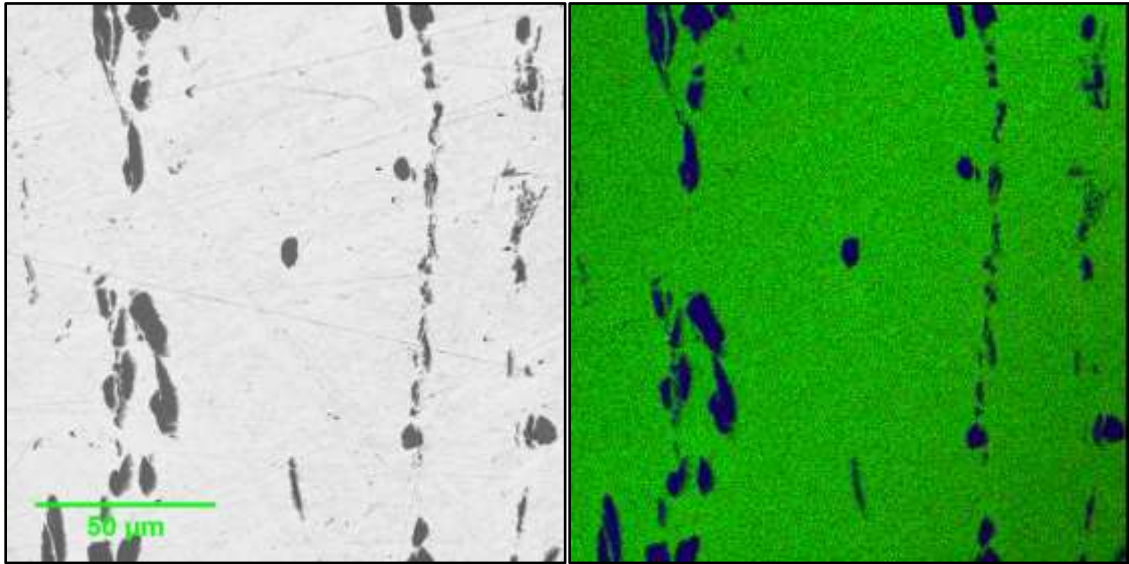


Figure A7-18: (left) BSE image and (right) EDX image of the same area of an extrusion 1 U-10Zr sample. The uranium is green and the zirconium is blue.

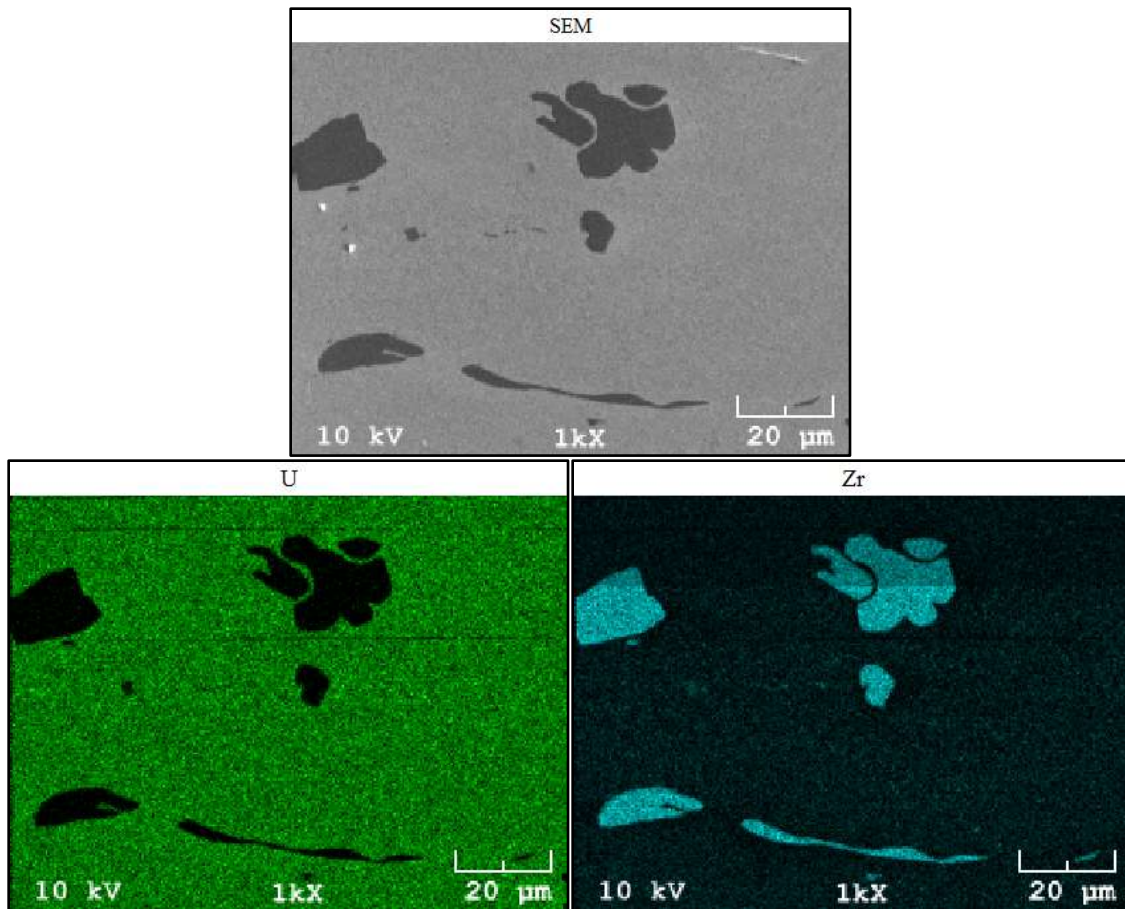


Figure A7-19: (top) BSE image and (bottom) EDX images of the same area of an extrusion 11 U-10Zr sample. The uranium is green and the zirconium is blue.

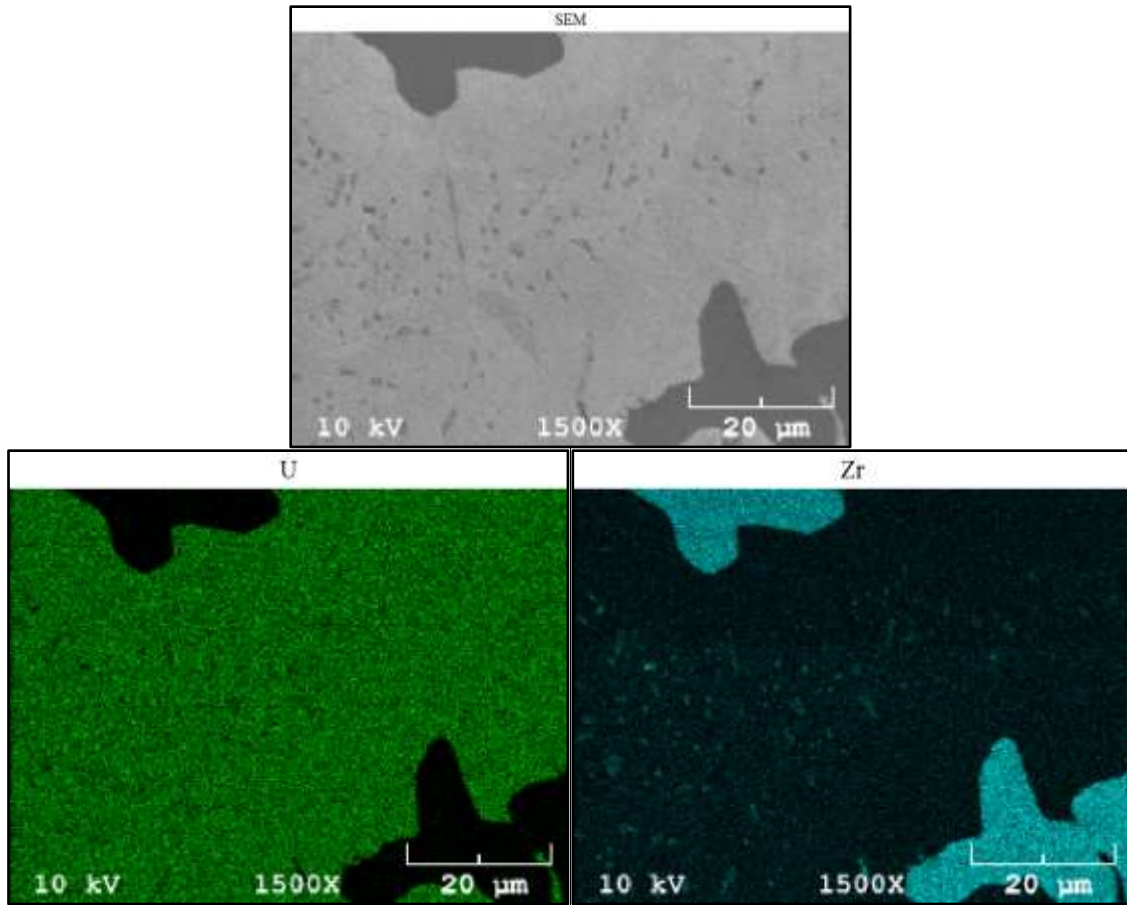


Figure A7-20: (top) BSE image and (bottom) EDX images of the same area of the heat treated extrusion 11 U-10Zr sample. The uranium is green and the zirconium is blue.

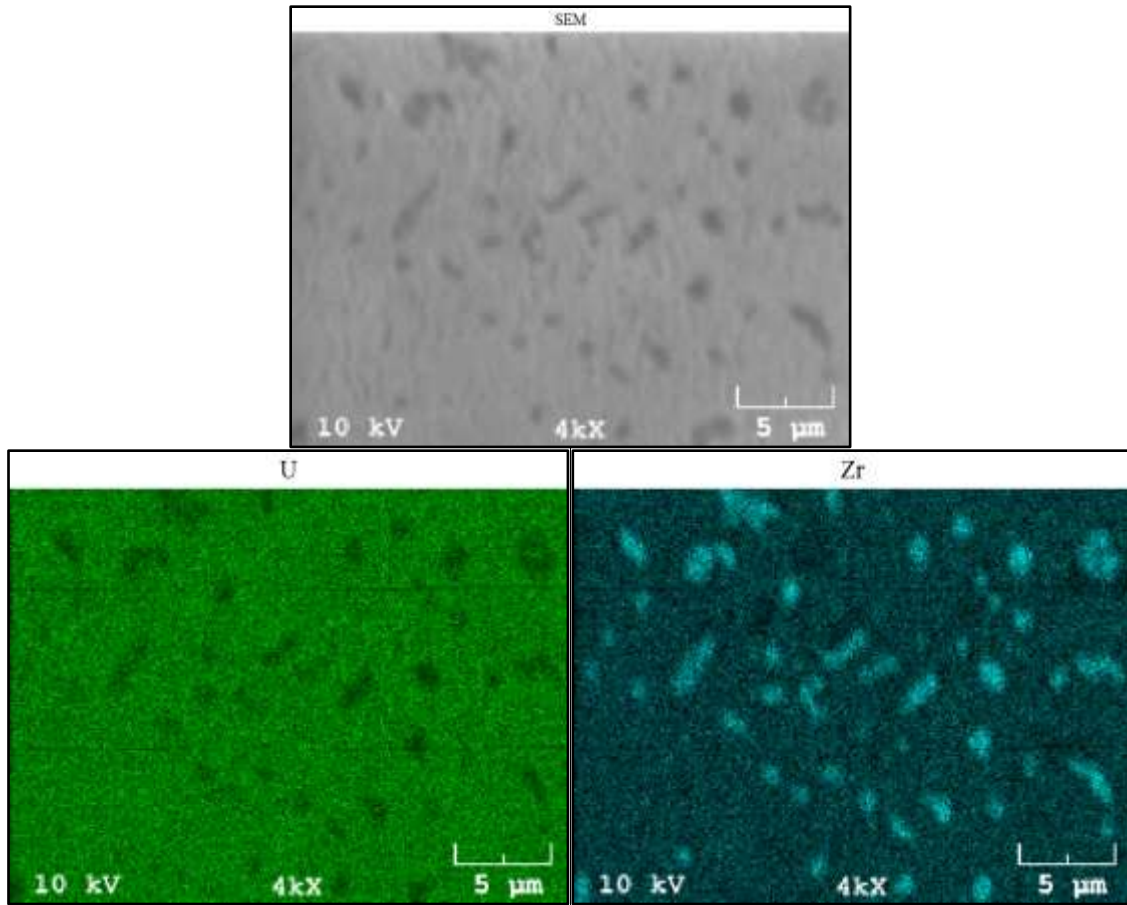


Figure A7-21: (top) BSE image and (bottom) EDX images of the same area of the heat treated extrusion 11 U-10Zr sample. The uranium is green and the zirconium is blue.